**FACULTY
OF MATHEMATICS
AND PHYSICS**
Charles University

DOCTORAL THESIS

Nikola Jajcay

Spatial and temporal scales of atmospheric dynamics

Department of Atmospheric Physics

Supervisor of the doctoral thesis: RNDr. Milan Paluš, DrSc.

Study programme: Physics

Study branch: Meteorology and Climatology

Prague 2018

I declare that I carried out this doctoral thesis independently, and only with the cited sources, literature and other professional sources.

I understand that my work relates to the rights and obligations under the Act No. 121/2000 Sb., the Copyright Act, as amended, in particular the fact that the Charles University has the right to conclude a license agreement on the use of this work as a school work pursuant to Section 60 subsection 1 of the Copyright Act.

In *Prague* date *4 May 2018*   *Nikola Jajcay*

Title: Spatial and temporal scales of atmospheric dynamics

Author: Nikola Jajcay

Department: Department of Atmospheric Physics

Supervisor: RNDr. Milan Paluš, DrSc., Institute of Computer Science, The Czech Academy of Sciences

Abstract: Earth climate, in general, varies on many temporal and spatial scales. In particular, climate observables exhibit recurring patterns and quasi-oscillatory phenomena with different periods. Although these oscillations might be weak in amplitude, they might have a non-negligible influence on variability on shorter time-scales due to cross-scale interactions, recently observed by *Paluš [2014b]*. This thesis supplies an introductory material for inferring the cross-scale information transfer from observational data, where the time series of interest are obtained using wavelet transform, and possible information transfer is studied using the tools from information theory. Finally, cross-scale interactions are studied in two climate phenomena: air temperature variability in Europe, in which we study phase-amplitude coupling from a slower oscillatory mode with an 8-year period on faster variability and its effects, and El Niño/ Southern Oscillation where we observe a causal chain of phase-phase and phase-amplitude couplings among distinct oscillatory modes.

Keywords: temporal scales; atmospheric dynamics; causal discovery; information transfer

I would like to dedicate this doctoral thesis to my childhood hero, Professor Stephen William Hawking. His book, *A Brief History of Time*, inspired me to pursue a path in science and still keeps inspiring me when trying to explain complex phenomena in an engaging and playful way.
Thank you, Professor Hawking.

"Remember to look up at the stars and not down at your feet. Try to make sense of what you see, and wonder about what makes the universe exist. Be curious!"
 Stephen Hawking, ⋆1942 – †2018

Contents

Introduction

To all facts there are laws,
The effect has its cause, and I mount to the cause.
  Owen Meredith (Lord Lytton)

With the rise of new technologies during the last, say, 5 decades the world around us changed, and arguably, so did the science. Fast technological advances allowed new data collection systems to emerge (satellites, buoys, in-situ measurements such as radiosondes or aircraft to name a few) and, of course, faster and more affordable computers in turn allowed for their faster and more precise processing and interpolation (e.g. reanalysis products). This combined generate a large, previously unthinkable, amount of experimental data, which promise new and unorthodox discoveries, hidden from us in the past. Therefore, the science in general needs new mathematical and computational approaches in order to process, and make sense of such large amounts of data. In the past, the physicists were usually divided into two groups: theoretical and experimental. I argue that now yet another category of scientists emerged — computational scientists or physicists — whose aim is to seek patterns, confirm old theories and mechanistic interpretations, and propose new ones, based (almost) solely on the data-driven research.

In the light of these advances, the purpose of this thesis is to update the classical view on atmospheric dynamics as a fluid dynamical system, which we need to model stochastically due to unresolved small-scale processes. Throughout the thesis, I will operate with the notion of a *complex system*, and argue that adopting this view while studying the interactions between atmospheric and oceanic processes could help to understand, and possibly even predict, the phenomena emerging from complex interactions within the climate system.

Exploiting the interdisciplinary options of today's science, I claim that borrowing the tools from information theory, in particular, the (conditional) mutual information and ideas of measuring entropy and information transfer, could help us tackle the old and prevailing problem of causality, i.e. directed relationships with a forecasting potential. The problem of distinguishing the cause-and-effect from spurious correlations dates back to the beginning of the 18thcentury when Irish philosopher Bishop Berkeley famously remarked that *"correlation does not imply causation"*. From that time onwards, the scientific community was puzzled by differentiating the apparent relationship (such as covariance or correlation) from the truly causal effect. The stakes were high — by claiming the causal relationship, one could indicate the predictive potential of the master variable towards the slave variable.

Connecting the complex systems paradigm with the advances in causal discovery algorithms became the recurrent theme, or leitmotif, in this thesis. The reasoning goes as follows: any experimental data, we are able to observe and measure (call them observables) emerged from an interplay between various physical processes. Let us imagine those various processes as subsystems or nodes in the complex network. By the means of applying the causal discovery algorithms we are able to find the connections, the edges, between the nodes such that they together indeed create a network. And from that network, which conceptualises the complex system we are studying, some observable emerges. Thus, we are trying to reverse-engineer the nature and find the subsystems and connections between them that are responsible for our observed measurement. The overview of the complex systems framework is presented in chapter 2.

With this particular view on complex atmospheric phenomena, I studied the interactions among temporal scales within atmospheric dynamics. Generally, the physical laws

that govern nature as we know it, are scale-invariant (at least in classical physics). Put simply, "they do not care" whether we are using them on length scales of 10 millimetres or tens of thousands of kilometres. However, this view of scientific reductionism is not completely true, since on various length scales we observe different energy injections and sinks. As an example, take the atmosphere: the energy from the Sun is the main energy injection at the planetary scale ($\sim 10^4$km spatial and roughly half a year to year temporal), then the large portion of this energy is transferred to a lesser, synoptic, scale and so on up to a so-called molecular scale, where the remainder of the energy is dissipated due to viscosity and molecular character of particles. From this description, it is immediately obvious that the energy transfer across the scales is omnipresent in such complex system as the atmosphere. The problem of scaling in the climate system in theory, and also in data, is addressed in the first half of chapter 3. The second half of this chapter is devoted to the general overview of the information transfer in atmospheric dynamics. That means the description of oscillatory patterns, the methods for extracting such patterns, the measures of dependence between the time series, followed by a quick introduction to information theory, and finally, a brief presentation of a topic of statistical hypothesis testing are all presented.

The reasonable assumption after claiming an energy transfer across temporal scales would be that also an information transfer across the temporal scales is present in atmospheric dynamics. This possibility was just recently studied by *Paluš [2014a,b]*, where he found that the slow atmospheric oscillatory phenomena with periods around 8 years are causally tied with faster oscillation, around one-year periodicities. In chapter 4 we follow up this direction and examine the effects of this 8–year cycle on faster temporal scales by extensively studying the behaviour of faster atmospheric modes, conditioned of the particular phase of the slower phenomenon. The general methodology of how to approach an information transfer in climate data and the results from various temperature station data, as well as gridded analysis data, are presented after the introduction to typical time scales governing the atmospheric dynamics in the European region. Within this chapter, the temporal, spatial and seasonal variations of the effect are also studied, in order to present the fullest possible picture of this interesting cross-frequency coupling phenomenon.

Whereas studying the cross-frequency coupling in Europe, in particular phenomena around 8 years, which may have stemmed from the dynamics of the North Atlantic Oscillation, was similar to studying the impacts of a large atmospheric mode on faster (therefore more localised) behaviour of temperature variability, the subsequent chapter 5 is dedicated to the atmospheric, or more precisely, atmospheric-oceanic phenomenon by itself — the El Niño/Southern Oscillation. The El Niño/Southern Oscillation is one of the, if not the oldest observed atmospheric-oceanic phenomenon in a history of humankind. Very shortly, it is an irregularly periodic variation in sea level pressure, associated winds, and sea surface temperatures over the tropical, mostly eastern and central, Pacific ocean. Because of its scale and mechanisms, it affects the climate not only in the tropics but through various teleconnections is able to perturb the typical circulation patterns in much of the subtropics and even midlatitudes. Following the reasoning developed earlier (the energy transfer gives rise to the information transfer), we adopted this view and exploited the causal discovery framework in order to depict

and study the low-frequency coupling to the high-frequency variability. The chapter firstly introduces the ENSO phenomenon, gives an overview of how we, as a humankind, observe ENSO and states the main physical mechanisms behind the oscillation. Since it is very well known that ENSO, as a complex system, constitutes of various temporal scales, or rather pacemakers that contribute to the overall variability, the overview of temporal scales in ENSO figures as a section just after the physical description. Afterwards, a short summary of ENSO modelling is presented. Finally, one of the observed ENSO time series — the Niño 3.4 index — underwent the cross-scale analysis, where we found a suite of significant interactions that, we believe, are instrumental in setting the extreme cold (La Niña), or warm (El Niño) event.

After studying the consequences of detected cross-frequency interactions, we also opted for studying the very same interactions in various ENSO models. The reasoning behind this is that we believe that the cross-scale interactions are a fundamental property of complex systems and any good, or close to reality, a model should, of course, also replicate the cross-scale interactions. With this goal in our minds, we studied two conceptual models of ENSO (one dynamical — the parametric recharge oscillator due to *Stein et al. [2014]*, and one statistical, based on the idea of linear inverse models and due to *Kondrashov et al. [2005]*) and a suite of CMIP5 global circulation models *[Taylor et al., 2012]*, concretely, their representation of ENSO dynamics, captured by the modelled Niño 3.4 index. As a final piece of the puzzle, we included the robustness analysis as the final part of chapter 5, where we contemplate the strength and significance of our findings.

As a good habit, this thesis is concluded and summarised in chapter 6, where the main theoretical viewpoints and results are outlined and possible outlook for similar work is presented. Furthermore, this thesis is accompanied by an appendix, where I describe my Python package `pyCliTS` (Python Climate Time Series) and its methods for analysing the spatio-temporal climate data, usually distributed as a `netCDF` archive. This package was used in order to perform all the computations needed in this thesis and was written throughout the course of my doctoral studies. I thought it would be a nice addition to the overall work I have done. Following the description of the package, I also included figures and tables associated with the chapters 4 and 5 that accompany the main text but are not in any way essential for the scientific points I am trying to make.

I wish to all potential readers that they learn something new from this thesis, which will stimulate their curiosity and keep them asking and wondering about our world.

Complex systems framework

Nature uses only the longest threads to weave her patterns, so that each small piece of her fabric reveals the organization of the entire tapestry.
  Richard P. Feynman

An introductory definition of complex systems would be that of a *"system composed of many components"*. However, this simple definition barely scratches the surface of how powerful the perspective of complex systems could be. To fully appreciate the notion of complex systems, one has to recognise strengths and weaknesses of how science has previously approached understanding the world around us *[Bar-Yam, 2002]*.

As *Bar-Yam [2002]* notes, one of the most important observations in science in general, is that everything is made out of parts. Then we proceed to figure out how its parts work; this will help us know how the systems as a whole work. Therefore, scientists consider a study of parts usually to be a study of the system in general. The problem is that we left out the relationships between the parts — how the parts interact.

From this emerges a better definition of complex systems as a *"new approach to science, studying how relationships between parts give rise to collective behaviours of a system, and how the system interacts and forms relationships with its environment" [Bar-Yam, 2002]*. This approach makes it possible for us to define and contemplate terms that shape the behaviour of complex systems such as *emergence*, *interdependence* and *self-organising patterns*.

As we will see later, these properties of complex systems will shape our understanding of some important phenomena emergent from Earth's climate system. The purpose of this chapter is to introduce the basic concepts and tools used in the study of complex systems: I will introduce and define dynamical system from a mathematical perspective, establish a notion of complex networks and relationships between the parts of such networks and lay the foundations of how we analyse different scales in atmospheric dynamics.

2.1 Dynamical systems

What is a dynamical system? Virtually *anything* that evolves over time can be thought of as a dynamical system. It consists of two main parts: a state vector, which exactly describes the state of some system, and a function (rule), which advances the state of the system to the next instant of time, given the current state *[Scheinerman, 2012]*. The state vector must completely determine the system's state, in the example of a simple pendulum, the state vector would consist of an angle, θ, and an angular velocity, ω. The function, which describes how these two variables evolve in time in the case would be Newton's second law (relating force applied to the pendulum with its mass and acceleration) and a simple formula relating angle with velocity, $\theta'(t) = \omega(t)$. The time in the notion of dynamical systems can be thought of as discrete, as separate chunks, each following the next, or as continuous, in which case it runs smoothly. Of course, in real-world applications like Earth's climate, the time is always continuous.

2.1.1 Autonomous systems

One of the most powerful and ubiquitous behaviours of systems, in general, is an oscillation. Oscillation is the repetitive variation, typically in time, of some measure about a central value. This central value serves as an equilibrium and the system oscillates between states around equilibrium. The pendulum from the former paragraph can serve

as a prototypical example of an oscillatory behaviour. By defining oscillatory behaviour, we shall progress to the division of dynamical systems into forced, conservative and self-sustained, of which the self-sustained oscillation is a prime example.

Self-sustained oscillators were introduced by *Andronov et al. [1937]* (much later edition available as *Andronov et al. [2013]*), although Rayleigh has already distinguished between forced and maintained oscillations, and H. Poincaré introduced the notion of the limit cycle. These oscillators are a subset of the class of dynamical systems and include chaotic oscillations and as such are omnipresent in nature: a pendulum clock, a firefly emitting light pulses, a vacuum tube radio generator, and a contracting human heart among many of such systems *[Pikovsky et al., 2003]*.

Mathematically, a self-sustained or *autonomous* system is defined by having a limit cycle in its phase space. That is, the trajectory in a phase space corresponds to a closed curve, and a particular state is repeated after the period T. As an example, consider a simple system, whose temporal dynamics as a time series and a phase space portrait is depicted in Fig. 2.1. In this picture, equivalent states $x(t)$ and $x(t + T)$, where T is the period of the system, correspond to the same point in the phase space, although correspond to different points in the time series representation, with the distance between them of one period. The form of this cycle, and hence the form of the oscillation itself is completely determined by the internal parameters of the system *[Pikovsky et al., 2003]*.
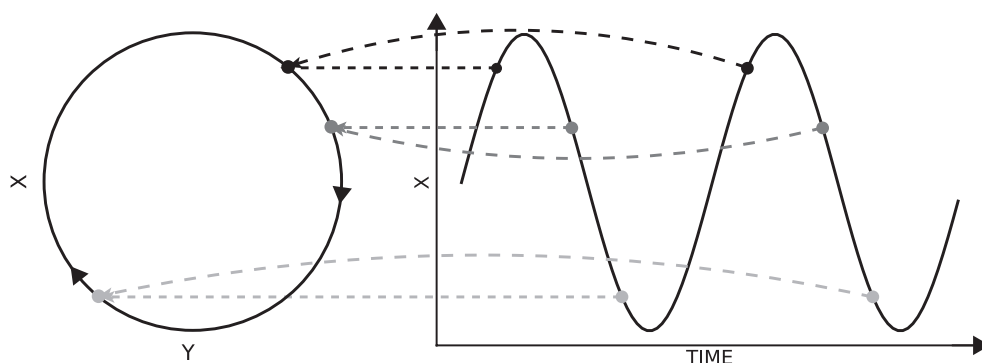
FIG. 2.1. | Example of a periodic oscillation, which is represented by a closed curve in the phase space (left) of the system: equivalent states $x(t)$ and $x(t + T)$ correspond to the same point on a limit cycle.

The limit cycle of linear (or quasilinear) oscillator is nearly a circle, hence the oscillation itself is a sine wave, and could be described mathematically as

$$x(t) = A \sin \omega_0 t + \phi_0, \tag{2.1}$$

where ω_0 denotes the angular frequency, which is related to the oscillation period T by $\omega_0 = 2\pi/T$. Next, the intensity of an oscillation is denoted by its amplitude A and $\phi(t) = \omega_0 t + \phi_0$ is its phase, with ϕ_0 being the initial phase. Having defined the amplitude and the phase of the oscillator, we shall proceed to state the main features of oscillators.

Self-sustained oscillations are non-decaying stable oscillations in autonomous dissipative systems. As an opposition to the self-sustained oscillators, we can think of

forced oscillators. Although, both of them are represented by closed curves in the phase space (recall Fig. 2.1 left), they have an essential difference: the phase on a limit cycle is free, but the phase on the stable closed curve of the forced system is unambiguously related to the phase of the external force *[Pikovsky et al., 2003]*. In the latter text, we will mainly work with autonomous systems as we will see later, they can exhibit interesting behaviour once they are coupled to some other autonomous system.

2.1.2 Introducing coupling and causal relations

On our route to complex systems, let us start with the simplest possible case, that is coupling two oscillators together. Generally speaking, the interaction between two systems is nonsymmetrical: either one oscillator is more powerful than the other, or they influence each other to different extents or both. On a descriptive level, let us denote the partial frequencies of two autonomous oscillators as ω_1 and ω_2 and let $\omega_1 < \omega_2$; and the observed frequencies of interacting oscillators by $\Omega_{1,2}$. Then, if the coupling is strong enough, frequency locking will appear as a mutual adjustment of frequencies, so that $\Omega_1 = \Omega_2 = \Omega$ and typically $\omega_1 < \Omega < \omega_2$ *[Pikovsky et al., 2003]*. This frequency locking is just one example of interesting behaviours that emerge from coupling dynamical systems together.

On a model level, one can imagine coupling, or interaction between systems, simply as introducing a variable from one such (sub)system to the equations of the other. If the influence is bi-directional, a variable from second such subsystems appears in the equations. Now, let assume that the coupling is uni-directional, from subsystem one to subsystem two. If we knew the systems equations, of course, we could infer that the systems are coupled and the exact nature of this coupling. On the other hand, if we did not know the full description of the system in the form of equations and only work with measured time series, the problem becomes much more interesting. With this, we stumbled upon one of the fundamental questions of the most natural and social sciences over the history: detection and clarification of *cause-effect* relationships, or shortly a causal discovery.

To define causality as such, one may spend numerous evenings reading literature and still not come to a satisfactory definition. Nevertheless, according to Wikipedia, a causality is *"the natural or worldly agency or efficacy that connects one process (the cause) with another process, or state (the effect), where the first is partly responsible for the second, and the second is partly dependent on the first" [wikipedia.org, b]*. Despite the fact, that causality expresses a kind of a "law" necessity, causal relationships are often investigated in situations which are influenced by uncertainty, and is viewed as a phenomenon which can be "measured" and quantified *[Hlaváčková-Schindler et al., 2007]*.

While considering deterministic approaches, or systems, the literature discusses two important conditions for causality to exist: necessity (*"if X occurs, then Y must occur"*), and sufficiency (*"if Y occurs, then X must have occurred"*) *[Granger, 1980]*. However, this deterministic formulation is not tractable in reality, since almost no real-life system is strictly deterministic in the sense, that its outcomes can be predicted with certainty *[Hlaváčková-Schindler et al., 2007]*. In the real-world applications, it makes much more sense to consider a so-called probabilistic notion of causality described by *Suppes [1970]*

as *"an event X is to cause to the event Y if: X occurs before Y, likelihood of X is non zero, and likelihood of occurring Y given X is more than the likelihood of Y occurring alone"*.

The question, of course, would be why do we want to know the causal relations in our system? What information can we get? Practically, three things: uncovering the underlying dynamics, assessing susceptibilities to perturbations in systems *[Runge et al., 2015]* and enhancing the prediction skill. To illustrate what I mean by these three reasons to bother with causality, consider the illustration in Fig. 2.2.

complex system consisting
of 3 oscillators

observable, e.g. temperature
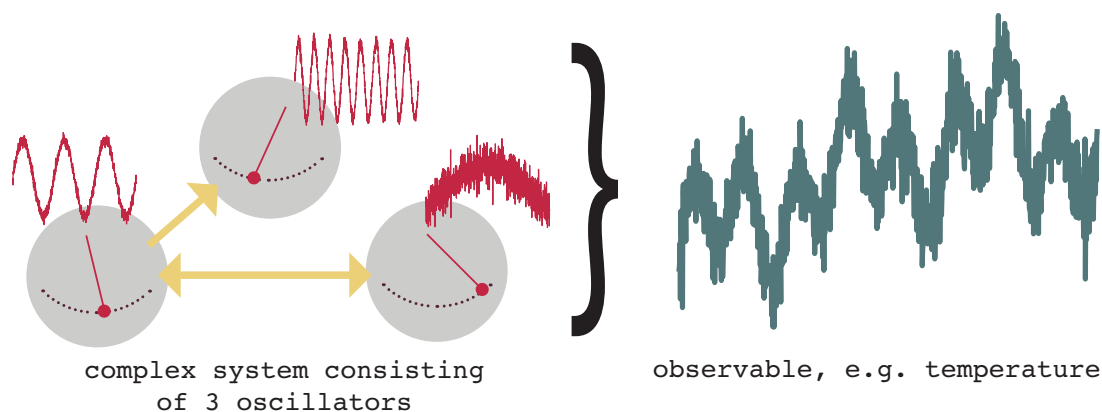
FIG. 2.2. | Illustration of causal relationships: on the left-hand side is complex systems with three autonomous oscillators with uni- and bi-directional coupling with different frequencies. From the intertwined dynamics of oscillators emerge the so-called observable — a time series we can measure, on the right-hand side, usually contaminated with noise.

On the left-hand side of the Fig. 2.2 we have three self-sustained (or autonomous) oscillators coupled together in some way. In this illustration, they exhibit uni-directional coupling from middle to fastest oscillator and bi-directional coupling between middle and slow oscillator. From the collective dynamics of these coupled oscillators (which we can call a complex system) emerges a so-called observable, i.e. a time series we can measure and analyse. For the purpose of this example, let it be a surface temperature time series from some station. One peculiar way how to imagine causal relations and consequences of them is to consider that nature works from left to right: the oscillators are parts of a complex system, their collective dynamics give rise to a variable, which we call the temperature. Now, we can (and should) measure temperature and record it, hence generate a time series. By applying causal discovery algorithms we are trying to reverse-engineer the nature and working from right to left: given the time series of our interest, we are trying to identify the subsystems (i.e. the individual oscillators), describe them (for example by their frequency, and instantaneous phase and amplitude), and infer the relationships between them.

Inferring the relationships between subsystems would certainly help in uncovering the underlying dynamics — in this case, it is very well defined by the subsystems themselves and their properties, and by the relationships between them. As for assessing susceptibilities — imagine introducing a perturbation into the fast oscillator in the illustration, e.g. in the form of elevated amplitude. This perturbation would spread and

mediate in the system and by knowing the relationships among subsystems, we would be able to predict what is going to happen and possibly take an appropriate course of action. As a perturbation imagine e.g. extreme events, volcanic eruptions, geoengineering etc. and as a system consider Earth's climate, hence it is of utter importance to study causal relations in this way *[Runge et al., 2015]*. Lastly, knowing the relationships between the subsystems could improve the prediction and forecasting, assuming that we are able to predict the subsystems' behaviour within particular uncertainty bounds.

2.2 Complex systems & networks

Although briefly defined in the short introduction to this chapter, complex systems definitely deserve more attention. As noted above, we can think of complex systems science as studying how relationships between parts of a system give rise to collective, usually nonlinear, behaviours. By definition, these systems exhibit behaviours, which is intrinsically difficult to model due to its dependencies, relationships, or interactions between their parts. This is the difference between various systems: general systems theory focuses on the collective behaviours, but in non-complex systems, the reductionist approach is usually taken. This means that the collective behaviour is some *linear* combination of individual behaviours of the systems' parts. The emerging nonlinear behaviour of complex systems is indeed the key difference — emergent properties (meaning they are not apparent from individual components in isolation but result from interactions of the individual parts), often chaotic nature (sensitive dependence on initial conditions) and the difficulty to make sensible model: all are rising from the nonlinearity of such systems.

The Earth is a highly complex system formed by a large number of subsystems, including biosphere, atmosphere, lithosphere, social and economic systems and more *[Donner et al., 2009]*. Each of this subsystems can be also viewed as a complex system, e.g. we can treat the atmosphere as a complex system consisted of synoptic-scale phenomena, and go even further and consider synoptic-scale phenomena as a complex system consisting of local interacting weather patterns and in turn consider those as complex systems consisting of individual particles of air, and so on. As a result of these interactions, the Earth can be portrayed as a complex and evolving network. As I stated before, if one studies only the part of the Earth's complex system, one would completely miss some of the relevant facts. To motivate with an example, consider that the tectonic activity and the resulting motion of plates as an important trigger for the formation of oceanic currents, which determines the climate on large scales through heat transfer *[Saltzman, 2002]*, for which there exists numerous concrete examples, such as the closure of the seaway between North and South America started an era of increasing glaciation in both poles *[Haug et al., 2001]*.

2.2.1 Complex network paradigm

Given the structure of complex systems, such as the Earth, we operate on several subsystems, but notably also on their relationships. A particularly helpful approach arises

by the name of complex networks. Complex networks paradigm is a powerful toolbox for studying non-trivial topological features in a graph and hence studying the structure of statistical interrelationships between various subsystems.

Networks as such are all around us. Think of electric power grids, the Internet, highway and subway systems, neural networks, social networks, and much more. Historically, they have been mainly in the domain of the branch of discrete mathematics known as graph theory. Mathematically, a complex network is represented by a graph $G = (\mathcal{N}, \mathcal{L})$, which consists of two sets: $\mathcal{N}$, such that $\mathcal{N} \neq \emptyset$, and $\mathcal{L}$ is a set of (un)ordered pairs of elements of $\mathcal{N}$. The elements of $\mathcal{N} \equiv \{n_1, n_2, \ldots, n_N\}$ are the *nodes* (or *vertices*, or *points*) of the graph G, while the elements of $\mathcal{L} \equiv \{l_1, l_2, \ldots, l_K\}$ are its *links* (or *edges*, or *lines*) *[Boccaletti et al., 2006]*.

In an undirected graph, each of the links is defined by a couple of nodes i and j and the order is not important: in an undirected graph, as expected, we have $l_{i,j} = l_{j,i}$. In a directed graph, the order is important, thus $l_{i,j} \neq l_{j,i}$. In a basic definition of a graph, the links are either there or not, hence they are binary. An extension to this exists in the form of weighted network, where each link possesses its weight. Examples of a graph with 7 nodes ($N = 7$) and 14 links ($K = 14$) are presented in Fig. 2.3.
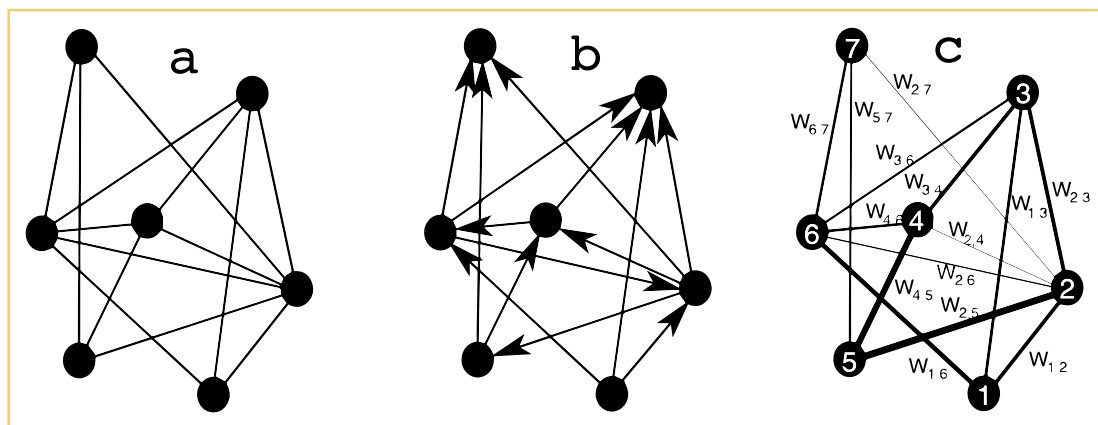
FIG. 2.3. | Graphical representation of undirected (**a**), a directed (**b**), and a weighted undirected (**c**) graph with 7 nodes and 14 links. Figure taken from *Boccaletti et al. [2006]*.

In climate science, the most used type of graph or network is undirected (similar to a network (a) in Fig. 2.3) — it is usually constructed with bivariate dependence measure such as correlation. Directed, or causal, graphs are used far less because of their complexity and the fact, that they are hard to interpret and often suffer from various robustness problems, in particular when using nonlinear approaches (for a discussion on linear vs. nonlinear approach see e.g. *[Hlinka et al., 2014b]*). Likewise, weighted networks are also not common in climate science, since they are hard to interpret and some of the measures commonly computed for unweighted networks are hard to generalise *[Boccaletti et al., 2006]*.

Although complex networks as defined above seem like a perfect match for studying systems in their full complexity, a question remains whether we can learn something new by using this approach. From its famous first use in climate science by *Tsonis and Roebber [2004]*, it gained much interested in the community and led to some significant advances in our understanding of climate (e.g. *Tsonis et al. [2006]; Ebert-Uphoff and Deng [2012]; Fountalis et al. [2015]; Wiedermann et al. [2016]; Hlinka et al. [2017b]* and much more). In a field of statistical climatology, a large body of approaches has been used in the past, including empirical orthogonal functions (EOF), maximum covariance analysis (MCA), or canonical correlation analysis (CCA) *[von Storch and Zwiers, 2002]*. Many classical approaches suffer from implicitly assuming linearity (EOF, MCA) and because of this, nonlinear generalisations of these methods emerged *[Donner et al., 2017]*. Another point of criticism would be that globally variance-maximising modes are not necessarily relevant locally, and the identified modes strongly depend on the spatial domain of the interest *[Monahan et al., 2009]*. Since complex networks has been successfully used in variety of other fields of application (see e.g. *Albert and Barabási [2002]; Newman [2003]; Boccaletti et al. [2006]*) as a methodological alternative, allowing to identify the general relevance of a given node within the graph, and also to highlight the important statistical associations among other nodes, it was only a matter of time until *Tsonis and Roebber [2004]* proposed to the apply complex networks framework in climate science.
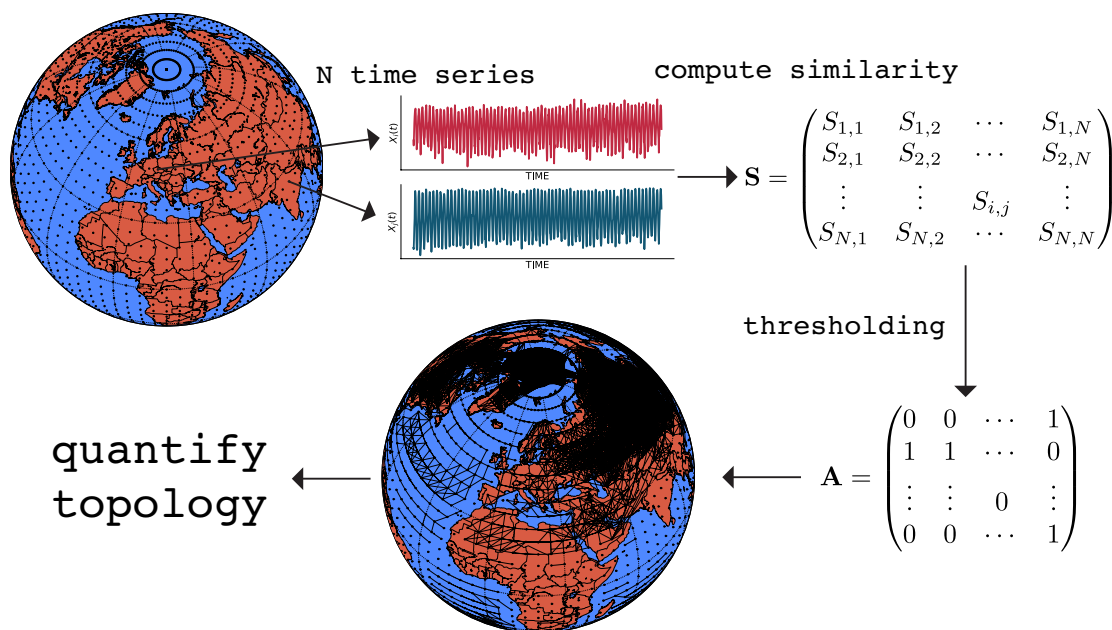
FIG. 2.4. | Schematic illustration of the construction of a climate network form a global gridded climatological data set. Inspired by a figure from *Donner et al. [2017]*.

To briefly illustrate the typical use of complex networks in climate science consider Fig. 2.4. First step consists of selecting the data and optionally preprocessing them, in order for the data to represent what we shall study. Next step is to compute a similarity between time series — here the options are vast. The first, and most natural choice would be to compute the correlation matrix, but we may opt to use other bi-directional measures, like mutual information or synchronisation. In this case, the similarity matrix

will be symmetric. Another family of similarity measures is uni-directional, e.g. Granger causality or transfer entropy, and of course, in this case, the matrix would be non-symmetric. Having computed the similarity matrix **S**, the usual step is to transform the similarity matrix into unweighted (binary) adjacency matrix **A** denoting whether the given statistical similarity is considered relevant. This nonlinear transformation corresponds to thresholding the similarity matrix as

$$A_{i,j} = \Theta(S_{i,j} - S^*)(1 - \delta_{i,j}), \tag{2.2}$$

where $\Theta(\cdot)$ denotes Heaviside function, $\delta_{i,j}$ the Kronecker delta and S^* denotes a threshold value *[Donner et al., 2017]*.

The last aforementioned step effectively creates a graph or a complex network, and subsequently, we can apply a variety of graph-theoretical measures to quantify a topology of such network. For a comprehensive review of network characteristics see e.g. *Albert and Barabási [2002]* or *Boccaletti et al. [2006]*.

The complex networks framework offers a powerful instrument in analyses of complex systems, and also a compelling concept when thinking about complex systems as such. In next chapter, I will describe how a temporal scales shape the behaviour of certain phenomena. It turns out that imagining processes at certain frequencies as nodes in a network, while the links would describe relationships between those processes is a robust portrayal of the studied system and presents a paradigm on which the state–of–the–art analyses of complex systems could be conducted.

Temporal scales in atmospheric dynamics

Big whirls have little whirls
that feed on their velocity,
and little whirls have lesser whirls,
and so on to viscosity.
    Lewis Fry Richardson

Physical laws of nature work with a notion of *scales*. Generally, a scale is a particular distance determined with the precision of one order of magnitude *[wikipedia.org, d]*. The concept of scale is of great importance, because of the decoupling phenomena, when it is believed that processes on different length scales are said they cannot affect each other. Scientific reductionism states that the physical laws on shortest scales can be used to derive a compact description at larger length scales. The scaling paradigm is, naturally, also present in the atmospheric physics, or more broadly, in fluid dynamics and thermodynamics.

3.1 Scaling in the climate system — theory

To see an origin of scaling, consider the basic equations of incompressible and dry hydrodynamics, the famous Navier–Stokes equations. They read

$$\frac{\partial \mathbf{v}}{\partial t} + (\mathbf{v} \cdot \nabla)\mathbf{v} = -\frac{\nabla p}{\rho_a} + \nu \nabla^2 \mathbf{v} + \mathbf{f} \tag{3.1}$$

$$\nabla \cdot \mathbf{v} = 0, \tag{3.2}$$

where $\mathbf{v}$ is the velocity of a fluid, t is time, p is the pressure, ρ_a is the air density, ν is kinematic viscosity, and $\mathbf{f}$ represents the body forces (per unit volume) due to stirring, gravity etc. Eqn. (3.1) expresses the conservation of momentum, while eqn. (3.2) expresses the conservation of mass in an incompressible fluid *[Lovejoy and Schertzer, 2013]*. These equations are formally invariant under isotropic "zooms" $\mathbf{x} = \lambda \mathbf{x}'$ as long as one rescales the other variables as

$$\mathbf{v} = \lambda^{\gamma_v} \mathbf{v}'$$

$$t = \lambda^{-\gamma_v + 1} t'$$

$$\nu = \lambda^{\gamma_v + 1} \nu' \tag{3.3}$$

$$\mathbf{f} = \lambda^{2\gamma_v - 1} \mathbf{f}',$$

where γ_v is an arbitrary scaling exponent. The rescaling of the viscosity may seem odd, but it may be understood as a rescaling of the eddy-viscosity or renormalised viscosity; similar remarks can be made for the forcing $\mathbf{f}$ *[Schertzer et al., 1998]*.

If an additional constraint is imposed, such as the conservation of energy flux, this is enough to determine the value of the coefficient γ_v. Indeed, considering the energy flux $\epsilon = -\partial v^2 / \partial t$, we find

$$\mathbf{x} = \lambda^1 \mathbf{x}'$$

$$\epsilon = \lambda^{-1 + 3\gamma_v} \epsilon'. \tag{3.4}$$

If the energy flux is scale-invariant, we get $\gamma_v = 1/3$; hence for fluctuations of the velocity Δv over distances Δx we obtain

$$\Delta x = \lambda^1 \Delta x'$$

$$\Delta v = \lambda^{1/3} \Delta v',$$

(3.5)

which gives us the famous *Kolmogorov [1941]* law:

$$\Delta v \approx \epsilon^{1/3} \Delta x^{H_v}; \quad H_v = \gamma_v = 1/3. \tag{3.6}$$

This Kolmogorov law is the prototype of emergent turbulent law, which communicates the fact, that the dynamics of fluids should be repeating scale after scale, or in other words, after some renormalisations, the dynamics is scale-invariant. However, the eqn. (3.6) does not hold at all observable scales: it breaks down due to a viscosity at small enough scales (the derivatives converge) and similarly, at large scales, the forcing term breaks the scaling symmetry *[Lovejoy and Schertzer, 2013]*. But since the outer scale is roughly the size of the planet and the inner ("viscous") scale is typically 0.1–1mm, the scaling range is potentially still of factor 10^{10}.

Let us make a transition from theoretical scaling based on the fluid dynamics equations to a more practical approach — consider the known atmospheric processes. Various atmospheric processes and their typical scales are summarised in Fig. 3.1 and Table 3.1. As the figure shows, processes in Earth's climate system span scales within a factor of 10^{10} in a spatial sense and even 10^{12} in a temporal sense. These processes exchange energy and influence each other in a non-trivial way. The energy is transferred in both directions simultaneously: the upscale cascade (smaller scales to larger), and the downscale cascade (larger to smaller). One can image energy as becoming a part of the atmospheric heat engine by entering at molecular level scale and exiting at the molecular level scale after a journey through weather systems (as illustrated in Fig. 3.1 and Table 3.1) at many temporal and spatial scales.

The upscale energy cascade begins with the interception of Sun's energy at Earth's surface by molecules and the energy is conducted to the air. Subsequently, the energy is transferred via convection, conduction, and radiation and through evaporation and condensation of water molecules to become the driving force of weather systems. On the other hand, the downscale energy cascade gets an injection at largest scales from the Sun (in the form of unequal heating which drives large-scale atmospheric motion), this energy is subsequently cascading downwards until the molecular level where is dissipated. Or alternatively, the molecules lose the energy while ascending or by radiation. In the light of both energy cascades, we see that the interaction between scales is important and as you can imagine, mathematically very complex. These cascades are usually local in Fourier space, or better said: the energy transfer is most efficient between neighbouring scales *[Lovejoy and Schertzer, 2013]*. According to *Rose and Sulem [1978]*, it is natural to consider a discrete hierarchy of eddies, which may be defined as a fluid "coherent" structures. Considering energy transfer from one scale to another, only the motions which can distort these eddies are dynamically important. After a short thinking and playing with important quantities, as in *Lovejoy and Schertzer [2013]*, we came to an
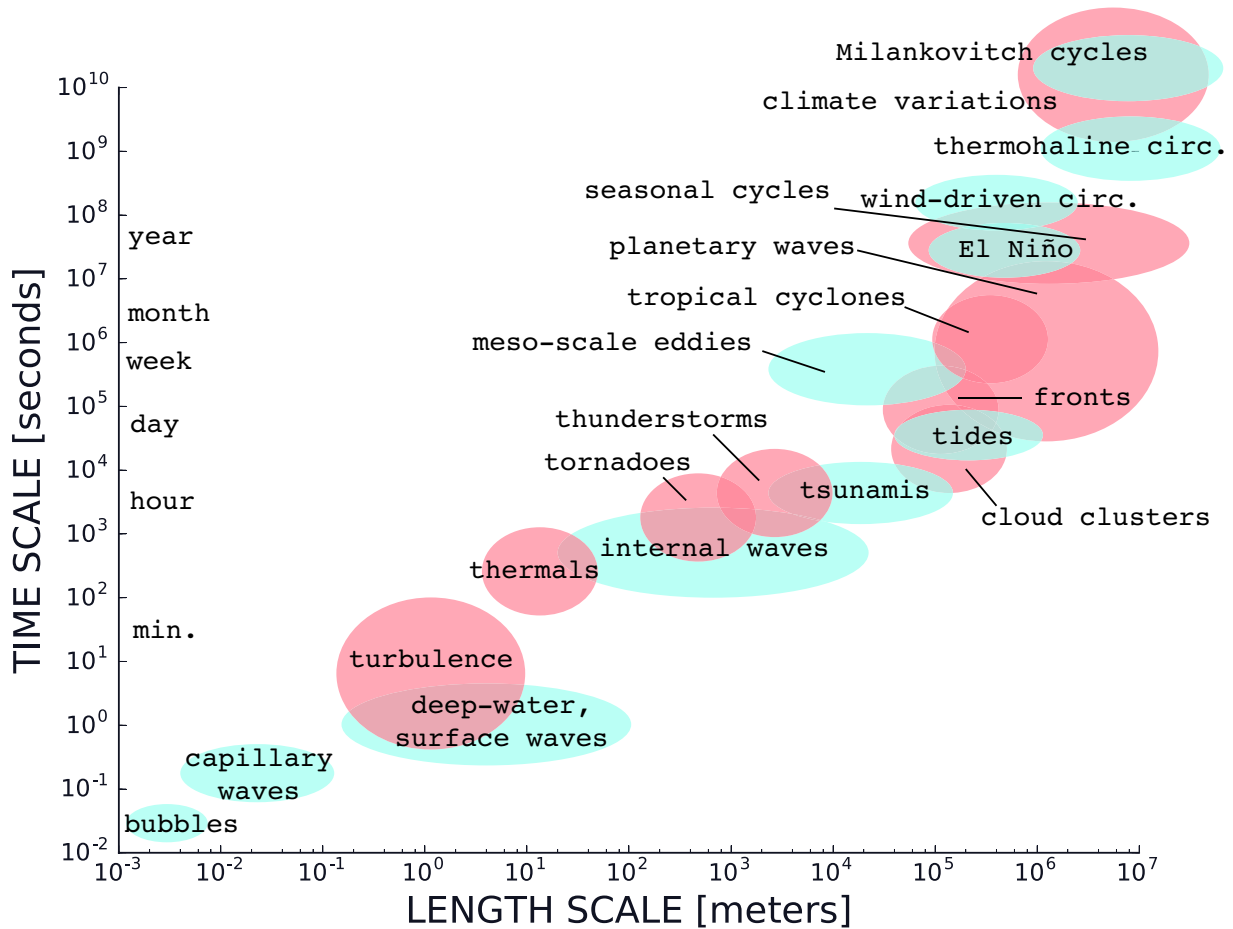
Fig. 3.1. | Illustration of various spatial and temporal scales of atmospheric processes. Processes taking place in atmosphere are shaded with pink colour, while oceanic processes are shaded with light blue. The figure demonstrates the vastness of scales — the factor is around 10^{10} in a spatial and 10^{12} in a temporal sense.

approximation of *"eddy turnover time"*, $\tau_n \approx l_n/v_n$, where l_n is a typical length scale and v_n is dynamically important velocity. This simple approximation ties the typical lifetime of structures of size l_n with their typical velocities, v_n.

Table 3.1 summarises exactly the typical scales both in a spatial and temporal sense, also giving an example of an atmospheric process operating on the respective scales. This table also states the typical source of energy at respective scales and from this we can somehow reconstruct the means how energy cascades downscale: from energy injections at planetary scale in the form of unequal distribution of solar heating it cascades to power the jet streams and atmospheric fronts, subsequently transforming into wind shear at mesoscale, and interaction with obstacles and air viscosity at microscale, finally dissipating due to molecular processes, which are best described using the kinematic theory of gases. It is only natural to expect that the peculiarities of the energy cascade will affect neighbouring scales, or said differently — due to energy transfer between scales, these scales are affecting each other.

horizontal scale	time (lifespan)	distance	example process	characteristic energy source
planetary	weeks to seasons	4000 – 40000km	westerlies, trade winds, long waves	unequal distribution of heating
synoptic	days to weeks	1000 – 4000km	mid latitude cyclones, hurricanes	jet stream, latent heat
mesoscale	minutes to hours	1 – 1000km	sea breeze, tornado, thunderstorm	diurnal heating, latent heat, wind shear
microscale	seconds to minutes	< 1km	dust devil, wind gust	uneven surface heating, viscosity
molecular	fractions of a second	< 1m	raindrops growth, evaporation, scattering	kinetic theory of gases

TABLE 3.1. | Summary of various typical scales in atmospheric dynamics: the span, typical lifetime, characteristic examples and energy sources. Table taken from *shorstmayer.com*.

3.2 Scaling in atmospheric data

Now, you should be convinced that scales as such are a very important concept from the theoretical point of view in the atmospheric dynamics, but what about the data? Fortunately, today we live in the "golden age" of atmospheric observations, when in-situ and remote data routinely span scale ratios of 10^3–10^4 in space or time and operational models are not particularly trailing *[Lovejoy and Schertzer, 2013]*.

"The climate is what you expect; the weather is what you get", famously written by Robert Heinlein in his 1973 novel could serve as an example of two different regimes in atmospheric dynamics. As far as the data-based evidence goes, this is partially true, with the addition of one more regime — the macroweather. As a typical example of scaling of the atmospheric field, see Fig. 3.2. In this figure, we observe three distinct scaling regimes in the atmospheric dynamics. The first regime is in the right-hand part of the figure and shows the typical "weather" regime. That is the regime in which the fluctuations increase with scale, or put differently: the difference between today's and tomorrow's

temperature is lower than between today's and the day after tomorrow's temperature. After the weather regime, we observe the first transition to the macroweather regime. This regime has statistics, which are very close to those predicted by simply extending the weather scale models to low frequencies, e.g. traditional global climate models (GCMs hereafter) when these are run without special anthropogenic, solar, orbital, or other climate forcings, i.e. "control runs". In this macroweather regime, the fluctuations are actually decreasing with increasing scale, since it obtains no new internal dynamical element nor forcing mechanisms *[Lovejoy and Schertzer, 2013]*. Finally, the left-most regime in the Fig. 3.2 corresponds to our usual ideas about climate — this includes the multidecadal, multicentennial and multimillennial variability *[Lovejoy and Schertzer, 2013]*. This example well documents the fact, that fields in the atmosphere are indeed scaling, therefore various scales are exchanging energy, and with that also information. For other examples of various scaling in both spatial and temporal sense, see *Lovejoy and Schertzer [2013]* and references therein.
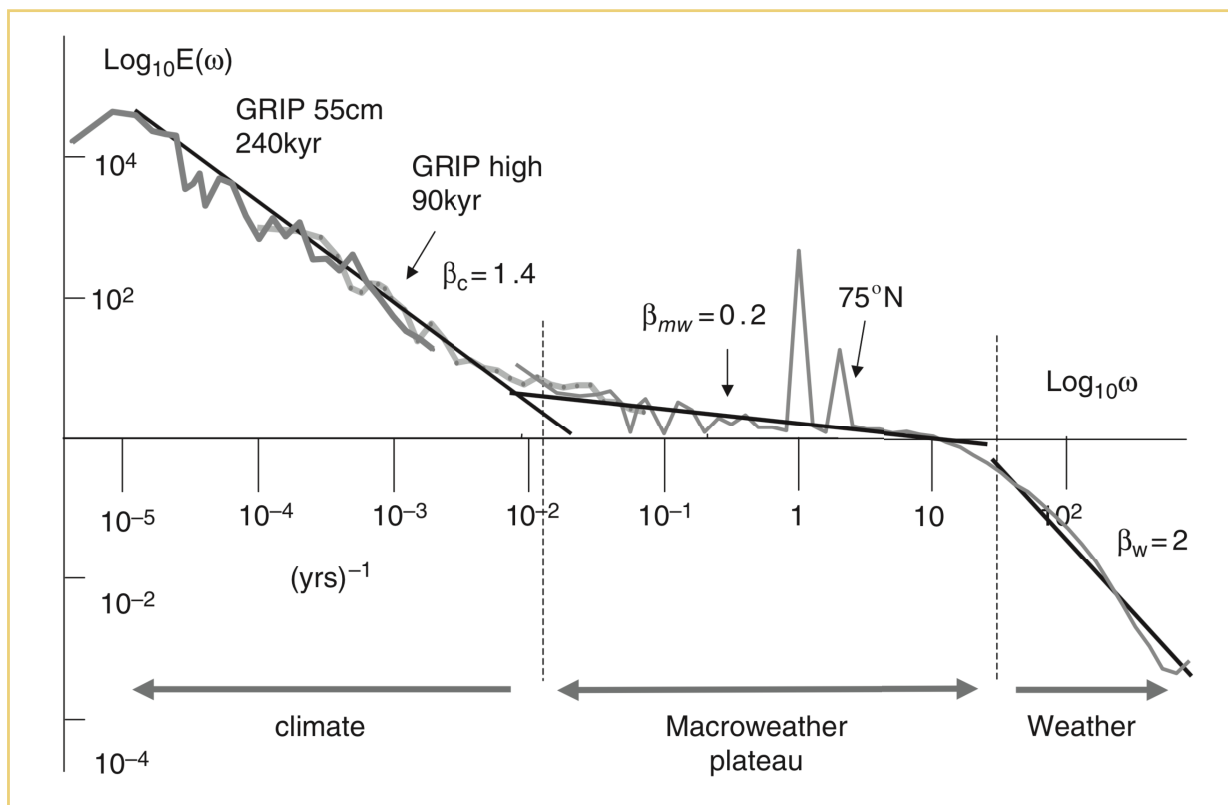
FIG. 3.2. | A composite spectrum of GRIP ice-core $\delta^{18}O$ (a temperature proxy), with the spectrum of the (mean) 75°N 20CR reanalysis temperature. All spectra are averaged over logarithmically spaced bins. Three distinct regimes are shown corresponding to the weather, the macroweather, and the climate. Figure taken from *Lovejoy and Schertzer [2013]*.

3.3 Information transfer in atmospheric dynamics: the synthesis

Having laid the foundations of complex systems, network theory and scaling in atmospheric dynamics both from a theoretical and data-driven perspective, let us synthesise these fields into a study of information transfer across temporal scales in atmospheric dynamics. In this section, I will build the necessary tools for studying and understanding information transfer, by the means of synchronisation and causal relationships, across various scales in climate phenomena.

3.3.1 Fourier domain: a description of oscillatory patterns

The frequency, or Fourier, domain refers to the analysis of mathematical functions or signals with respect to frequency, rather than time. Simply, a time-domain plot shows how a signal changes over time, whereas a frequency-domain plot visualise how much of the signal lies within a given frequency band *[Broughton and Bryan, 2011]*. The description of any process in a frequency domain is particularly useful when dealing with oscillatory or quasi-oscillatory processes and recurring patterns. The coupled climate system exhibit a number of large-scale phenomena, the so-called climate modes such as El Niño/Southern Oscillation, the Asian monsoon, the North Atlantic Oscillation, the Madden–Julian Oscillation, and much more. While these modes are not exactly periodic, they are indeed oscillatory in character *[Viron et al., 2013]*. When we include with these the higher-frequency cycles apparent in climate dynamics, such as the annual cycle, their harmonics, diurnal cycle and so on, we come to the conclusion that many distinct behaviours in climate dynamics can be described in frequency-domain. Or put differently, they exhibit oscillatory or quasi-oscillatory behaviour, the maxima and minima are recurring with some approximate period and the dynamics of the climate as a whole can be thought of as a collection (or a network) of these coupled phenomena, from which arises complex multi-scale behaviour we can measure by the means of temperature, pressure and other atmospheric observables *[Paluš, 2014a]*.

The immediate connection one usually makes with the word "Fourier" is that of a spectrum. The spectrum, or spectral density, describes how the energy of a signal is distributed with frequency. Simply it shows on which frequency the power in the signal resides. From the first data-driven atmospheric spectrum by *Panofsky and Van der Hoven [1955]*, various spectral methods were used to identify and study oscillatory phenomena in various fields, from wind, temperature and pressure fields, to boundary conditions in the form of terrain roughness. For identifying spectral peaks, probably the most used algorithm is Fourier transform (e.g. *[Bracewell and Bracewell, 1986]*), which is a decomposition technique that takes an input in the form of function in time and outputs its frequency components. Mathematically, a Fourier transform of a function $f(x)$ is defined as

$$\hat{f}(\xi) = \int_{-\infty}^{\infty} f(x)e^{-2\pi i x \xi} dx, \tag{3.7}$$

for any real number, $\xi \in \mathbb{R}$. Having defined the Fourier transform, or more precisely its algorithmic implementation, which goes by the name Fast Fourier Transform (e.g. *Cooley and Tukey [1965]*), the route to defining a spectral density is rather straightforward with

$$S_{xx}(f) = |\hat{x}(f)|^2 \tag{3.8}$$

where $\hat{x}(f)$ is a Fourier transform of the signal and f is the frequency. In words, one computes a Fourier transform of desired time series over frequency bins of interest and squaring the Fourier coefficients gives an estimate of spectral density. As an example of spectral content in atmospheric data, consider Fig. 3.3. As the figure clearly shows, and as one would expect from daily average surface air temperature time series, a clear spectral peak is occurring at exactly one year — the annual, solar, cycle. Apart from the main annual peak, we see clearly see various local maxima and minima, e.g. peak in 7–8-year periodicity.
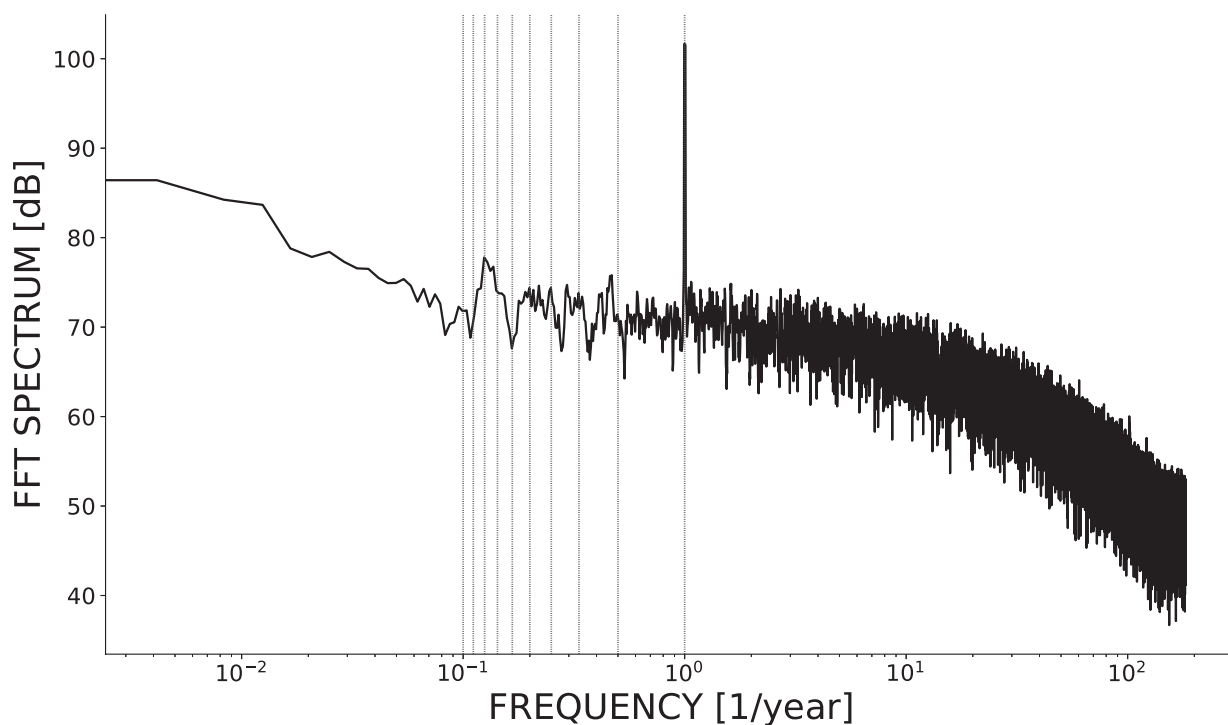
Fig. 3.3. | FFT spectral density of daily average surface air temperature from station Prague – Klementinum with temporal span 1. January 1770 – 1. January 2016. Data from ECA&D project *[Klein Tank et al., 2002]*. The dotted vertical lines show frequencies between 1 and 10 years with an annual span.

By the means of spectral analysis, as shown here, one can detect typical periodicities, or cycles, in the given signal. From the spectral representation, it is obvious, that the signal is of multi-scale nature, i.e. is a mix of various sources of cyclicities together (recall Fig. 2.2). Our goal is to study the relationships between these various cycles obtained in the data, so we would need a means of extracting the oscillatory modes from data.

3.3.2 Extracting oscillatory modes from observables

In order to study distinct oscillatory phenomena in the observational data, we would need tools to extract the modes. Since the observational data, e.g. surface air temperature, reflect complex atmospheric dynamics on multiple temporal scales, the phase dynamic approach *[Pikovsky et al., 2003]* is of particular use. In accordance with *Gans et al. [2009]* we can write for arbitrary time series $s(t)$, the analytic signal $\psi(t)$ as a complex function of time defined as

$$\psi(t) = s(t) + i\hat{s}(t) = A(t)e^{i\phi(t)}. \tag{3.9}$$

In this phase dynamics approach, one expects the time series to have an oscillatory character and these are conveniently described by the means of the instantaneous amplitude $A(t)$ and phase $\phi(t)$. We expect these to be a function of time and are allowed to fluctuate. From the eqn. (3.9) we obtain the description of instantaneous phase as

$$\phi(t) = \arctan\frac{\hat{s}(t)}{s(t)}, \tag{3.10}$$

and instantaneous amplitude as

$$A(t) = \sqrt{s^2(t) + \hat{s}^2(t)}. \tag{3.11}$$

Given this convenient description of oscillatory modes in time series, one has practically two options how to proceed. The imaginary part of the time series, $\hat{s}(t)$, is usually obtained by the means of the Hilbert transform of $s(t)$ *[Pikovsky et al., 2003; Gans et al., 2009]*. It simply extends the signal into a complex plane in such a manner, that it satisfies the Cauchy–Riemann equations in order for the complex representation of the time series to be holomorphic, i.e. complex differentiable *[Benedetto, 1996]*. Since the Hilbert transform is a unit gain filter at each frequency, broadband signals from multi-scale processes should be prefiltered to the frequency band of interest. This can be done using methods from signal processing e.g. band-pass filter centred around the frequency of interest.

The second option is to exploit the theory of wavelets, particularly the continuous complex wavelet transform (CCWT hereafter) *[Torrence and Compo, 1998]*. A wavelet transform is a form of a time-frequency representation of a continuous-time signals (analog signal in signal processing terminology) and therefore is related to the harmonic analysis. Given a signal of finite energy, by the means of continuous wavelet transform, it is projected on a family of frequency bands. This projection of a function x onto the subspace of scale a has the form

$$x_a(t) = \int_{\mathbb{R}} \mathrm{WT}_\psi\{x\}(a, b) \cdot \psi_{a,b}(t)\mathrm{d}b, \tag{3.12}$$

with wavelet coefficients

$$\mathrm{WT}_\psi\{x\}(a, b) = \langle x, \psi_{a,b}\rangle = \int_{\mathbb{R}} x(t)\psi_{a,b}(t)\mathrm{d}t. \tag{3.13}$$

In words, one simply convolves the signal of interest with predefined mother wavelet. The beauty of this approach is that in each time scale (frequency) of interest, the complex wavelet coefficients can be directly applied to eqns. (3.10) and (3.11) in order to obtain the time series of instantaneous phase and amplitude. Therefore, the continuous complex wavelet transform provides both filtering to the frequency band of interest and estimation of instantaneous phase and amplitude.
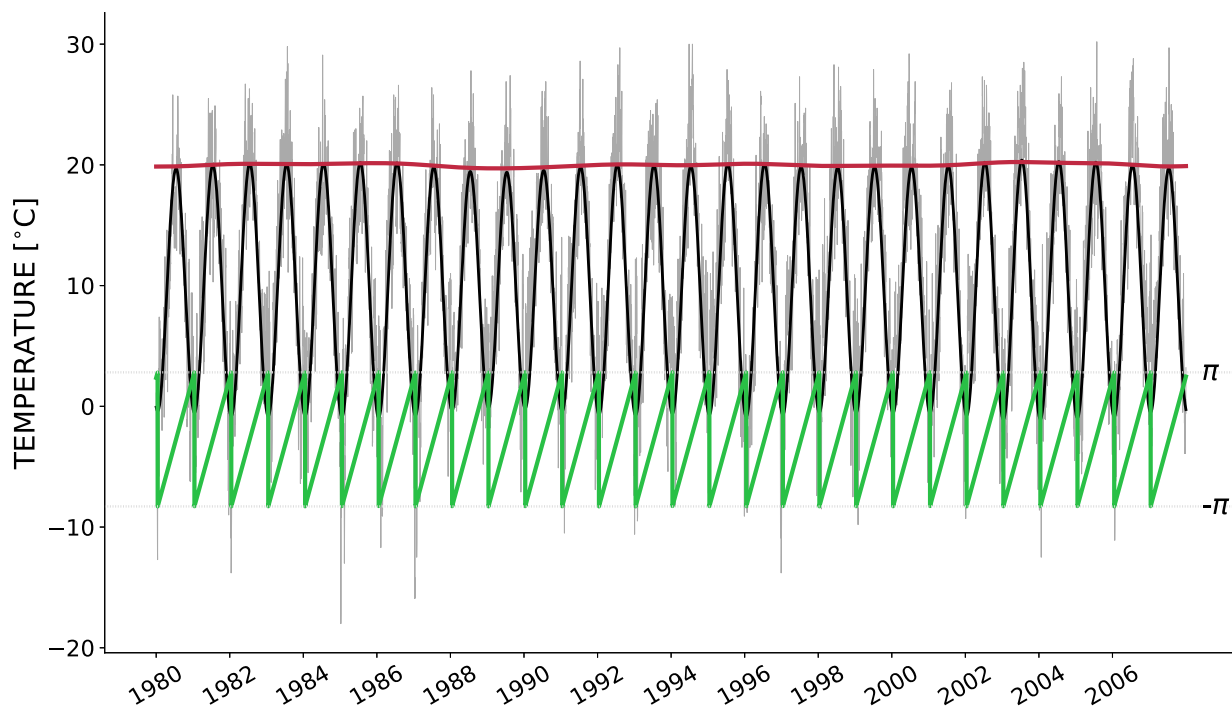
FIG. 3.4. | Illustration of continuous complex wavelet transform on daily average surface air temperature from station Prague – Klementinum. Shown are raw temperature in light grey, amplitude A_{1yr} of the annual cycle decomposed using CCWT in red, phase ϕ_{1yr} of the annual cycle in green and reconstructed signal, $A_{1yr}(t) \cos \psi_{1yr}(t)$, in black. Data from ECA&D project *[Klein Tank et al., 2002]*.

The oscillatory modes in atmospheric dynamics are rarely completely and absolutely regular. The cycles could speed-up, slow-down, suddenly jump to a different place in a cycle and so on. Phases of this cyclic components do fluctuate and, thus, offer an additional information to analyse: one could compute instantaneous frequency *[Gans et al., 2009; Paluš and Novotná, 2009; Jirsa and Müller, 2013]* as a temporal derivative of the instantaneous phases (in a data-driven fashion one would compute a linear regression to obtain a slope as an estimate of a derivative). Yet another variable for analyses of oscillatory modes would be a phase fluctuation — a difference between instantaneous phase obtained from the data and ideal regular cycle, e.g. annual when computing the fluctuations of annual phase as a shift of season timing, which was done e.g. by *Paluš et al. [2005]*.

3.4 Measuring the dependence: linear and nonlinear methods

Let us take a break from the atmosphere and its dynamics and dive into basics of probability theory. In probability theory, a cornerstone is a random variable, also called random quantity or stochastic variable. It is a variable whose possible values are numerical outcomes of a random phenomenon *[Grinstead and Snell, 2012]*. It is common that these outcomes depend on some physical variables that are not very well understood. This definition mirrors a definition of observables (recall subsection 2.1.2 and Fig. 2.2), thus it is convenient to think of the observables as random variables. Mathematically, a random variable $X : \Omega \to E$ is a measurable function from a set of possible outcomes Ω to a measurable space E and usually X is real-valued, i.e. $E = \mathbb{R}$. The probability that X takes a value in a measurable set $S \subset E$ is written as

$$\Pr(X \in S) = \mathsf{P}\left(\{\omega \in \Omega | X(\omega) \in S\}\right), \qquad (3.14)$$

where P is the probability measure equipped with Ω. We will work only with real-valued variables, hence in our case $E = \mathbb{R}$ always.

When given a random variable $X : \Omega \to \mathbb{R}$, one can ask e.g. how likely is that the outcome of X is equal to 2, and the answer is, of course, the same as the probability of an event $\{\omega : X(\omega) = 2\}$, which can be also written as $\mathsf{P}(X = 2)$ for short. Recording all these probabilities of ranges yields the probability distribution of X and can always be captured by its cumulative distribution function

$$F_X(x) = \mathsf{P}(X \leq x). \qquad (3.15)$$

3.4.1 Basic dependence measures

Having defined a random variable, we can move on into statistical dependence, which is defined as any statistical relationship (causal or not) between two random variables or bivariate data. The most used and known such measure is the *correlation*. Correlation measures linear dependence and can be thought of as indicating predictive power that may be exploited in practice. In general, correlation is not sufficient to claim any causal relationship, which, unfortunately, is an often used logical fallacy. But one needs to carry in mind that *cum hoc ergo propter hoc* ("with this, therefore because of this") is not always true.

For building a proper definition of correlation as a statistical dependence, we need to begin with covariance. Covariance is, as its name suggests, a measure of how two random variables jointly vary. In words, if the greater values of one variable correspond to greater values of the other variables (and vice versa), we say that the variables show similar behaviour and the covariance is positive. Mathematically, covariance is defined as the expected product of their deviations from their individual expected values as

$$\text{cov}(X, Y) = \sigma_{X,Y} = \mathsf{E}\left[(X - \mathsf{E}\left[X\right])(Y - \mathsf{E}\left[Y\right])\right] = \mathsf{E}\left[XY\right] - \mathsf{E}\left[X\right]\mathsf{E}\left[Y\right]. \qquad (3.16)$$

A similar definition holds for random vectors $\mathbf{X} \in \mathbb{R}^m$ with

$$\mathrm{cov}(\mathbf{X}, \mathbf{Y}) = \sigma_{\mathbf{X}, \mathbf{Y}} = \mathsf{E}\left[(\mathbf{X} - \mathsf{E}\,[\mathbf{X}])\,(\mathbf{Y} - \mathsf{E}\,[\mathbf{Y}])^{\mathsf{T}}\right] = \mathsf{E}\,[\mathbf{X}\mathbf{Y}^{\mathsf{T}}] - \mathsf{E}\,[\mathbf{X}]\,\mathsf{E}\,[\mathbf{Y}]^{\mathsf{T}}, \qquad (3.17)$$

where $\cdot^{\mathsf{T}}$ denotes a transpose of a vector or a matrix. Finally, for a vector $\mathbf{X} = [X_1, X_2, \ldots, X_m]^{\mathsf{T}}$ of m jointly distributed random variables we define its covariance matrix as

$$\Sigma(\mathbf{X}) = \mathrm{cov}(\mathbf{X}, \mathbf{X}). \qquad (3.18)$$

There are several correlation coefficients measuring the degree of dependence. The most common of these is Pearson product-moment correlation coefficient, commonly called just Pearson's correlation coefficient *[Lee Rodgers and Nicewander, 1988]*. It is defined simply as normalised covariance, therefore

$$\rho_{X,Y} = \mathrm{corr}(X, Y) = \frac{\mathrm{cov}(X, Y)}{\sigma_X \sigma_Y} = \frac{\mathsf{E}\left[(X - \mu_X)\,(Y - \mu_Y)\right]}{\sigma_X \sigma_Y}, \qquad (3.19)$$

with μ_X being the expected value of X and σ_X its standard deviation. Pearson's correlation coefficient exhibit some nice properties, e.g. cannot exceed 1 in its absolute value and is symmetric, i.e. $\mathrm{corr}(X, Y) = \mathrm{corr}(Y, X)$. If the variables are independent, $\rho_{X,Y} = 0$, but the converse is not true, since Pearson's correlation coefficient detects only linear relationship. This is beautifully visualised in Fig 3.5.
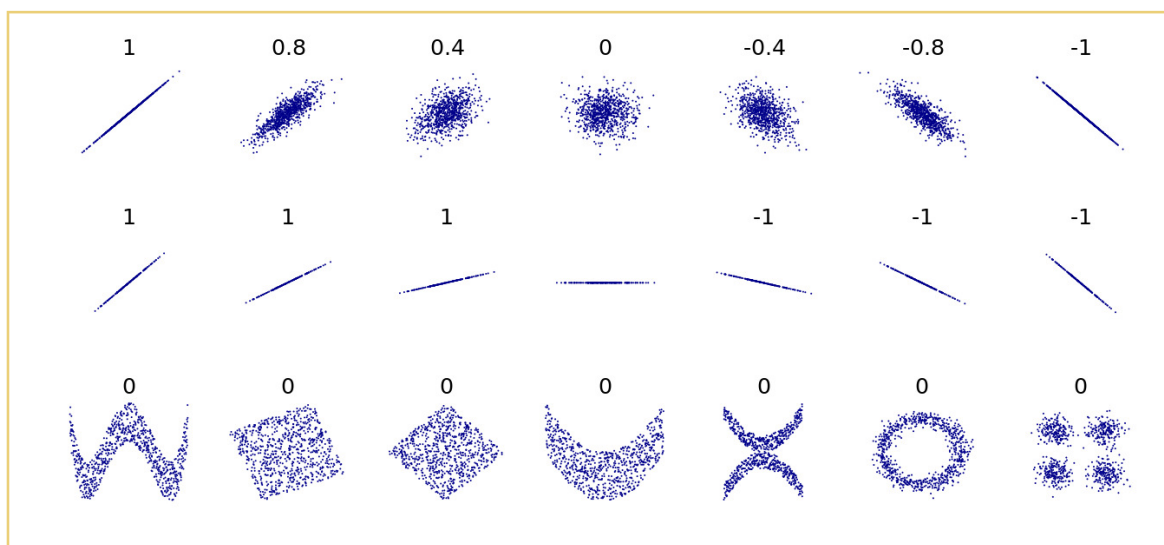
FIG. 3.5. | Several sets of (x, y) points, with the Pearson's correlation coefficient of x and y for each set. Note that correlation cannot detect nonlinear relationships (bottom row). Figure by Denis Boigelot, taken from *wikipedia.org [c]*.

When we start in the middle of the top row, we observe independent variables (multivariate Gaussian with diagonal covariance matrix), hence $\rho_{x,y} = 0$. As we increase the diagonal elements in the covariance matrix of multivariate Gaussian, by the same token we also increase (in absolute value) the correlation coefficient ρ. This is visualised

in the top row on both sides from the middle. In the middle row, we can see various slopes of the dependence, but always with the perfect correlation coefficient of ±1, except the middle example, when it is undefined as the variance of y, σ_y, is zero. Finally, exploring the third row in the Fig. 3.5, one immediately see some dependence between variables, but this time it is nonlinear dependence, and, as expected, in all cases the Pearson's correlation coefficient equals 0.

The Pearson's correlation coefficient is widely used in data-driven fashion, because it can be easily rewritten from original definitions via random variables, to a definition with series of measurements of X and Y, written as x_i and y_i with $i = 1, 2, \ldots, n$, as sample correlation coefficient with

$$r_{x,y} = \frac{\sum\limits_i^n (x_i - \bar{x})(y_i - \bar{y})}{(n-1)s_x s_y} = \frac{\sum\limits_i^n (x_i - \bar{x})(y_i - \bar{y})}{\sqrt{\sum\limits_i^n (x_i - \bar{x})^2 \sum\limits_i^n (y_i - \bar{y})^2}}, \tag{3.20}$$

where $\bar{x}$ and $\bar{y}$ are the sample means, and s_x and s_y are the corrected sample standard deviations of X and Y, respectively. Although Pearson's (or rather sample) correlation coefficient is widely used with atmospheric data in order to infer relationships, it is able to detect linear relationships, and only mere "visual similarity" — not causal.

One step further would be to assess the relationship, that possesses a true potential for prediction, and the *Granger causality* exactly offers that. As the name suggests, it was brought into computational practice by Clive Granger *[Granger, 1969]* and it characterises to what extent a process X is leading another process Y. We say, that the process X *Granger causes* another process Y if future values of Y can be better predicted using the past values of X and Y rather than just Y alone. The ideas behind such definition come from the work of Norbert Wiener *[Wiener, 1956]* and Granger in his Nobel lecture *[Granger, 2004]* identified two components for the statements about causality:

- the cause precedes the effect, and

- the cause contains information about the effect that is unique and is in no other variable.

The standard test for Granger causality (GC hereafter) is based on a linear regression model and consists of series of t-tests and F-tests on lagged values of X. The hypothesis Granger proposed to test has the following form:

$$\mathsf{P}[Y(t+1) \in A | \mathcal{I}(t)] \neq \mathsf{P}[Y(t+1) \in A | \mathcal{I}_{-X}(t)], \tag{3.21}$$

where P refers to probability, A is arbitrary non-empty set, and $\mathcal{I}(t)$ and $\mathcal{I}_{-X}(t)$ respectively denote the information available as of time t in the entire universe, and that in the modified universe from which X is excluded. If this hypothesis is accepted, we say that X Granger-causes Y *[Granger, 1980]*.

The mathematical statement of Granger causality to test the null hypothesis that x does not Granger-cause y would firstly find the proper lagged values of y to include in a univariate autoregression:

$$y(t) = a_0 + a_1 y(t-1) + a_2 y(t-2) + \cdots + a_m y(t-m) + \eta(t). \tag{3.22}$$

Next, the autoregression is augmented by including the lagged values of x:

$$y(t) = a_0 + a_1 y(t-1) + a_2 y(t-2) + \cdots + a_m y(t-m) + b_p x(t-p) + \cdots + b_q x(t-q) + \xi(t). \quad (3.23)$$

All lagged values of x that are individually significant according to their t-statistics will be kept, providing that collectively they add explanatory power to the regression according to the F-test. The null hypothesis that x does not Granger-causes y is accepted only if no lagged values of x are retained in the regression. The extension of this test for multivariate analysis is straightforward: the autoregression has the form

$$\mathbf{X}(t) = \sum_{\tau=1}^{L} A_\tau \mathbf{X}(t - \tau) + \epsilon(t). \quad (3.24)$$

A time series X_i is called a Granger-cause of another time series X_j if at least one of the elements of $A_\tau(j, i)$ for $\tau = 1, \ldots, L$ is significantly larger than zero in absolute value [Lütkepohl, 2005].

In the following section, I will review the basic concepts of information theory and define a very useful measure called mutual information, which can be used in detecting predictive causality even in nonlinear systems.

3.4.2 A quick introduction to information theory

Information theory, originally proposed by Claude Shannon in a pioneering paper "A Mathematical theory of computation" in 1948 published during his work at Bell Systems [Shannon, 2001], studies the quantification, storage and communication of information [Cover and Thomas, 2012]. A key measure is an entropy, which quantifies the amount of uncertainty involved in the value of a random variable. As an example, consider that identifying an outcome of a fair coin flip (with two equally possible outcomes) provides less information (lower entropy) than specifying the outcome of a fair die (with 6 equally probable outcomes).

The Shannon entropy is mathematically defined as

$$H(X) = -\sum_{x \in X} p(x) \ln p(x) \quad (3.25)$$

for discrete random variable X. When one works with continuous variables, the sum in eqn. (3.25) transforms to integral $\int_{x \in X} \cdot \, dx$. From the above definition, it is obvious that in the case of $p(x) = \delta_{x,x_0}$ the Shannon entropy is $H(X) = 0$, while for $p(x) = 1/N$ for $x = 1, 2, \ldots, N$ the Shannon entropy is maximised with $H(X) = \ln N$. The base of the logarithm in the definition of Shannon entropy (eqn. (3.25)) can, in theory, be arbitrary, however one would usually use either base of 2 ($\log_2$), which renders the unit of entropy as "bits", while using natural logarithm (ln) changes the unit to "nats".

The close parallels between Shannon entropy and thermodynamic entropy, defined by Ludwig Boltzmann and J. Willard Gibbs in the 1870s, exist and these were also commented on by Shannon himself. The definition of thermodynamic entropy is very

similar to the Shannon entropy:

$$S = -k_B \sum_i p_i \ln p_i,$$

(3.26)

where p_i is a probability of a microstate i taken from an equilibrium ensemble and k_B is Boltzmann constant. The differences between the two are mainly theoretical *[Bérut et al., 2012]*, e.g. the information entropy H can be computed for *any* probability distribution, while the thermodynamic entropy S refers to thermodynamic probabilities p_i specifically.

The joint entropy is merely the entropy of their pairing and this also implies that if X and Y are independent, then their joint entropy is just the sum of their individual entropies. It is defined as

$$H(X, Y) = -\sum_{x,y} p(x, y) \ln p(x, y).$$

(3.27)

In a similar fashion, one can define a conditional entropy, which refers to the conditional uncertainty of X given random variable Y as

$$H(X|Y) = -\sum_{y \in Y} p(y) \sum_{x \in X} p(x|y) \ln p(x|y)$$

$$= -\sum_{x,y} p(x, y) \ln p(x|y).$$

(3.28)

A basic property of the conditional entropy is then

$$H(X|Y) = H(X, Y) - H(Y).$$

(3.29)

A very important concept in information theory is that of the mutual information. It quantifies the amount of information that can be obtained about one random variable by observing another. It is defined as

$$I(X, Y) = \sum_{x,y} p(x, y) \ln \frac{p(x, y)}{p(x)p(y)}.$$

(3.30)

We can also write

$$I(X, Y) = \sum_{x,y} p(x, y) \ln \frac{p(x, y)}{p(x)p(y)}$$

$$= \sum_{x,y} p(x|y)p(y) \ln \frac{p(x|y)}{p(x)}$$

$$= H(X) - H(X|Y)$$

$$= H(Y) - H(Y|X).$$

(3.31)

from which we can immediately see that knowing Y, we can save on average $I(X, Y)$ bits/nats in encoding X compared to not knowing Y. Moreover, mutual information is symmetric, thus

$$I(X, Y) = I(Y, X) = H(X) + H(Y) - H(X, Y). \tag{3.32}$$

Finally, mutual information can be expressed as the average Kullback–Leibler divergence (relative entropy) *[Kullback and Leibler, 1951]* between the posterior probability distribution of X given the value of Y and the prior distribution on X. In other words, it measures how much the probability distribution of X changes when we are given the value of Y, therefore

$$I(X, Y) = D_{KL} \left(p(x, y) \| p(x) p(y) \right), \tag{3.33}$$

where Kullback–Leibler divergence itself is defined for two probability densities $p(x)$ and $q(x)$ as

$$D_{KL}(p(x)\|q(x)) = \sum_{x \in X} -p(x) \ln q(x) - \sum_{x \in X} -p(x) \ln p(x) = \sum_{x \in X} p(x) \ln \frac{p(x)}{q(x)}, \tag{3.34}$$

and quantifies how far from each other are the "true" probability distribution $p(x)$ and an arbitrary probability distribution $q(x)$.

Mutual information possesses very useful properties, in particular

- $I(X, Y) \geq 0$,

- $I(X, Y) = 0$, if and only if X and Y are independent.

We can see the latter is true when we realise that if two random variables are independent, then $p(x, y) = p(x)p(y)$ and therefore the logarithm in eqn. (3.30) equals to zero.

Similarly to the conditional entropy, we can define the conditional mutual information of the variables X and Y given the variable Z equivalently to eqn. (3.32) as

$$I(X, Y|Z) = H(X|Z) + H(Y|Z) - H(X, Y|Z), \tag{3.35}$$

which, after breakdown, gives us

$$
\begin{aligned}
I(X, Y|Z) &= \sum_{z \in Z} p(z) \sum_{y \in Y} \sum_{x \in X} p(x, y|z) \ln \frac{p(x, y|z)}{p(x|z)p(y|z)} \\
&= \sum_{z \in Z} \sum_{y \in Y} \sum_{x \in X} p(x, y, z) \ln \frac{p(z)p(x, y, z)}{p(x, z)p(y, z)}.
\end{aligned} \tag{3.36}
$$

For Z independent of X and Y we, of course, have $I(X, Y|Z) = I(X, Y)$. The conditional mutual information characterises the dependence between X and Y without a possible influence of another variable (Z). Finally, conditional mutual information could be rewritten using just the mutual information between the variables as

$$I(X, Y|Z) = I(X, Y, Z) - I(X, Z) - I(Y, Z). \tag{3.37}$$

All possible combinations of information theoretical measures between three variables, X, Y, and Z, are shown in Fig. 3.6. Each of the three circles represent a random
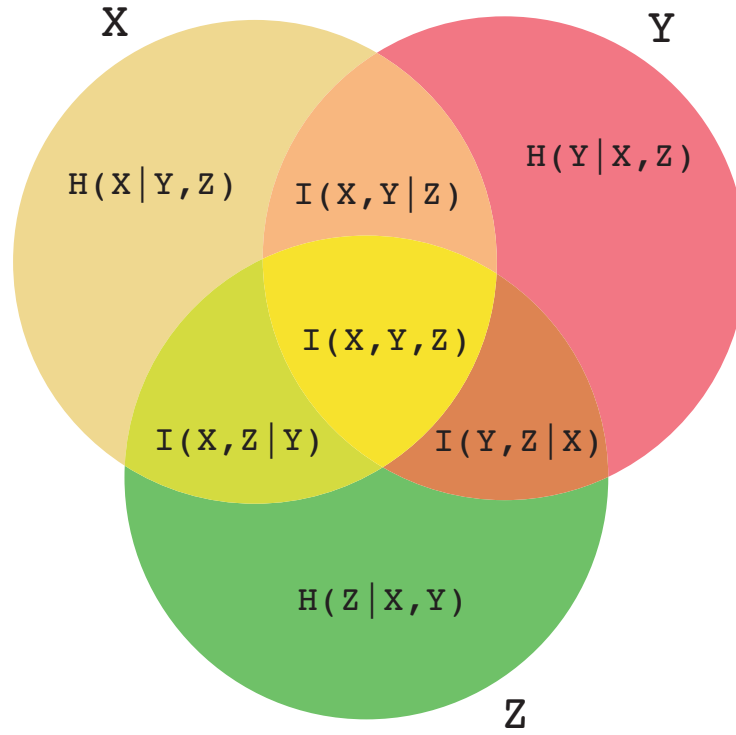
FIG. 3.6. | Venn diagram of information theoretic measures for three variables X, Y and Z represented by the upper left, upper right and bottom circles, respectively. The appropriate conditional entropy, mutual information or conditional mutual information is written in the respective part of the diagram.

variable with its own entropy ($H(X)$, $H(Y)$, and $H(Z)$ respectively) and in the intersections are defined their conditional entropies ($H(X|Y, Z)$, $H(Y|X, Z)$, and $H(Z|X, Y)$)) and combinations of conditional mutual information and mutual information between all three variables. From this, we can also see that mutual information can be defined for n variables as

$$I(X_1, X_2, \ldots, X_n) = H(X_1) + H(X_2) + \cdots + H(X_n) - H(X_1, X_2, \ldots, X_n). \quad (3.38)$$

In a similar fashion, one can define also conditional mutual information of a group of variables and also multivariate generalisations of conditional mutual information *[Paluš, 1996]*. As already mentioned, all these functionals can be defined also for continuous random variables rather than discrete ones, simply by interchanging all the sums for integrals and the PDFs for the probability distribution densities *[Paluš et al., 1993; Cover and Thomas, 2012]*.

## 3.4.3 Computational approaches for mutual information

When computing the information theoretic measures from measured data (the observables) one additional step has to be done, that is to estimate the PDF. In theory, when computing entropy or mutual information for random variables, the theoretical PDF is

known (consider an example of a fair coin, or a die). When working with observables, one has to discretise the phase space in order to get partitions and subsequently estimate the PDF. For an exhaustive overview of various computational methods tackling the information theoretical measures, see *Hlaváčková-Schindler et al. [2007]*.

Various strategies have been proposed to partition the observational space, one of the most popular and easiest to implement is the fixed partitioning of the space using the histogram method *[Butte and Kohane, 1999]*. In this approach, the range of the variable is partitioned into m_X discrete bins with fixed, constant width h_X. If the k_i is the number of measurements laying in the bin a_i, then the probability $p(x_i)$ is estimated by relative frequencies of occurrence, so

$$p_X(a_i) = k_i/N, \tag{3.39}$$

where N is the size of the dataset. This method is usually referred to as the equidistant binning method, as all the bins have same distances between each other. However, it can be demonstrated *[Steuer et al., 2002]* that the estimate of MI fluctuates around a true value or gets systematically overestimated, in particular in higher dimensions when insufficient amount of data leads to low occupancy of many bins giving an incorrect estimate of probability distributions *[Hlaváčková-Schindler et al., 2007]*. The illustration of the equidistant binning partition of the phase space is shown in Fig. 3.7, A, where the phase space is partitioned using 2 bins.
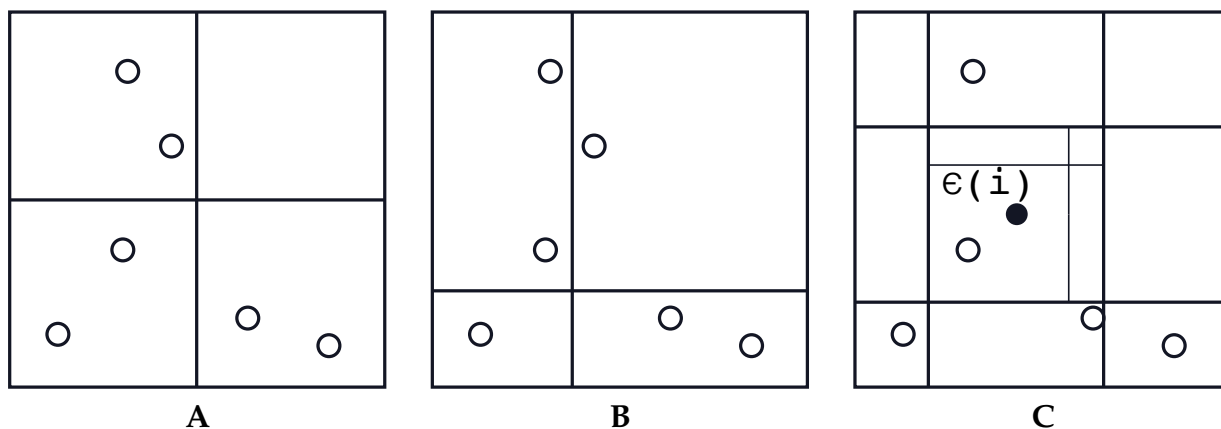
FIG. 3.7. | Illustration of three methods for estimating the probability density from the data: (**A**) equidistant binning method, (**B**) equiquantal binning method, and (**C**) k-nearest neighbours algorithm. See text for details to each method.

The simplest adaptive partitioning method was proposed by *Paluš et al. [1993]; Paluš [1995]* based on marginal equiquantisation. In this method, the marginal boxes are not defined equidistantly (i.e. having the same size), but rather so that there are approximately same number of samples in each marginal box. The choice of a number of bins is, however, crucial. For this, *Paluš [1995]* proposed that the number of marginal bins should not exceed the $(n + 1)^{st}$ root of the size of the dataset, i.e. $q \leq \sqrt[n+1]{N}$. This equiquantisation method effectively transforms each variable in its dimension into uniform distribution and then the mutual information is fully determined by the value of the joint entropy of the studied variable. Moreover, this method is invariant against any

monotonous (even nonlinear) transformation of the data *[Paluš, 1996]* and due to this property, it is useful when statistically testing against surrogate data. The example of equiquantal binning of the phase space is shown in Fig. 3.7, B and one can see that the bins are of different sizes, albeit they contain the same number of data points (in marginal distributions).

Estimators of Shannon entropy based on k-nearest neighbours search are studied for more than 60 years, however, they cannot be directly generalised to higher-dimensional spaces *[Hlaváčková-Schindler et al., 2007]*. The idea of these neighbours searching algorithms is to rank the neighbours by distance for each point and then to estimate the entropy from the average distance to the k-nearest neighbour, averaged over all data points. Mathematically, Shannon entropy $H(X) = -\int p(x)\ln p(x)\mathrm{d}x$ can be understood as an average of $\ln p(x)$. One of the specific algorithms for computing an estimate of mutual information is due to *Kraskov et al. [2004]* (the KSG algorithm) and is fully described in the respective paper. The mutual information estimated using this algorithm works well also on non-Gaussian general distributions. An extension of the KSG algorithm for estimating conditional mutual information in arbitrary dimensions is due to *Frenzel and Pompe [2007]*. A naïve illustration of k-nearest neighbours algorithm is provided in Fig. 3.7, C, where the $\epsilon(i)$ denotes the distance to a 2nd nearest neighbour from the black point.

Giving the description of three frequently used methods for estimating the (conditional) mutual information raises a question of which one to use? This is an open problem and the number of various estimators with a diverse range of assumptions and statistical properties is abundant in the research literature. The criteria which point to the best one would be that of a consistency and good performance in the sense of small systematic and statistical error for a wide class of PDFs *[Hlaváčková-Schindler et al., 2007]*. To best of my knowledge, this problem is not yet solved and the use of particular algorithm heavily depends on the intent, various statistics of the data, computational resources available, and time.

3.4.4 Inferring the causality from information theoretic measures

Let us show how one can infer the causal relationship using the conditional mutual information defined in the former sections. Let $\{x(t)\}$ and $\{y(t)\}$ be realisations of stationary and stochastic ergodic processes $\{X(t)\}$ and $\{Y(t)\}$, respectively, for $t = 1, 2, \ldots$. Recalling the previous section, the mutual information $I(y(t), x(t + \tau))$ measures the average amount of information contained in the process $\{Y\}$ about a process $\{X\}$ in its future, in particular, τ time steps ahead (or so-called τ-future). The mutual information will, however, also contain an information about the τ-future of the process $\{X\}$ contained in the past of the process itself, if the processes $\{X\}$ and $\{Y\}$ are independent (i.e. if $I(X, Y) > 0$). In order to obtain the net information about the τ-future of the process $\{X\}$ contained in the process $\{Y\}$, one has to estimate the conditional mutual information $I(y(t), x(t + \tau)|x(t))$. This was e.g. used by *Paluš et al. [2001]* in order to define a coarse-grained trans-information rate able to detect the direction of coupling in

unidirectionally coupled dynamical systems.

Since we usually work with dynamical systems evolving in measurable spaces, instead of stochastic processes, the respective conditional mutual information should be considered as n- and m-dimensional vectors, if we assume that the dynamics is evolving in n and m dimensions. Because one regularly records only one observable, instead of the original vector components $\vec{X}(t)$ and $\vec{Y}(t)$, the time-delay embedding vectors due to *Takens [1981]* are taken. Then the mutual information is written as

$$
\begin{aligned}
I(y(t), x(t+\tau)|x(t)) = I(y(t), y(t-\rho), \ldots, y(t-(m-1)\rho), x(t+\tau) \\
| x(t), x(t-\eta), \ldots, x(t-(n-1)\eta)),
\end{aligned}
\tag{3.40}
$$

where η and ρ are time lags used for embedding of trajectories $\vec{X}(t)$ and $\vec{Y}(t)$, respectively. Formally, $\vec{X}(t+\tau)$ should also be expanded using the *Takens [1981]* theorem, albeit only one component is usually used for simplicity. The same idea can be exploited and formalised with Markov processes of finite orders m and n, thus *Schreiber [2000]* proposed a "transfer entropy", which is equivalent to conditional mutual information *[Hlaváčková-Schindler et al., 2007; Paluš and Vejmelka, 2007]*.

Numerical experiments due to *Paluš and Vejmelka [2007]* suggest that the conditional mutual information in the form

$$
I(y(t), x(t+\tau) \,|\, x(t), x(t-\eta), \ldots, x(t-(n-1)\eta)))
\tag{3.41}
$$

is sufficient to infer the coupling direction between the systems $\vec{X}(t)$ and $\vec{Y}(t)$. The dimensionality of condition n must contain the full information about the state of the system $\vec{X}(t)$, while single components $y(t)$ and $x(t+\tau)$ provide sufficient information about the directional coupling.

As an example consider two unidirectionally coupled Rössler systems, studied extensively by *Paluš and Vejmelka [2007]*, which is given by

$$
\begin{aligned}
\dot{x}_1 &= -\omega_1 x_2 - x_3 \\
\dot{x}_2 &= \omega_1 x_1 + a_1 x_2 \\
\dot{x}_3 &= b_1 + x_3(x_1 - c_1)
\end{aligned}
\tag{3.42}
$$

for the autonomous system $\{X\}$, and

$$
\begin{aligned}
\dot{y}_1 &= -\omega_2 y_2 - y_3 + \epsilon(x_1 - y_1) \\
\dot{y}_2 &= \omega_2 y_1 + a_2 y_2 \\
\dot{y}_3 &= b_2 + y_3(y_1 - c_2)
\end{aligned}
\tag{3.43}
$$

for the driven, or response, system $\{Y\}$. The parameters are fixed as $a_1 = a_2 = 0.15$, $b_1 = b_2 = 0.2$, $c_1 = c_2 = 10.0$, and frequencies $\omega_1 = 1.015$ and $\omega_2 = 0.985$, hence the two systems have a very similar period. The system $\{X\}$, defined by eqns. (3.42), is autonomous ("master") and is driving the system $\{Y\}$, defined by eqns. (3.43), via the diffusive coupling term $\epsilon(x_1 - y_1)$ in the right-hand side of the driven, or "slave", system. The parameter ϵ stands for the coupling strength and after integrating the
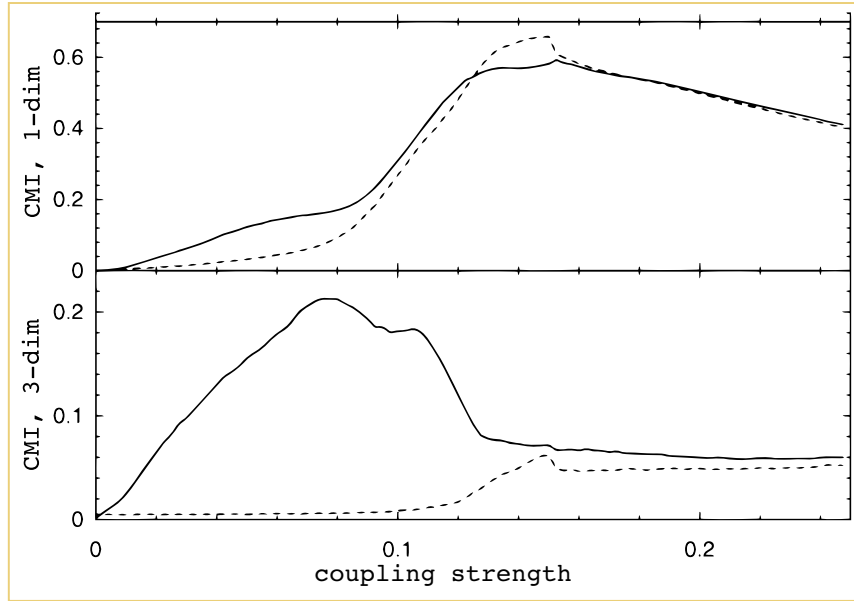
FIG. 3.8. | Conditional mutual information for unidirectionally coupled Rössler systems (3.42) and (3.43), as functions of coupling strength ϵ. Top row is the conditional mutual information with 1-dimensional condition, $I(x(t), y(t + \tau)|y(t))$ as solid line and in the other direction, $I(y(t), x(t + \tau)|x(t))$ as dashed line. Bottom row is the same, expect the condition is 3-dimensional. Figure taken from *[Paluš and Vejmelka, 2007]*.

above eqns. (3.42) and (3.43) for different coupling strengths, the conditional mutual information is estimated in order to assess the existence of directional coupling *[Paluš and Vejmelka, 2007]*.

Observing the Fig. 3.8 brings important observation: the direction of coupling can be reliably detected when the systems are coupled, but not yet fully synchronised *[Paluš and Vejmelka, 2007]*. Additionally, *Paluš and Vejmelka [2007]* conclude, that if one uses only one-dimensional condition in the conditional mutual information, the estimates of CMI are biased and this bias is different in different directions. Typically, the bias is larger in the direction from slower to a faster system (considering typical periods, in this case, the frequencies ω_1 and ω_2), or from a system with simpler dynamics to a system with more complex dynamics (e.g. a periodic system seemingly drives a chaotic system) *[Paluš, 2014a]*. The noise level can also bias the estimates of CMI. For correct and robust inference of a causal influence, the causality measure must asymptotically vanish in the uncoupled direction. For this particular example, the needed embedding dimension is 3 as seen in Fig. 3.8 bottom plot, where the estimates of CMI differ for different directions for coupling strengths ϵ lesser than approximately 0.12. This is not true for the one-dimensional embedding as seen in the top plot. For this particular example, the behaviour is the same irrespective of whether the 3-dimensional condition is constructed using the original components $x_1(t), x_2(t), x_3(t)$ of the system (3.42) or a time-delay trajectory reconstruction $x_1(t), x_1(t - \eta), x_2(t - 2\eta)$. The embedding delay η is usually chosen as a first minimum of the auto-mutual information $I(x_1(t), x_1(t + \eta))$ following the *Fraser and Swinney [1986]* recipe, or one would simply use a rule of thumb:

the embedding delay η should be approximately one quarter of a typical period of embedded system *[Fraser and Swinney, 1986]*.

3.5 Statistical hypothesis testing

We saw that in the case of deterministic dynamics, the conditional mutual information is able to find the direction of coupling. Now imagine, that instead of working with although chaotic, but deterministic dynamics and known system, we have to infer causal relationships in measured real-world data. These are usually contaminated with noise (the best-case scenario is additive uncorrelated white noise, but this is rarely true, e.g. *Vasseur and Yodzis [2004]; Sura et al. [2005]; Kang et al. [2014]*), moreover with various levels. Also, when we observe these systems, we somehow capture their dynamics in some confined temporal span and we have no means by saying whether we "saw everything" that systems are capable of doing. In other words, when our measurements hint that the system is occupying some area in the phase space, we have no guarantee that before we started to measure, the system did not undergo a phase transition, switched limit cycles, or went through a tipping point and back. Because of these difficulties, we almost never encountered a value of conditional mutual information of 0. A typical value of CMI between two normalised time series is between 0 and 0.5 and we, unfortunately, have no means by saying whether it is enough (and say, yes, there is a causal relation) or not. For these reasons we need to perform some kind of test, whether our result is significant or not — just then we can say that we observe causal relationship, usually with an addendum "on a 0.05 significance level".

The field of statistics is concerned with collecting, analysing, interpreting and explaining some data. Using statistical models, one might draw an inference about a process underlying the data. The birth of modern statistics is dated with Karl *Pearson*'s paper *[1900]* on goodness-of-fit test, although the field itself is older.

A statistical hypothesis (also called confirmatory data analysis) is a hypothesis that is testable on the basis of observing a process, which is modelled using a set of random variables *[Stuart et al., 1999]*. The statistical hypothesis test is a method of statistical inference, where commonly two data sets are compared (one of the data sets could be synthetic from an idealised model). A hypothesis of statistical relationship is proposed, as an opposition to the idealised null hypothesis, which proposes no relationship. Finally, the relationship is deemed statistically significant if this would be an unlikely realisation of the null hypothesis according to the threshold probability. This process is aided by identifying two conceptual types of errors and is referred to as Neyman–Pearson's hypothesis testing *[Neyman and Pearson, 1933]*.

The testing process has usually the following reasoning *[Hogg and Craig, 1995]*:

1. initial search for a hypothesis,
2. stating the null and alternative hypotheses, usually denoted as H_0 and H_1, respectively,
3. considering statistical assumptions; e.g. about independence or the form of distributions,
4. deciding on the test and stating relevant test statistic,

5. deriving the distribution of the statistic under the null hypothesis, H_0,
6. selecting a significance level, α — a probability threshold below which the null hypothesis H_0 will be rejected,
7. partitioning the possible values of statistic for which the null hypothesis is rejected, a so-called critical region,
8. computing the observed value of test statistic,
9. and finally, deciding to either reject the null hypothesis in favour of alternative one, H_1, or not reject it.

The problem is, that when choosing whether to reject the null hypothesis, an error might occur. The Neyman–Pearson's approach tries to minimise this error: in this framework, the significance α is called Type I error (a false positive result, i.e. incorrectly rejecting the null hypothesis in favour of the alternative one), and β is so-called Type II error (a false negative result, i.e. incorrectly accepting the null hypothesis, although the alternative one should be accepted). The validity of errors is understood in a long run: in repeated use of this procedure, the long-run average actual errors should not be greater than the long-run average reported error [Berger et al., 2003].

In the preferred approach, the discriminating statistics are carefully selected to match the null hypothesis, and ideally, it should follow a standard, or at least "standardised", distribution. In that case, the distribution can be analytically derived, and the critical value for a given significance level α can be easily computed using a known formula (or can be found in a table in various statistical textbooks, e.g. *Burington and May* [1953]). However, sometimes (or rather, almost all the times) the theoretical distribution is not known and one has to refuge to computational approach, so-called Monte Carlo simulation [Hope, 1968; Noreen, 1989; Efron and Tibshirani, 1994], which is able to accurately estimate the distribution of test statistics and its confidence range. The idea is to compute values of test statistics for many different realisations of the null hypothesis in order to derive the distribution of the statistics empirically. One of the Monte Carlo methods is a surrogate data method, which was proposed for inference of nonlinearity in the data by constructing a synthetic dataset as realisations of linear stochastic model replicating the linear properties [Theiler et al., 1992]. Shortly, the surrogate data method is a proof by contradiction technique, when one generates surrogate data according to specified null hypothesis using Monte Carlo method. The discriminating statistics are computed for the original time series and set of surrogates.

As a motivating example consider the spurious correlation between the number of Republican senators in the U.S. Senate and sunspot number, which I will briefly describe here and is described in full length in *Paluš* [2007]. It concerns the historical data of the two, for clarity shown in Fig. 3.9. Both quantities are normalised to zero mean (by subtracting the mean) and unit variance (by dividing the standard deviation). We can immediately observe that the apparent relationship, in particular in the first say 20–30 years, is remarkably good. In fact, the sample correlation coefficient between the two for period 1960–1986 is $r = 0.52$. Sample correlation is one of the most used statistics, therefore considering the null hypothesis of linear independence ($H_0 : r = 0$), its distribution under this null hypothesis is known for datasets sampled from an independent identically distributed normal population (or IID Gaussian). The critical value for correlation to be significant given the degrees of freedom, df, and significance

level, α, can be easily computed analytically, or simply found in statistics textbooks. In our case, hence df = 12 and $\alpha = 0.05$, the critical value is $\gamma = 0.458$. This means, that the null hypothesis of no linear dependence should be rejected, and therefore interpreted as an evidence for the causal relationship. However, this is obviously wrong. Where did we make a mistake?
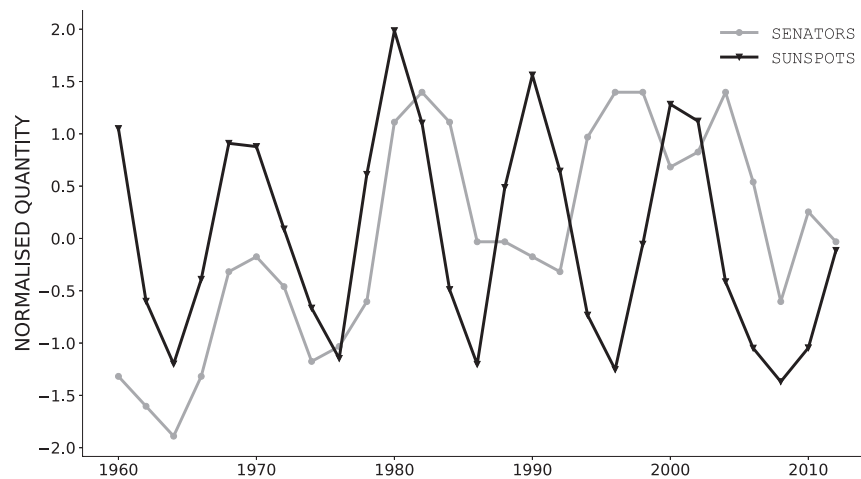
FIG. 3.9. | The normalised number of Republicans in the U.S. Senate in grey and normalised number of sunspots in black. Adapted from *Paluš [2007]*.

The problem is in the null hypothesis when we assumed IID Gaussian process, which, besides other things, means that there should not be a relation between any x_i and x_{i+j}. This is not true, though. The subsequent values in both datasets are not independent, in particular, the time series of sunspot number with its cyclic behaviour (roughly 11-year cycle) is exhibiting autocorrelation, thus $r(x_i, x_{i+j}) \neq 0$ for $j \neq 0$. This serial correlation, of course, violates the assumption of IID Gaussianity and the null hypothesis is ill-posed.

The solution lies in using surrogate data, when one generates a set of synthetic data from sunspot numbers (in this case using the *Barnes et al. [1980]* model, in full detail described in *Paluš [2007]*), say 100 000 realisations and computes a sample correlation r between the senators time series and each synthetic sunspot number time series. Using this approach the p-value of the sample correlation is now $p < 0.14$, which is not considered small enough to reject the null hypothesis. The statistical test with proper null hypothesis showed that this rather high correlation ($r = 0.52$) occurred by chance.

In general, the surrogate data generation algorithms can be classified into two groups:

- *typical realisations:* surrogate data are generated as outputs of some well-fitted model to the original data

- *constrained realisations:* surrogate data are generated directly from the original data by some suitable transformation of them.

In the following text, I will introduce some of the most known and used techniques for generating surrogate time series that are useful in the context of climate science.

3.5.1 Fourier Transform surrogates

Probably the most known type of surrogate data is Fourier transform (FT) surrogates, also called Random Phases surrogates. The algorithm was developed by *Theiler et al. [1992]*, who sought an appropriate test for rejecting the null hypothesis of a linear stochastic process, thus testing for nonlinearity in the data. It is a non-parametric method (constrained realisation), which preserves the so-called linear properties of the original time series.

For a Gaussian process, its linear properties are specified by squared amplitudes of the Fourier transform *[Paluš, 2007]*, and the required transformation is generated by multiplying the Fourier transform of the data by random phases and transforming back into the time domain, so for the surrogate series $\{x'(t)\}$ it is

$$x'(t) = \sum_{k=0}^{N-1} e^{i\alpha_k} \sqrt{P(k)} e^{-i2\pi kt/N}, \tag{3.44}$$

where $0 \geq \alpha_k \geq 2\pi$ are independent, uniformly distributed random numbers and $P(k)$ is a periodogram of the original time series $\{x(t)\}$, so

$$P(k) = \left| \left(\sum_{t=0}^{N-1} x(t) e^{i2\pi kt/N} \right)^2 \right|. \tag{3.45}$$

In summary, the Fourier transform surrogates are widely used as a surrogate data representing a null hypothesis of a linear stochastic process with the same spectrum as the original data. However, they performance can be jeopardised by various caveats: *Chan [1997]* shows that asymptotically the FT surrogates are valid for Gaussian circular processes; *Schreiber [1999]* notes, that FT surrogates preserves the periodic autocorrelation function rather than the standard autocorrelation function; and *Paluš [1995]* finds that for strongly cyclic data (such as e.g. surface temperature with strong annual cycle) and limited length of the available data, the FT surrogates exhibit blurred spectral peak and have weaker autocorrelation than the original data, which can introduce a falsely rejecting the null hypothesis.

Apart from the original FT method, a few extensions exist. *Theiler et al. [1992]* proposed a histogram transformation (rescaling the data) ensuing equal histograms of the original data and the surrogates because realisations of pure FT surrogates tend to have Gaussian distribution. This new method is called Amplitude Adjusted FT surrogates, or AAFT surrogates. Histogram transformation is, however, a static nonlinear transformation (static as it has nothing to do with the dynamics of the process) *[Paluš, 2007]*, hence the null hypothesis must be appropriately updated.

Nevertheless, *Schreiber and Schmitz [1996]* found that for short strongly autocorrelated time series, the improved AAFT method biases towards a flatter spectrum. Hence, they introduce an even more improved method, when they iteratively correct the deviations in the spectrum and the distribution, switching between randomising the phases in the Fourier domain, and correcting the histogram of the raw data values. Since this process

is iterative, the algorithm is named Iterative Amplitude Adjusted FT surrogates, thus IAAFT.

The Fig. 3.10 summarises all three presented algorithms for generating FT surrogates and their derivatives. The daily air surface temperature data from Prague – Klementinum *[Klein Tank et al., 2002]* was taken, climatologically normalised (or deseasonalised according to some authors, e.g. *Paluš [2014b]*), that is the climatological mean was removed as was the climatological standard deviations. Then, 5 surrogates of each type (that is FT, AAFT and IAAFT) were generated and the climatological standard deviation and mean subsequently multiplied in and added, respectively. The Fig. 3.10 shows the time series themselves (panel A), Welch spectra (panel B), autocorrelation function (panel C), and histograms of the data with their respective kernel density estimates using Gaussian kernel (panel D). As one can see, all the measures coincide almost perfectly (with one exception in the form of one FT surrogate realisation exhibiting greater power in the annual cycle as seen in Fig. 3.10, panel B). From this, we conclude that indeed the FT surrogates and their derivatives preserve basic linear properties of the original time series, and therefore are suitable as a null model for a linear stochastic process.
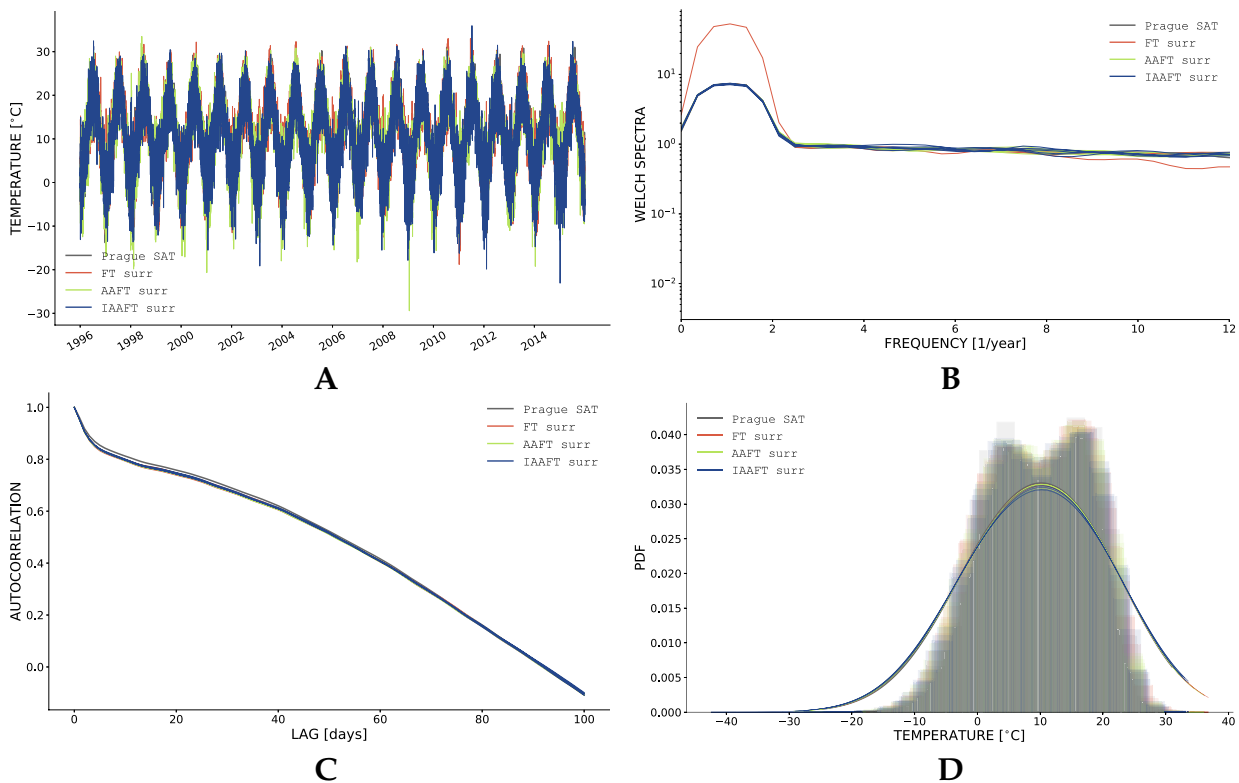
FIG. 3.10. | An example of Fourier transform surrogate data and its derivatives. Shown are the time series themselves (**A**), Welch linear spectra (**B**), autocorrelation function (**C**), and histogram with kernel density estimate (Gaussian kernel) of the data (**D**). Shown are always the original time series of surface air temperature from Prague – Klementinum, and 5 realisations of each type of surrogate data: FT, AAFT and IAAFT.

## 3.5.2 Autoregressive (moving average) surrogates

Another widely used type of surrogate data is based on autoregressive (AR) model, or more generally on autoregressive moving average (ARMA) models. Autoregressive models are based on a definition of a linear stochastic model (e.g. *Priestley [1981]*)

$$X(t) = X(0) + \underbrace{\sum_{i=1}^{\infty} a_i X(t-i)}_{\text{autoregression}} + \underbrace{\sum_{i=0}^{\infty} b_i \mathcal{N}(t-i)}_{\text{moving average}} + \underbrace{\xi(i)}_{\text{residual}} , \tag{3.46}$$

where $b_0 = 1$, $\sum_{i=1}^{\infty} |a_i| < \infty$, $\sum_{j=0}^{\infty} |b_j| < \infty$, and $\{\mathcal{N}(t)\}$ is iid Gaussian process with zero mean and finite variance. The ARMA model is defined as autoregression and moving average terms in the eqn. (3.46) (hence, in general, without the residual term), while the AR model is defined without the moving average term in the eqn. (3.46) and with the residual term. Of course, this is a theoretical definition of infinite AR (or ARMA) model, in practice, the first, autoregressive, term has p (m) summands for AR (ARMA) model, while the second, moving average, term has n summands. Shortly, we write AR(p) as an autoregressive model of order p, and ARMA(m,n) as an autoregressive moving average model of orders m and n.

When one would use an AR surrogate for testing this would be a typical realisation (in opposition with constrained realisation of FT surrogate) as firstly one needs to fit the model and estimate the coefficients a_i for $i \leq p$ when using AR model, or estimate the coefficients a_i and b_j for $i \leq m$ and $j \leq n$. After fitting an ARMA model to the data, one finds the coefficients and residuals, there are two options how to generate the surrogate itself: either using shuffled residuals as the innovations in the model or use Gaussian random process as the innovations. Using ARMA surrogate data represents the null hypothesis of a linear process without any cycles in the data. The order selection criteria are usually estimated as approximations to Schwarz's Bayesian Criterion (SBC) *[Schwarz et al., 1978]* or Akaike's Final Prediction Error (FPE) *[Akaike, 1970]*.

Similarly as for FT surrogates, Fig. 3.11 illustrates basic linear measures describing the original time series (again, daily surface air temperature from Prague – Klementinum *[Klein Tank et al., 2002]*) and 5 realisations form each model. Shown are two different models: an autoregressive model of order $p = 1$, which is routinely used as basic typical realisation model of a linear process with no cycles, and then more complex model of order $p = 7$. The order of the more complex model was estimated as ideal using the SBC (note, that in this case, the FPE gives the same estimate of order). As with the FT surrogates, AR surrogates are able to mimic the linear statistics of the data (with a little offset in the autocorrelation function, see Fig. 3.11, C). In this case, the AR surrogates were created using deseasonalised data (translated to climatological zero mean and unit variance, as before with FT surrogates) and therefore we are creating surrogate data from the normalised anomalies, hence they look like they are able to resemble the annual cycle. Although resembling the FT surrogates, the difference is that AR surrogates are a typical realisation, whereas FT surrogates are constrained (by the particular spectrum). Fourier Transform surrogates would mimic the variability of the AR surrogates if we randomised not only the phases but the amplitudes as well.
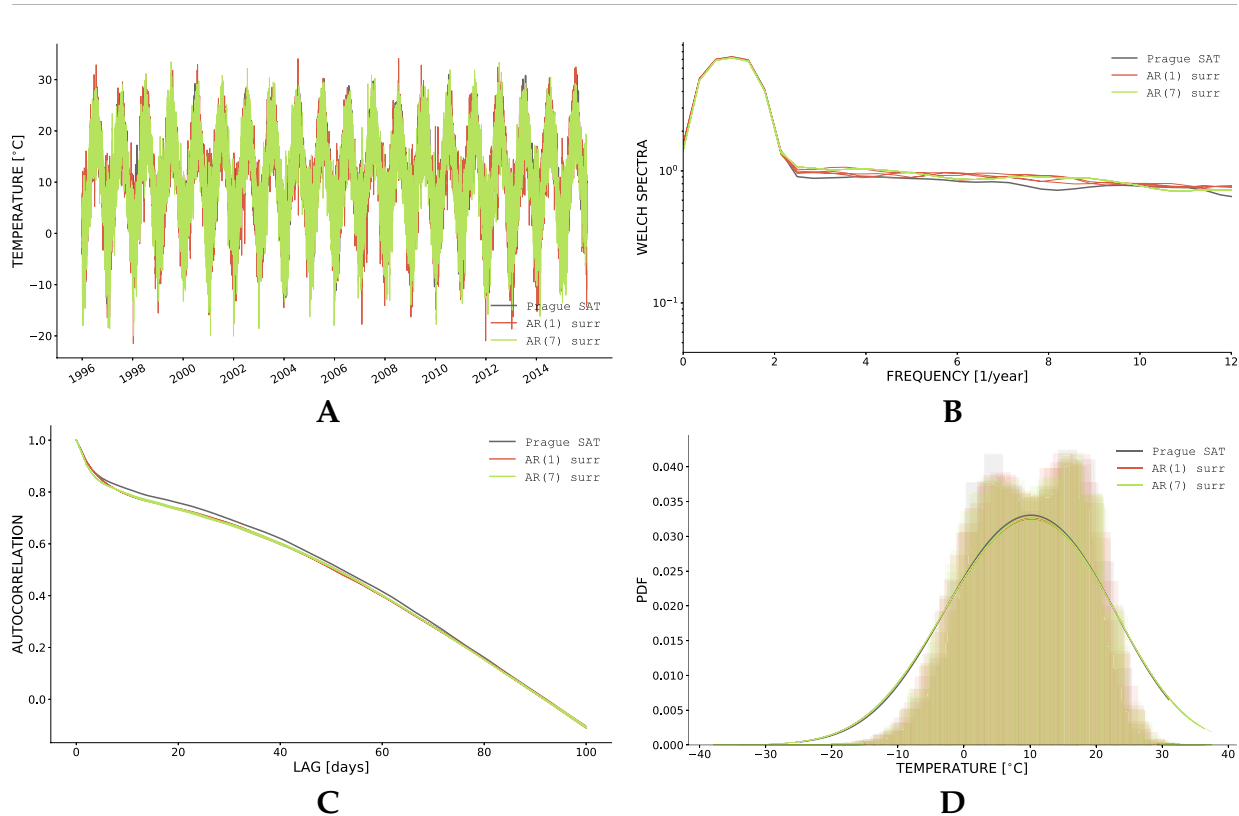
Fig. 3.11. | An example of autoregressive (AR) surrogate data and its derivatives. Shown are the time series themselves (**A**), Welch linear spectra (**B**), autocorrelation function (**C**), and histogram with kernel density estimate (Gaussian kernel) of the data (**D**). Shown are always the original time series of surface air temperature from Prague – Klementinum, and 5 realisations of two different models: one with order $p = 1$, and with ideal order estimated using Schwarz's Bayesian Criterion (SBC) as $p = 7$.

3.5.3 Complicated null models

As can be anticipated, throughout time many different methods for generating surrogate data in order to test statistical hypotheses have been developed. Preservation of spectra and amplitude was solved in FT surrogates by amplitude adjustments and iterative procedures as in IAAFT (recall sec. 3.5.1). Since preserving autocorrelation function, and therefore, the linear spectrum can be easily done in Fourier domain, *Breakspear et al. [2003]* introduced surrogate data based on discrete wavelet transform *[Daubechies, 1992]*, where the randomisation is done by manipulating the wavelet coefficients in one of the following ways:

- a random permutation,

- cyclic rotation with a random offset, or

- block resampling — a random permutation of a block of wavelet coefficients.

All these approaches preserve so-called linear properties (i.e. the first and second moments), however any possible nonlinear dependence between the signal at time $s(t)$

43

and its past $s(t - \eta)$ is destroyed, as are the potentially hierarchical, multi-scale interactions. *Angelini et al. [2005]* articulated a need for bootstrapping methods for testing the hierarchical structure in atmospheric turbulence data. Same authors also proposed a sophisticated block resampling technique, only with partial success, as the multifractal properties were not fully reproduced in the synthetic dataset. *Thiel et al. [2006]* suggested using a "twin" surrogate data, which preserve nonlinear dependence in trajectories in the phase space of the process, however, the method is not suitable, since the process of generating the surrogate data violates the recurrence condition.

Finally, *Paluš [2008]* proposed a method, that the resampled data replicate multifractal properties of the original input data. The construction preserves multifractal spectrum, as well as the nonlinear dependence structure. The so-called multifractal surrogates are based on the idea of *Arneodo et al. [1998]*, who proposed a cascade process using the dyadic tree structure to construct a self-similar process whose properties are defined multiplicatively. Naïvely, applying a discrete wavelet transform to an experimental measured time series $\{s(t)\}$ yields a set of wavelet coefficients $\{c_{j,k}\}$, which are randomly permuted, rearranged in order to preserve the amplitudes, and finally inverse-transformed back into temporal domain. The new coefficients $\{\tilde{c}_{j,k}\}$ preserve the statistical relationship among the scales due to recurrent cascade from coarse to finer scales *[Paluš, 2008]*.

Another possibility to generate synthetic time-series for statistical testing would be a use of a statistical model, based on the idea of linear inverse models *[Penland, 1989, 1996]*. Statistical, or data-driven, models are constructed using the ideas of stochastic inverse models, where one models the evolution of a time series as

$$\mathrm{d}\mathbf{x} = \mathbf{B}^0 \mathbf{x} \mathrm{d}t + \mathrm{d}\mathbf{r}^0, \tag{3.47}$$

where the linear operator $\mathbf{B}^0$ and the covariance matrix of the residual noise $\mathbf{Q} \equiv \langle \mathbf{r}^0 \mathbf{r}^{0\mathrm{T}} \rangle$ can be directly estimated from the observed statistics of $\mathbf{x}$ by multiple linear regression *[Darlington and Hayes, 2016]*. These models are usually constructed in a phase space spanned by first few empirical orthogonal functions *[Hannachi et al., 2007]*. Models like these have shown success in predicting ENSO *[Penland and Sardeshmukh, 1995; Kondrashov et al., 2005]*, tropical Atlantic variability *[Penland and Matrosova, 1998]*, as well as extratropical atmospheric variability *[Winkler et al., 2001]*.

Kondrashov et al. [2005] and *Kondrashov et al. [2015]* extended the idea to include nonlinear terms, as well as more levels, where the residual in eqn. (3.47) is subsequently modelled in a linear fashion, thus adding the next level to the model. This is to be continued until the residual at the level L is white in time.

This type of model opens a possibility to exploit the idea behind multilevel nonlinear models in a surrogate testing when one includes as many levels, or as many nonlinear terms, to correspond with the properties one wishes to preserve. This was experimentally tested when testing for statistical significance in a study of causal relationships in ENSO *[Jajcay and Paluš, 2016b]*.

The scientific literature on the uses of surrogate data in geosciences is, to this day, abundant and I refer the potential reader to exhaustive reviews, e.g. due to *Schreiber and Schmitz [2000]* and *Venema et al. [2006]*.

Time scales of the European surface air temperature variability

Shallow men believe in luck or in circumstance.
Strong men believe in cause and effect.
   Ralph Waldo Emerson

Over the past few decades many authors and teams studied the low-frequency variability in climate variables in order to assess and possibly separate the anthropogenic climate change from the natural variability on long temporal scales (see e.g. *Ghil and Vautard [1991]; Mann and Park [1993]; Allen and Smith [1994]; Plaut and Vautard [1994]; Dettinger et al. [1995]; Folland et al. [2002]; Viron et al. [2013]* and many more). This is crucial for our understanding of the climatic response to increasing greenhouse-gas and aerosol concentration, and ultimately for the prediction of future climate on Earth. However, studying the variability over time scales beyond the synoptic range turned out to be extremely challenging because of two properties in particular: nonlinearity and unpredictability *[Plaut and Vautard, 1994]*. All studies conducted in the past found that significant, albeit irregular, warming has occurred on a global scale since 1850. This trend is rather flat from the middle of the nineteenth century till 1910, followed by an increase of more than 0.1°C/decade during 1910–1940 and the last two decades, with an even larger increase in the most recent past *[Moron et al., 1998]*. The two episodes were separated by mild cooling, especially in the Northern Hemisphere *[Parker et al., 1994, 1996; Folland et al., 2002]*. Recent global warming has been associated by some authors with abrupt changes in the North Pacific around 1976 or with a gradual changes in the sea surface temperature in the tropical Pacific *[Pan and Oort, 1990; Trenberth, 1990; Kerr, 1994; Latif and Barnett, 1994, 1995]*, as well as with other regional phenomena *[Folland et al., 1986; Kumar et al., 1994; Hurrell, 1996]*.

Since this trend is irregular, and the tentative identification of anthropogenic, or any other external influence on it, it is not feasible to isolate it from the natural climate variability. This so-called natural climate variability is usually interpreted as a red noise background *[Hasselmann, 1976]*, and it has been recently argued, that it has some regularity embedded into it. The existence of such regularities on the interannual time-scales is well established and attributed mostly to an instability of the coupled ocean-atmosphere system in the tropical Pacific *[Philander, 1983; Rasmusson et al., 1990]*. The distinct periodicities of roughly 2–3 years and 4–6 years have been associated with the El Niño/Southern Oscillation phenomenon *[Rasmusson and Carpenter, 1982; Barnett, 1991; Allen, 1992; Mann and Park, 1994; Jiang et al., 1995]*, and although the evidence for similar regularities on the decadal and even longer time scales exists *[Ghil and Vautard, 1991; Allen and Smith, 1994; Plaut et al., 1995; Mann and Park, 1996b]*, it is hard to establish the significance of these results, mainly due to shortness of instrumental records of temperature, sea surface temperature, or pressure.

Moving away from the equator and ENSO, the extratropical atmosphere is, as well as the tropical, dominated by low-frequency motions. It is true, though, that the synoptic fluctuations are more noticeable in our daily lives, or when we look at the next day forecast. The manifestation of low-frequency phenomena involves planetary waves that generally have *e*-folding times much longer than baroclinic transient waves in mid-latitudes. The key phenomenon is that the synoptic transients are able to maintain low-frequency motions by themselves through nonlinear feedback *[Egger and Schilling, 1984; Metz, 1987]*. Starting in the 1980s with the work of *Wallace and Gutzler [1981]*, various researchers correlated the oscillations across large regions, spanning thousands of kilometres, giving rise to *teleconnection* patterns. These turned out to explain a large portion of low-frequency variability and have been attributed to several causes, including

the propagation of atmospheric Kelvin and Rossby waves, changes in thermally direct circulations, intrinsic modes of atmospheric variability, and changes in the oceans' wind-driven thermohaline circulation *[Feliks et al., 2010]*. In the former literature the terms "teleconnection" and "oscillation" are often used synonymously, ever since the discovery of the North Atlantic, North Pacific and Southern oscillations by *Walker [1931, 1932]*. Although the pioneering studies did not explicitly imply the presence of distinct spectral peaks, *Walker [1931]* did hint at their presence in the Southern Oscillation. Since then, the teleconnection patterns, or oscillations over the globe became one of the most studied phenomena in the climate science.

4.1 Overview of modes of variability and their temporal scales in Europe

4.1.1 The North Atlantic Oscillation

Probably the most prominent and studied weather phenomenon in the Northern Hemisphere is the North Atlantic oscillation (usually abbreviated as *NAO*) *[Rogers, 1990; Hurrell, 1995]*. NAO manifest itself as fluctuations in the difference of atmospheric pressure at sea level between the semi-permanent synoptic Icelandic low and the Azores high. By the means of fluctuations of these semi-permanent centres, NAO controls the strength and direction of westerly winds onto European continent, and location and storm tracks across the North Atlantic *[Hurrell et al., 2003]*. The situations is, that westerlies blowing across the Atlantic bring moist air into Europe: strong westerlies imply cool summer, mild winters, and frequent rain, while suppressed westerlies entail more extreme temperatures both in summer and winter, heat waves, freezes and reduced rainfall *[ncdc.noaa.gov; cpc.ncep.noaa.gov]*. Now, a positive phase of NAO (*NAO+*) result in a large difference in the pressure between Azores high and Icelandic low and this leads to increased westerlies. In contrast, during a negative phase of NAO (*NAO-*), the pressure difference is small, and consequently, the westerlies are suppressed, meaning, apart from cold dry winters, also a southward shift in storm tracks towards the Mediterranean Sea, which in turn brings rainfall to southern Europe and North Africa. Moreover, NAO is responsible for strength and position of the North Atlantic jet stream. All these effects turn NAO into the most important cause of climate variability in the North Atlantic area on interannual time scales *[Hurrell, 1995; Hurrell and Van Loon, 1997; Osborn et al., 1999; Rodrigo et al., 2001]*. The illustration of NAO dipole centres during both phases, as well as effect on humidity, is shown in Fig. 4.1 with positive phase, *NAO+*, on the left-hand side, and negative phase, *NAO-*, in the right-hand side.

In order to study the NAO temporal variability, it is crucial to have some kind of time series representing the phenomenon. For this purpose, the NAO index was proposed and in the recent years several other NAO indices emerged with various definitions and time-averaging *[Hurrell and Van Loon, 1997; Jones et al., 1997]*. In general, the indices described NAO phenomenon could be split into two: station-based index and PCA-based index. The station-based index of the NAO is based on the difference of normalised sea

positive phase
NAO+
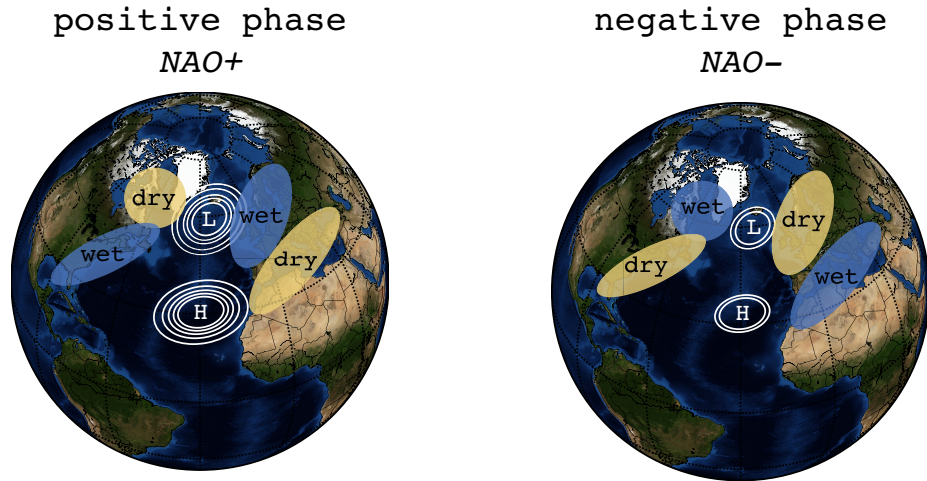
negative phase
NAO−

Fɪɢ. 4.1. | An illustration of NAO's two distinct phases: (left) the positive NAO phase and (right) the negative NAO phase. The dipole structure of semi-permanent action centres of Icelandic low and Azores high is render with white ellipses. The effects of both phases on humidity during winter months November–April are renderer in yellow for dry and blue for wet conditions. Adapted from *windows2universe.org*.

level pressure between Lisbon, Portugal and Stykkishólmur/Reykjavik, Iceland *[Hurrell, 1995]*. The data goes back to 1864. Positive values of this index are associated with a positive phase of NAO (recall Fig. 4.1, left-hand side), hence stronger-than-average westerlies. This index is usually taken in monthly resolution, although daily, annual, and seasonal resolution are not uncommon. *Jones et al. [1997]* instead of using the station in Lisbon, Portugal uses either Gibraltar or Ponta Delgada, Azores for defining the NAO index.

The other family of NAO indices are PCA-based. PCA, which stands for Principal Component Analysis *[Hannachi et al., 2007]* is a statistical procedure that uses an orthogonal transformation to convert a set of observations of possibly correlated variables into a set of values of linearly uncorrelated variables called principal components. Shortly, PCA analysis is usually done by the means of singular value decomposition *[Golub and Van Loan, 1996]* of spatio-temporal matrix X as

$$X = \sum_{k=1}^{r} \lambda_k \mathbf{a}_k \mathbf{u}_k^{\mathrm{T}}, \qquad (4.1)$$

with λ_k being the kth eigenvalue, $\mathbf{u}_k$ the right singular vector, or the EOF (empirical orthogonal function) loading pattern, and $\mathbf{a}_k$ the left singular vector representing the time series of the respective loading, or sometimes called PC, as a principal component. This method is often used for dimensionality reduction, by truncating the sum in eqn. (4.1) and keeping just first M elements, where M is generally much smaller than r. The goal of PCA analysis is to maximise the second-order moment (the variance), and by this, we also minimise the squared error between the original field and its PCA representation.

While the station-based index has its strength in the temporal span, as the indices extend back to the mid-19$^{\mathrm{th}}$century, they may not be the optimal representation of the
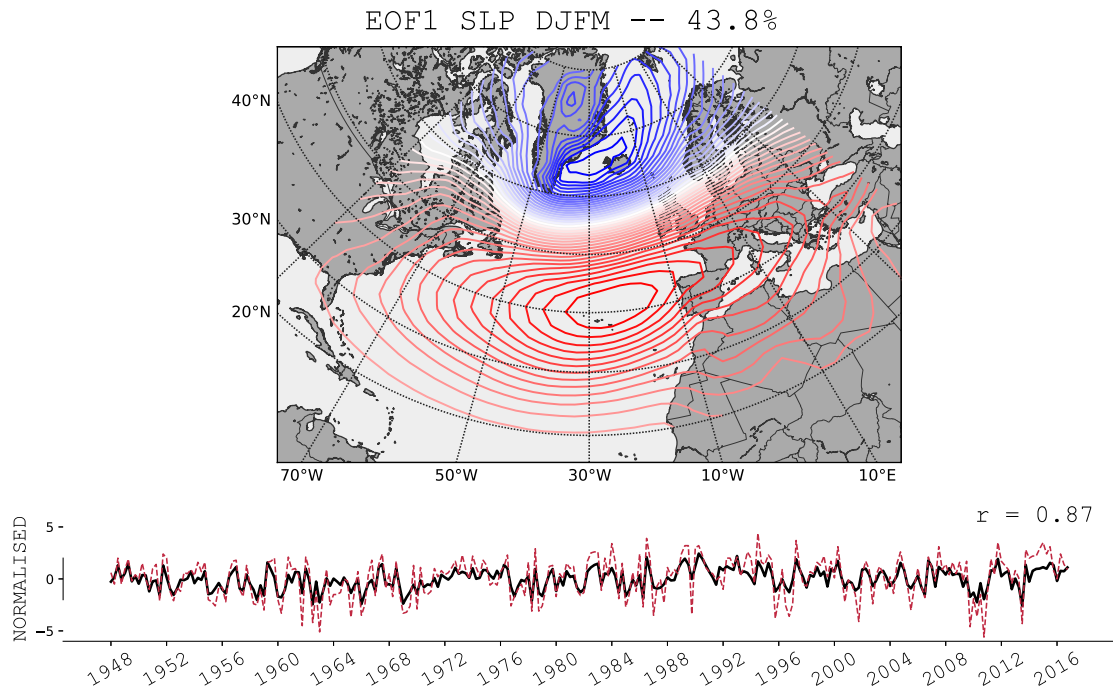
Fig. 4.2. | PCA-based NAO index. (top) Shown is first EOF loading pattern of DJFM sea level pressure anomalies (SLPA) which represent the North Atlantic Oscillation. Data from NCEP/NCAR reanalysis *[Kalnay et al., 1996]*. This first component explains 43.8% of the total variance in the SLPA field over the Atlantic sector. (bottom) The normalised time series (PC) of the respective EOF pattern in black. Shown is also station-based NAO index with dashed red line and the Pearson's correlation coefficient between the two is at 0.87 level.

associated spatial pattern. Since the stations are fixed in space, they cannot track the movement of the NAO centres of action through the annual cycle, and their individual pressure readings can be noisy due to small-scale and transient meteorological phenomena unrelated to NAO. As with the station-based indices, also PCA-based indices come in more flavours. The original PCA-based NAO index due to *Hurrell [1995]* is defined as the first principal component (i.e. the time series of first EOF loading pattern) of sea level pressure anomalies over the Atlantic sector, $20°-80°N$, $90°W-40°E$. As written above, the PCA-based index is used to track the seasonal movements of the Icelandic low and Azores high. As an example, Fig. 4.2 shows the first EOF loading pattern of sea level pressure anomalies (SLPA) in winter time — December – March (DJFM). The principal component time series (PC) is shown in bottom part of the figure in thick black as normalised time series to zero mean and unit variance. Also shown is station-based NAO index for the same temporal span and the Pearson's correlation coefficient between the two is at 0.87 level. The first EOF loading pattern, which represents the NAO, explains 43.8% of the total variance in the SLPA field over the Atlantic sector.

Apart from the usual PCA-based NAO mode found in the SLPA field, some authors also seek modes of circulation variability over the Atlantic sector in other types of data, most notably in 500hPa level of geopotential height field (HGTA500) (e.g. *Van den Dool [2007]; Beranová and Huth [2008]*). The first EOF loading pattern of HGTA500 field from
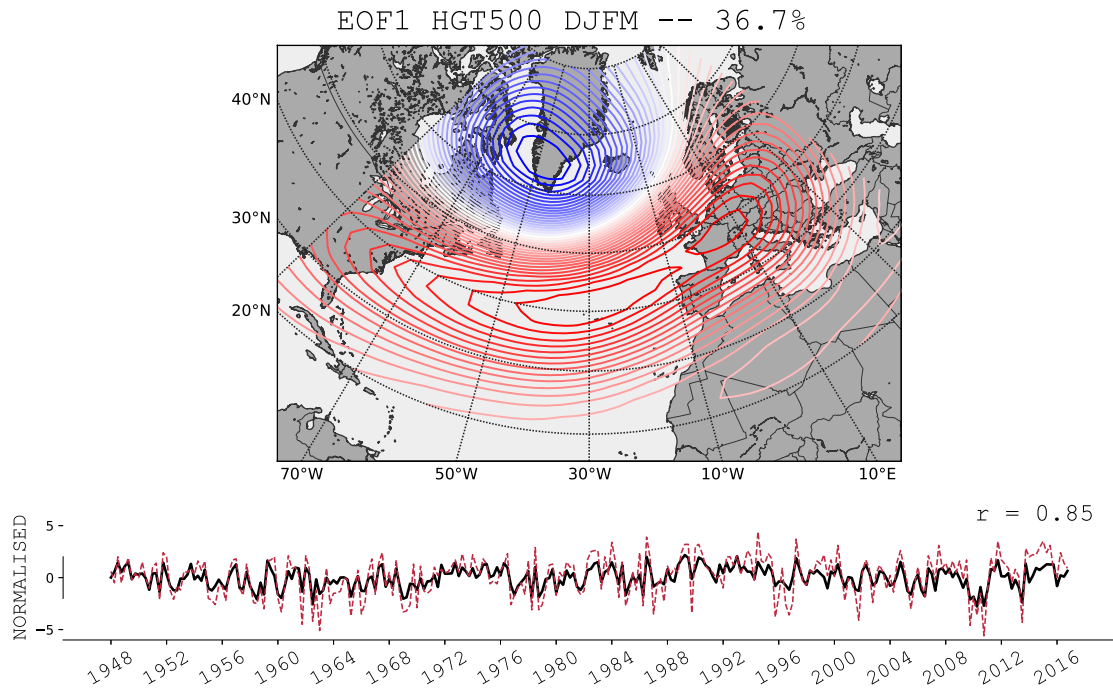
FIG. 4.3. | PCA-based NAO index. (top) Shown is first EOF loading pattern of DJFM geopotential height at 500hPa anomalies (HGTA500) which represent the North Atlantic Oscillation. Data from NCEP/NCAR reanalysis *[Kalnay et al., 1996]*. This first component explains 36.7% of the total variance in the HGTA500 field over the Atlantic sector. (bottom) The normalised time series (PC) of the respective EOF pattern in black. Shown is also station-based NAO index with dashed red line and the Pearson's correlation coefficient between the two is at 0.85 level.

NCEP/NCAR reanalysis data *[Kalnay et al., 1996]* is shown in Fig. 4.3. As can be seen from the figure, the EOF pattern very much resembles the EOF pattern from SLPA field (compare Figs. 4.3 with 4.2), with small deviations, such as the negative centre of action in the HGTA500 field is shifted westward over Greenland (in SLPA field it is between the Greenland and Iceland) and the positive centre of action in the HGTA500 field is spread in the zonal direction. The respective time series of this EOF loading pattern correlates with the station-based NAO index at the 0.85 level, and the mode of variability associated with this EOF pattern is responsible for 36.7% of the total variance in the HGTA500 field.

Now, given the effect of NAO on European temperatures and precipitation (see e.g. *Huth [1997]; Chen and Hellström [1999]; Jones et al. [2003]; Trigo et al. [2004]; Beranová and Huth [2008]*) one might ask whether the NAO phenomenon is associated with some typical frequency. Despite intense research in the last few decades, the physical mechanisms underlying the temporal variability of the NAO remain unclear. The spectral analysis of the NAO indices, both using classical and also wavelet analysis, provides a near-white noise like behaviour *[Gámiz-Fortis et al., 2002]*. Others claim, that the spectral behaviour of NAO resembles a pink noise (pink noise exhibits $1/f$ spectrum, opposed to a white noise, which exhibits flat power spectrum) with very little predictability *[Fernández et al., 2003]*. However, some significant power associated with periods around 2 years, between 5 and 6 years and at quasi-decadal scales have been reported *[Rogers,*
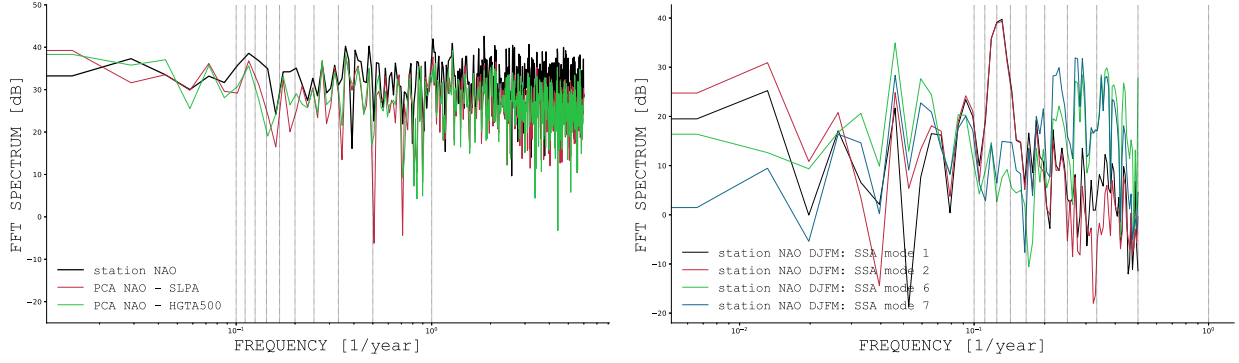
Fig. 4.4. | (left) FFT spectra of three distinct NAO indices. Station-based NAO index *[Hurrell, 1995]* FFT spectrum in black, PCA-based indices in colour: EOF1 derived from SLPA in red, and derived from HGTA500 in green. Note elevated power between 2 and 3 years and around 8 years. (right) FFT spectra of 4 different SSA modes (see text) of station-based NAO winter index (mean over DJFM values).

1984; Pozo-Vázquez et al., 2000; Stephenson et al., 2000; Pozo-Vázquez et al., 2001]. Some of these significant power can be also estimated using basic FFT spectrum as in Fig. 4.4, left. This low-frequency variability has been associated with processes involving the North Atlantic ocean basin *[Delworth, 1996; Taylor and Stephens, 1998; Timmermann et al., 1998]*, and also internally generated atmospheric processes *[Perlwitz and Graf, 1995]*.

Since NAO behaviour resembles a noise process, it would be beneficial to use a more sophisticated method for identification and distinction the signal from noise in some measured variable. Many authors used the Singular Spectrum Analysis (SSA hereafter) for this purpose, which is based (similarly as PCA) on an orthogonal decomposition of a covariance matrix of the data. In the field of climate science when dealing with one variable, one would use a univariate form of SSA and time-lagged covariance matrix, i.e. instead of several components of multivariate data, a time series and its time-lagged counterparts are considered *[Vautard and Ghil, 1989; Ghil and Vautard, 1991; Allen and Smith, 1994].* This decomposition can provide us with a set of orthogonal components with different dynamical properties, therefore phenomena of interest such as slow modes, or trends, and regular and quasi-regular oscillations can be identified and retrieved from the noise background.

Mathematically, let $\{y(i)\}$ be a univariate time series — a realisation of stochastic process $\{Y\}$ which is stationary and ergodic. Now, map into space of n-dimensional vectors $\mathbf{x}(i)$ with components $x^k(i)$ as

$$x^k(i) = y(i + k - 1). \tag{4.2}$$

The sequence of vectors $\mathbf{x}(i)$ is usually referred to as the $n \times N$ trajectory matrix $\mathbf{X} = \{x_i^k\}$, the number n is the embedding dimension. Now, the covariance matrix from trajectory matrix $\mathbf{C} = \mathbf{X}^T\mathbf{X}$ have elements

$$c_{kl} = \frac{1}{N} \sum_{i=1}^{N} x^k(i) x^l(i), \tag{4.3}$$

51

where $1/N$ is a normalisation and the components $x^k(i)$ are supposed to have zero mean. Then the symmetric matrix $\mathbf{C}$ is decomposed as

$$\mathbf{C} = \mathbf{V}\Sigma\mathbf{V}^{\mathrm{T}}, \tag{4.4}$$

where $\mathbf{V} = \{v_{ij}\}$ is an $n \times n$ orthogonal matrix, $\Sigma = \mathrm{diag}\,(\sigma_1, \sigma_2, \ldots, \sigma_n)$ is a diagonal matrix of non-negative eigenvalues of $\mathbf{C}$ by convention in descending order. Finally, the modes ξ_i^k

$$\xi_i^k = \sum_{l=1}^{n} v_{lk} x_i^l, \tag{4.5}$$

for $k = 1, \ldots, m$ are considered as the "signal" part, and the modes for $k = m + 1, \ldots, n$ are considered the noise part of the original time series. The signal modes can be used to reconstruct the "signal" part of the original time series

$$\tilde{x}_i^k = \sum_{l=1}^{m} v_{kl} \xi_i^l, \tag{4.6}$$

and the original time series, including also the noise part, would be reconstructed as

$$x_i^k = \sum_{l=1}^{n} v_{kl} \xi_i^l. \tag{4.7}$$

The modes ξ_i^k can be interpreted as time-dependent coefficients (something like principal components in PCA), and the orthogonal vectors $\mathbf{v}_k = \{v_{kl}\}$ as basis functions, called empirical orthogonal functions. The eigenvalue signal-noise distinction can, unfortunately, be obtained only in idealised conditions, many Monte Carlo approaches emerged to address this issue, the most prominent being the Monte Carlo SSA (MC-SSA), where the synthetic AR(1) time series are constructed, and subsequently the spectra from original data-based eigenvalues and synthetic eigenvalues are compared.

Gámiz-Fortis et al. [2002] and *Paluš and Novotná [2004]* used the SSA approach in order to detect dominant modes in lagged covariance matrix of NAO index. With the use of embedding window of 40 years, the pair of dominant modes were found to exhibit a spectral peak around 7.8 years *[Gámiz-Fortis et al., 2002; Paluš and Novotná, 2004]*. This can be seen also in Fig. 4.4, right, where I show the FFT spectra of 4 distinct SSA modes: the pair of leading modes 1 and 2, and then the 6 and 7 modes, which exhibit elevated variance in the period around 4.8 years.

Since NAO is the most prominent phenomenon that largely affects the weather in Europe, it was important to lay the basics for its understanding and to study on which temporal scales the NAO exhibits notable variance. As we will soon see, some of the European station data exhibit power at frequencies around 8-year cycle, or at least the cycle around 8 years turns out to be prominent in information transfer across temporal scales.
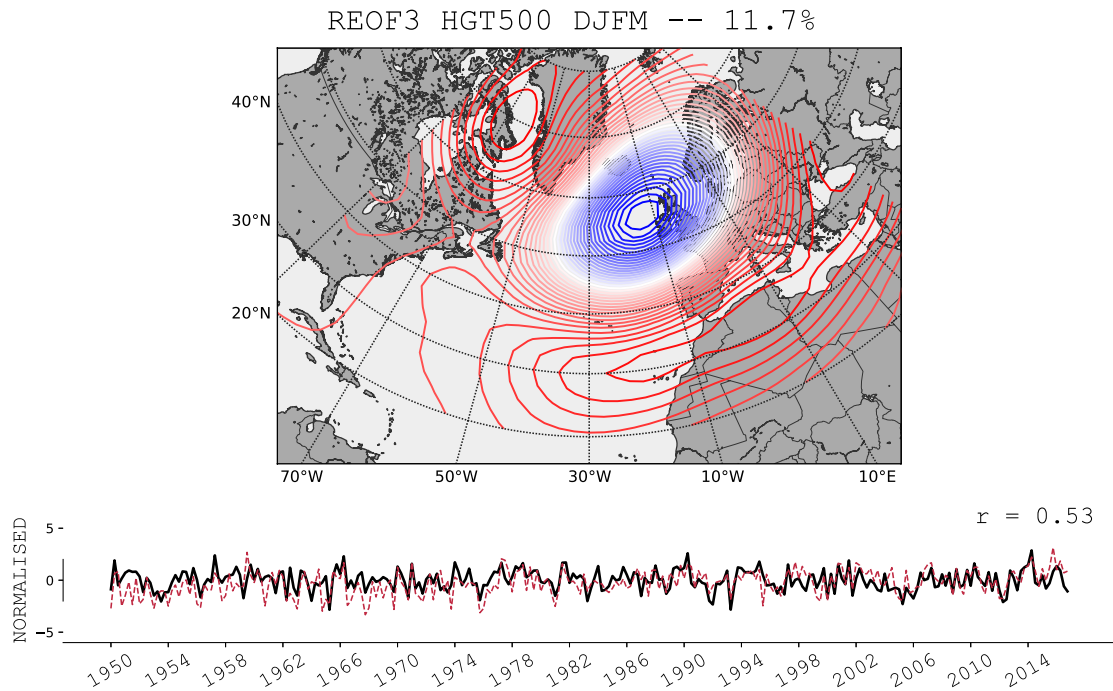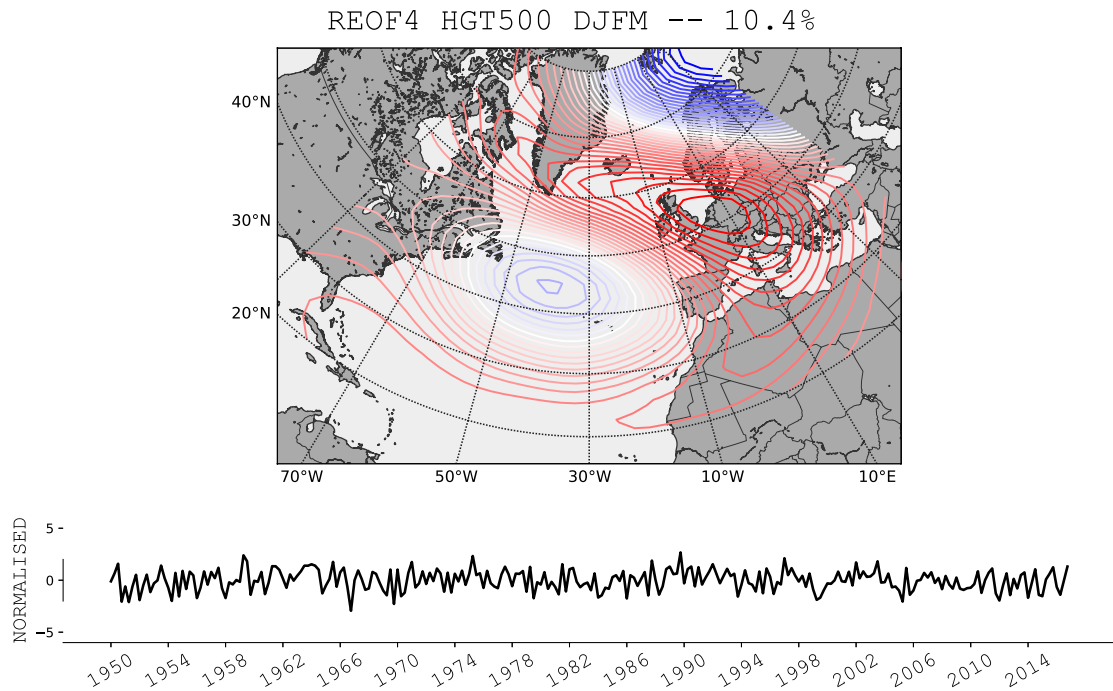
Fig. 4.5. | RPCA-based EA index. (top) Shown is third rotated EOF loading pattern of DJFM geopotential height at 500hPa anomalies (HGTA500) which represent the East Atlantic pattern. Data from NCEP/NCAR reanalysis *[Kalnay et al., 1996]*. This third rotated component explains 11.7% of the total variance in the HGTA500 field over the Atlantic sector. (bottom) The normalised time series (PC) of the respective EOF pattern in black. Shown is also EA index (based on rotated PCA) with dashed red line and the Pearson's correlation coefficient between the two is at 0.53 level.

4.1.2 Other modes of variability over Europe

In addition to already mentioned and described NAO, other circulation patterns, or modes, are active in the Euro-Atlantic area, and these include the East Atlantic (EA) pattern and two Eurasian patterns (EU1 and EU2) *[Barnston and Livezey, 1987]*. However, studies of relationships between these teleconnection patterns other than the NAO and temperature or precipitation in Europe have been scarce. *Beranová and Huth [2008]* demonstrate that the circulation variability patterns in Europe are strongly related to both temperature and precipitation over Europe and these relationships are non-stationary.

Apart from NAO, the somewhat prominent mode of variability is East Atlantic (EA). It can be identified as a strong centre over the North Atlantic with a strong northwest-southeast gradient towards western Europe. Its usual pattern is depicted in Fig. 4.5. Also shown is the time series of third rotated EOF loading pattern, that represent EA in black, with EA index *[ncep.noaa.gov]* in dashed red. The two indices correlate at 0.56 level. The EA pattern is useful for explaining interannual variations of sensible climate variables such as temperature, wind, and precipitation in particular over southern Europe, where some argue that its impact is even higher than that of NAO *[Sáenz et al., 2001; Vicente-Serrano and López-Moreno, 2006; Rodríguez-Puebla et al., 2010]*. The effect on larger-scale

REOF4 HGT500 DJFM -- 10.4%

FIG. 4.6. | RPCA-based EU2 index. (top) Shown is fourth rotated EOF loading pattern of DJFM geopotential height at 500hPa anomalies (HGTA500) which represent the East Atlantic pattern. Data from NCEP/NCAR reanalysis *[Kalnay et al., 1996]*. This third rotated component explains 10.4% of the total variance in the HGTA500 field over the Atlantic sector. (bottom) The normalised time series (PC) of the respective EOF pattern in black.

circulation in southern Europe, in turn, affects the regional- to local-scale ecosystems *[deCastro et al., 2006; Josey et al., 2011; Salmaso, 2012]*. As with NAO, its predictability is somewhat limited, although some attempts have been made *[Iglesias et al., 2014]*.

Other prominent modes of variability that explain a large portion of variance over Atlantic sector include the so-called Eurasian patterns 1 and 2 (EU1 & EU2). Their description, to this date, differs from study to study and as an example of the spatial pattern consider Fig. 4.6 which represents EU2 pattern as fourth rotated EOF loading pattern.

As in the case of NAO, let us look at the spectral content of other modes of variability: Fig. 4.7 renders linear FFT spectra of three indices: EA index *[ncep.noaa.gov]* in black, EA index based on our rotated PCA of HGTA500 in red, and finally EU2 index based on rotated PCA of HGTA500 in green. As the figure clearly shows, the spectral power of two EA indices differs, namely official EA index shows elevated power on 2 years and between 4 and 5 years band, whilst our RPCA-derived EA index shows a peak in spectral power on roughly 1.5 year period. Similarly as official EA index, RPCA-derived EU2 index shows power between 4 and 5 years band.

Of course, this list of modes is by no means exhaustive, it should serve a purpose of informing a reader about typical techniques that might be used for determining dominant modes of variability. Studying the spectral content of such modes proves to

54
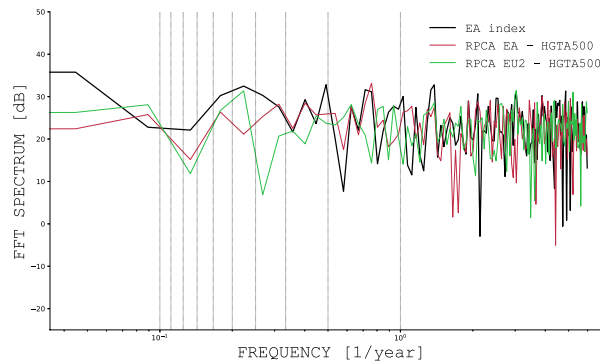
Fig. 4.7. | FFT spectra of three indices that represent other modes of variability over Euro-Atlantic sector: EA index *[ncep.noaa.gov]* FFT spectrum in black, RPCA-based EA index in red and RPCA-based EU2 index in green.

be useful in determining their typical periodicities and might hint us to an association between these circulation modes of variability and particular phenomena in temperature or precipitation time series that one might observe from station data. For extended and more detailed studies of various circulation modes in Euro-Atlantic sector (or global modes of variability) consider reading e.g. *Barnston and Livezey [1987]; Beranová and Huth [2008]; Vejmelka et al. [2015]; Ionita et al. [2015].*

4.2 Information transfer across temporal scales

With the noble goal of understanding the very complex behaviour of the atmospheric dynamics, many attempts have been made to infer possibly nonlinear dynamical mechanisms from meteorological data that date back to 1980s. It all started with researchers claiming detection of climate attractor of low dimensions *[Nicolis and Nicolis, 1984; Fraedrich, 1987; Tsonis and Elsner, 1988].* Whilst this was happening, the pioneers of chaos, including Lorenz himself, were in opposition and pointed at the limited reliability of algorithms for detection of chaotic attractors and claimed the observations of low-dimensional climate attractor as spurious *[Grassberger, 1986; Lorenz, 1991].* Some authors even claim that e.g. temperature could be explained even in a linear paradigm of stochastic process *[Paluš and Novotná, 1994; Hlinka et al., 2014b].* *Sura et al. [2005]* claim that statistics of atmospheric circulation, although not exactly Gaussian, are consistent with a paradigm for a linear system perturbed by multiplicative noise. In simpler words: nonlinearity is not needed for circulation statistics to become non-Gaussian — the state-dependent variations of stochastic feedbacks from unresolved system components, which we identify as multiplicative noise, are enough to perturb the system away from strictly Gaussian statistics.

On the other hand, search for more local patterns on specific temporal scales in the temperature, but also other atmospheric fields, led to the identification of various oscillatory phenomena, possibly possessing nonlinear origin, expressing various relationship with global modes of climate variability. An example can be given in the form of oscillatory modes in Eastern Mediterranean synchronising with the aforementioned

NAO *[Feliks et al., 2010]*, or oscillatory phenomena in temperature with approximately 7–8 years period couples to geomagnetic activity and solar activity *[Paluš and Novotná, 2009]*, or the same oscillatory phenomena in temperatures exhibiting coherent patterns in relation with the same frequencies in NAO variability *[Paluš and Novotná, 2004]*.

The task of detecting the oscillatory phenomena and inferring the relationship between them and other modes of climate (or even oceanic) variability gained momentum lately and is associated with reward by the means of possible successful forecasting of such phenomena with high societal impact. Besides the prediction question, the search is also driven by pure curiosity of uncovering the dynamical mechanisms underlying various modes and phenomena responsible for the weather and climate we observe and experience every day.

4.2.1 Detecting cross-frequency coupling

Synchronisation, as one of the specific types of dependence, plays a very important role in the study of the cooperative behaviour of complex systems or their parts. It has been observed in many scientific fields and phenomena such as cardio-respiratory interactions *[Schäfer et al., 1998; Palus and Hoyer, 1998]*, neural signals on various levels of organisation of brain tissues *[Rodriguez et al., 1999; Paluš et al., 2001; Lehnertz et al., 2009]*, or coherent variability in the atmosphere *[Rybski et al., 2003; Paluš and Novotná, 2009; Feliks et al., 2010; Paluš and Novotná, 2011]*. Going beyond the synchronisation, one may attempt to infer and distinguish mutual interactions from the directional coupling, that is to identify drive-response relationship between the systems, or subsystems.

Typically, the causal relation is sought between pairs of different variables or different modes of atmospheric variability. By contrast, *Paluš [2014a,b]* suggested an approach, where the complexity is examined by identifying causal relations between processes operating on different temporal scales within a single climatic time series. This makes sense when you recall Fig. 2.2 where a number of autonomous oscillatory subsystems with their dependencies gave rise to a process, which we can measure (an observable). Now, with the suggested approach of identifying causal relationship within one variable, we are effectively adapting the view as depicted in the figure, when the variable we are studying is the observable, and the sought causal phenomena are the interactions between the subsystems in the left-hand side of the figure.

I tried to built the theory of how to infer causal relations in (quasi-)oscillatory phenomena in the preceding chapter, namely on how to extract the oscillatory modes of variability from the observable (sec. 3.3.2), then on how one can measure the dependence between the variables in general (sec. 3.4), and how in measure synchronisation and causal relationships, in particular, utilising the (conditional) mutual information (sec. 3.4.4), and finally, how to establish the statistical significance of the results (sec. 3.5). Just a short recapitulation: from the experimental time series the oscillatory modes are extracting by the means of complex continuous wavelet transform (we use Morlet mother), and subsequently the phase $\phi(t)$, and amplitude $A(t)$ time series are used in computation of the synchronisation or causal phenomena as $I(\phi_1(t); \phi_2(t))$ for determining synchronisation, $I(\phi_1(t), \phi_2(t + \tau) \,|\, \phi_2(t), \dots)$ for determining phase coupling (causality), and finally $I(\phi_1(t), A_2(t + \tau) \,|\, A_2(t), A_2(t - \eta), \dots)$ for determining phase-

amplitude coupling.

For a numerical experiment in the aforementioned setting, let us follow *Paluš [2014a]*, section 3. For the first experiment, 65 536 samples of Gaussian white noise were generated. Next, the CCWT was used to decompose the time series into components related to time scales from 181 to 23170. Subsequently, cross-scale phase-phase interactions were studied using the mutual information $I(\phi_1(t); \phi_2(t))$, where the phases ϕ_1 were taken for the larger scales from 2436 to 23170 samples, and phases ϕ_2 for the smaller scales from 181 to 1722 samples. The results are summarised in Fig. 4.8. Even though the Gaussian white noise does not support any cross-scale interactions (by definition), some values of the mutual information I were elevated (upper left-hand side in Fig. 4.8, a), where the large and small scales are the closest. Clearly, this results from a spectral leakage of the CCWT producing false positives. Since this is an artefact of the extraction method, it is also present in the Fourier Transform surrogates and this prevents from claiming the interactions as statistically significant, as observed in Fig. 4.8, b. Both the z-score (Fig. 4.8, c) and statistical significance (or p-values, Fig. 4.8, d) show no significant nonzero values of mutual information. After taking into an account the multiplicity of statistical tests, we can still encounter up to 5% of false positive results, which would appear as random spots or blobs in the significance plots.
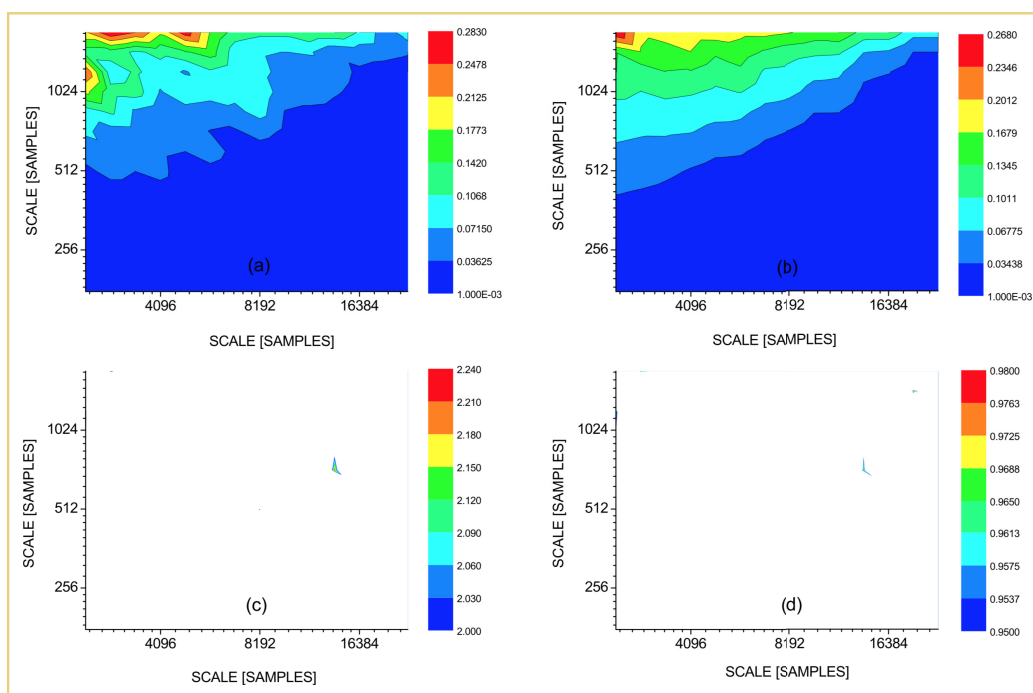
FIG. 4.8. | (a) Cross-scale phase-phase interactions measured by $I(\phi_1(t); \phi_2(t))$ for the Gaussian white noise decomposed using CCWT. (b) The mean $\bar{I}_s(\phi_1(t); \phi_2(t))$ for 1000 realisations of the FT surrogate data for the GWN. (c) z-score (colour-coded for $z > 2$) and (d) significance levels (colour-coded if $p < 0.05$). Figure taken from *Paluš [2014a]*.

For the second numerical experiment, *Paluš [2014a]* has chosen a dyadic tree of wavelet coefficients, which is constructed using random multipliers with a log-normal distribution *[Paluš, 2008]*. Same sample size as before is generated from this multifractal

process and similar methodology is applied to infer the cross-scale interactions in this sample. The results are summarised in Fig. 4.9. In this case, the scales were used in the same range of 8–1024 samples, hence the maximum of mutual information $I(s_1; s_2)$ is located on the diagonal in Fig. 4.9, a, where the two scales are identical. As before, from the values of mutual information itself, we cannot distinguish true interactions from artefacts of the method, so the empirical distribution evaluated using 1000 FT surrogate realisations was generated, and subsequently compared with the values from the actual data. The result, seen in Fig. 4.9, b, confirms the cross-scale interactions with the scale ratio of 1:2 (i.e. scales 8 and 16, or 16 and 32, etc are coupled). Other question would be whether these cross-scale interactions are symmetrical or directed, and *Paluš [2014a]* answered the question by computing the conditional mutual information in form $I(\phi_1(t); \phi_2(t + \tau) \,|\, \phi_2(t), \phi_2(t - \eta), \phi_2(t - 2\eta))$ to estimate the directed phase-phase coupling. Again, the true cross-scale directed interactions are visible only after estimating the empirical distribution using 1000 FT surrogate data realisations. From Fig. 4.9, d we can clearly see the direction of the influence, which goes from scale s to scale $s/2$ (in frequencies as $f \rightarrow 2f$), i.e. from scale 32 to scale 16 and so on. This result motivates our next goal, thus apply the methodology presented here on real-world data — surface air temperatures. The reader is advised to see *Paluš [2014a]* for a discussion concerning the results of the last two numerical experiments.

4.2.2 Cross-scale information transfer in temperature records

In the previous chapters and sections, I tried to build a strong case for seeking relationships in complex weather phenomena such as quasi-oscillatory systems or recurrent patterns in atmospheric variables. As written before, oscillations exhibiting periods between 6 and 11 years have been observed in various meteorological variables from European and Mediterranean areas by many authors (recall sec. 4.1). Since the amplitudes of these oscillations are typically small, therefore hidden in the red-noise background, they lack adequate assessing of their effect on shorter time scales. Following the methods developed earlier in this thesis, *Paluš [2014a,b]* studied possible cross-scale interactions between oscillatory modes with periods between 6 and 12 years and variability with typical time scales from a few months to 4 years. As before, the modus operandi starts with CCWT using the Morlet mother wavelet in order to extract the oscillatory modes of the desired period, and continues with estimating the phase and amplitude time series and mutual information between a pair of variables, and finally finishes with establishing the statistical significance of the results. The analysis examined phase-phase and phase-amplitude interactions, with the former ones not present in the considered European station data sets *[Paluš, 2014a]*. On the other hand, the phase-amplitude interactions in the form of phase ϕ_1 of slow oscillations influencing the amplitude A_2 of higher-frequency phenomena studied with functional

$$I(\phi_1; A_2(t + \tau) \,|\, A_2(t), A_2(t - \eta), \ldots, A_2(t - m\eta)) \tag{4.8}$$

(τ is the forward time lag, η is the backward time lag in the $m + 1$-dimensional condition) were present in various station data.
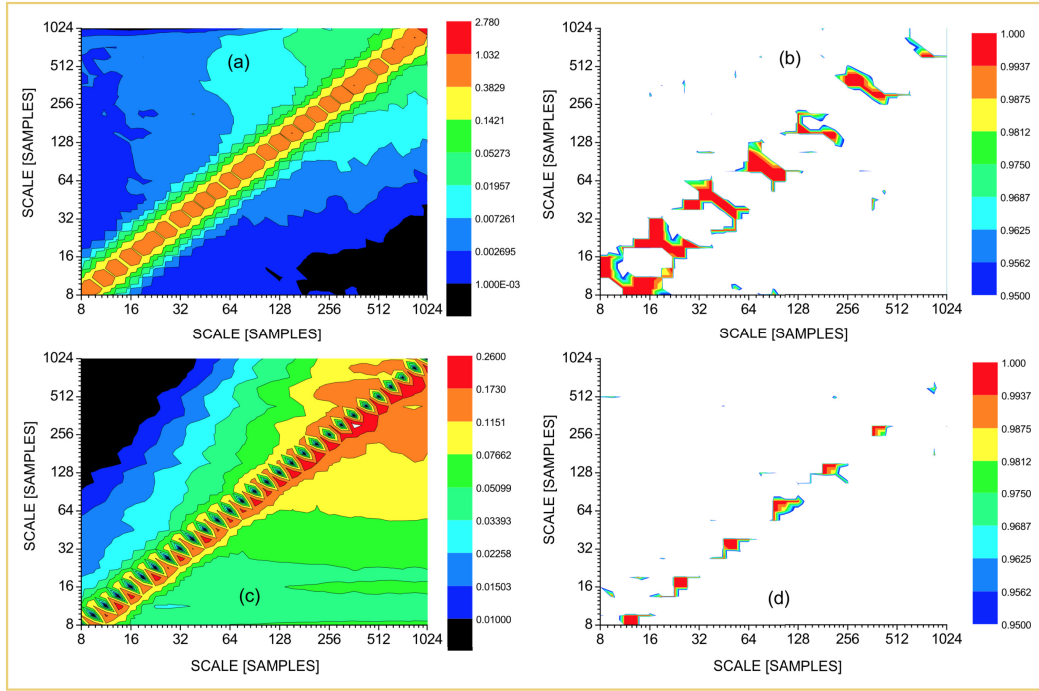
Fig. 4.9. (a) Cross-scale phase-phase interactions measured by $I(s_1(t); s_2(t))$ for a multifractal process decomposed using CCWT. (b) Significance levels (colour-coded if $p < 0.05$) for (a) using 1000 realisations of FT surrogate data. (c) Cross-scale phase-phase directed interactions — information transfer measured by $I(\phi_1(t); \phi_2(t + \tau) | \phi_2(t), \phi_2(t - \eta), \phi_2(t - 2\eta))$ for a multifractal process. (d) Significance levels (colour-coded if $p < 0.05$) for (c) using 1000 FT surrogate data realisations. Figure taken from *Paluš [2014a]*.

Paluš [2014a] used daily mean surface air temperature (SAT) records from various European stations, in particular stations with temporal span 1901–1999 were located in Bamberg (DE), Basel (CH), De Bilt (NL), Potsdam (DE), Vienna (AT), and Zurich (CH). Other stations with longer temporal span until 2008 or 2011 were Prague – Klementinum (CZ) and various German weather stations. The inclusion criterion for Paluš's study was the availability of at least 90 years of uninterrupted daily record since the computations of the conditional mutual information were performed using time series of length 32 768 samples. This was required due to reliability and sensitivity of subsequent statistical testing procedures. In the study, the functional in eq. (4.8) is evaluated and averaged for forward time lags τ from 1 to 750 days, while the backward lag η is set to 1/4 of the period of the slower oscillations characterised by the phase ϕ_1 *[Paluš, 2014a]*.

Temperature records, in particular from midlatitudes exhibit a strong spectral peak at the annual period since the evolution is dominated by the solar annual cycle. In many studies, the annual cycle is removed from the data, thus forming anomalies (SATA), however *Paluš [2014a]* was interested in discovering interactions between all relevant scales, therefore used raw SAT data for the computation of CMI. Surrogate data testing pose as an integral part of the method to infer cross-scale relationships, but the problem arises because they might not be able to accurately reproduce such a strong cyclic

component, and even the FT surrogate procedure fails to reproduce strong cyclicity and/or long coherence times *[Paluš, 1995]*. Fortunately, a doable workaround is available — to remove the seasonality both in mean and variance from the data (thus create normalised SATA time series) before entering the randomisation procedure. This is easily done by subtracting the mean for each calendar day and then dividing by the standard deviation of each calendar day. Then, the randomisation procedure generates a surrogate time series of deseasonalised nature and then finally the original seasonal standard deviation and mean is added to the surrogate time series. Surrogate data generated this way conserve the desired linear properties of the time series and also reproduce strong annual component in the raw SAT data *[Paluš, 2014a]*.
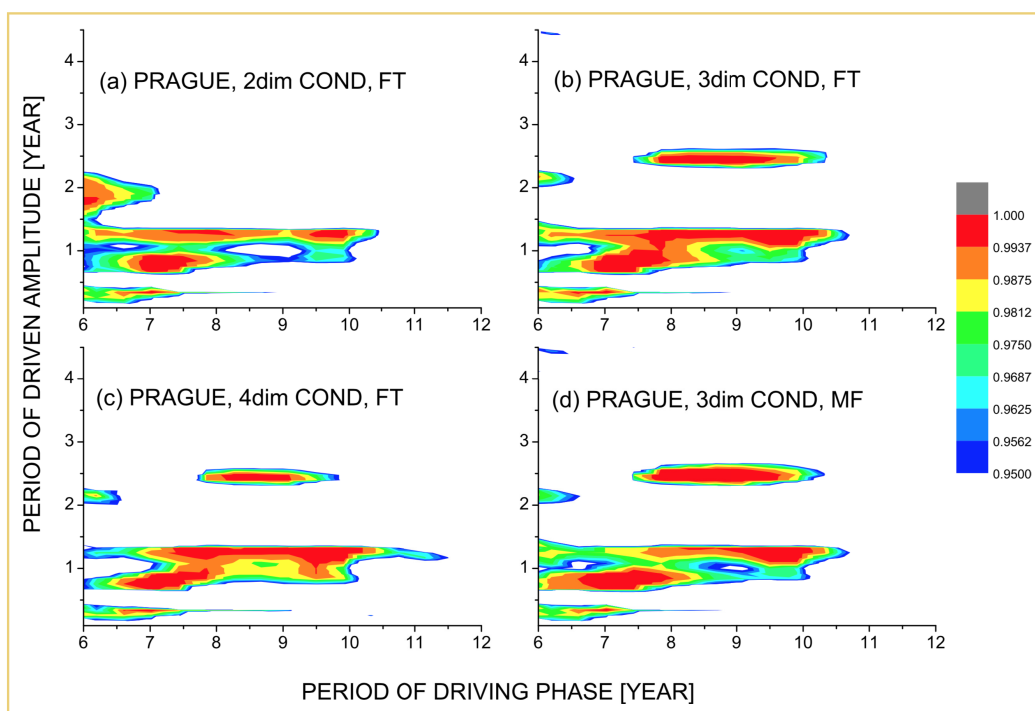
FIG. 4.10. | Causal influence of the phase of slower oscillations on the amplitude of faster fluctuations in the daily surface air temperature from Prague – Klementinum (CZ). The significance levels (colour-coded if $p < 0.05$) for the conditional mutual information with (a) 2-dimensional, (b,d) 3-dimensional and (c) 4-dimensional condition, obtained using the (a-c) FT surrogate data and (d) multifractal surrogate data. Figure taken from *Paluš [2014a]*.

The significance levels for the CMI as in eq. 4.8 obtained from the Prague – Klementinum daily SAT record are presented in Fig. 4.10. The results for CMI using 2, 3, and 4 conditioning variables are shown in subpanels a–c, respectively. Since the increase of conditioning dimensions does not substantially change the patterns of causal relationships, we shall use conditioning dimension of 3 in subsequent analyses. Also, using alternate null hypothesis by the means of multifractal surrogate data *[Paluš, 2008]* instead of widely-used FT surrogates leads to the same conclusions. Therefore, we also declare the results as robust.
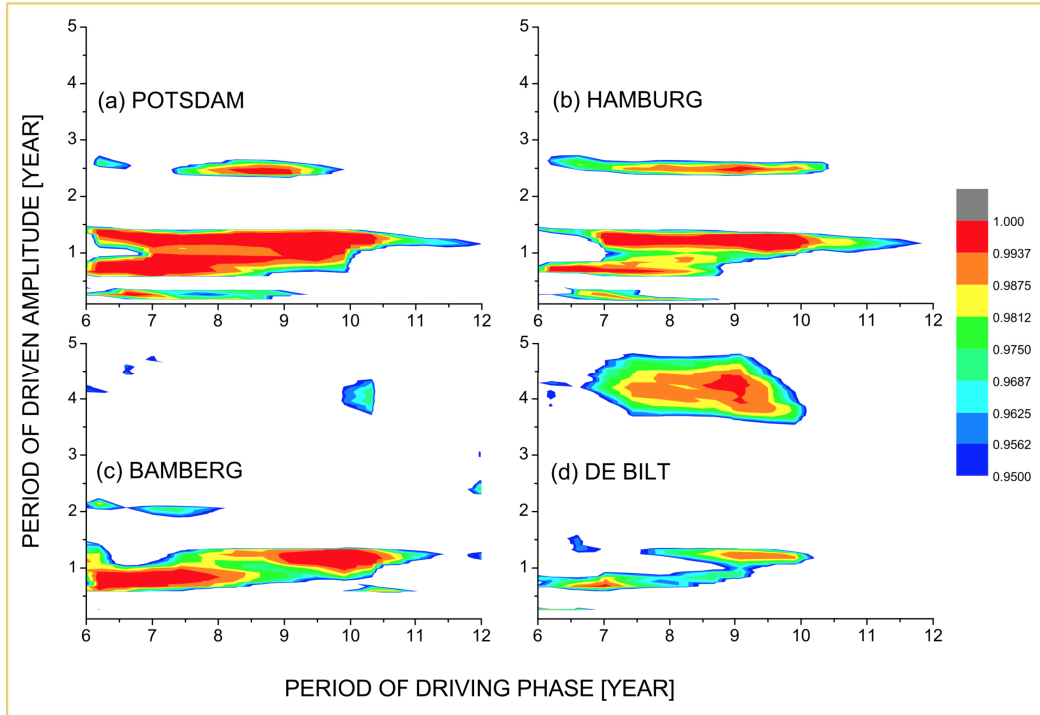
FIG. 4.11. | Causal influence of the phase of slower oscillations on the amplitude of faster fluctuations in the daily surface air temperature from (a) Potsdam (DE), (b) Hamburg (DE), (c) Bamberg (DE), and (d) De Bilt (NL). The significance levels (colour-coded if $p < 0.05$) for the conditional mutual information with 3-dimensional condition, obtained using the FT surrogate data. Figure taken from *Paluš [2014a]*.

The pattern of the $\phi_1 \rightarrow A_2$ directional interactions in SAT from Prague – Klementinum (14°25'E x 52°05'N, Fig. 4.10, c) is almost the same as that from Potsdam (13°04'E x 52°23'N, Fig. 4.11, a) and very similar to the pattern from Hamburg (10°0'E x 53°33'N, Fig. 4.11, b). The pattern from Bamberg (10°53'E x 49°53'N, Fig. 4.11, c) is slightly different, without the interactions with a period of driven amplitude around 3 years. Even more changes can be seen in pattern from a coastal city, De Bilt (5°11'E x 52°06'N, Fig. 4.11, d) with lesser interaction around annual driven amplitude, but reversely, large blob appears in longer time scales of the driven amplitude.

These interesting observations due to *Paluš [2014a]* support the conclusion of unidirectional cross-scale interactions or an information transfer from slower to faster scales present in atmospheric dynamics. In particular, the phase of the slower oscillatory phenomenon of periods between 7–9 years influence the amplitude around annual frequency, and also slower phenomena between 7–8 years influence amplitude around 2.5 years period. These findings hold throughout few stations in central Europe, while coastal stations of Hamburg and De Bilt exhibit slightly different patterns, which might point to the fact that the phase-amplitude coupling is present, but the interactions themselves are modulated via some other process in the atmospheric dynamics. Presented results provide an evidence for the existence of previously unknown phenomenon in atmospheric physics, although the understanding of its physical mechanisms still remains

a challenge for further research. The outputs of this statistical tests, however, provide us only with a qualitative description of the cross-scale interactions, and another step is needed to qualitatively assess their effect on climate variability on shorter time scales.

4.3 Evaluating the effect of cross-scale interactions

The significance plots presented in the previous section provide us with a qualitative description of phase-amplitude interactions. However, they do not give us the information of what magnitude the effect is. The simple approach to quantify the effect of cross-scale interactions by the name of conditional means was proposed by *Paluš [2014a,b]* and further used to study the spatial and temporal variability of the effect itself by *Jajcay et al. [2016]*.

The technique of conditional means is computing using the simple binning. In order to study the effect of phase of the slower phenomena, we conditioned on the phase of 8-year cycle. The phase interval $(-\pi, \pi)$, representing the full period, is divided into 8 bins, such that one bin roughly represents one year. For each bin, the mean (in fact any statistical moment, such as the second moment — the variance) is evaluated and thus discretised estimate of a studied variable is obtained. If the 8-year cycle has no influence on the studied variable, the conditional means in all 8 bins should be the same, equal to the unconditional, global mean. Or rather, due to finite sample effect, the conditional means would randomly fluctuate around the unconditional mean. On the other hand, if the conditional means vary as a function of the phase of the particular cycle, we would conclude that cycle has an effect on a studied variable, and the overall size of the effect can be approximated by taking the difference between the maximum and minimum conditional mean. As before, the statistical significance of such an effect is evaluated using the surrogate data method.
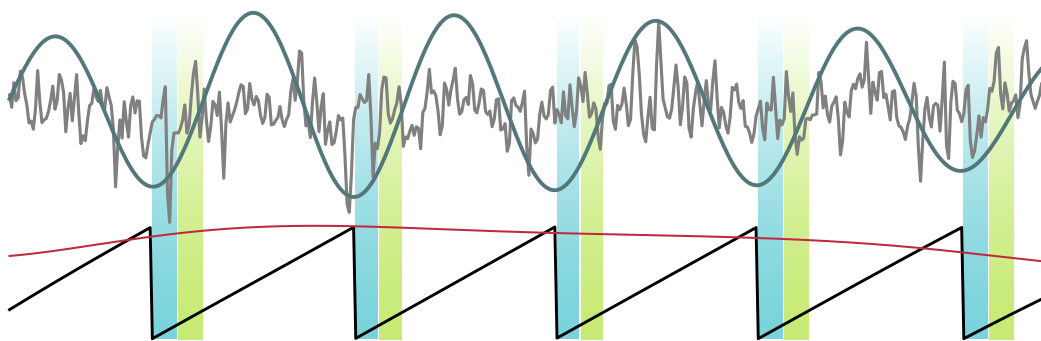
FIG. 4.12. | Conditional means technique illustration. Phase of the 8-year cycle $\phi_{8yr}(t)$ extracted from Prague – Klementinum SAT data *[Klein Tank et al., 2002]* in bottom part of the figure in black, amplitude of the 8-year cycle $A_{8yr}(t)$ in orange. The original SATA data shown in grey, while the reconstructed component $A_{8yr}(t)\cos\phi_{8yr}(t)$ shown in darker grey. Also shown are first two bins (bright blue and green, respectively) used for computation of conditional means.

The conditional means technique is visualised in Fig. 4.12. The full interval of phase cycle (in this example the phase of 8-year cycle $\phi_{8yr}(t)$ in black) is divided equidistantly

into 8 bins, in the figure visualised with blue bin as the first bin (representing roughly first year of the cycle) and with green bin representing the second one (or second year of the 8-year cycle). Then the mean (or any other statistical moment) of some studied variable (e.g. the Prague SATA, shown in grey in the Fig. 4.12) is taken conditionally on the bin, thus on the phase of the cycle.

The strongest mode of variability in the European midlatitudes is without a doubt an annual cycle, which is manifested by strongly cyclic, sinusoidal signal. Although the boundary conditions that gave rise to annual cycle (insolation from Sun accompanied by Earth's rotation) are constant along the zonal circles, the annual cycle (both in phase and amplitude) varies in time and space *[Mann and Park, 1996a; Wallace and Osborn, 2002; Zveryaev, 2007; Stine et al., 2009]*. When a reader recalls Fig. 4.10, we concluded that the phase of slower phenomena influences the amplitude of (roughly) annual cycle. The apparent relationship between the two can be seen from Fig. 4.13, where, among others, the CCWT reconstruction $A_{8yr}(t) \cos \phi_{8yr}(t)$ of the 8-year cycle is drawn in red, and the CCWT amplitude $A_{1yr}(t)$ in blue — their Pearson's correlation coefficient is at -0.82 level. Also drawn are the raw SAT data from Prague – Klementinum station *[Klein Tank et al., 2002]* in grey, the CCWT reconstruction $A_{1yr}(t) \cos \phi_{1yr}(t)$ of the annual cycle in black, and finally two distinct "climatological" amplitudes. Firstly, one climatological amplitude is defined as the difference between mean summer temperature (June until August, JJA) and mean winter temperature (December until February, DJF) in each year, shown in Fig. 4.13 as orange dots, while the second climatological amplitude is estimated as the difference between the means of daily temperatures above the upper quartile and below the lower quartile in each year, shown in yellow dots. Both amplitudes are in good agreement with the CCWT extracted amplitude $A_{1yr}(t)$ in blue, therefore we conclude that the CCWT extracted amplitude indeed reflects the temporal variations in the strength of the annual cycle in this particular location.

Similar to *Paluš [2014a]*, I was interested in spatial variations of the basic apparent relationship between the annual cycle and 8-year cycle. From station datasets compiled by ECA&D *[Klein Tank et al., 2002]* I selected a set of 10 stations (including Prague) with uninterrupted period from at least the beginning of 20[th]century. The list of used stations is given in Table. A.1 and their spatial locations are shown in Fig. A.2. Time series of surface air temperatures from these 9 remaining stations for the same time span are plotted in Figs. A.3 and A.4. Also plotted are the cycles of our interest: that is the CCWT reconstruction $A_{8yr}(t) \cos \phi_{8yr}(t)$ of the 8-year cycle, the CCWT reconstruction $A_{1yr}(t) \cos \phi_{1yr}(t)$ of the annual cycle, the CCWT amplitude $A_{1yr}(t)$, and two distinct climatological amplitudes, defined similarly as in the case of Prague – Klementinum shown in Fig. 4.13.

In all studied station data the apparent relationship between the 8-year cycle and the annual amplitude is confirmed (Pearson's correlation coefficient between the reconstruction of 8-year cycle and the annual amplitude is with the exception of Orenburg and CET at levels lower than -0.80). Also noticeable is the approximate agreement of the climatological amplitude of all studies stations with the annual amplitude extracted by the means of CCWT. Therefore, we may extend the conclusion from the Prague – Klementinum station to other stations throughout Europe and say that the 8-year cycle exhibit apparent relationship with the annual amplitude and this annual amplitude
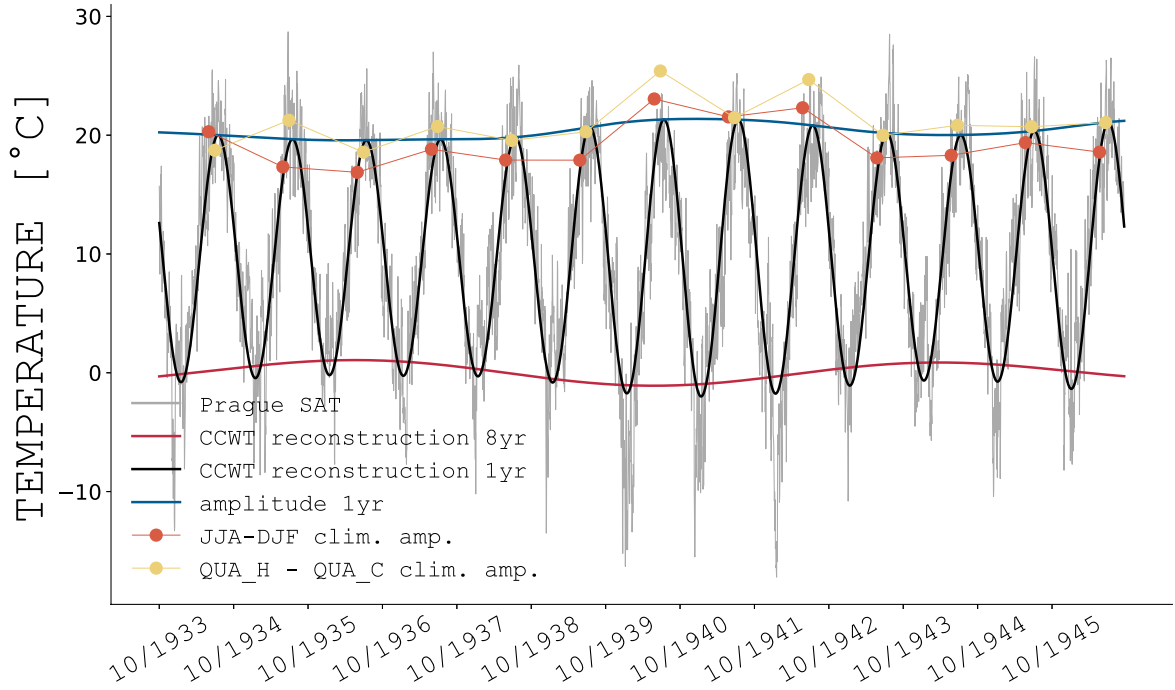
Fig. 4.13. | Cycles of our interest in SAT data from Prague – Klementinum station *[Klein Tank et al., 2002]* in the period 10 October 1933 to 30 September 1946. Shown are the SAT daily average in grey, the CCWT reconstruction $A_{8\mathrm{yr}}(t)\cos\phi_{8\mathrm{yr}}(t)$ of the 8-year cycle in red, the CCWT reconstruction $A_{1\mathrm{yr}}(t)\cos\phi_{1\mathrm{yr}}(t)$ of the annual cycle in black, the CCWT amplitude $A_{1\mathrm{yr}}(t)$ in blue, and two various estimates of climatological amplitude (see text for details) as orange and yellow circular marks.

indeed reflects the climatological amplitudes in Europe. In the next sections, we will evaluate the effect of 8-year cycle on the amplitude of annual cycle, as well as the overall surface air temperature anomalies (SATA) variability using both linear and nonlinear methods. Also, we will see how this effect varies in both spatial and temporal sense, as well as between various seasons.

4.3.1 Conditional means of the annual amplitude

As written above, there is an apparent relationship between the amplitude of annual cycle and the 8-year cycle in temperatures. This is visually clear from Fig. 4.13, and this is a partial confirmation of found cross-scale coupling between the phase of slower phenomena and the amplitude of faster cycles as qualitatively found by the CMI analysis (recall Fig. 4.10). This relationship is further studied using the conditional means technique, which is visualised in Fig. 4.12. This was done by computing the means of the amplitude of annual cycle (AAC), $A_{1\mathrm{yr}}(t)$, conditioned on the phase of the 8-year cycle, $A_{1\mathrm{yr}}(t)$. The histogram of the conditional means of AAC is presented in Fig. 4.14, A. In the panel A is shown the full period 1779–2009. Due to the cone-of-influence in the computation of the CCWT, the first and last 4 years (as half of the cycle of interest) are cut, since the phase in this regions is not estimated robustly. The maximum mean
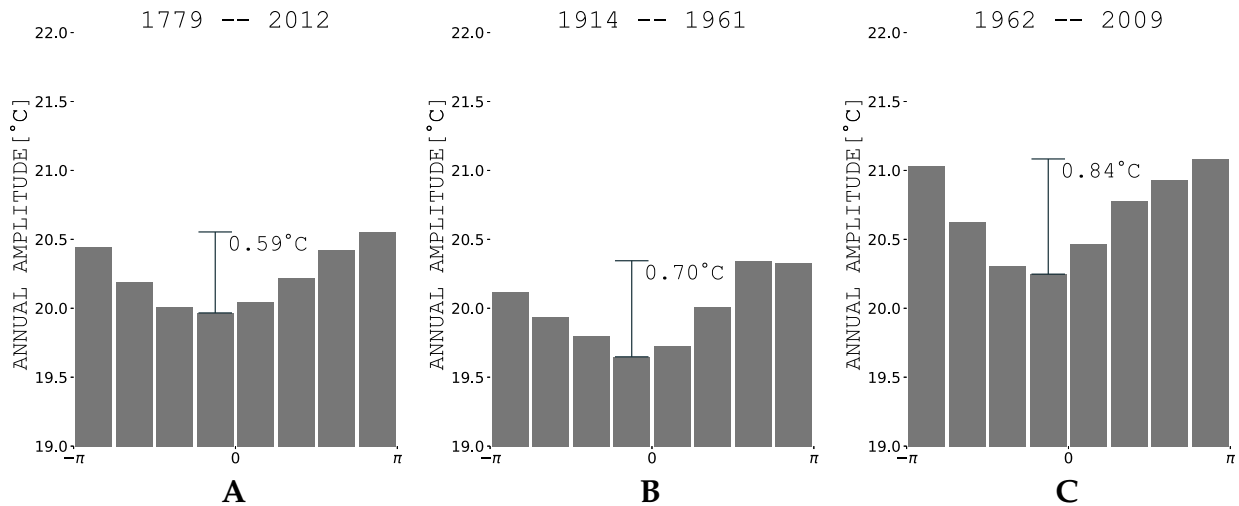
FIG. 4.14. | Conditional means for the amplitude of annual cycle (AAC), $A_{1yr}(t)$, for the Prague – Klementinum SAT data within the period (**A**) 1 January 1779 to 31 December 2012; (**B**) 1 January 1914 to 31 December 1961; and (**C**) 1 January 1962 to 31 December 2009, conditioned on the phase of the 8-year cycle, $\phi_{8yr}(t)$, divided into 8 equidistant bins. Note, that each bin represents approximately 1 year of the 8-year cycle.

(conditioned on the phase of 8-year cycle) is located in the eight, last, bin at 20.55°C, while the minimum is located in the fourth, middle, bin at 19.97°C. This directly implies, that through the 8-year cycle, the AAC changes, on average, within the range of 0.59°C. This change of 0.59°C is the average change for the 29 8-year cycles. However, using the different segments of the data, the results differ due to nonstationarity of the temperature data and their cross-scale interactions. As an example, consider panels B and C in Fig. 4.14, where two distinct segments of the data underwent the same analysis. The segments were 1 January 1914 to 31 December 1961, and 1 January 1962 to 31 December 2009, respectively. Both segments represent the average change due to 8-year cycle in six cycles. The difference between the maximum and minimum bin in each panel, which we call the effect of 8-year cycle, is larger in the shorter segments than on the average in full temporal span of the data. This implies that the effect of 8-year cycle fluctuates around the overall value (given by the analysis on the full temporal span, hence 1 January 1979 to 31 December 2012) and sometimes is larger and sometimes smaller.

A similar analysis with other statistical moments can be done instead of computing the average. As an example, we were also interested whether the standard deviation around the mean is also subject to variations due to the 8-year cycle. The technique is the same — that is to compute the standard deviation of the amplitude of the annual cycle conditioned on the phase of 8-year cycle. The results are summarised in Fig. 4.15. The overall shape of the conditional histograms is different from the means. The conditional means (Fig. 4.14) exhibit convex behaviour with the minima in the middle of the cycle and maxima in the beginning and the end of the cycle. Moreover, the shape is somewhat regular, resembling sinusoid. On the other hand, the shape of the conditional standard deviation histograms is irregular, with more fluctuations. In particular, the overall histogram for the full period exhibit very low difference between the maximum and
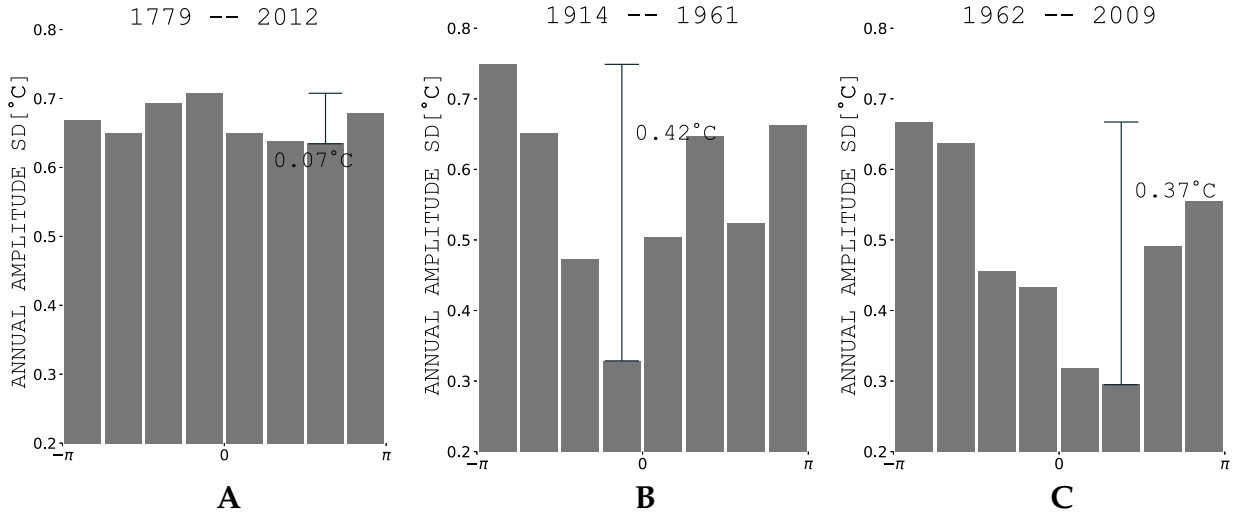
Fig. 4.15. | Conditional standard deviations for the amplitude of annual cycle (AAC), $A_{1yr}(t)$, for the Prague – Klementinum SAT data within the period (**A**) 1 January 1779 to 31 December 2012; (**B**) 1 January 1914 to 31 December 1961; and (**C**) 1 January 1962 to 31 December 2009, conditioned on the phase of the 8-year cycle, $\phi_{8yr}(t)$, divided into 8 equidistant bins. Note, that each bin represents approximately 1 year of the 8-year cycle.

minimum bin, suggesting that the 8-year cycle modulates the mean of the AAC, but not its standard deviation. The effect on standard deviation in the overall histogram is only 0.07°C. However, the effect is larger when selecting shorter periods, such as panels B and C in Fig. 4.15. This, again, suggests that the standard deviation conditioned on the phase of 8-year cycle fluctuates in the temporal sense.

Other station temperature data underwent the same analysis as Prague – Klementinum, which serves as a test bed. Recall, that list of all stations used in this thesis is in Table A.1 and their respective spatial locations are depicted in Fig. A.2. Additional figures for conditional means of AAC changing with the phase of 8-year cycle can be seen in Figs. A.5, A.6, and A.7 in the appendix. From the additional figures, it seems clear, that similar effect as in Prague can be detected in other stations throughout Europe. The overall effect varies between 0.29°C for CET, UK and 0.87°C for Potsdam. Also, connecting the spatial locations of studied stations with their respective values of the difference between the maximum and minimum bin suggests that there is an approximately east-west gradient, with lower values in the west and higher in the east. This will be studied later using the gridded temperature data. Moreover, we conclude that all studied stations exhibit the same behaviour concerning the effect of 8-year cycle on AAC, that is the shape of the histograms is similar, resembling the sinusoid, with maxima in the beginning and the end of the cycle and minima in the middle of the cycle. The analysis suggests that 8-year cycle in European temperatures might have a profound effect on the amplitude of annual cycle.

4.3.2 Overall temperature variability in the 8-year cycle

Since the estimation of causal linkage in the air temperature variability showed a possible influence of 8-year cycle not only on the amplitude of the annual cycle, but the significant interactions were spread around an annual cycle from 6 up to 18 months (recall Figs. 4.10 and 4.11) *[Paluš, 2014a]*. Therefore we also examined the effect of 8-year cycle on overall variability represented by the surface air temperature anomalies (SATA). As before, the conditional mean technique was employed, this time not on the amplitude of annual cycle, but on the SATA itself. The Fig. 4.16 visualises the effect of 8-year cycle on the overall temperature variability. The negative temperature anomalies (or "cold bins") prevail in the beginning and the end of the 8-year cycle (with minimum in the eighth bin at -0.45°C), while the positive anomalies ("warm bins") dominate the middle of the cycle (with the warmest, fourth, bin having 0.35°C anomaly). In this case, the difference between coldest and warmest bin is 0.81°C, hence we conclude that the 8-year cycle has an effect on the overall temperature variability and this effect is of overall magnitude at 0.81°C. As in the case of AAC, this effect seems to vary depending on temporal span used for the estimation. On shorter spans (see panels B and C of Fig. 4.16) the effect is larger — 1.08°C and 1.51°C in periods 1914 to 1961 and 1962 to 2009, respectively.
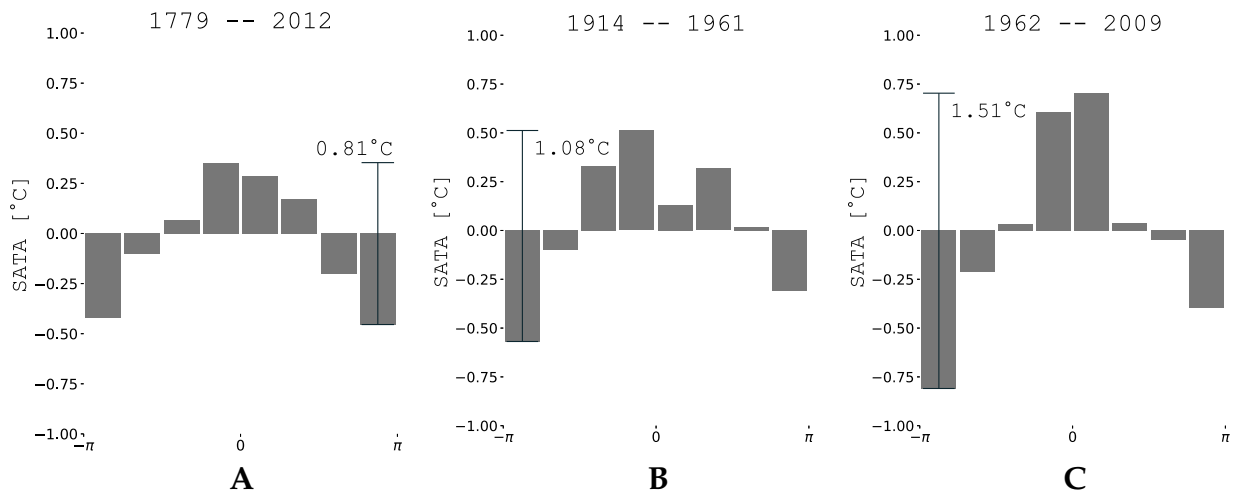
FIG. 4.16. | Conditional means for the surface air temperature anomalies (SATA), for the Prague – Klementinum data within the period (**A**) 1 January 1779 to 31 December 2012; (**B**) 1 January 1914 to 31 December 1961; and (**C**) 1 January 1962 to 31 December 2009, conditioned on the phase of the 8-year cycle, $\phi_{8yr}(t)$, divided into 8 equidistant bins. Note, that each bin represents approximately 1 year of the 8-year cycle.

As for the spatial variations of this effect, the conditional means of SATA from other European stations are rendered in the appendix (sec. A.2.3), in particular, Figs. A.8, A.9, and A.10. The effect of the 8-year cycle is visible in all other station, exhibiting itself strongest in St. Petersburg station and weakest in CET — Central England Temperature. This suggests, as in the case of AAC, an approximate east-west gradient of the influence with strong influence in the eastern part of Europe. As with Prague – Klementinum station, the effect is variable in the temporal sense for all the stations, but the shape of

the influence, with cold bins in the beginning and the end of the 8-year cycle and warm bins in the middle, holds throughout the datasets.
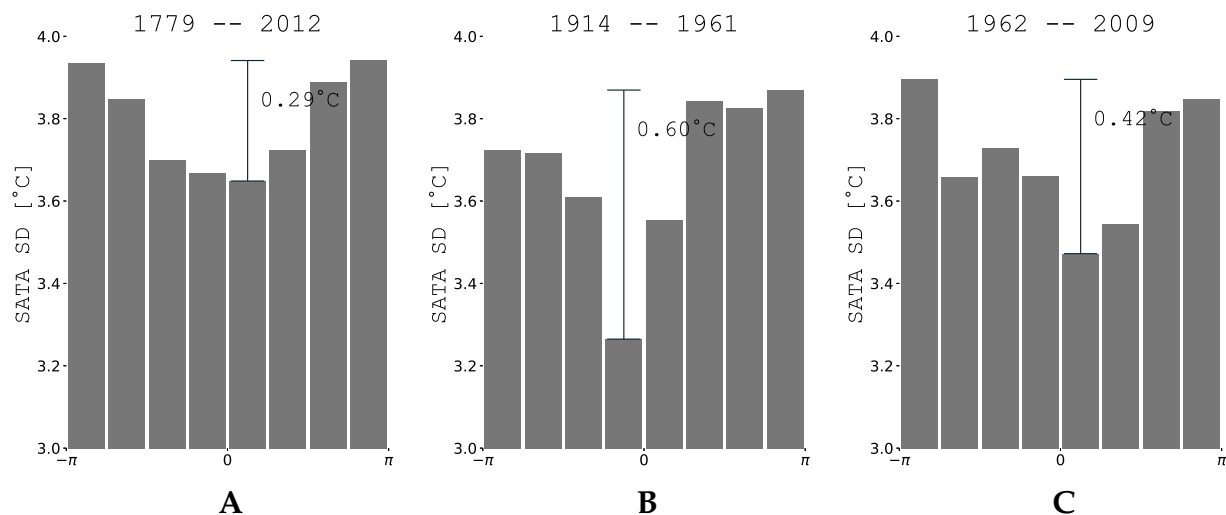

Fig. 4.17. | Conditional standard deviations for the surface air temperature anomalies (SATA), for the Prague – Klementinum data within the period (**A**) 1 January 1779 to 31 December 2012; (**B**) 1 January 1914 to 31 December 1961; and (**C**) 1 January 1962 to 31 December 2009, conditioned on the phase of the 8-year cycle, $\phi_{8yr}(t)$, divided into 8 equidistant bins. Note, that each bin represents approximately 1 year of the 8-year cycle.

The conditional standard deviations of SATA, computed in the similar fashion as conditional means, are presented in Fig. 4.17 for overall period and two distinct shorter periods. They are behaving the opposite way as the conditional means, meaning low standard deviation while the anomaly is high — in the middle of the 8-year cycle, and high standard deviation when the anomaly is low — in the beginning and the end of the 8-year cycle. This is not really surprising, as it is known that the winter standard deviations are generally larger than the summer ones (e.g. *Glaser and Riemann [2009]; Jones et al. [2014]*).

As a final look onto this effect of the 8-year cycle, we were interested whether the difference in SATA can or cannot be explained by the amplitude of the 8-year cycle only, omitting any cross-scale interactions. For the period 1 January 1962 to 31 December 2009 (for SATA see Fig. 4.16, C; and for AAC see Fig. 4.14, C), we also looked at the distribution of values in the synthetic dataset. Namely, we employed Fourier Transform surrogates, generated 5000 synthetic time series, and each of these time series underwent the same analysis as actual Prague – Klementinum SAT data. We were interested in two measures: first, the difference between the maximum and the minimum bin when computing conditional means of SATA, and then in the value of the amplitude of 8-year cycle. If the amplitude of the 8-year cycle would be approximately the same as the difference between the bins, this would suggest the difference in SATA conditional means can be explained by an 8-year component, linearly added to a background variability *[Jajcay et al., 2016]*. However, as seen from Fig. 4.18, the value of the difference in the data exceeds the 95th percentile of the related surrogate data distribution (Fig. 4.18, A), i.e.
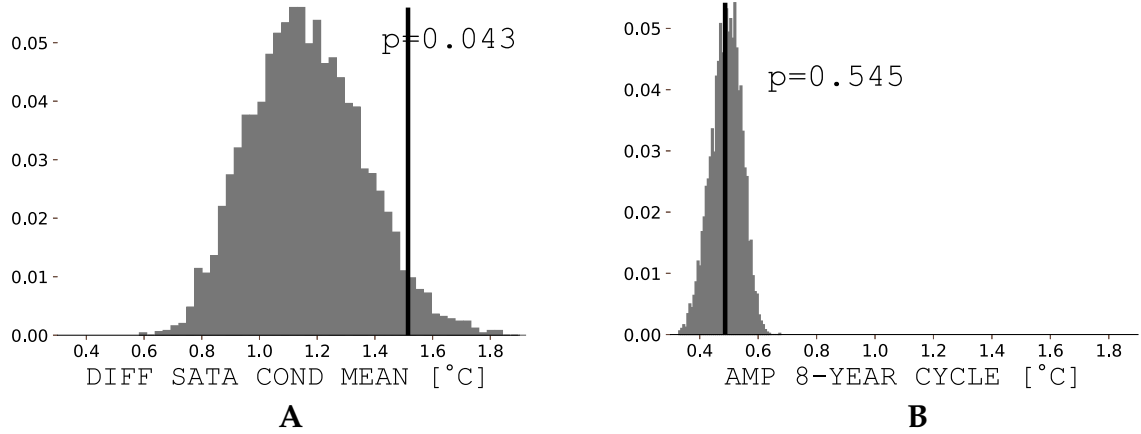
FIG. 4.18. | (A) The difference between the maximum and the minimum SATA conditional mean depicted by the position of the black thick line ($\approx 1.5°$C) and the distribution of the same differences obtained from 5000 realisations of the FT surrogate data (grey histogram). Shown is also the p-value of the significance. (B) The mean amplitude of the 8-year cycle depicted by the position of the black thick line ($\approx 0.5°$C) and the distribution of the mean amplitudes of the 8-year cycle obtained from 5000 realisations of the FT surrogate data (grey histogram). Shown is also the p-value of the significance.

it is statistically significant at $p < 0.05$. On the other hand, the mean amplitude of the 8-year cycle estimated from the data is less than 0.5°C and is well reproduced in the FT surrogate data (Fig. 4.18, B). These computational statistics support the hypothesis that the 1.5°C difference in the SATA conditional means is not a result of a random variability, neither can be explained by an 8-year component, linearly superposed to a background variability. Since the amplitude of the 8-year cycle itself is smaller than 0.5°C, it seems that the difference 1.5°C of the annual means during the 8-year cycle mainly results from the cross-scale interactions of the 8-year cycle with the variability on shorter time scales, represented here with SATA *[Jajcay et al., 2016]*.

4.3.3 Temporal variations in the effect of the 8-year cycle

As we have seen in the previous sections (and from the additional datasets presented in the appendix), the effect of the 8-year cycle on the shorter time scales, in the form of phase-amplitude coupling, possesses substantial temporal variability. In order to depict the nonstationarity of the temperature data itself, and their cross-scale interactions, the temporal evolution of the difference between the maximum and minimum conditional means was characterised using the sliding window of 16 384 daily SAT samples. The analysis went as follows: in each temporal window of 16 384 samples (this was chosen because of the requirement of multifractal surrogates, which were employed in statistical testing, for a time series length of $2^n, n \in \mathbb{N}$), which roughly represents 44 years and 10 months, the conditional means of AAC and SATA were computed, their difference as the proxy of the cross-scale effect was recorded, and finally the same analysis was done on 5000 realisations of synthetic surrogate data, in order to establish a statistical significance of the results.

We used three different types of surrogate data: Fourier Transform (FT) surrogates (see sec. 3.5.1 and references therein), autoregressive surrogates of order 1 (AR1) (see sec. 3.5.2 and references therein), and finally multifractal (MF) surrogates (see sec. 3.5.3 and references therein). The three different methods of how to generate surrogate data represent three different null hypothesis that we wanted to test. The weakest null hypothesis supposes that no cycles are present in the data and it is represented by AR1 surrogates. Fitting the AR model of order 1 to the deseasonalised data yields the AR coefficients and the respective residuals. Each surrogate data realisation is generated using the estimated AR1 model with innovations obtained as shuffled residuals. The FT surrogates represent the null hypothesis of a linear stochastic process with the same spectrum as the sample spectrum of the tested experimental data. Note, that no interactions between different temporal scales (frequencies) can exist — this is due to the randomisation of phases in the Fourier domain, hence any nonlinear properties of the original data, including possible cross-scale interactions are destroyed. Finally, the most sophisticated hypothesis is represented by the MF surrogates in which possible information transfer from larger to smaller scales, explained by the random cascades on wavelet dyadic trees, is preserved. Since the generation of the MF surrogates is based on a model of turbulent cascade in which a dynamical model on the time scale S influences (transfers energy and information onto) a mode on the scale $S/2$ ($f \rightarrow 2f$), but no other cross-scale relations are present *[Jajcay et al., 2016]*.

In all three cases, the seasonal variance and mean are returned to the surrogate data after they are generated. After processing all 5000 surrogates, the results are sorted in ascending order and the value of the 4750th element is considered as the estimate of the 95th percentile of the surrogate data distribution. If the data value is greater than the 95th percentile, we consider it statically significant with $p < 0.05$. Note that the tests are not corrected for their multiplicity (by the means of False Discovery Rate, or Bonferroni correction), so we can encounter up to 5% of false positive results.

The temporal evolution of differences between the maximum and the minimum bin (thus the effect of the 8-year cycle) in the amplitude of annual cycle (AAC) was computed as described formerly with Prague – Klementinum station data *[Klein Tank et al., 2002]*. The plot is rendered in Fig. 4.19, in this case, tested against 5000 autoregressive surrogates of order 1 (AR1). As the figure clearly shows, 65 windows of effective length 36.86 years (the window used for sliding was indeed 16 384 daily samples, which equals to 44.86 years, but due to edge effect of wavelet transformation, half of the 8-year cycle is cut both from beginning and the end of the wavelet representation of the data) were found significant, mainly in the last 90 years. The values of the difference peak at roughly 1.2°C, thus we might conclude that the effect of the phase of 8-year cycle on the amplitude of the annual cycle can reach up to 1.2°C and that this effect varies substantially over the time span of the data, sometimes low and not significant, but last approximately 90 years somewhat higher and usually statistically significant.

Tightening the null hypothesis from the weakest one of no cycles present in the data to the null hypothesis of a linear stochastic process, represented by Fourier Transform surrogates (FT), we expect some changes in significance levels. When you compare AR surrogates (Fig. 4.19) with the same plot, but this time, tested against 5000 FT surrogates (Fig. 4.20), the change in surrogate distribution is visible instantly: the mean of the
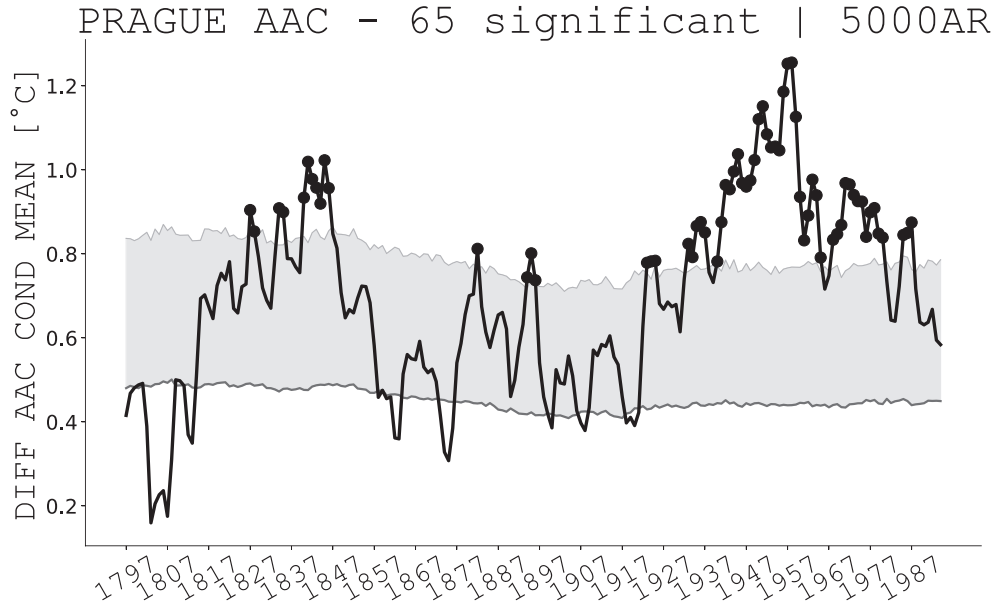
FIG. 4.19. | Temporal evolution of the effect of 8-year cycle on the amplitude of annual cycle, $A_{1yr}(t)$, in the Prague – Klementinum daily SAT. The differences between the minimum and maximum AAC conditional means (thick black curve), tested against 5000 AR1 surrogates (the means over the surrogate distribution as thinner grey curve; the 95th percentile of the distribution is plotted using light grey curve, connected with the mean by grey filling). Windows with statistically significant differences are marked with black dots, plotted in the middle of the window of the effective length 36.86 years.

surrogate distribution (grey line) is higher, and the surrogates, in general, replicate the overall curve estimated with the data. In case of AR surrogates, the surrogate mean and 95th percentile were more-or-less stationary, while the FT surrogates distribution varies in the same way as data does. Still, the majority of temporal windows are significant in tests against both null hypothesis, and we still conclude that the profound effect of 8-year cycle on the amplitude of annual cycle is present, can reach up to 1.2°C and is larger and usually statistically significant in the last 90 years.

Finally, the most sophisticated null hypothesis, which generation allows for cross-scale interactions to exist (although only in the $f \rightarrow 2f$ mode) is represented by multi-fractal (MF) surrogates. The Fig. 4.21 visualises the distribution of differences between the maximum and minimum bin of conditional means of AAC of 5000 MF surrogates. Shown is also the data curve for comparison. The figure clearly shows different behaviour of the synthetic data set, which can be seen both from the mean of the surrogate distribution and from the curve signifying the 95th percentile. The pattern of significant temporal windows is the same as in the case of testing against FT or AR1 surrogates, suggesting that the method for determining the effect of the 8-year cycle is robust, and moreover is robust against different null hypotheses. In the case of testing against MF surrogates, the test is the most conservative one, leaving 58 significant temporal windows. Still, the fact, that the effect of 8-year cycle on the amplitude of the annual cycle is somewhat stronger and usually statistically significant in the last 90 years, holds.

In a similar fashion, we studied the effect of 8-year cycle on overall temperature
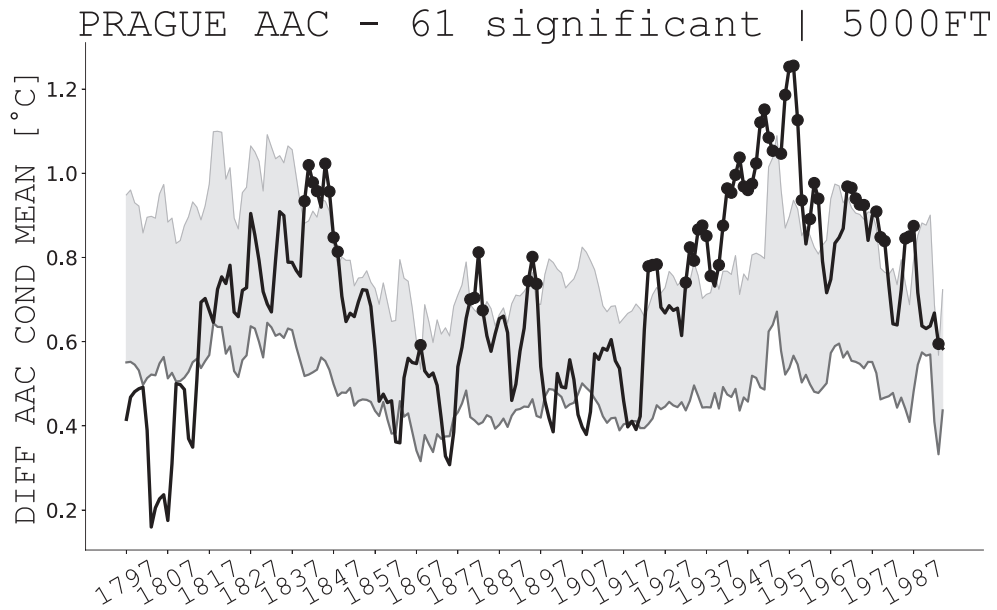
FIG. 4.20. | Same as Fig. 4.19 but tested against 5000 FT surrogates.
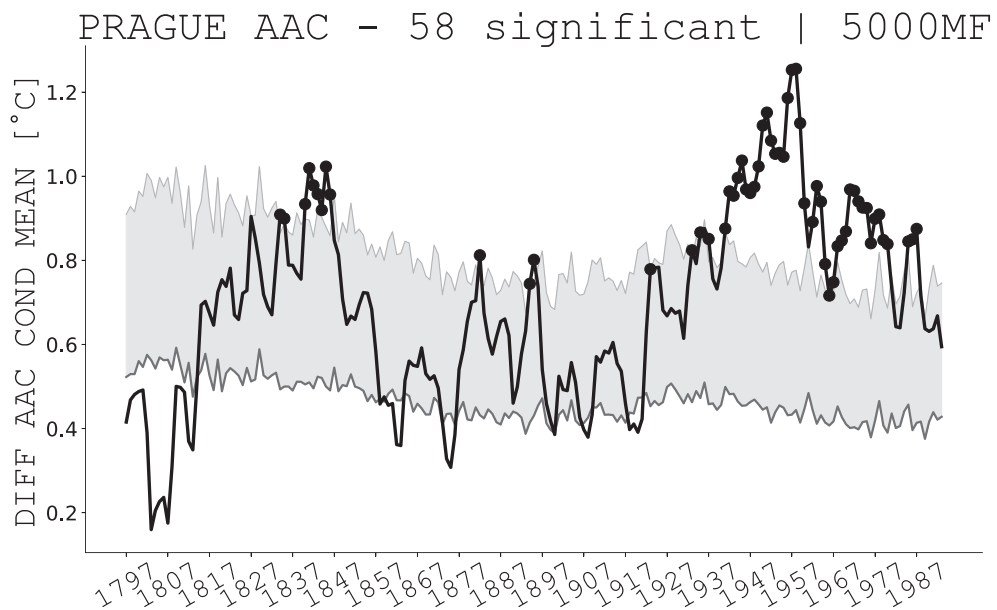
FIG. 4.21. | Same as Fig. 4.19 but tested against 5000 MF surrogates.

variability, represented by the anomalies from surface air temperature. The modus operandi was the same: we evaluated the difference between maximum and minimum bin of conditional means of SATA, conditioned on the phase of the 8-year cycle, in a temporal window of 16 384 daily samples, then shifted the window by one year and evaluated the same difference in 5000 surrogate data realisations in order to assess the statistical significance. Fig. 4.22 renders the temporal evolution of the effect of the 8-year cycle on overall temperature variability in the actual Prague – Klementinum data, as well as the mean and 95th percentile of empirical surrogate data distribution, obtained

72
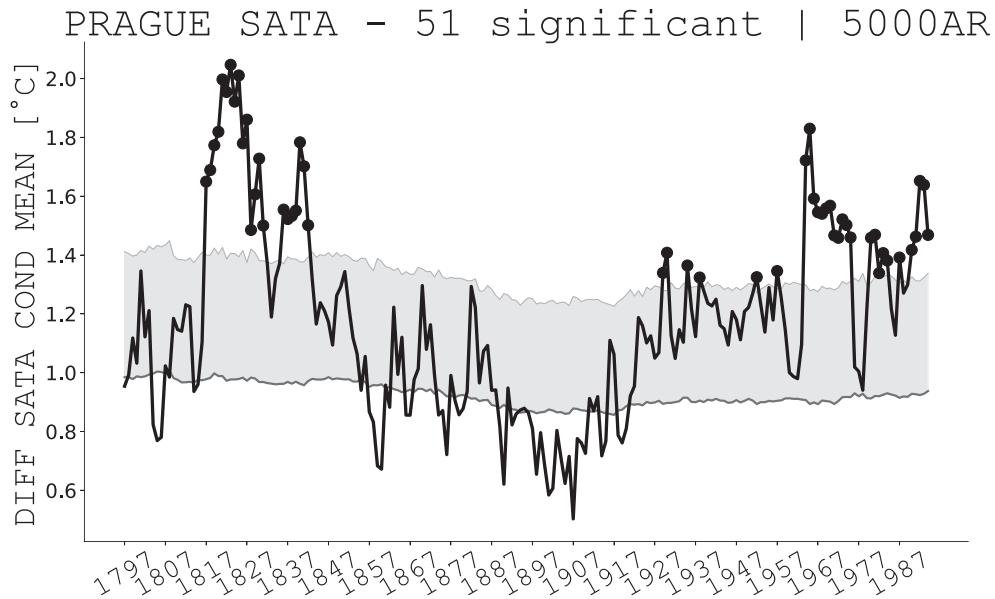
Fig. 4.22. | Temporal evolution of the effect of 8-year cycle on the surface air temperature anomalies (SATA) in the Prague – Klementinum daily SAT. The differences between minimum and maximum SATA conditional means (thick black curve), tested against 5000 AR1 surrogates (the means over the surrogate distribution as thinner grey curve; the 95[th]percentile of the distribution is plotted using light grey curve, connected with the mean by grey filling). Windows with statistically significant differences are marked with black dots, plotted in the middle of the window of the effective length 36.86 years.

as 5000 Monte Carlo realisations of AR1 model. In contrast with the effect on AAC, the effect on overall temperature variability is larger, peaking at more than 2°C. As in the case of AAC, the effect seems higher in the last approximately 80 years and also, in this period is usually statistically significant.

When we recall the values of the effect of the 8-year cycle shown in histograms (Fig. 4.16), now we see that the value of overall period (the difference between the maximum and minimum bin) of 0.81°C almost the lowest one in our temporal sliding window analysis. From the beginning till the middle of the 19[th]the effect of the 8-year cycle was rather strong (also seen from the AAC temporal window analysis, Figs. 4.19–4.21), then for about a century was substantially weaker, and then again, at the beginning to the middle of 20[th]century the effect was stronger and usually statistically significant. The effect on SATA varies from about 0.5°C up to more than 2°C, which suggests that the cross-scale interactions are themselves non-stationary.

As a last addition to the puzzle, the effect of the 8-year cycle on SATA was studied and tested against other types of surrogate data, representing distinct null hypotheses. The hypothesis of no cycles is, again, represented with AR1 surrogates and the respective testing is shown in Fig. 4.22. More conservative null hypothesis of a linear stochastic oscillator is represented by FT surrogates and the appropriate testing is shown in Fig. 4.23. Finally, the most complex and sophisticated null hypothesis is represented by multifractal surrogates, which allow for certain cross-scale interactions to be present in synthetic data. The mean and 95[th]percentile of such distribution is shown in Fig. 4.24.
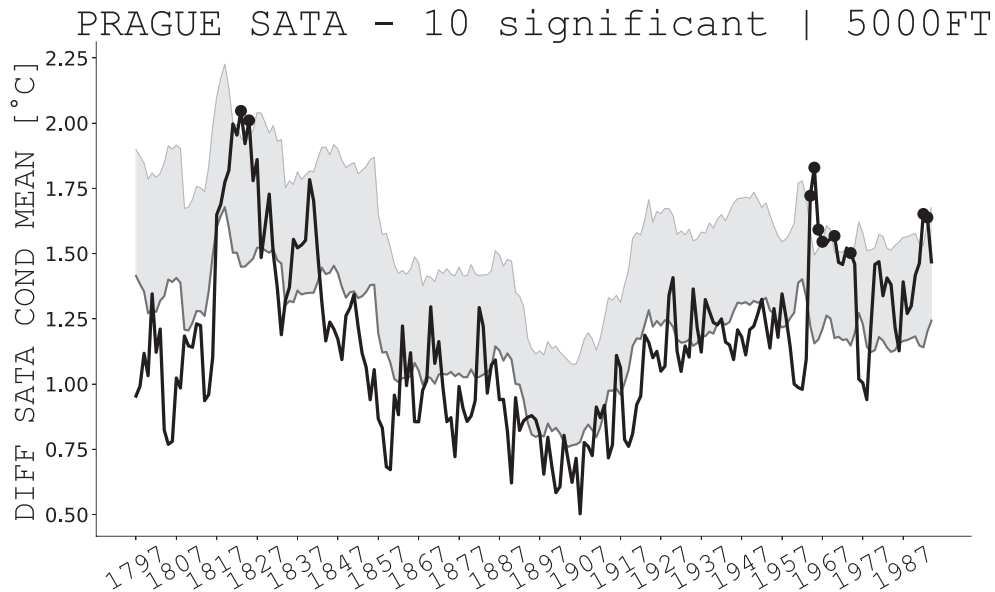
Fig. 4.23. | Same as Fig. 4.22 but tested against 5000 FT surrogates.

As seen from the different figures, the FT surrogates are much more conservative than the autoregressive surrogates, leaving only 10 significant temporal windows. Most of the still significant windows are present in the last 70 years of the data. Finally, the effect of 8-year cycle on the overall temperature variability was tested against 5000 MF surrogates and although one would expect less significant temporal windows as in the case of testing against FT surrogates, the MF surrogate testing yielded actually more significant windows, turning the MF surrogates hypothesis of possible cross-scale transfer less conservative than the FT surrogates hypothesis of linear stochastic oscillator. The explanation of this result, howsoever interesting, is unfortunately behind the scope of this thesis, hence the only thing taken further from this would be the fact that the Fourier Transform surrogates represent the most conservative null hypothesis as a testing ground for statistical significance.

As before, we were also interested on spatial variations of the effect of the 8-year cycle, hence we repeated the analysis of the temporal variability for other European stations with long enough available daily time series. The results are summarised in the appendix (sec. A.2.4), namely in Figs. A.11–A.19, where in the left column is plotted the effect of the phase of 8-year cycle on the amplitude of annual cycle (AAC), while in the right column the effect on overall temporal variability, represented by SATA. The first row in the figures visualises tests against AR surrogates, middle row against FT surrogates, and finally, the last row shows testing against MF surrogates. From the figures, we can conclude that the effect is present in all stations, usually more significant in AAC than in SATA, and in general the value of the effect is between 0.2°C up to 2.7°C. We also note, that as before, the east-west gradient of strength of the effect of the 8-year cycle seems to exists, where the westernmost station (CET, UK — Fig. A.17) exhibit considerably lower values of the effect than eastern stations (Orenburg and St. Petersburg , both RU — Figs. A.15 and A.16, respectively). We, therefore, looked into this spatial variability with more sophisticated tools than a collection of stations — specifically, let us work out the
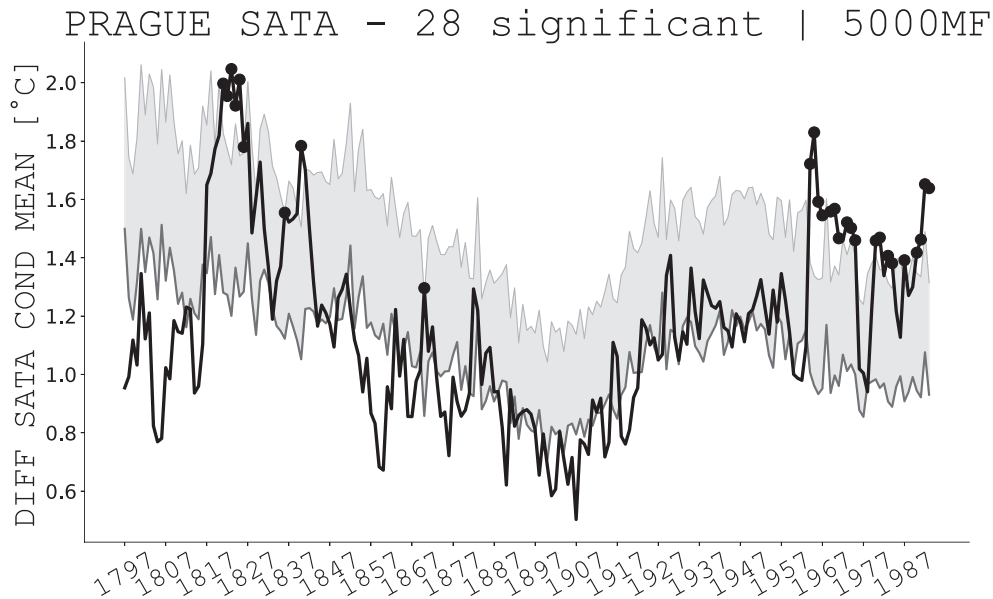
**Fig. 4.24.** | Same as Fig. 4.22 but tested against 5000 MF surrogates.

effect of the 8-year cycle on AAC and SATA in analysed, gridded data.

4.3.4 Spatial variability of the effect of the 8-year cycle

The ECA&D project, which provided us with the various station data, also offers E-OBS gridded data set with 0.5°×0.5° resolution of average daily surface air temperature *[Haylock et al., 2008]*. We made use of this data set, in particular, we selected temporal span of 1 January 1950 to 31 August 2017 and spatial span bounded by the box of 35°N–70°N and 12.5°W–60°E. Each grid point in this dataset underwent the same analysis as before, thus for each grid point, we computed the effect of the 8-year cycle on the amplitude of the annual cycle (AAC) as well as the overall temperature variability represented by the anomalies of surface air temperature (SATA). The effect was estimated as the difference between maxima and minima in conditional means technique over 8 bins, representing 8 distinct years of the cycle. Each grid point was subsequently tested against 1000 Fourier Transform surrogates in order to establish a statistical significance of the result.

The results of analysis on gridded data are rendered in Fig. 4.25. The areas with the statistically significant effect of the 8-year cycle on the amplitude of annual cycle ($\phi_{8yr}(\mathbf{x}) \rightarrow A_{1yr}(\mathbf{x})$) are marked with a hatch pattern. The grey areas on the map stand for *NaNs* (not a number) — this means that particular grid point includes some missing data and therefore the analysis could not be done. The effect on AAC overall ranges from values around 0.2°C in the south-western Europe up to 1.6°C in the Baltics and Finland. The statistical significance of the effect exhibit rather smooth pattern, with significance in the areas with quantitatively elevated effect — these areas include the eastern part of France, whole central Europe, the Baltics, Finland and Scandinavia and part of Balkans. This analysis confirms our finding when estimating the effect from various stations over Europe that the effect of the 8-year cycle on the AAC varies spatially and this variation
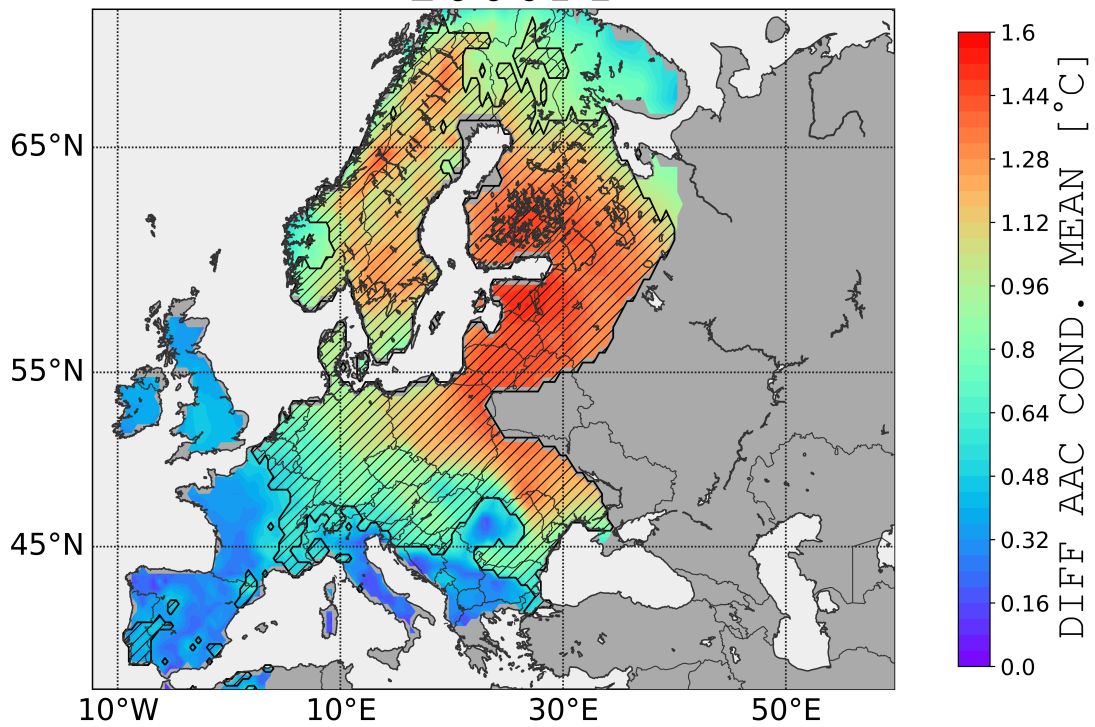
FIG. 4.25. | Spatial variability of the effect of the 8-year cycle on the amplitude of the SAT annual cycle in Europe. Differences of the maximum and minimum conditional means of the ECA&D reanalysis SAT annual cycle amplitude, $A_{1yr}(\mathbf{x}, t)$, conditioned on the phase of the 8-year cycle, $\phi_{8yr}(\mathbf{x}, t)$, are plotted in colour. The hatch pattern marks the areas where the effect is statistically significant ($p < 0.05$) when testing using 1000FT surrogates.

is rather strong (between 0.2 and 1.6°C for the 1950–2017 period).

We also performed a similar analysis in order to study the effect of 8-year cycle on overall temperature variability, represented by the anomalies of surface air temperatures (hence $\phi_{8yr}(\mathbf{x}, t) \rightarrow T(\mathbf{x}, t)$, where T represents the spatio-temporal field of surface air temperature anomalies). The respective result is plotted in Fig. 4.26. Although the differences, which is a proxy for the overall effect of 8-year cycle, reach up to 2.3°C in western Russia, the effect is mostly not significant when testing using 1000 Fourier Transform surrogates. The statistical significance is only established in a very small region with the maximal difference in western Russia. Other, even smaller, "blobs" of statistical significance (e.g. one around Dresden, DE, other in north-western Hungary) are ascribed to the multiple comparison problem, which we do not address, hence these are probably false positives.

From the analysis done on the gridded dataset, we conclude that the effect of 8-year cycle, in particular, the phase of 8-year cycle $\phi_{8yr}(\mathbf{x}, t)$, indeed affects the faster time scales. Concretely, its effect on the amplitude of the annual cycle, $A_{1yr}(\mathbf{x}, t)$ varies
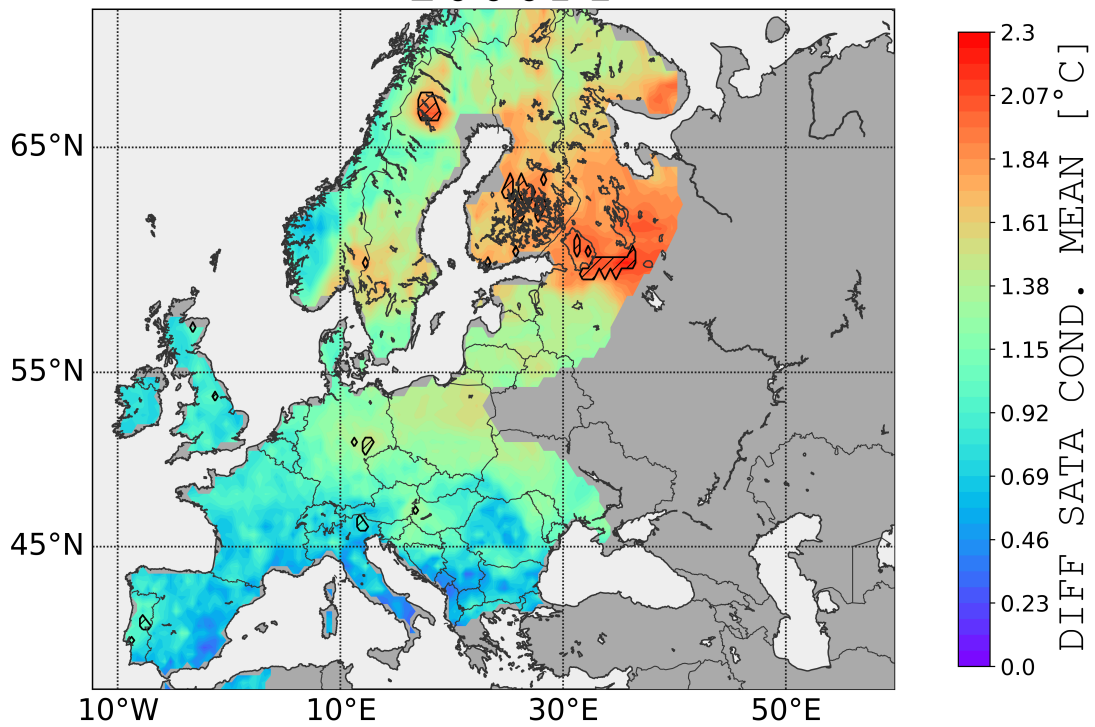
FIG. 4.26. | Spatial variability of the effect of the 8-year cycle on the overall temperature variability, represented by surface air temperature anomalies. Differences of the maximum and minimum conditional means of the ECA&D reanalysis SATA data, $T(\mathbf{x}, t)$, conditioned on the phase of the 8-year cycle, $\phi_{8yr}(\mathbf{x}, t)$, are plotted in colour. The hatch pattern marks the areas where the effect is statistically significant ($p < 0.05$) when testing using 1000FT surrogates.

throughout Europe, is lowest in south-western Europe with values around 0.2°C, and peaks in the Baltics with 1.6°C. The effect on the AAC is mostly statistically significant and therefore, at least in the period 1950–2017, the phase of the 8-year exhibit statistically significant cross-frequency coupling with the amplitude of the annual cycle and alter its values up to 1.6°C. On the other hand, although the effect of the phase of the 8-year cycle reaches up to 2.3°C and its spatial variations resemble the spatial pattern of the effect on AAC (Fig. 4.25), it was not deemed statistically significant.

4.3.5 Seasonal effects of the 8-year cycle

As a final piece of the puzzle, we opted to repeat the former analysis of the effect of the 8-year cycle on overall temperature variability represented by SATA on seasonally divided data. That is, everything is done as before, but instead of taking the time series as they are, we selected only particular months. In accordance with a huge body of climatological literature, we worked with seasons defined as follows: the winter season,
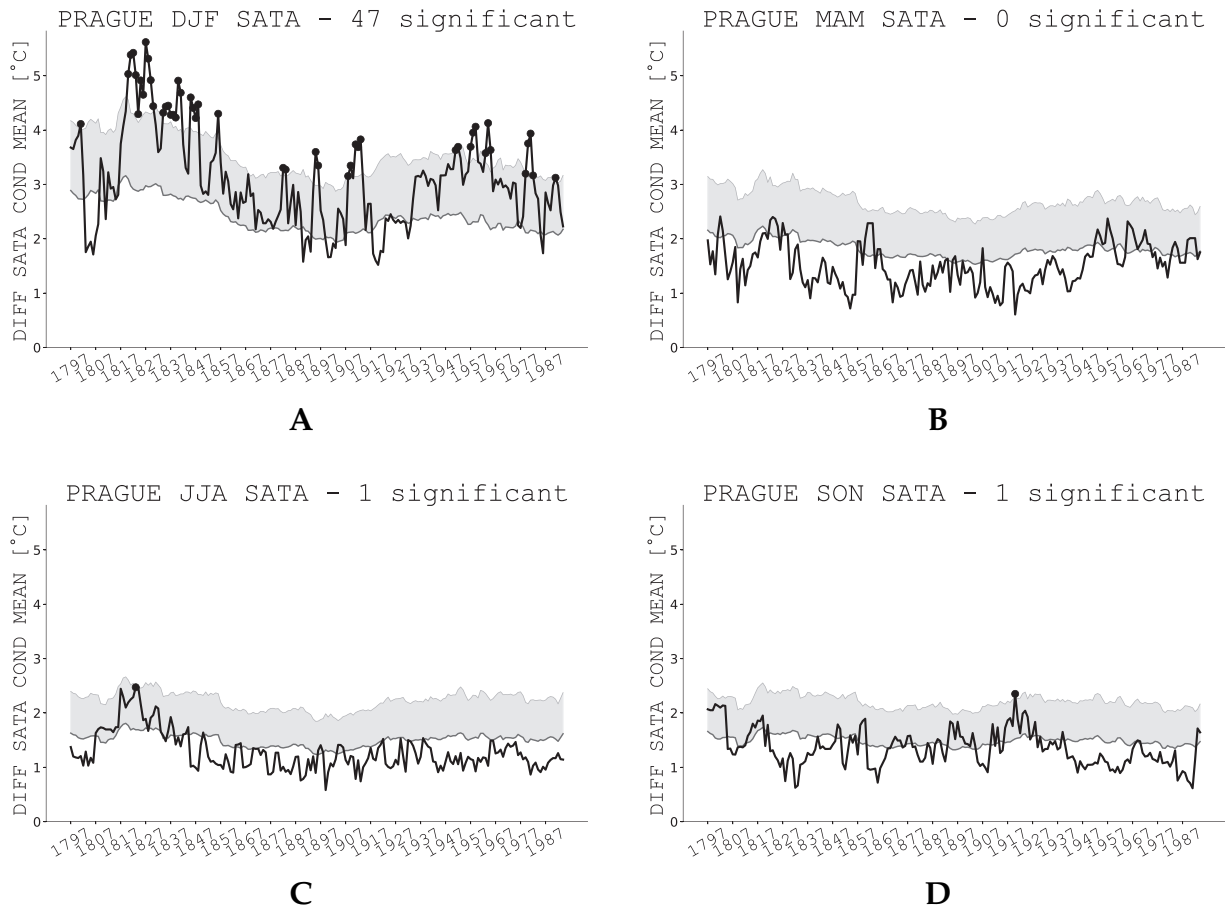
Fig. 4.27. | Temporal evolution of the effect of 8-year cycle on the surface air temperature anomalies (SATA) in the Prague – Klementinum daily SAT for (**A**) winter, DJF, season; (**B**) spring, MAM, season; (**C**) summer, JJA, season; and (**D**) autumn, SON, season. The differences between minimum and maximum SATA conditional means (thick black curve), tested against 5000 FT surrogates (the means over the surrogate distribution as thinner grey curve; the 95th percentile of the distribution is plotted using light grey curve, connected with the mean by grey filling). Windows with statistically significant differences are marked with black dots, plotted in the middle of the window of the effective length 36.86 years.

including months December, January, and February (*DJF*); the spring season, including March, April, and May (*MAM*); the summer season, including June, July, and August (*JJA*), and finally, the autumn season with September, October, and November (*SON*). The seasonally depended analysis was done only on SATA data, not on the AAC since the amplitude of the annual cycle is constant (at least in the approximation) during a calendar year, therefore such analysis would not yield any relevant information.

The first analysed data set was daily station SAT from Prague – Klementinum. The plots are shown in Fig. 4.27. The first obvious thing to consider is how much the strength of the effect heavily depends on the season. During MAM, JJA, and SON seasons, the effect reaches up to 2°C, albeit is not significant. Contrarily, the effect in the winter season can reach up to 6°C and is usually statistically significant. The differences between cold

78

and warm bins were highest during the first half of the 19[th]century with differences more than 5°C, while in the recent times, they fell to approximately 4°C, but they are still significant with respect to the surrogate testing using 5000 FT surrogates.

On the other hand, other seasons than winter one, the difference between warm and cold bins resemble the temporal evolution of the whole year analysis (recall Fig. 4.23), with the majority of the record yielding the effect below 2°C and almost no significance with respect to surrogate testing.

The analysis of the seasonal effect of the 8-year cycle onto SATA variability was conducted on other stations from the compiled dataset as well and the results are summarised in the appendix (sec. A.2.5), particularly in Figs. A.20–A.24. In summary: for all stations hold that the effect is strongest in the winter season in comparison with the other (the winter effect ranges from 2°C to over 6°C), the east-west gradient modulates the strength of the effect itself (eastern stations exhibiting stronger effect of the 8-year cycle) and also the seasonal dependence — western stations show lesser seasonal modulation of the effect, while the effect in the eastern stations heavily depends on the season. This is further studied in the gridded data set.

The gridded data set yielded the same picture as analyses done before (Fig. 4.28): the effect of the 8-year cycle is strongest in the winter (DJF), reaching up to 6.6°C in the Baltics, southern Finland and the westernmost part of Russia. Clearly, the effect is statistically significant (shown by the hatching in Fig. 4.28). Apart from the regions with the highest effect, the areas over central Europe (Poland, Germany, the northern part of Czech Republic, and parts of Ukraine) were also deemed statistically significant with overall strength of the effect between 3°and 4°C. The effect itself exhibit southwest-northeast gradient towards western Europe with a weak effect of the 8-year cycle in the southern and western part of Europe, and strong effect in the northern and eastern part of Europe. For the spring (MAM) and autumn (SON) season, the effect is considerably weaker throughout Europe, with the maximum values around 2°C and is not statistically significant almost nowhere (omitting the expected false positives, up to 5% of the grid point-wise results). Finally, the summer season (JJA) supports rather a weak effect, but stronger than in the transient seasons of spring and autumn. The effect reaches up to 2.5°–3°in the Baltics and southern Finland and is statistically significant. The seasonal modulation of the effect itself is also spatially variable (as expected per previous station-based analyses): in the southern and western Europe the effect is almost of the same magnitude throughout the year, while the magnitude of this effect in the northern and eastern parts of Europe varies substantially in the range between 2°–6.6°C.

4.3.6 Discussion

Considering air temperature variability in a range of time scales, *Paluš [2014b]* presented a statistical evidence for a cross-scale-directed information flow from larger to smaller time scales in long-term SAT records from European stations. The phase of a slow oscillatory process influences temperature variability on shorter time scales. The influencing oscillatory phenomenon has variable frequency; however, its most probable period is close to 8 years, and for this period it has also the strongest effect (see *Paluš [2014b]*, Figures 2b and 3a). These periods (time scales) are consistent with the observations of
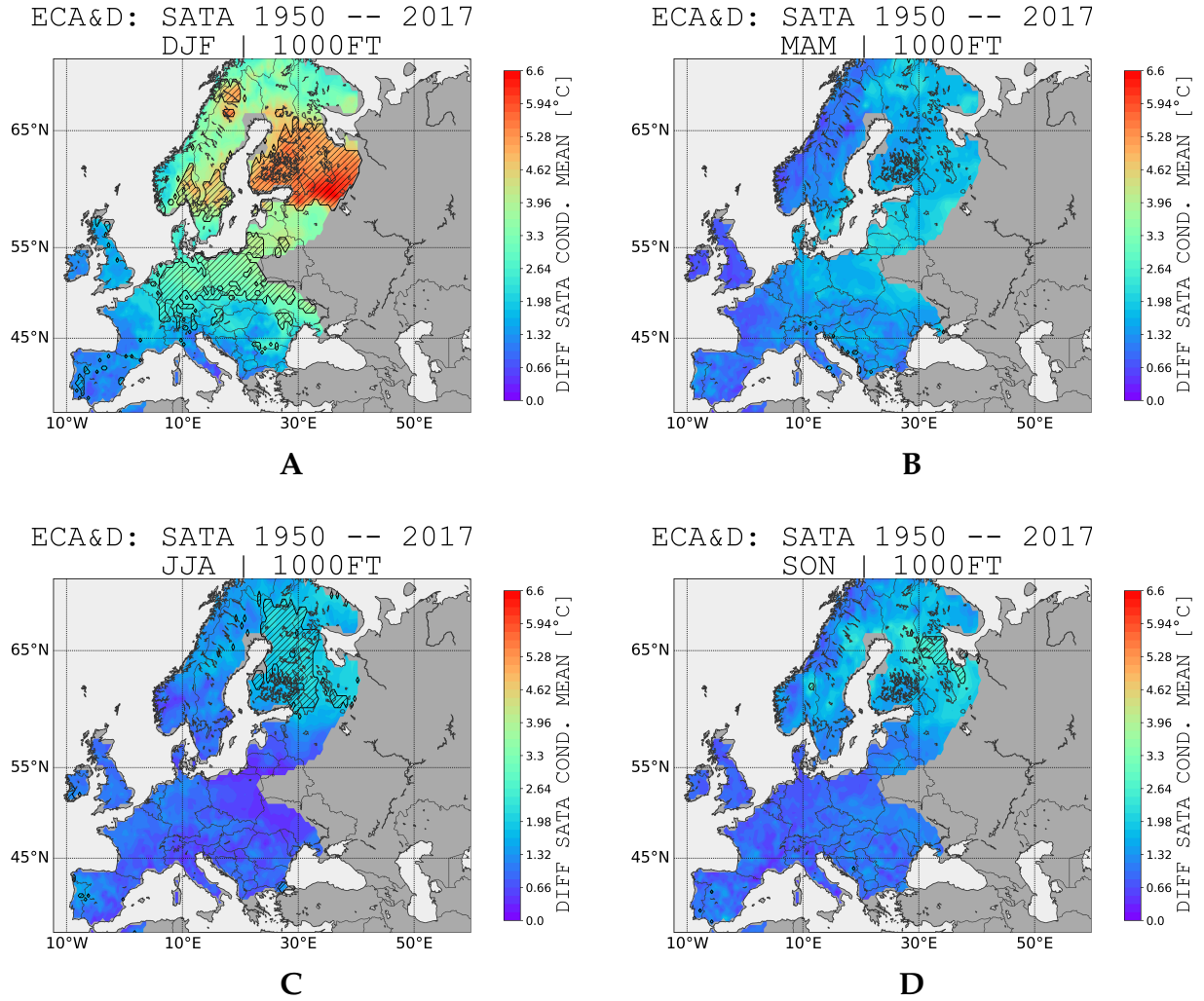
FIG. 4.28. | Spatial variability of the effect of the 8-year cycle on the overall temperature variability, represented by surface air temperature anomalies, SATA, for (**A**) winter, DJF, season; (**B**) spring, MAM, season; (**C**) summer, JJA, season; and (**D**) autumn, SON, season. Differences of the maximum and minimum conditional means of the ECA&D reanalysis SAT annual cycle amplitude, $A_{1\mathrm{yr}}(\mathbf{x}, t)$, and SATA data, $T(\mathbf{x}, t)$, respectively, conditioned on the phase of the 8-year cycle, $\phi_{8\mathrm{yr}}(\mathbf{x}, t)$, are plotted in colour. The hatch pattern marks the areas where the effect is statistically significant ($p < 0.05$) when testing using 1000 Fourier Transform surrogates.

an oscillatory mode with the period between 7 and 8 years in long-term temperature and other meteorological records in Europe. Therefore, in this study, we have applied a simple conditional mean technique in order to quantitatively estimate the effect of the oscillatory mode with the period close to 8 years on the surface air temperature variability in Europe. The cycle itself has a small amplitude (<0.5°C in the presented example of the station SAT record from Prague – Klementinum, see Fig. 4.18, b) and is hidden in overall temperature variability. However, due to the cross-scale interactions, the 8-year cycle influences the temperature variability on shorter time scales. The amplitude of the annual cycle in SAT changes within this cycle by 0.7°–1.4°C, and the overall variability of

SAT anomalies changes in annual means by 1.5°–1.7°C. The strongest effect of the 8-year cycle has been observed in the winter season — the DJF SATA means change in the range 4°–5°C. (This summary is restricted to twentieth-century central Europe, where we have available both the station and reanalysis data giving consistent results.) These results suggest that the weak 7–8-year cycle plays a very important role in the temperature variability on interannual and shorter time scales. Therefore, this phenomenon deserves further study and understanding of its mechanisms.

Paluš [2014b] hypothesizes that in the analysed SAT data, we have observed a regional manifestation of a general phenomenon of cross-scale interactions in the atmospheric dynamics in which global, low-frequency modes influence local, high-frequency variability. For instance, *Chekroun et al. [2011]* reported that the phase of the low-frequency modes of the El Niño/ Southern Oscillation influences high-frequency variability ("weather noise") of the sea surface temperature in the tropical Pacific. For the data analysed in this study, the most relevant global mode is probably the North Atlantic Oscillation (NAO). The influence of the NAO on the air temperature in Europe is known *[Marshall et al., 2001]*, and its mechanisms depending on the phase of the NAO are described, e.g., by *Hurrell and Dickson [2005]*. Typically, Pearson's correlations have been computed between (mostly winter) air temperature records and NAO indices (see, e.g., *Pokorná and Huth [2015]*); however, specific time scales have not been considered yet, although the 7–8-year cycle has also been detected in the NAO index *[Gámiz-Fortis et al., 2002; Paluš and Novotná, 2004]*. Our results demonstrate the importance of understanding the climate variability in scale-specific regional modes and their cross-scale interactions and causal relations with global circulation variability modes which are localised not only in space *[Vejmelka et al., 2015]* but also in a time scale or in a frequency range *[Groth and Ghil, 2011, 2015]*.

Complex dynamics and extremes in El Niño / Southern Oscillation

In an El Niño year, you have winners and losers.
  Walter Baethgen

In the last chapter, we introduced a somewhat peculiar phenomenon of cross-scale interaction, where the phase of the slower oscillatory phenomenon (in our case approximately 8-years) affects the amplitude of faster cycles. We hypothesise that what we actually observed was a mere regional manifestation of a general phenomenon of these cross-scale interactions in the atmospheric dynamics in which a global, low-frequency modes influence local, high-frequency variability *[Paluš, 2014b; Jajcay et al., 2016]*. As an example, *Chekroun et al. [2011]* reported that the phase of the low-frequency modes of the El Niño/ Southern Oscillation influences high-frequency variability ("weather noise") of the sea surface temperature in the tropical Pacific. The aforementioned result motivated us to exploit the framework developed by *Paluš [2014a,b]*, and used by *Jajcay et al. [2016]*, in order to study the possible cross-scale coupling in the dynamics of El Niño/ Southern Oscillation, to which this chapter is devoted.

5.1 Overview of El Niño/ Southern Oscillation

El Niño/ Southern Oscillation (commonly referred to as ENSO) is a well known coupled ocean-atmosphere phenomenon, which manifests itself as a quasi-periodic fluctuation in a sea surface temperature (El Niño part) and air pressure of the overlying atmosphere (Southern Oscillation part) across the equatorial Pacific Ocean. The warming phase of the sea surface temperature is known as El Niño and is accompanied with high air surface pressure in the tropical western Pacific, while the cooling phase of the sea surface temperature is known as La Niña, and is, in turn, accompanied by low air surface pressure *[Jones et al., 2007]*. The two periods last several months each, they are typically occurring every few years (with exceptions), and their effects vary in intensity.

Although the exact causes for initiating warm or cool ENSO events are not fully understood, the two components of ENSO — sea surface temperature and atmospheric pressure — are strongly related, therefore, even in the end of 1960s, *Bjerknes [1969]* hypothesised that ENSO is a consequence of slow feedbacks in the ocean-atmosphere coupled system, that allow the growth of small disturbances to the large-scale ocean state.

After *Bjerknes [1969]* published his hypothesis, it was not until the 1980s that ENSO was extensively studied. The intense warm episode of the 1982 – 83 El Niño, which was not recognised until it was well developed, galvanised the tropical climate research community towards understanding, and ultimately, predicting ENSO *[Wang et al., 2016]*. This motivated the ten-year international TOGA (Tropical Ocean-Global Atmosphere) program to study and predict ENSO. During TOGA program (1985–94) the successful observing system for ENSO was built *[McPhaden et al., 1998]* and the understanding of its mechanisms was hugely advanced by focusing on the interaction between the tropical Pacific and the atmosphere *[Neelin et al., 1998]*. After TOGA program finished, the ENSO community shifted its focus on more intricate details of ENSO dynamics, such as different types of ENSO events, ENSO low-frequency variability, and ENSO variability under global warming *[Wang et al., 2016]*. In the following text, I will give a summary of ENSO observations, a brief overview of physical mechanisms behind ENSO, and of various models (from global circulation models, through conceptual dynamical

models, to statistical models based on the past data) that were developed during past few decades.

5.1.1 Observing ENSO

Modern observational data associated with ENSO can go back to the late 19[th]century. Since the actual observations of sea surface temperature in the ocean are sparse, in particular at the beginning of the record, the produced data sets are in general produced from the sparse data using models, and other statistical methods (e.g. interpolation). One of the most used observational records of ENSO are without a doubt the ENSO indices. All of them were design to monitor the tropical Pacific, and all of them are based on sea surface temperature (SST) anomalies averaged across a given region. The Niño regions are labelled 1, 2, 3, and 4 and correspond with the labels assigned to ship tracks that crossed these regions, and the measurements from these tracks enabled the historic records of El Niño. The regions are depicted in Fig. 5.1.
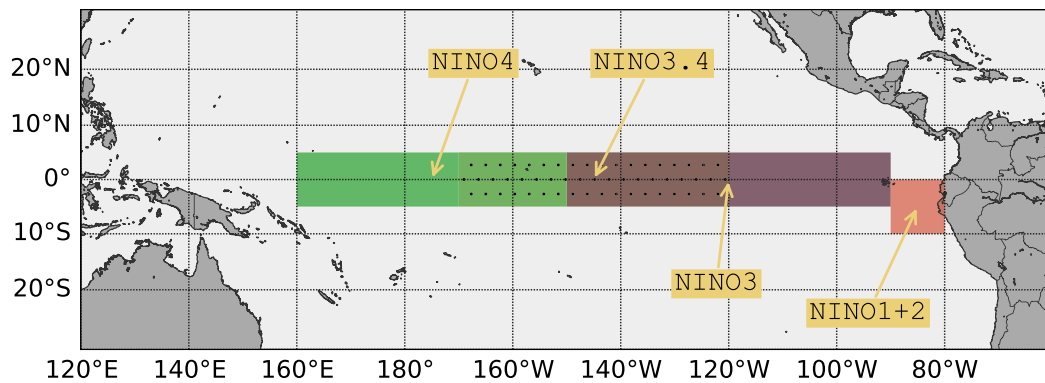
FIG. 5.1. | Illustration of 4 different Niño regions, from which the indices are derived as spatial average of SST over the region. Niño 3.4 regions, which is the most used one, is visualised with dotted patch.

The Niño 1+2 region (Fig. 5.1, light red) is the smallest and easternmost of the Niño SST regions and corresponds with the region of coastal South America where El Niño was first recognised by the local population. It spans the box 0°– 10°S, 90°W – 80°W, and tends to have the largest variance of the SST Niño indices.

Next, the Niño 3 region (Fig. 5.1, violet) was once the primary focus for monitoring and predicting El Niño, but later researchers learned that the key region for the coupled ocean-atmosphere interactions for ENSO lies further west *[Trenberth, 1997]*. It spans the rectangle of 5°S – 5°N and 150°W – 90°W.

The favoured region for defining El Niño and La Niña events is the 3.4 region (Fig. 5.1, dotted patch). Its anomalies may be thought of representing the average equatorial SSTs across the Pacific from about the dateline to the South American coast. The Niño 3.4 index typically uses a 5-month running mean, and the individual events are defined when the Niño 3.4 SST exceed +/− 0.4°C for a period of six months or more. It lies between the Niño 3 and 4 regions, therefore spans the rectangle of 5°S – 5°N and 170°W – 120°W.

The last of the Niño regions, the Niño 4 region (Fig. 5.1, green), captures the SST anomalies in the central equatorial Pacific and tends to have less variance than the other Niño regions. It spans the rectangle of 5°S – 5°N and 160°E – 150°W.

Other indices also exist, most notably the Oceanic Niño Index (ONI) which uses the same region as Niño 3.4 index, but rather is defined as 3-month running mean. Moreover, the individual events to be classified as a full-fledged El Niño or La Niña, the anomalies must exceed +0.5°C or -0.5°C for at least five consecutive months. As a last notable index, *Trenberth and Stepaniak [2001]* introduced the Trans-Niño Index (TNI) in order to define the unique character of each El Niño or La Niña event. This index should be used in combination with Niño 3.4 index and is defined to be the difference in normalised SST anomalies between the Niño 1+2 and Niño 4 regions. Thus it measures the gradient in SST anomalies between the central and eastern equatorial Pacific.

The temporal evolution of aforementioned Niño indices and their derived version are plotted in Fig. 5.2. The time series all of the plotted indices are taken from *Rayner et al. [2003]*. Moreover, their basic characteristics (first four standardised statistical moments and their correlation with others) are depicted in Table 5.1. Both from the table and the plotted time series we immediately see the statements from previous paragraphs to be true. In particular, the Niño 1+2 having the largest variance, while the Niño 4 region the lowest. We can also observe that the Niño 4 region is the warmest one, with the mean over last 70 years of data larger than other by more than 1.5°C. Also noticeable from the histograms and from the measures of skewness is the fact, that the Niño 1+2 and 3 are skewed towards colder SSTs, while Niño 4 and 3.4 are skewed towards warmer SST, in particular, the Niño 4 exhibit high negative skewness of -0.47. On the other hand, all basic Niño indices exhibit slightly to moderately negative kurtosis, hence have light-tailed (or platykurtic) distributions.
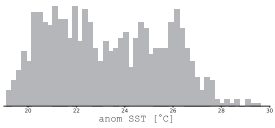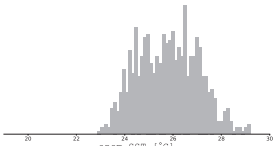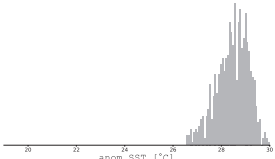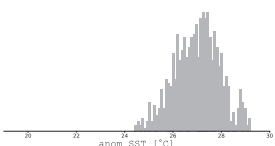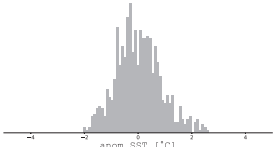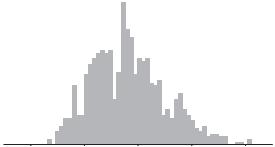
When looking at the Pearson's correlation coefficient between the various Niño indices (Table 5.1), the first thing that comes to mind is a rather high correlation between Niño 3.4 and Niño 3, and 4 (0.86 and 0.84, respectively). This is a good thing since it means that Niño 3.4 is indeed able to capture the SST in both central and eastern Pacific. On the other hand, a very low correlation between Niño 1+2 and Niño 4 index at 0.04 level suggests that the difference between the easternmost region in the Pacific and central Pacific are huge when it comes to the temporal evolution of SST. A high correlation between the ONI and Niño 3.4 index is not a surprise since both are based in the same region.

From the anomalised Niño 3.4 index (Fig. 5.2, bottom) it seems like the ENSO exhibited an oscillatory behaviour with 3–5 years preferred time scale, in spite of considerable irregularity in the record. The second point to be made, ENSO events show quite a large asymmetry between the El Niño warm events and La Niña cold events, with anomalies of El Niño larger than those of La Niña*[Wang et al., 2016]*.

Apart from indices described above, the evolution of ENSO can be seen in the zonal wind, surface air pressure, and 20°C isotherm depth fields. The zonal wind anomalies indicate ENSO because of the ocean-atmosphere coupling. The Southern Oscillation part of the ENSO is an oscillation pattern in surface air pressure between the tropical eastern and the western Pacific ocean waters. The strength of the oscillation is measured by the Southern Oscillation Index (SOI), which is computed from fluctuations in the surface
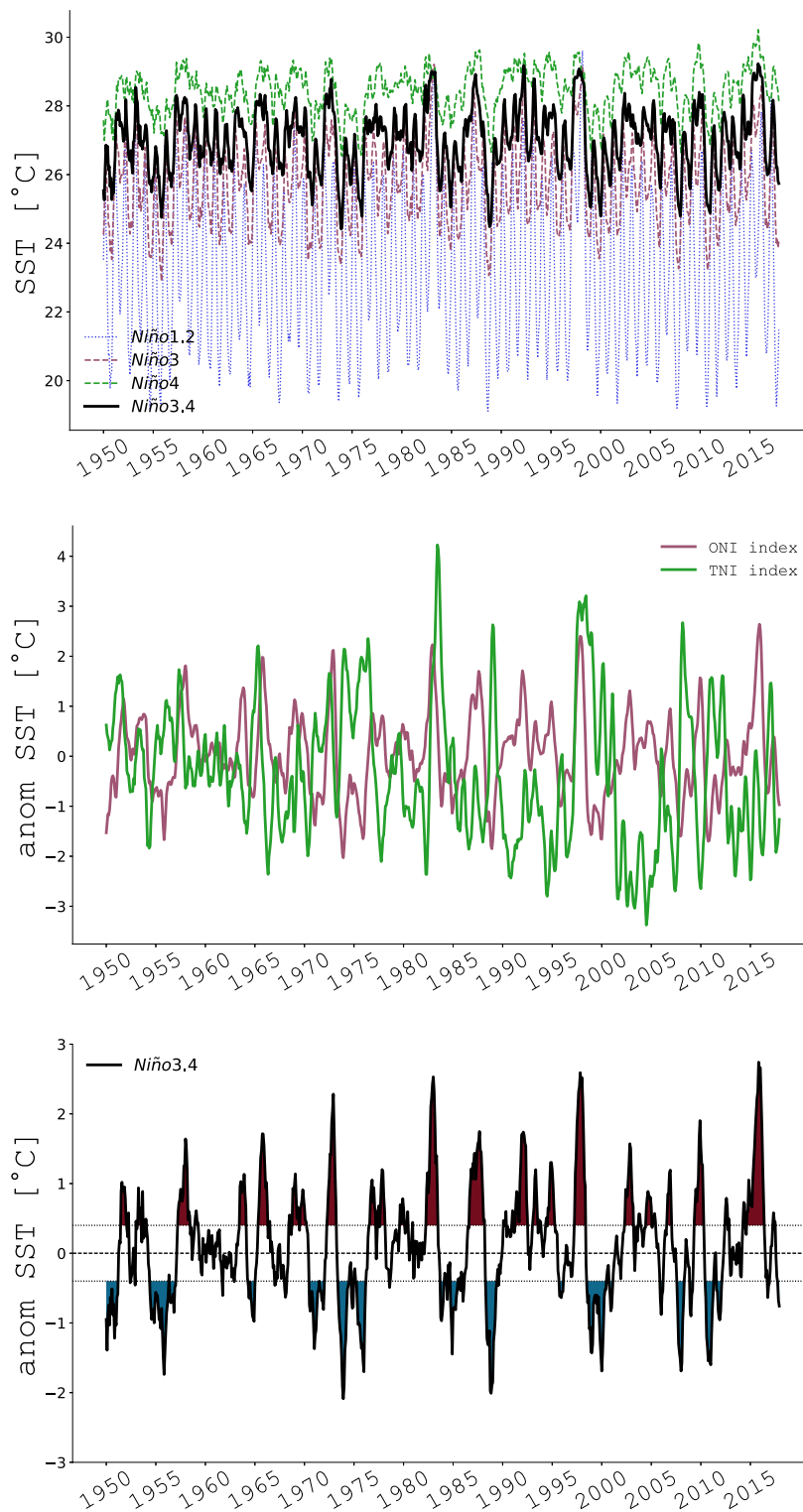
Fig. 5.2. | Time series of various Niño indices in the temporal span of January 1950 to December 2017. (top) 4 raw SST time series, spatially averaged over 4 distinct Niño regions. (middle) Derived Niño indices ONI and TNI. (bottom) Anomalised Niño 3.4 index, using 1950 – 1980 climatology, shown is 5-months running mean. The threshold is ±0.4°C.

	1950–2017				correlation with Niño:				histogram
region	mean	var	skew	kurt	1+2	3	4	3.4	
Niño 1+2	23.29	5.36	0.21	-1.02	X	0.80	0.04	0.43	
Niño 3	25.80	1.57	0.11	-0.65	0.80	X	0.49	0.86	
Niño 4	28.46	0.44	-0.47	-0.13	0.04	0.49	X	0.84	
Niño 3.4	27.00	0.89	-0.12	-0.31	0.43	0.86	0.84	X	
ONI	0.03	0.70	0.35	0.12	0.30	0.63	0.83	0.85	
TNI	-0.36	1.86	0.44	-0.09	0.24	0.04	-0.51	-0.22	

TABLE 5.1. | Summary of time series of various Niño indices. The table states first four statistical moments, their correlation matrix (correlations among the indices), and plots their histograms.

air pressure difference between Tahiti and Darwin, Australia. El Niño episodes exhibit negative SOI, meaning lower pressure over Tahiti and higher pressure over Darwin, while La Niña episodes have positive SOI, hence higher pressure in Tahiti and lower in Darwin. This also means that the SOI and Niño 3.4 indices are anticorrelated. Finally, the 20°C isotherm depth in the ocean serves as a proxy for thermocline depth. The variations of the thermocline, in particular, its slope and depth, is very important feature of ENSO, but unfortunately, the subsurface ocean temperature measurements have been sparse in the past.

One of the goals of TOGA initiative was to build and maintain the observing system in the tropical Pacific. This goal was accomplished and the system was built, containing
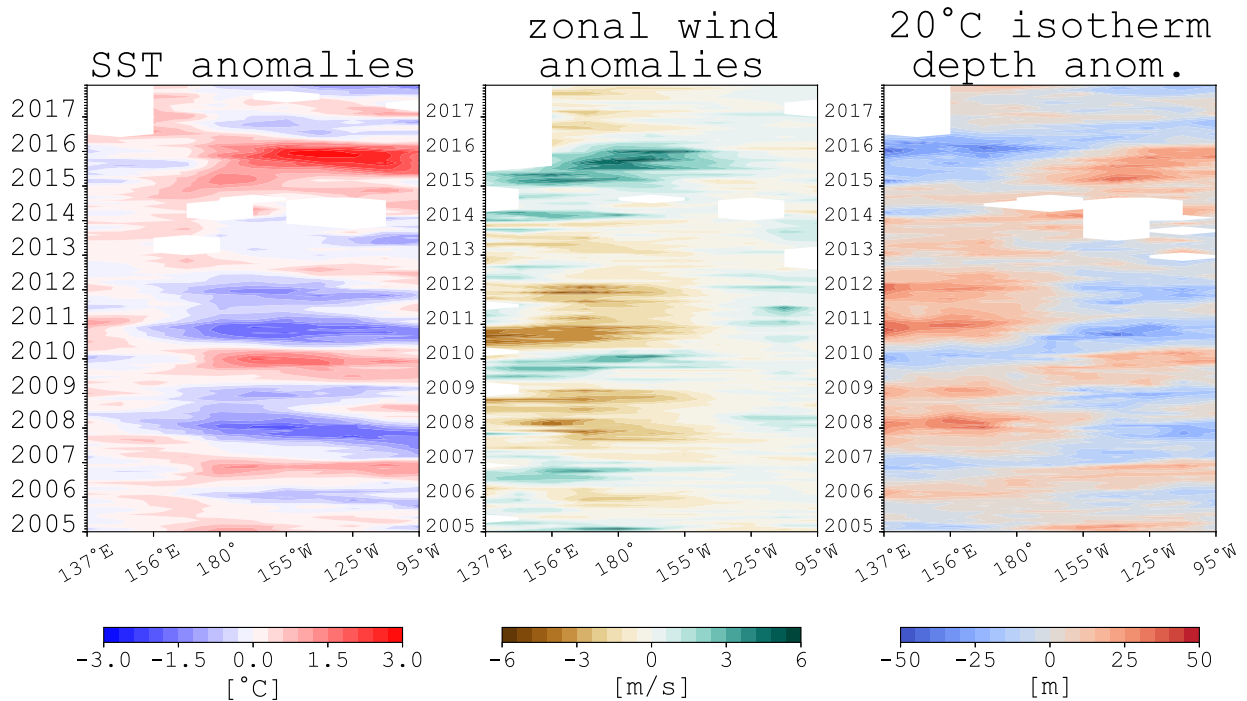
FIG. 5.3. | Time-longitude sections of monthly (left) sea surface temperature, (middle) zonal wind, and (right) 20°C isotherm depth anomalies between 5°S and 5°N from January 2005 to December 2017. White rectangles signify data gaps. Data provided by the TAO/TRITON array *[Hayes et al., 1991]*.

about 70 moored buoys *[Hayes et al., 1991; McPhaden, 1995]*. The system was named TAO/TRITON array and as of now is maintained by the USA and Japan. Most of the buoys are equipped with a 500-m thermistor chain and meteorological sensors. Moreover, at the equator, five to seven moorings are equipped with acoustic Doppler current profiler and current meters *[McPhaden et al., 1998]*. The example of data from TAO/TRITON can be seen in Fig. 5.3, where the time-longitude sections of sea surface temperature, zonal wind, and 20°C isotherm depth anomalies are rendered. The data clearly show close relationships among zonal wind anomalies, SSTs and thermocline depth anomalies. Moreover, they allow us to see the temporal evolution of the warm event 2014 – 16, as well as the cold event 2010 – 11.

In the middle of 2014, a positive anomaly of the thermocline (meaning deeper thermocline, thus warmer subsurface waters) begins to spread from the western Pacific eastward. This is usually viewed as a precursor of El Niño. This propagation is supported by westerly zonal wind anomalies. As the depression of thermocline extends to the east, warm subsurface waters are carried to the surface due to the equatorial upwelling. Once the SSTs becomes anomalously warm, the Bjerknes feedback begins — the westerly wind anomalies in the central Pacific cause the eastern Pacific thermocline to deepen even further, leading to additional warming of the surface waters. However, the shallower thermocline accompanied by cold subsurface waters in the western Pacific poses as a balancing agent, since this leads to the termination of the event. As the cold anomalies below the surface of the ocean propagate eastward, they cause the gradual

erosion of the surface warm anomalies. This, in fact, reverses the chain of events of the Bjerknes feedback and the coupled system is driven towards a La Niña phase. During La Niña phase all the processes reverse direction, and as the cold waters are extending eastward, the easterly zonal wind anomalies act to deepen the eastern thermocline, thus cooling the surface waters.

5.1.2 A physical description

In the previous sections we saw how the El Niño or La Niña events are built, now let us see what is actually happening physically in the tropical Pacific region. As written above, ENSO exhibit three distinct phases: neutral, warm phase (El Niño), and cold phase (La Niña). All the phases of ENSO are depicted in Fig. 5.4, where the schematics of atmospheric and oceanic circulation, as well as sea surface temperature, and thermocline depth are drawn.
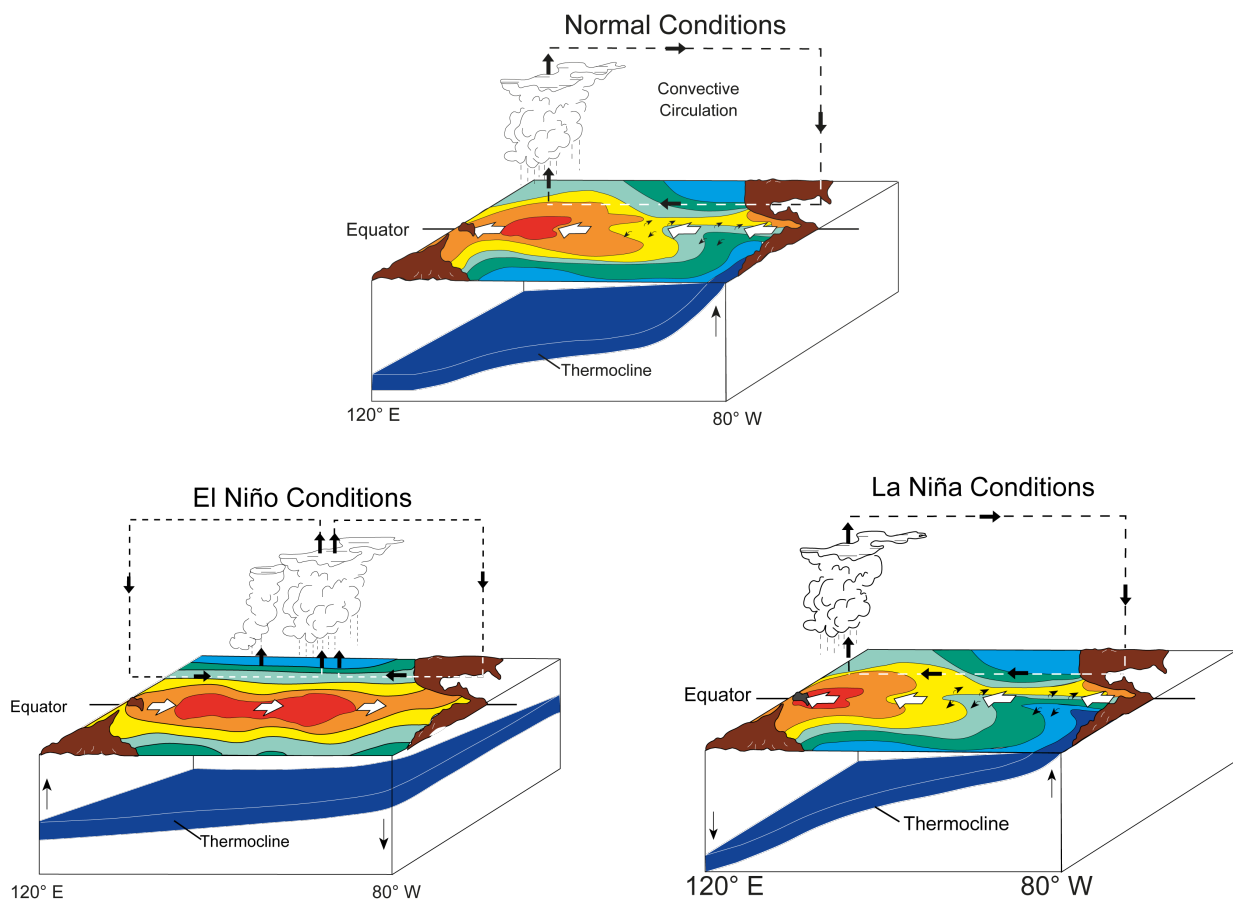
Fig. 5.4. | Illustration of circulation patterns in the atmosphere and the ocean, sea surface temperature and thermocline depth during (top) neutral conditions, (bottom left) El Niño conditions, and (bottom right) La Niña conditions. Figures by "Fred the Oyster", taken from *wikipedia.org [a]*.

The normal circulation pattern in tropical Pacific ocean is termed the Walker circulation. It consists of the surface trade winds blowing from the east to the west across

the tropical Pacific. Since these trade winds gather warm water pool towards the west, the air rises above this region. Then the upper-level winds blow from the west to the east, and finally, the sinking air is returned back to the surface in the tropical eastern Pacific, finishing the circulation. The Walker circulation further sustains the region of permanent precipitation over the warm pool, since the rising air is very moist and during its vertical advection it condensates. Gathering of the warm pool in the western Pacific also influences the depth and inclination of the thermocline, which acts to maintain the current state via equatorial upwelling. When the thermocline is deeper than the upwelling level, the water brought to the surface is warm (a normal state in the western Pacific), and vice versa — shallower thermocline means that the upwelling brings cold waters to the surface (a normal state in the eastern Pacific). All of these processes are depicted in Fig. 5.4, top panel.

Although the exact mechanisms that trigger the change of neutral state to an El Niño state are not known, the El Niño phase starts to building up by weakening, or even reversing, the Walker circulation which causes the ocean surface to be warmer than the average, as upwelling of cold water occur less or not at all in the eastern Pacific. With the disruption of Walker circulation, we observe westerly wind anomalies and these, via already mentioned Bjerknes feedback, cause the thermocline to deepen even further in the eastern Pacific, leading to additional warming. Since the warm pool extends to central, even eastern Pacific, the El Niño phase also shifts the belt of permanent precipitation eastward. Since condensation is a particularly rich source of latent heat, the El Niño event disturbs the storminess and heating in the tropics, which affects the Hadley circulation. The El Niño event supercharges the poleward flow, which in turn causes further changes in atmospheric flow, including the jet stream over the Pacific. Through these profound changes in the atmospheric flow, even if El Niño is specific to the tropical Pacific, it does have worldwide impacts.

The La Niña event displays the opposite behaviour of aforementioned fields. That is, the Walker circulation is strengthened, meaning the trade winds exhibit easterly anomalies, warm pool shifted even more westward and the slope of the thermocline is more inclined — shallower in the eastern Pacific and deeper in the western Pacific. The belt of permanent precipitation is shifted westward.

The theoretical explanations of ENSO can be loosely grouped into two frameworks: in the first El Niño is one phase of a self-sustained, unstable, and naturally oscillatory mode of the coupled ocean-atmosphere system; in the second El Niño is a stable (or damped) mode triggered by, or interacted with, stochastic forcing or noise such as westerly wind bursts and Madden–Julian oscillation events (e.g. *Gebbie et al. [2007]; Wang et al. [2016]*), and the tropical instability waves in the eastern Pacific (e.g. *An [2008]*). Both of the frameworks involves the *Bjerknes*'s *[1969]* feedback.

Bjerknes [1969] first hypothesised that the interaction between the atmosphere and the equatorial eastern Pacific ocean gives rise to El Niño, due to initial positive SST anomaly in the eastern Pacific, which reduces the east-west SST gradient and therefore the strength of Walker circulation, ultimately resulting in weaker trade winds. The weaker trade winds, in turn, reinforce the SST anomalies by driving the ocean circulation. However, this positive feedback would result in a never-ending warm state of the equatorial Pacific, and therefore a negative feedback is needed in order to make the coupled system

oscillatory. Whilst searching for necessary negative feedbacks, four conceptual ENSO oscillator models have been developed: the delayed oscillator *[Suarez and Schopf, 1988; Battisti and Hirst, 1989]*, the recharge oscillator *[Jin, 1997a,b]*, the western Pacific oscillator *[Weisberg and Wang, 1997; Wang et al., 1999]*, and the advective-reflective oscillator *[Picaut et al., 1997]*. Each of these oscillator models emphasised different negative feedback in the Pacific: the delayed oscillator counts on reflected Kelvin waves at the ocean boundary, the recharge oscillator works with a discharge process due to Sverdrup transport, the western Pacific oscillator relies on wind-forced Kelvin waves, and the advective-reflective paradigm depends on anomalous zonal advection *[Wang et al., 2016]*.

The delayed oscillator of *Suarez and Schopf [1988]* introduced the candidate mechanism for ENSO, modelling the effects of equatorially trapped oceanic wave propagation. On one hand, the positive coupled feedback leads to SST anomaly into the warm state. On the other hand, the delayed negative feedback, due to free Rossby waves generated in the eastern Pacific coupling region and propagated to and reflected from the ocean western boundary ultimately to be returned as Kelvin waves, reverses the SST anomaly to the neutral state.

Wyrtki [1975, 1985] was first to suggest a buildup in the western Pacific of warm water as a precondition of El Niño. The warm water volume over the entire tropical Pacific would build up (or charge) gradually, and during the warm event, the water is discharged to higher latitudes, while the tropics are filled with cold water. In the meantime, the warm water again slowly charges in the upper subsurface layer of the ocean. Using these ideas about the necessary buildup, and based on a coupled model of *Zebiak and Cane [1987]*, *Jin [1997a,b]* derived and formulated his recharge oscillator model. In this conceptual model, the recharge-discharge process of equatorial heat content makes the coupled system oscillate. The discharge process is initiated during a warm, El Niño, phase due to the divergence of Sverdrup transport associated with westerly wind anomalies and eastern SST warm anomalies. This discharge of the warm water leads to a transition phase, when the entire equatorial thermocline is anomalously shallow, and thus leading to cold waters upwelling to the surface, and ultimately to a La Niña phase. During a cold phase, the converse effects occur, giving rise to an oscillatory behaviour of the coupled system.

The western Pacific oscillator model, due to *Weisberg and Wang [1997]; Wang et al. [1999]*, emphasise the role of western Pacific in ENSO, which was overlooked in the delayed oscillator model. In particular, the off-equatorial SST anomalies, and off-equatorial anomalous anticyclones. The equatorial westerly wind anomalies act to deepen the thermocline and increase SST via positive feedback (classical Bjerknes feedback). Although, in contrast, the off-equatorial cyclones raise the thermocline via Ekman pumping, and thus a shallow off-equatorial thermocline anomaly expands over the western Pacific leading to a decrease in SST and increase in sea level pressure (SLP) in the off-equatorial western Pacific *[Wang et al., 1999]*. During the mature phase of El Niño, the off-equatorial anticyclones initiate equatorial easterly wind anomalies in the western Pacific, and they in turn cause upwelling and cooling that proceed eastward as a forced ocean response providing a negative feedback, allowing the coupled system to oscillate *[Wang et al., 2016]*.

Finally, the advective-reflective oscillator proposed by *Picaut et al. [1997]* stresses the

importance of zonal currents, in particular, the anomalous zonal currents associated with wave reflections at both, eastern and western, ocean boundaries, and the mean zonal currents converging at the eastern edge of the warm pool. In the course of El Niño event, the westerly anomalies produce upwelling Rossby and downwelling Kelvin waves that propagate westward and eastward, respectively. After Rossby waves reach the western boundary, the waves are reflected as upwelling Kelvin waves, whereas the Kelvin waves after they reach the eastern boundary, reflect as downwelling Rossby waves. Since both the upwelling Kelvin, and downwelling Rossby waves have westward zonal currents, they tend to push the warm pool back to its original position in the western Pacific. This, again, makes the coupled system oscillate.

As many people use to say that truth is somewhere in the middle, more than one conceptual model may operate in nature. Motivated by the existence of the four oscillator models, *Wang [2001]* formulated a unified ENSO oscillator model, which includes the physics of all oscillators models discussed above. As suggested by the unified oscillator model, ENSO is a multi-mechanisms phenomenon and the relative importance of different mechanisms is time-dependent.

Another, conceptually different, view of ENSO is that various El Niño events are a discrete series punctuating the periods of natural or cold conditions. In this view, ENSO is characterised as a stable (or damped) mode triggered by stochastic atmospheric/oceanic forcing (e.g. *[Lau, 1985; Penland and Sardeshmukh, 1995; Philander and Fedorov, 2003]*). The difference in comparison with the aforementioned oscillator models is that the disturbances that drive ENSO are external, and therefore suggests a natural explanation for the irregularity of ENSO events in terms of noise. The external atmospheric forcing can include the Madden–Julian Oscillation and westerly wind bursts (e.g. *Gebbie et al. [2007]*), and the oceanic noise may include the tropical instability waves (e.g. *An [2008]*). However, even a sequence of independent warm events can still be consistent with delayed oscillator physics, since the termination of an individual El Niño event still requires negative feedback that can be provided by wave reflection at the western boundary *[Mantua and Battisti, 1994]*.

5.1.3 Typical scales in El Niño/Southern Oscillation

After years of extensive research, the scientific community reached a general consensus on the fundamental features of ENSO phenomenon itself, and on other processes that contribute to its dynamics. I refer the potential reader to reviews by *Rasmusson and Carpenter [1982]* or *Neelin et al. [1998]*. One of the results of the extensive research refers to the temporal scales involved in ENSO dynamics. As an example, it is now widely accepted that the occurrence frequency of ENSO peaks in approximately 3- to 5-year periods. In addition, a secondary peak at approximately 2-year periodicity was noted by several authors, firstly by *Rasmusson et al. [1990]*. The oscillator hypotheses, briefly described in the previous section, are all in agreement with these interannual periodicities. However, the ocean-atmosphere interactions (which are modelled via the oscillators) can explain the principal features of ENSO, its observed intrinsic characteristics exhibit profound irregularities. The individual El Niño and La Niña events are often dissimilar from each other in terms of their amplitude or evolution pattern *[Yeo and Kim, 2014]*.

This irregularities and uniqueness of each individual event make it almost impossible to grasp and comprehend the nature of ENSO as a whole. One obvious way how to better understand the nature of this phenomenon is to decompose its measurements — the SSTs, and therefore its dynamics — into less complicated categorical modes. Various authors used various methods to achieve this. *Barnett [1991]* used simple temporal filters and complex empirical orthogonal functions (CEOF) and came to a conclusion that ENSO is principally a three time-scales process, consisting of an annual cycle, a quasi-biennial oscillation, and a lower frequency variation pattern. Few years after, *Latif et al. [1997]* also identified three modes of variability, though the use of principal oscillation pattern (POP) analysis and these were an interannual mode, a decadal mode, and a trend or unresolved ultra-low frequency variability pattern. *Kim [2002]* decomposed tropical Pacific SST variability into two dominant modes — a biennial mode and a low-frequency mode — via cyclostationary empirical orthogonal functions (CSEOF) analysis. *Yeo and Kim [2014]* repeated the CSOEF analysis to identify, again, three modes of variability in a 140-year long SST dataset: a global warming mode (ultra-low frequency), a low-frequency variability mode, and a biennial oscillation mode.

In addition to decomposition efforts, some authors reported various individual time scales that play a role in ENSO dynamics. *Rasmusson et al. [1990]* was one of the first that noted the existence of biennial component in ENSO dynamics (SSTs and zonal wind) through the use of SSA. He also identified a low-frequency peak with a period between 4 and 5 years. *Jiang et al. [1995]* confirmed these findings of quasi-biennial variability in the ENSO region, and also described a quasi-quadrennial peak in principal components from decomposed SSTs via multichannel SSA (M-SSA).

Aside from these interannual and longer time scales involved in ENSO, one always needs to keep in mind our Sun, which forces undoubtedly one of the most profound cycles — the annual cycle. There are many observational studies documenting the annual evolution of SST and its associated atmospheric counterparts *[Wyrtki, 1965; Hastenrath and Lamb, 1978; Mitchell and Wallace, 1992; Wang, 1994]*. It is an important point to realise that the annual cycle in the tropics, similarly as ENSO itself, arises from coupled tropical atmosphere-ocean interactions, and it not only coexists with ENSO but also strongly interacts with it, enriching its characteristics (e.g. *Jin et al. [1994]; Jin [1996]; Stuecker et al. [2013, 2015]; Chen and Jin [2017]*).

One of the processes with interesting interplay between the annual cycle and ENSO is definitely ENSO's synchronisation to the annual cycle. Firstly, the observational evidence in the form of a similar pattern of developing individual ENSO events with building during boreal summer and peaking during boreal winter was found *[Rasmusson and Carpenter, 1982; Larkin and Harrison, 2002]*. As *Stein et al. [2014]* noted, the exact mechanisms responsible for this synchronisation are not known, although two possible candidates exists: frequency locking of ENSO to periodic forcing by the annual cycle *[Jin et al., 1994; Tziperman et al., 1994]*, and the modulation of ENSO's coupled stability due to the seasonal variation of the background state of equatorial Pacific *[Philander et al., 1984; Hirst, 1986]*.

The last, but also very important, point I wanted to make is that some studies *[An and Wang, 2000; Wang and An, 2001]* have shown that the frequency of ENSO is dependent on the spatial structure of zonal wind stress anomalies, in particular, the longitudinal

position of the westerly anomalies. *An and Wang [2000]* argue that the delayed oscillator theory only qualitatively describes the effect of the zonal location of the wind anomalies on ENSO frequency. They also identify yet another feedback — zonal advective feedback — where the zonal position of the zonal wind stress anomalies influences the zonal currents in the central equatorial Pacific. This zonal advective feedback favours the transition of the ENSO, rather than its growth, and consequently supports a shorter oscillation of 2–4 years with a lower amplitude when the zonal wind stress is shifted westward. Conversely, when the wind stress is shifted eastward, it favours the growth of ENSO cycle rather than its transition and therefore a longer oscillation of 4–6 years with larger amplitude tend to happen *[An et al., 1999; An and Wang, 2000]*. The leading interpretation of such studies is that the balance between the zonal advective feedback and the thermocline feedback (anomalous easterlies in the eastern Pacific caused mean upwelling to increase) is a key parameter in the structure and dynamics of the coupled ENSO mode and the frequency of ENSO cycle: the thermocline feedback favours the recharge oscillator mode with a strong, 4 – 6 years periodic ENSO, while the zonal advective feedback is characterised by a weaker and shorter (2 – 4 years) ENSO *[An and Jin, 2001]*.

Similar results were reported by *Fedorov and Philander [2001]* via stability analysis of Cane–Zebiak coupled model *[Zebiak and Cane, 1987]*, where the 2 distinct unstable modes emerged: the "delayed oscillator" mode with longer (5-year) oscillations driven by vertical movements of the thermocline and the "SST" mode with shorter time scale (approximately 2 years), controlled by advection and entrainment across the thermocline. In conclusion, it seems that both feedbacks are very important, and as noted before with the unified oscillator paradigm, both of them coexists and their significance varies over time.

A couple of recent studies also addresses the temporal variations in shorter time scales than ENSO itself. *Chen and Jin [2017]* used a linear coupled framework to quantify the internal dynamics and external forcing that determine the amplitude of the annual cycle. *Wang et al. [2017]* argue for enhanced biennial variability in the Pacific due to the Atlantic capacitor effect, arguing that since the 1990s a warmer Atlantic and global warming provided favourable background state for the Atlantic capacitor effect, ultimately giving rise to enhanced biennial variability in the Pacific basin.

The purpose of this section was to give an overview of temporal scales that are central to the dynamics of ENSO. With the richness of its spectrum and various processes involved in influencing it, it would be even unnatural if the temporal scales would not be coupled in some intrinsic way via cross-scale interactions introduced earlier.

5.2 Modelling of El Niño/ Southern Oscillation

Because of the immense impact of ENSO in a global scale, ranging from disturbed circulation patterns, precipitation changes, and warm or cold spells even outside of the tropical belt *[Lau and Nath, 2001; Alexander et al., 2002]* which result in societal and economic impacts, the great emphasis is put in forecasting and simulating the ENSO phenomenon. The efforts are focused into understanding and simulating ENSO through

the conceptual models, forecasting its effects on seasonal-to-interannual time scales, and predicting how its impacts may change over coming decades, in the light of global warming.

The modelling systems of ENSO usually fall into a large hierarchy of models, ranging from simple conceptual models (similar to oscillator models mentioned earlier) to high resolution fully-coupled general circulation models. These models are based on the equations emerging in fluid dynamics, or their conceptualised versions. However, another large category exists and that is the so-called statistical models of ENSO, which are in opposition to dynamical models. They are not based on the underlying physical description of the phenomenon, but rather use a statistical formulation and are trained on past observed data, in order to capture and subsequently simulate the temporal and spatial patterns displayed by the phenomenon.

In the tropics, the question of forecasting at the seasonal time-scale is linked to the availability of accurately predicted SST. Because the characteristic time scales (or a lifetime of planetary-sized structures) of the ocean are considerably longer than those of the atmosphere, the predictability limit is also expected to be longer in the ocean. Based on this, it can be argued that the climate predictions at lead times of one to a few seasons are primarily the matter of predicting SSTs *[Goddard et al., 2001]*. The respond of the tropical atmosphere to the SST forcing was first thought to be coherent and reproducible (e.g. *Stern and Miyakoda [1995]; Shukla [1998]*), however, has been challenged and shown to be inadequate in the summer monsoon regions *[Wang et al., 2005]*. Moreover, *Fu et al. [2003]* and *Zheng et al. [2004]* have suggested that this "forecast the SSTs and the atmosphere will follow" approach has shortcomings for predicting intraseasonal oscillations as well.

The dynamical models can be subdivided into two categories: conceptual models which are usually low-dimensional, and comprehensive fully coupled ocean-atmosphere general circulation models (COAGCM). Apart from the level of physical detail and the overall dimensionality, the difference also lies in typical use. Conceptual models serve as a test-bed for theoretical advances in understanding the ENSO phenomenon, but their forecasts are not particularly skilled. The COAGCMs, on the other hand, serve exactly the purpose of forecasting the ENSO at the longest lead-lag possible.

The in-depth review of COAGCMs and their ability to simulate ENSO is far beyond the scope of this section, chapter and even thesis, but I will mention a few important points for our work. Although the representation of ENSO in coupled models has advanced considerably during the last two decades, several aspects of the simulated climatology and ENSO are not well reproduced by the current generation of COAGCMs *[Jin et al., 2008]*. The systematic errors in SST are often largest in the equatorial Pacific, and the model representation of ENSO variability are often weak and/or incorrectly located *[Delecluse et al., 1998; Davey et al., 2002]*. In addition to initial condition error (the memory of the system resides in the upper ocean, thus it is imperative to determine the initial state as accurately as possible), most models simulate an equatorial cold tongue that is too prominent *[AchutaRao and Sperber, 2002; Davey et al., 2002]*, and finally the models differ in their representation of intraseasonal variability both due to weather noise and organised structures as the Madden–Julian Oscillation (e.g. *Lau and Waliser [2011]*).

Yet another important point to realise is that the coupled models initialised from observed initial states tend to adjust toward their own climatological mean and variability, leading to forecast errors. The errors associated with such adjustments tend to be more pronounced during boreal spring *[Jin et al., 2008]*. This suggests that the so-called "spring predictability barrier" (e.g. *Webster [1995]*) may be associated with a "spring variability barrier" in coupled models *[Schneider et al., 2003]*. Apart from the spring barrier problem, *Wittenberg [2009]* pointed out, using a 2000 years control run, that ENSO exhibits strong interdecadal and intercentennial modulation of its events. To the extent that such modulation is realistic, it could attach large uncertainties to ENSO metrics diagnosed from centennial and shorter records — with important implications for historical and paleo records, climate projections, and model assessment and inter-comparison *[Wittenberg, 2009]*. Moreover, his analysis of the wait times between ENSO warm events do not require multidecadal memory; it can simply arise from Poisson statistics applied to ENSO's interannual time scale and seasonal phase-locking.

While the purpose of the last two paragraphs was not to criticise the COAGCMs and their skills, it was to state the problems associated with them. With constantly improving computational capacities, parametrisation schemes, and resolution, the COAGCMs still offer a very promising avenue for successfully forecasting ENSO and its events.

5.3 Synchronisation and causality in El Niño/ Southern Oscillation

In order to examine the possible synchronisation and causality in El Niño/ Southern Oscillation phenomenon, we adopted the methodology developed by *Paluš [2014a,b]* and described in detail in sec. 4.2.2. We were interested in studying the interactions between the processes dominated by different temporal scales using the phase dynamic approach. As a quick recapitulation, we first applied, to the monthly Niño 3.4 index *[Rayner et al., 2003]* with temporal span of 1900–2010, the continuous complex wavelet transform with Morlet wavelet (*Torrence and Compo [1998]* and sec. 3.3.2) and obtained time-dependent complex wavelet coefficients $\psi_p(t)$ for a given central period p as

$$\psi_p(t) = s_p(t) + i\hat{s}_p(t) = A_p(t)e^{i\phi_p(t)} \tag{5.1}$$

From the wavelet coefficients we subsequently extracted the instantaneous phase, $\phi_p(t)$, and amplitude, $A_p(t)$, time series are given by

$$\phi_p(t) = \arctan\frac{\hat{s}_p(t)}{s_p(t)} \tag{5.2}$$

$$A_p(t) = \sqrt{s_p^2(t) + \hat{s}_p^2(t)}. \tag{5.3}$$

To study the possible cross-scale interactions, we computed the mutual information, as well as the conditional mutual information (*Paluš and Vejmelka [2007]* and sec. 3.4.2), based on the phase and amplitude time series associated with variability at two different

time scales, p_1 and p_2. In particular, mutual information

$$I\left(\phi_{p_1}(t); \phi_{p_2}(t)\right) \tag{5.4}$$

characterises phase synchronisation between two time series *[Paluš, 1997]*. Conditional mutual information

$$I\left(\phi_{p_1}(t); \phi_{p_2}(t+\tau) - \phi_{p_2}(t) \mid \phi_{p_2}(t)\right), \tag{5.5}$$

where τ is forward time lag, describes the information in ϕ_{p_1} about the future of ϕ_{p_2}, hence measures phase-phase causality. Similarly, the functional

$$I\left(\phi_{p_1}(t); A_{p_2}(t+\tau) \mid A_{p_2}(t), A_{p_2}(t-\eta), A_{p_2}(t-2\eta)\right), \tag{5.6}$$

with η being the backward time lag and τ the forward time lag, is a measure of phase-amplitude causality. The (conditional) mutual information was estimated using k-nearest neighbours algorithm. For additional details please see previous sections of this thesis (sec. 3.4.4 and 4.2.1), and references therein.

The statistical significance of our results was estimated using a randomisation procedure by generating Fourier Transform surrogate data from the Niño 3.4 time series, which creates surrogate data set with the same spectrum as that of the original data, but with no interactions between processes of different time scales (for details of the FT surrogates, see sec. 3.5.1).

5.3.1 Interactions in the observed ENSO

We examined the synchronisation and causal interactions in the Niño 3.4 time series for the quasi-oscillatory modes with periods ranging from 5 to 96 months. In Fig. 5.5 we are looking for the observed interactions characterised by causality estimate exceeding the 95[th]percentile of the distribution of this quantity for the surrogate data samples, where the surrogate time series were generated using a Monte Carlo method, yielding synthetic time series with the same spectrum, but void of any cross-scale interactions.

There exist three pairs of modes that exhibit phase synchronisation (Fig. 5.5, A). The mode with a period between 1.8 – 2.1 years — let us call it quasi-biennial (QB) mode — is synchronised with the range between 8 and 14 months. Besides the obvious annual cycle (AC), this range also includes the so-called combination tones (CT) described by *Stuecker et al. [2013]* as a nonlinear atmospheric response to combined seasonal and interannual SST changes. The combination tones themselves seem to result from an interaction of two distinct processes — the annual cycle and the low-frequency (LF) ENSO mode. In our analysis, the combination tones further interact with the annual cycle via synchronisation. Finally, the third synchronisation pair is the low-frequency mode (periods between 5 and 6 years) with somewhat higher frequency QB mode, with period above 2 years. We attribute other small significant "blobs" to the existence of false positive since, during a statistical test, each pair of modes is tested independently, therefore a problem with multiple comparisons arise. Because we do not address this problem by applying a correction, we anticipate for up to 5% false positive rate.

These results reconfirm an important role of the annual cycle in ENSO dynamics, with strong events peaking in boreal winter *[Torrence and Webster, 1998; Larkin and Harrison,*

observed Niño 3.4
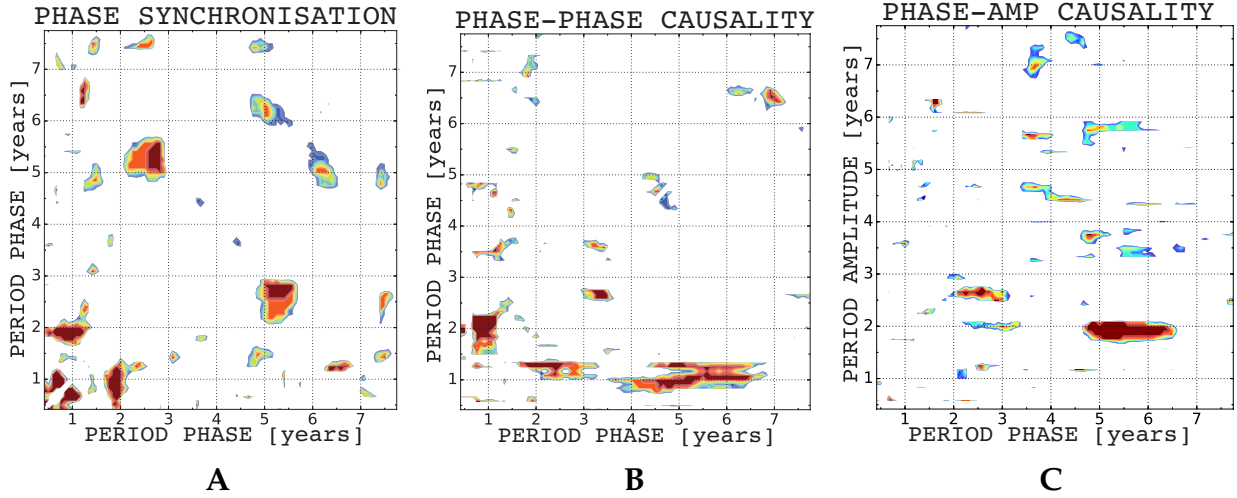
Fig. 5.5. | Cross-scale (**A**) phase synchronisation, (**B**) phase-phase causality, and (**C**) phase-amplitude causality in the observed Niño 3.4 time series. The phase synchronisation is a symmetrical relation, hence the plot is symmetric, while causality plots are shown with the period of the driver (master) time series on the *x*-axis and driven (slave) time series on the *y*-axis. Shown are (positive) significance-level deviations from 95th percentile of the *k*-nearest neighbour estimates of (conditional) mutual information, tested using 500 FT surrogates.

2002], and point to the link between QB and LF modes which may be responsible for extreme ENSO events *[Barnett, 1991; Jiang et al., 1995; Kim, 2002]*; thus, this synchronisation analysis brings out known ENSO properties consistent with previous research.

The phase-phase causality (Fig. 5.5, B), on the other hand, provides an additional information that complements the phase synchronisation results and addresses the causes of these synchronisations by elucidating important directed connections between the LF, QB and AC/CT ENSO modes. The phase of LF modes (with periods between 4 – 6 years) affects the range of AC/CT, which means that the "shape" of the annual cycle depends on whether the LF mode is in its extreme warm or extreme cold phase. Furthermore, the phase of the AC mode is a skilful precursor for the phase of QB modes with the periods of 1.8 – 2.1 years, while the phase of QB modes with periods of 2 – 3 years dictates in part the phase of the CT modes (period 12 – 16 months).

The only pronounced phase-amplitude causality link (Fig. 5.5, C) is the one between the phase of the LF ENSO mode (periods of 5 – 6 years) and the amplitude of QB modes (periods of 1.8 – 2.1 yr).

A little note considering the frequency width of found modes. In general two options exist: the range of frequencies we see in our results is, in fact, multiple processes with similar frequency, co-interacting together and with the distinct modes as captured by our synchronisation analysis. The second option is that the range represents one process either with temporally variable frequency or a wider bandwidth properties. Since the Morlet mother wavelet itself contain wider range of frequencies and is not really sharp-peaked in the Fourier domain, we also need to keep in mind the subsequent effect on

the "resolution" in the frequency domain. Finally, the temporal mode is not necessarily associated with only one physical process — it might be an oscillatory representation of more processes that interact together, e.g. a positive or negative feedback loop.

Our analysis thus identifies the three fundamental time scales in ENSO dynamics — AC, QB and LF — consistent with previous work *[Barnett, 1991; Kim, 2002; Yeo and Kim, 2014]*, but offers further details on the interaction between these modes. Some of the interactions we identified rigorously here have been previously theorised to exist, but, to the best of our knowledge, were never detected in a data-driven way. Based on our results, it is natural to consider the AC and CT processes in combination to define the quasi-annual (QA) variability. The QB modes can be divided into two — "faster" and "slower" — sub-ranges, with the periods of 1.8 – 2.1 yr and 2.1 – 3 yr, respectively. Similarly, the LF processes can be divided into the ones associated with 4 – 5 year and 5 – 6 year periods.

We observe a pronounced connection between the (phase of) the slower LF mode and both the phase and amplitude of the faster QB mode. In particular, the slower LF mode affects the phase of the QA mode, and, therefore, — indirectly — the phase of the faster QB mode, which tends to be affected by and phase-synchronised with the QA mode; the slow LF mode also directly affects the amplitude of the faster QB mode. The connections between the phase of slow LF mode and the phase of QA mode important in the causal sequence above are both direct and indirect. In the latter indirect case, the connection works through the phase synchronisation between the slow LF mode and the slow QB mode and subsequent causal effect of the latter on the phase of the QA mode. The faster LF modes add to the picture by also affecting the phase of the QA mode, and, therefore, indirectly, the phase of the faster QB mode.

5.3.2 Consequences of causal connections

One of the main findings of our study is the apparent importance, in ENSO dynamics, of the LF phase→QA phase→QB phase causal linkages, as well as LF phase→QB amplitude causal linkages. To illustrate these causal connections further, we utilised an approach of conditional composites, in which we first identified three distinct phases (by dividing the span between maximum and minimum values into three bins) of the low-frequency (LF) ENSO component: LF–, LF0 and LF+; and subsequently computed the composites (mean values) of any variable of interest over the data points associated with these three phases.

Fig. 5.6 visualises the response of the AC frequency to changes in the phase of the LF ENSO variability, thus illustrating the LF phase→QA phase causal linkage. Here, we composited the instantaneous frequencies of the annual cycle computed as the slope of the continuous 12-month-long snippets of the AC-phase time series via the robust regression. These results are presented in the form of histograms and suggest that the positive phase of the LF cycle speeds up the annual cycle (thus shortens its period and increases its frequency), while the negative period of LF cycle causes the AC period to become longer than a year. Not surprisingly, the annual cycles associated with neutral LF0 conditions, as well as climatological annual cycles, have the average period of exactly one year.
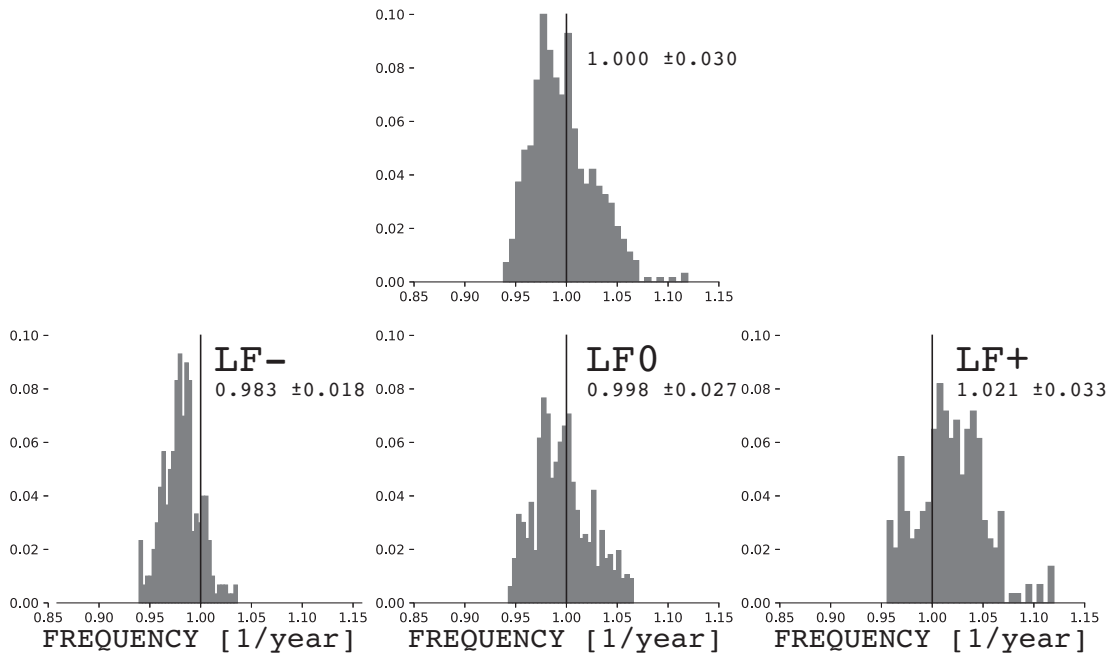
FIG. 5.6. | Histograms of instantaneous frequencies of the Niño 3.4 annual cycle. Top panel: unconditioned (using all data); bottom: histograms conditioned on the phase of the low-frequency (LF) ENSO mode, from left to right: negative LF phase, neutral LF phase, and positive LF phase. The black vertical line marks exactly 1 year period, and also given are respective means ± one standard deviation of instantaneous frequencies for all 4 panels.

In fact, not only the effective frequency but also the entire shape of the annual cycle changes depending on the phase of the LF ENSO mode. Fig. 5.7 shows conditional composites of the annual cycle associated with the LF−, LF0 and LF+ phases of the low-frequency ENSO cycle; these composites were computed by averaging the raw Niño 3.4 data associated with a given phase of LF variability for each month. The neutral LF conditions correspond to the seasonal cycle of Niño 3.4 temperatures, that is close to a climatological seasonal cycle. The latter cycle is not purely harmonic and is characterised by relatively fast warming between January and May and a slower cooling afterwards. The annual cycle conditioned on LF− phase has the same general character but is on average cooler than the climatological AC. The annual cycle associated with the LF+ phase of interannual ENSO signal is, of course, warmer on average due to El Niño–type conditions, but also has a very different, more harmonic shape, with September-through-December warming absent from the LF−, LF0 and climatological annual cycles. Also shown in Fig. 5.7 are the Niño 3.4 time series during two extreme El Niño events (namely, 1982/83 and 1997/98 events). Note how a very strong biennial ENSO signal during those years completely masks any visible AC variability that may be present in the Niño 3.4 time series at that time. An episodic character of such pronounced biennial extreme events makes it difficult to associate the QB ENSO variability with alterations between weak and strong annual cycles, as was suggested previously *[Meehl, 1987]*. We argued that such extreme ENSO events arise due to synchronisation between a suite of different

QB modes, which are individually characterised by a relatively small variance.
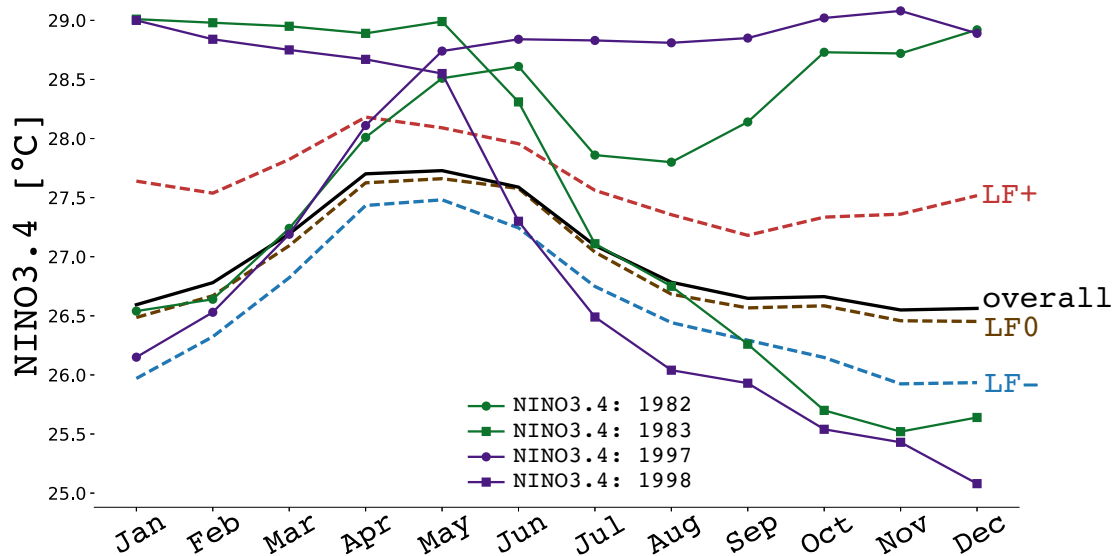
FIG. 5.7. | Annual cycle composites of Niño 3.4 index conditioned on the phase of low-frequency (LF) ENSO mode. Also shown are snippets of the Niño 3.4 time series during two particular extreme ENSO events: 1982/83 and 1997/98.

We hypothesise here that these "internal" QB synchronisations arise due to causal interactions represented by the QA phase→QB phase causal linkage identified by our conditional mutual information analysis. This linkage is further illustrated, albeit indirectly, in Fig. 5.8, which shows that the composite annual cycles associated with QB−, QB0 and QB+ phases of QB variability closely match those associated with LF−, LF0 and LF+ phases, respectively, consistent with LF phase→QA phase→QB phase directed connections.

Moreover, Fig. 5.9 identifies clear growth in the amplitude of the BC and QB variability as the low-frequency phase changes from La Niña (LF−) to El Niño (LF+) conditions, consistent with the LF phase→QB amplitude causal interaction. On the other hand, the changes in the amplitude of AC anomalies conditioned on the LF phases are non–monotonic and somewhat less pronounced compared to those in BC and QB amplitudes.

We hypothesise that the interactions identified above are instrumental in setting up extreme ENSO events (Fig. 5.10). In particular, during all of the strong El Niño events of years 72/73, 82/83 and 97/98, the QA, QB and LF modes were characterised by synchronous pronounced maxima. Note, however, that strictly speaking, the synchronisation with LF mode is not really necessary for an extreme ENSO event to materialise, since the "peak" of this mode spans a good part of the year (for example, the peak of LF mode did not really occur in winter 1982/83, but the LF wintertime "background" during that time was still abnormally warm), while the amplitude of the QA mode is, in general, small, so that this mode does not contribute much directly to the magnitude of a given event. Instead, what appears to be essential for an extreme ENSO to occur is the synchronisation of multiple QB modes with each other. We believe that this "internal" QB synchronisation is what has been picked up by our conditional mutual information analysis in the form of LF→QA→QB phase connections and also LF phase→QB
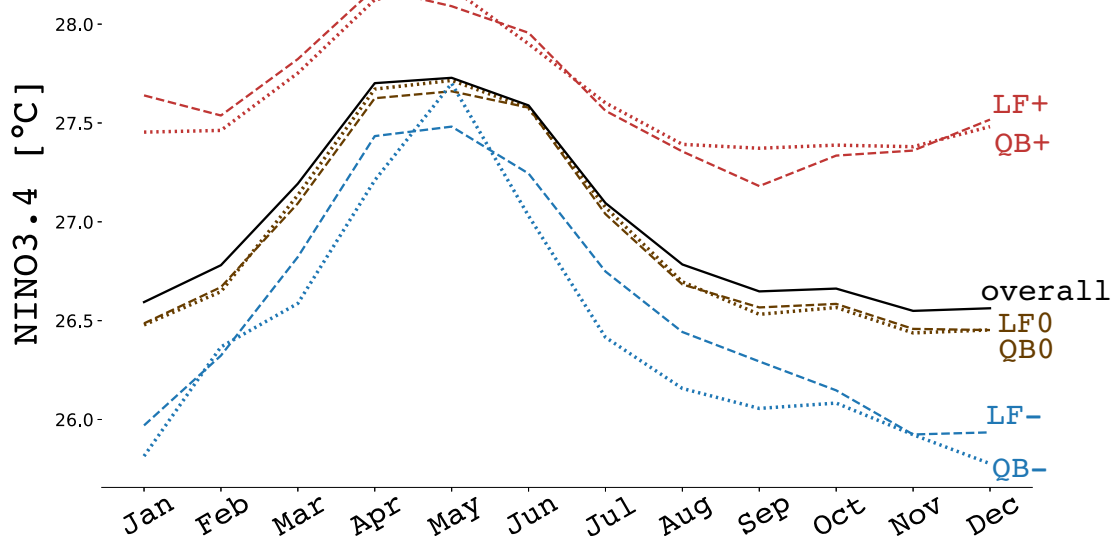
Fig. 5.8. | Annual cycle composites of Niño 3.4 index associated with different phases of QB variability with central periods between 18 and 30 months. Also shown are annual cycle composites associated with different phases of LF variability.
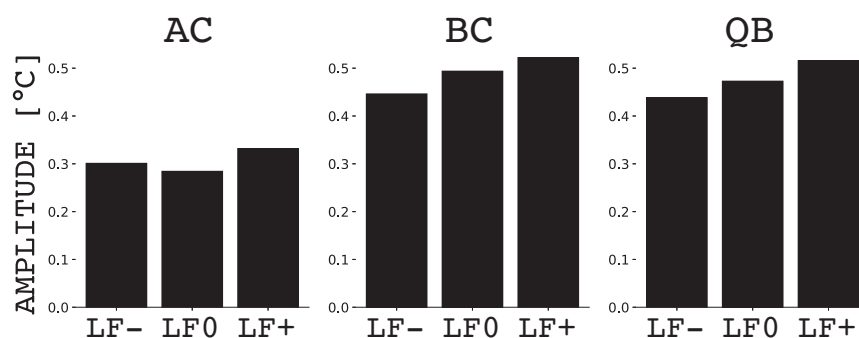

Fig. 5.9. | The amplitudes of AC, BC, and QB cycles conditioned on the phase of LF ENSO mode. AC, BC and QB stand for wavelet reconstructed time series associated with annual cycle anomalies, biennial cycle, and quasi-biennial variability with central periods between 18 and 30 months, respectively. The climatological annual cycle was subtracted from the raw Niño 3.4 data prior to the wavelet analysis.

amplitude connections (since synchronisation of phases of different QB modes should automatically result in a large-amplitude event). By contrast, during a moderate El Niño of 87/88, the LF, QB and QA modes exhibited phase shifts, with lower-frequency modes leading the higher-frequency modes (in particular a suite of QB modes) instead of being "stacked" on top of one another, thus limiting the magnitude of this event. Notably, strong La Niña events do not seem to be associated with the minimum of the LF mode but instead, occur during near-neutral LF conditions when the minima of the QA modes and the minima of the whole range of QB modes synchronise. Thus, in both El Niño and La Niña cases, the behaviour of the QB modes has a vital control on the magnitude of the ENSO events.
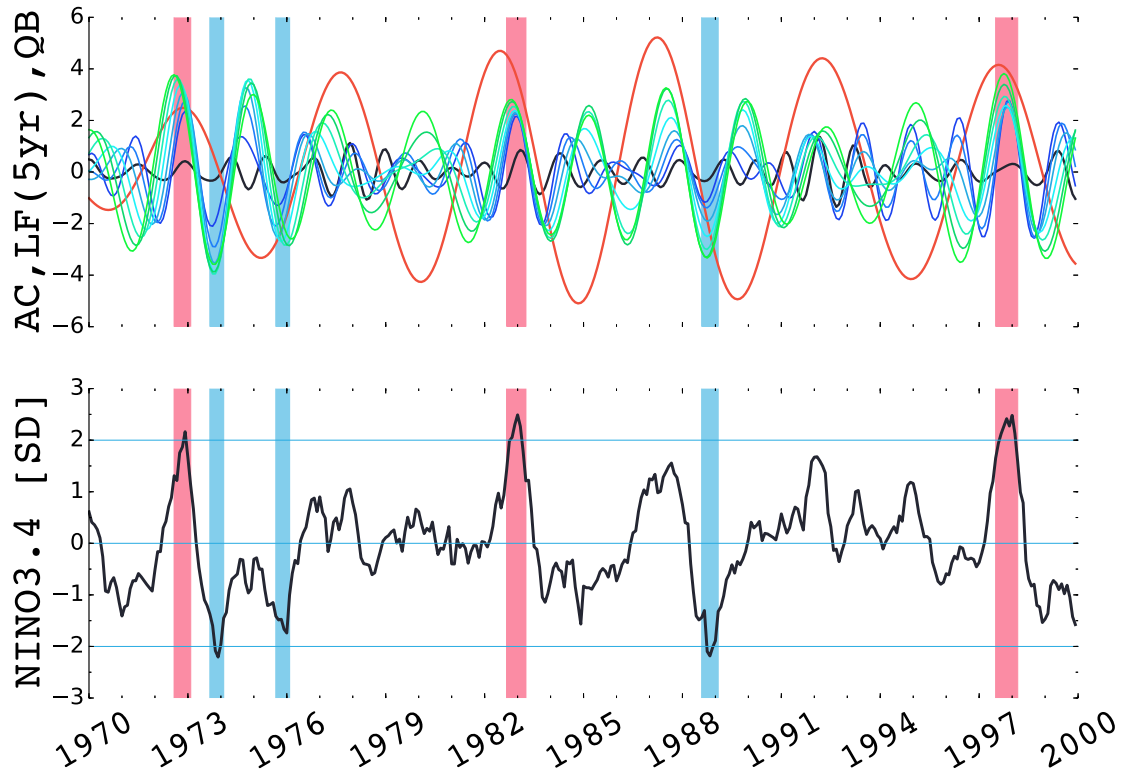
Fig. 5.10. | (top) Wavelet reconstructions of the observed Niño 3.4 index (1970 – 1999): reconstruction of the annual cycle (AC; in black), quasi-biennial cycle (QB, for a range of periods from 18 to 30 months, with 2 months step; shades of blue to green), and low-frequency cycle (LF, 5 year period; in red) of ENSO. All of these reconstructions were computed via continuous complex wavelet transform (CCWT) as $A_p(t) \cos \phi_p(t)$, for the corresponding central wavelet periods p. (bottom) The full observed normalised Niño 3.4 index. The years of strong El Niño and La Niña events are marked with the red and blue shading, respectively.

5.4 Causal relationships in ENSO models

Apart from seeking cross-scale interactions in the observed Niño 3.4 time series, we also sought these interactions in synthetic time series obtained from a variety of models. In particular, we were interested in seeking the interaction in a conceptual, low-dimensional dynamical model due to *Stein et al. [2014]* — the parametric recharge oscillator, then in the empirical stochastic model of Pacific sea surface temperatures due to *Kondrashov et al. [2005]*, and finally in the ENSO representations (the Niño 3.4 spatial average) within the Coupled Model Intercomparison Project Phase 5 (the famous CMIP5 framework) *[Taylor et al., 2012]*.

We sought the cross-scale interactions in the low-dimensional conceptual models for a slightly different reason than in the GCMs of CMIP5. If the interactions would be present in the low-dimensional conceptual models, that would mean that a physical mechanism present and conceptualised by the model, is (at least in part) responsible for the particular interaction. This would point us towards the mechanistic interpretation

of described interactions. On the other hand, seeking cross-scale interactions in the CMIP5 models had the purpose of validating the dynamical representation of ENSO in the COAGCMs. If any discrepancies should arise, understanding them would possibly be the key to an improved ENSO prediction.

5.4.1 Conceptual models

The first model of our interested was the parametric recharge oscillator (PRO) *[Stein et al., 2014]* which is based on the recharge oscillator *[Jin, 1997a,b]* mentioned earlier. The parametric part is due to seasonally varying coefficients *[Stein et al., 2010]*, taking the form of a stochastic parametric oscillator

$$\frac{\mathrm{d}T}{\mathrm{d}t} = -\lambda(t)T + \omega(t)H + \xi(t) \tag{5.7}$$

$$\frac{\mathrm{d}H}{\mathrm{d}t} = -RT, \tag{5.8}$$

where T represents eastern equatorial Pacific SST anomalies, H represents the zonal mean equatorial Pacific thermocline depth anomalies, $\lambda(t)$ and $\omega(t)$ are the seasonally varying growth rate and angular frequency parameters of the oscillator, the constant R relates to the time scale of the geostrophic adjustment of the thermocline to wind stress anomalies, and $\xi(t)$ is Gaussian white noise representing the forcing by the atmosphere. The parameters λ and ω can be derived from a statistical-dynamical estimation of the linearised upper ocean heat budget based on the Bjerknes index *[Jin et al., 2006]*, and model runs utilising the estimated growth parameter reproduce the observed seasonal cycle of ENSO variance *[Stein et al., 2010]*.

Modulation of the angular frequency parameter (ω) was shown to have little effect on the seasonal variance of ENSO *[Stein et al., 2010]*, hence the model is further reduced to

$$\frac{\mathrm{d}T}{\mathrm{d}t} = -\lambda(t)T + \omega_e H + \xi(t) \tag{5.9}$$

$$\frac{\mathrm{d}H}{\mathrm{d}t} = -\omega_e T, \tag{5.10}$$

where $\omega_e = \sqrt{\omega R}$. The eqns. (5.9) and (5.10) constitute the PRO model of ENSO.

Following *Stein et al. [2014]*, we used two traits of the parametric recharge oscillator: *neutral* model, which is purely deterministic with $\xi(t) = 0$ and $\lambda(t) = \lambda_0 \cos(\omega_a t)$ (ω_a being the annual frequency) in eqn. 5.9 and *damped* model with the non-zero damping parameter ($\lambda(t) = \bar{\lambda} + \epsilon \cos(\omega_a t)$ with $\bar{\lambda}$ being the mean damping rate based on statistical-dynamical fit of the PRO model to output from a high-resolution GCM reanalysis *[Stein et al., 2010]*) and Gaussian white noise $\xi(t)$ driving present in eqn. (5.9).

In the neutral case, the system exhibits both the phase synchronisation and phase-phase causality over a broad range of scales as shown in Fig. 5.11. The parametric recharge oscillator is not a multi-scale process; in fact, it contains one oscillation (ENSO) mode and a periodically changing parameter (the annual cycle). These two modes interact and create the combination tones. The main (ENSO) mode is quasi-periodic,

PRO neutral
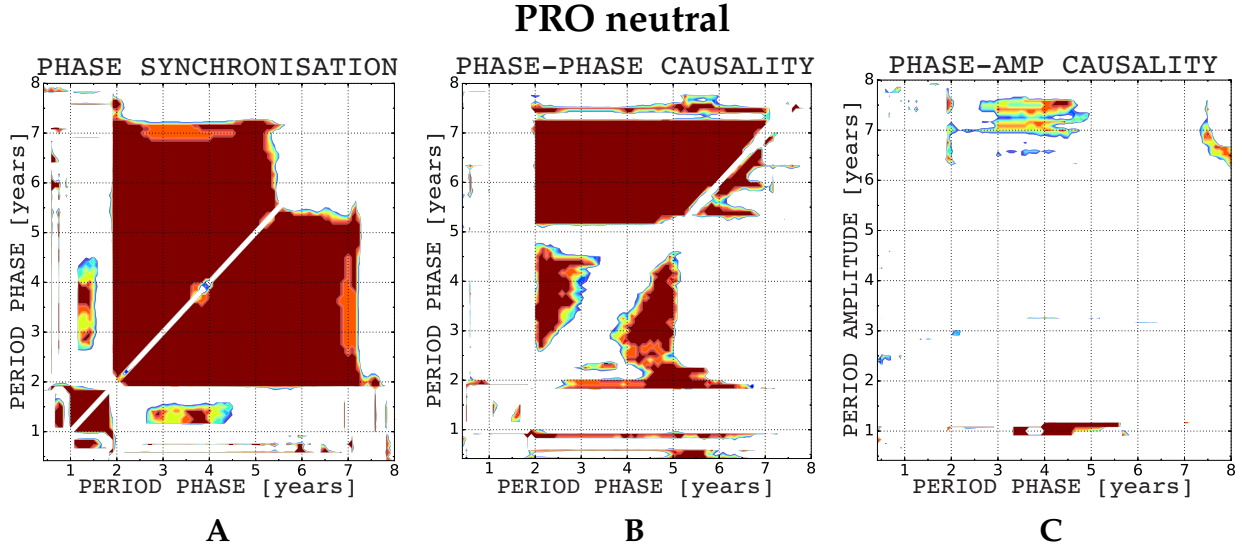
Fig. 5.11. | Same as Fig. 5.5, but for synthetic Niño 3.4 time series simulated by neutral PRO model.

appearing in the wavelet spectrum as a broadband peak. Since all the oscillatory modes are driven by the main PRO mode, all of them are coherent and provide a picture of mutually phase-synchronised modes over a wide range of periods, while the observed LF→QB phase-amplitude causality is lacking completely, as depicted in Fig. 5.11.

For the damped PRO model, the presence of noise destroys the synchronisation and causality phenomena observed in the deterministic neutral model. The corresponding results are presented in Fig. 5.12 in the form of aggregated thresholded binary maps. The colour shading in these plots shows the number of realizations (out of 20) in which the respective synchronisation/causality relationship was significant. The interactions depicted in Fig. 5.12 exhibit huge variance from one model realisation to another and no significant interactions seem to be systematically present. We thus conclude that the low-order damped PRO model is unable to simulate synchronisation and causality phenomena robustly, as significant interactions identified in each realisation are driven by the noise sampling, rather than by any underlying low-order dynamics.

The second conceptual model of our interest was an empirical model based on the idea of linear inverse modelling (LIM) *[Penland, 1989]*. We built the inverse stochastic model following the empirical model reduction (EMR) methodology introduced by *Kondrashov et al. [2005]*.

As a starting point in developing the ENSO model hierarchy, *Kondrashov et al. [2005]* used a concept of inverse stochastic models. Let us denote the climate-state vector by $\mathbf{X}$, its temporal means by $\bar{\mathbf{X}}$, and $\mathbf{x} = \mathbf{X} - \bar{\mathbf{X}}$ the vector of anomalies, then the evolution of $\mathbf{x}$ can be expressed as

$$\dot{\mathbf{x}} = \mathbf{L}\mathbf{x} + \mathbf{N}(\mathbf{x}), \tag{5.11}$$

where the dot denotes a time derivative, $\mathbf{L}$ is a linear operator, and $\mathbf{N}$ represents nonlinear terms; both $\mathbf{L}$ and $\mathbf{N}$ may be a function of $\bar{\mathbf{X}}$, but this dependence is not taken into account here.

The simplest type of inverse model is the linear stochastic model *[Penland, 1989, 1996]*,

PRO damped
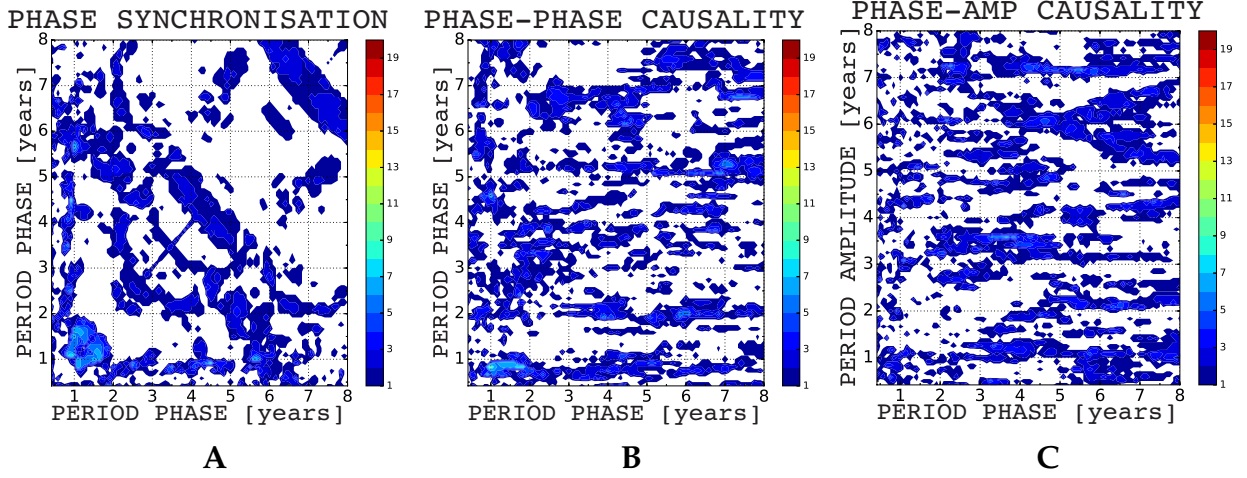
FIG. 5.12. | Same as Fig. 5.5, but for synthetic Niño 3.4 time series simulated by damped PRO model. Shown in each panel are aggregates (sums) of thresholded binary maps over 20 realisations of this model.

which is obtained by assuming, in eqn. (5.11), that $\mathbf{N(x)}dt \approx \mathbf{Tx}dt + d\mathbf{r}^{(0)}$, where $\mathbf{T}$ is the matrix describing linear feedbacks of unresolved processes on $\mathbf{x}$, and $\mathbf{r}^{(0)}$ is a white-noise process that can be spatially correlated. Considering this assumption eq. (5.11) becomes

$$d\mathbf{x} = \mathbf{B}^{(0)}\mathbf{x}dt + d\mathbf{r}^{(0)}, \quad \mathbf{B}^{(0)} = \mathbf{L} + \mathbf{T}. \tag{5.12}$$

The matrix $\mathbf{B}^{(0)}$ and the covariance matrix of the noise process $\mathbf{Q} \equiv \langle \mathbf{r}^{(0)}\mathbf{r}^{(0)\mathrm{T}} \rangle$ can be directly estimated from the observed statistics of $\mathbf{x}$ by multiple linear regression *[Wetherill, 1987]*. *Penland and Sardeshmukh [1995]; Johnson et al. [2000a,b]* have shown some success in predicting ENSO variability. This type of models are usually constructed in a phase space of the system's leading empirical orthogonal functions (EOFs), hence the state vector, $\mathbf{x}$, or predictor-variable vector, consists of amplitudes of the corresponding principal components (PCs), while the vector of response variables contains their tendencies $\dot{\mathbf{x}}$.

Kondrashov et al. [2005] noted that the assumptions of linear, stable dynamics, and of additive white noise used to construct LIMs are only valid to a certain degree of approximation. In particular, the stochastic forcing $\mathbf{r}^{(0)}$ in eqn. (5.12) typically involves serial correlations, thus is not white in a temporal sense. First major modification due to *Kondrashov et al. [2005]*, based on previous results and methodology of *Kravtsov et al. [2005]*, is assuming a polynomial, rather than a linear form of $\mathbf{N(x)}$ in eqn. (5.11), in particular, a quadratic dependence. The ith component $N_i(\mathbf{x})$ of $\mathbf{N}$ is then written as

$$N_i(\mathbf{x})dt \approx \left(\mathbf{x}^{\mathrm{T}}\mathbf{A}_i\mathbf{x} + \mathbf{t}_i\mathbf{x} + c_i^{(0)} \right) dt + dr_i^{(0)}. \tag{5.13}$$

The matrices $\mathbf{A}_i$ represents blocks of a third-order tensor, while the vectors $\mathbf{b}_i^{(0)} = \mathbf{l}_i + \mathbf{t}_i$ are the rows of the matrix $\mathbf{B}^{(0)} = \mathbf{L} + \mathbf{T}$ (compare with eqn. (5.12)). These objects, as well as the components of the vector $\mathbf{c}^{(0)}$, are estimated here by multiple polynomial regression *[McCullagh and Nelder, 1989]*.

The final quadratic model, *Kondrashov et al. [2005]* used, reads

$$dx_i = \left(\mathbf{x}^T \mathbf{A}_i \mathbf{x} + \mathbf{b}_i^{(0)} \mathbf{x} + c_i^{(0)}\right) dt + dr_i^{(0)}; \quad i = 1, \ldots, D \tag{5.14}$$

where $\mathbf{x} = \{x_i\}$ is the state vector of dimension D. However, the stochastic forcing $\mathbf{r}^{(0)}$ in eqn. (5.14) typically involves serial correlations (as noted earlier) and might also depend on the modelled process $\mathbf{x}$. To address the issue, *Kondrashov et al. [2005]* included an additional model level to express the known time increments $d\mathbf{r}^{(0)}$ as a linear function of an extended space vector $[\mathbf{x}, \mathbf{r}^{(0)}] \equiv \left(\mathbf{x}^T, \mathbf{r}^{(0)T}\right)^T$. More levels could be added in the same way, until the L^{th}level's residual $\mathbf{r}^{(L+1)}$ becomes white in time, and its lag-0 correlation matrix converges to a constant matrix, therefore the multi-level model is written as

$$\begin{aligned}
dx_i &= \left(\mathbf{x}^T \mathbf{A}_i \mathbf{x} + \mathbf{b}_i^{(0)} \mathbf{x} + c_i^{(0)}\right) dt + r_i^{(0)} dt, \tag{5.15} \\
dr_i^{(0)} &= \mathbf{b}_i^{(1)}[\mathbf{x}, \mathbf{r}^{(0)}] dt + r_i^{(1)} dt, \tag{5.16} \\
dr_i^{(1)} &= \mathbf{b}_i^{(2)}[\mathbf{x}, \mathbf{r}^{(0)}, \mathbf{r}^{(1)}] dt + r_i^{(2)} dt, \tag{5.17} \\
&\vdots \\
dr_i^{(L)} &= \mathbf{b}_i^{(L)}[\mathbf{x}, \mathbf{r}^{(0)}, \ldots, \mathbf{r}^{(L)}] dt + dr_i^{(L+1)}; \tag{5.18} \\
i &= 1, \ldots, D.
\end{aligned}$$

These equations describe a wide class of processes in a fashion that explicitly accounts for the modelled process $\mathbf{x}$ feeding back on noise statistics: the vectors $\mathbf{b}_i^{(l)}$ are the rows of matrices $\mathbf{B}^{(l)}$ that represent this "eddy feedback". The multi-level linear model is obtained by setting, in eqn. (5.15), $\mathbf{A}_i \equiv 0$ and $\mathbf{c}^{(0)} \equiv 0$. Further details for the particular ENSO model appear in *Kondrashov et al. [2005]*, while the general details of the methodology and discussion can be found in *Kravtsov et al. [2005]*.

As a final contribution to the model was to include the seasonal dependence in the dynamical part of the first level (eqn. (5.15)), namely by assuming the matrix $\mathbf{B}^{(0)}$ and vector $\mathbf{c}^{(0)}$ to be periodic with period $T = 12$ months:

$$\begin{aligned}
\mathbf{B}^{(0)} &= \mathbf{B}_0 + \mathbf{B}_s \sin(2\pi t/T) + \mathbf{B}_c \cos(2\pi t/T) \tag{5.19} \\
\mathbf{c}^{(0)} &= \mathbf{c}_0 + \mathbf{c}_s \sin(2\pi t/T) + \mathbf{c}_c \cos(2\pi t/T). \tag{5.20}
\end{aligned}$$

This was done in order to account for seasonal variations in the mean state of the linear, dynamical, stochastically forced model, since *Thompson and Battisti [2000, 2001]* demonstrated that this helps to qualitatively reproduce the observed seasonal patterns of variance and lagged autocovariance in tropical Pacific SSTs.

In this work, we trained the linear model (hence set $\mathbf{A}_i \equiv 0$ and $\mathbf{c}^{(0)} \equiv 0$) three level ($L = 3$) model using the monthly ERSSTv.4 dataset *[Huang et al., 2015]* in the phase space of leading 20 EOFs of SST($30°S - 60°N$) and used it to obtain multiple independent synthetic ENSO time series of the same simulation length as the observational data record. We also tried to use the quadratic model (results not shown here), but the results with the linear model were more satisfactory, hence in the further research, we opted to use the linear model only.

statistical EMR

PHASE SYNCHRONISATION   **PHASE–PHASE CAUSALITY**   **PHASE–AMP CAUSALITY**

A   **B**   **C**
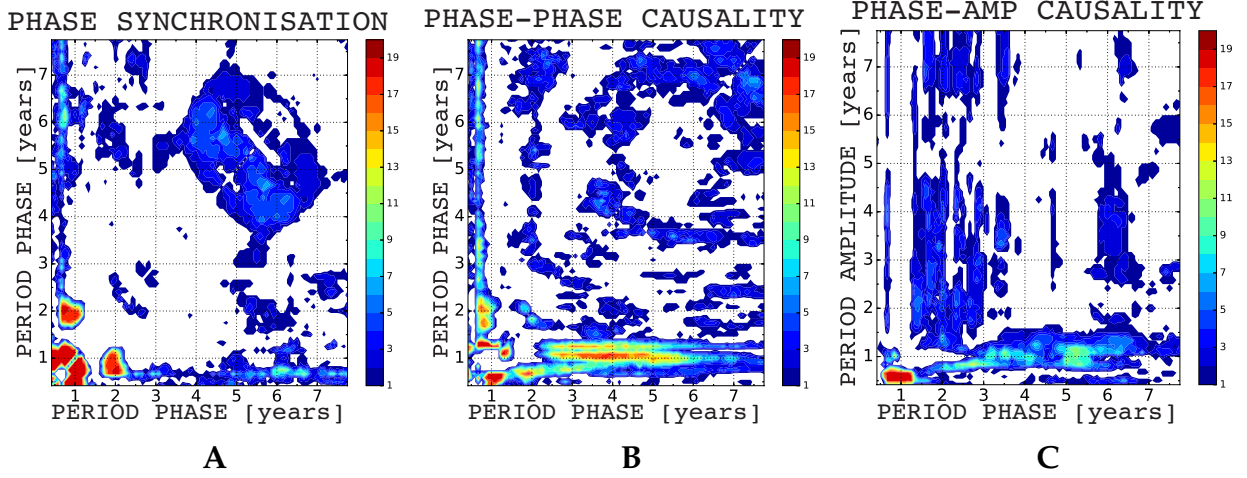
Fig. 5.13. | Same as Fig. 5.5, but for synthetic Niño 3.4 time series simulated by the empirical stochastic three level EMR. Shown in each panel are aggregates (sums) of thresholded binary maps over 20 realisations of this model.

At the simulation stage, we used three different schemes for modelling stochastic forcing $r_i^{(3)}$, all of which where based on random sampling from the library of the "observed" third-level residual forcing arising from the model construction (regression) procedure. In the first scheme, the forcing was randomly sampled from the library of the observed residuals, and did not depend on the simulated state of the model, corresponding to the classical LIM model. The second scheme chose the model forcing using the entry in the observed residual library that corresponded to the month on which the observed ENSO state was the closest to the current simulated ENSO state; note that the random forcing so computed depends on the state of the system, and thus represents the so-called multiplicative noise. The third forcing scheme was similar to scheme 2, but used 5-month-long snippets from the observed forcing library instead of the single state *[Chekroun et al., 2011]*.

The results for the EMR model driven by multiplicative noise snippets are shown in Fig. 5.13 in the form of aggregated plots, which are analogous to those for the damped PRO model (Fig. 5.12) .

Unlike the low-order dynamical PRO model, the empirical stochastic model is clearly able to simulate synchronisation phenomena, in which QB mode is synchronised with the AC and that the AC is phase synchronised with the combination tones. The same synchronisation behaviour was observed in the observational data (recall Fig. 5.5). The majority (though not all) of the empirical model realisations were also able to correctly simulate the observed phase-phase causal relationships, with directional connection from LF mode to the AC modes, as well as from the AC modes to the modes in the QB range (compare the B panels of Fig. 5.5 and Fig. 5.13). However, only a few realisations of the empirical stochastic model could capture the observed phase-amplitude causality from the LF mode to the QB mode; hence, we conclude that the present empirical model is not able to accurately simulate this aspect of the observed phase-amplitude causal re-

phase–phase causality in EMR: various noise parametrisations
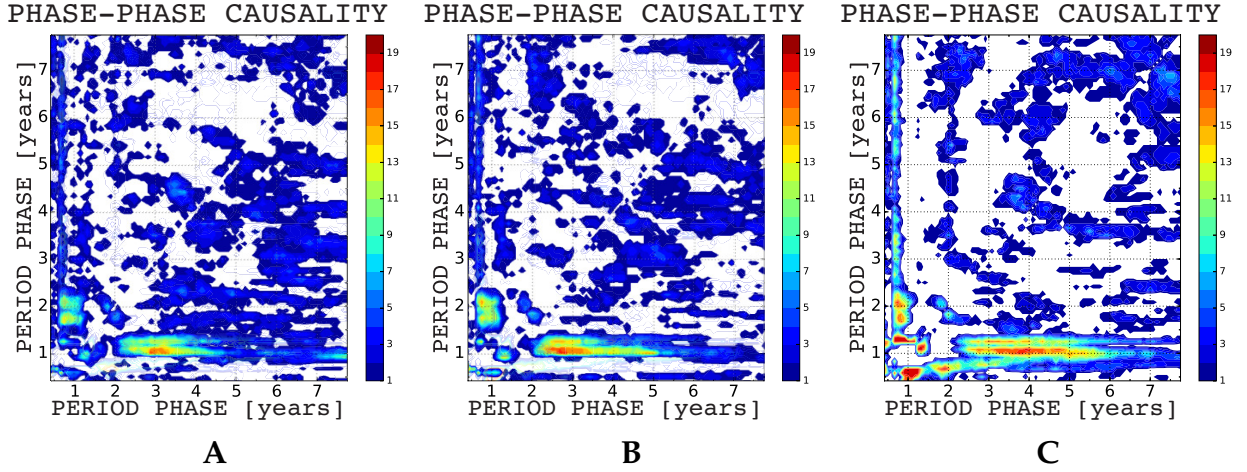
FIG. 5.14. | Phase-phase causality diagnosis in three versions of the *Kondrashov et al. [2005]* three-level empirical (EMR) model of ENSO: (**A**) model driven by additive noise; (**B**) model driven by multiplicative noise computed as the observed residual forcing $r_i^{(3)}$ for the month in which the observed sea-surface temperature state is the closest to the current simulated state; (**C**) model driven in the same way as in (**B**), but using 5-month snippets (instead of the single monthly value at each time) from the observed forcing library (this panel is the same as panel (**B**) of Fig. 5.13).

lationships in ENSO. Further improvements may perhaps be achieved by experimenting with the empirical model formulation (changing the number of variables, a degree of nonlinearity etc.), but these experiments are beyond the scope of the present study.

Fig. 5.14 shows phase-phase causality results for the EMR model utilising three different stochastic forcing schemes (see above). Note that the LF→QA→QB causal links are present in all of the plots, but become progressively more pronounced from the scheme utilising additive noise (A), to the one with multiplicative noise (B), to, finally, the scheme using multiplicative noise snippets (C). This argues that: (i) the QB dynamics is present in the algebraic structure of the deterministic operator of the EMR model, since the model driven by the additive noise does possess these dynamics; but also that (ii) causal interactions that involve QB modes are sensitive to the structure of the state-dependent (multiplicative) noise forcing.

To conclude, the PRO dynamical model fails to reproduce any of the observed causal interactions (recall Figs. 5.11 and 5.12) whereas the statistical EMR does offer promising results, especially with regards to reproducing the observed LF→QA→QB phase causality (recall Fig. 5.13). Our analyses suggest that the QB modes in the EMR are inherently present in the algebraic structure of this model's deterministic propagator (thus are at least partially seen in the model driven by any type noise, see Fig. 5.14), but are strongly influenced by the feedbacks that involve state-dependent, multiplicative noise. On the other hand, nonlinearity in the propagator is not needed to reproduce the phase-phase causality interactions.

5.4.2 The Coupled Model Intercomparison Project Phase 5

For the purpose of validating the dynamical representation of ENSO and its cross-scale interactions, we analysed in same manner the time series of the sea surface temperature obtained from the individual runs of COAGCMs within The Coupled Model Intercomparison Project Phase 5 (CMIP5) *[Taylor et al., 2012]* framework, which aims for providing global circulation models (GCMs) outputs from various modelling groups. The Table A.2 states the models and number of their different realisations used in this thesis. All of the realisations were historical 20thcentury runs with a temporal span of 1850 − 2005.

The overview of comparison between the observed Niño 3.4 and simulated time series from CMIP5 models is visualised in Fig. 5.15. To start with, we measured the similarity between the observed and simulated wavelet spectra *[Torrence and Compo, 1998]* using root-mean-square distance and Pearson's correlation coefficient, with zero distance and unit correlation coefficient indicating the perfect match. The ensemble-mean values of these two measures for individual CMIP5 models are shown in the first two columns of Fig. 5.15. The models exhibit great variations in their ability to match the observed Niño 3.4 spectra, with correlation coefficients ranging from 0.2 to 0.8 and rms distances from 30 to 120; furthermore, there are also substantial sampling variations in the NINO3.4 spectra from multiple runs of a single model (not shown). This means that the ENSO tends to exhibit different epochs of sampling variability in models, in which its strength, spectrum and other properties may vary significantly *[Wittenberg, 2009]*.

Similarly to the wavelet spectra, the synchronisation and causality maps (see examples in Fig. 5.16 analogous to the observed maps of Fig. 5.5), vary considerably from model to model (Fig. 5.15, right columns), as well as between individual runs of a single model (not shown). We compared the observed and simulated maps using, once again, the standard Pearson's correlation coefficient, as well as the so-called Adjusted Rand Index (ARI), which is especially well suited to measure the similarity of clustered data *[Hubert and Arabie, 1985]*. Both measures were computed for the pairs of interaction maps (observation vs. individual simulation) filled with ones or zeros depending on whether the significant interaction between the processes of different time scales was identified or not (so the coloured areas of maps in Figs. 5.5 and 5.16 would be filled with ones and white areas — with zeros); hereafter, we will call the maps so constructed the thresholded binary maps.

The above similarity measures averaged over the ensembles of individual model simulations (Fig. 5.15, right columns) are in fact fairly low. For phase synchronisation, the highest similarity was detected in the *CanESM2* model, at the 0.24 level. The phase synchronisation map for the best run of the *CanESM2* model (Fig. 5.16, A) indicates synchronisation between the processes with the same time scales as in the observed data (Fig. 5.5, A), that is, between the LF, QB and AC/CT modes. This, however, is more of an exception than a rule, as the time scales of significant phase synchronisation in most of the runs do not match the observed time scales.

The similarity levels between phase-phase causality maps from observations and model simulations are about the same as for phase synchronisation maps, with the maximum ensemble-mean correlation of 0.23 obtained for the *CCSM4* model. The causality map for the best run of this model (Fig. 5.16, B) is correlated with the observed
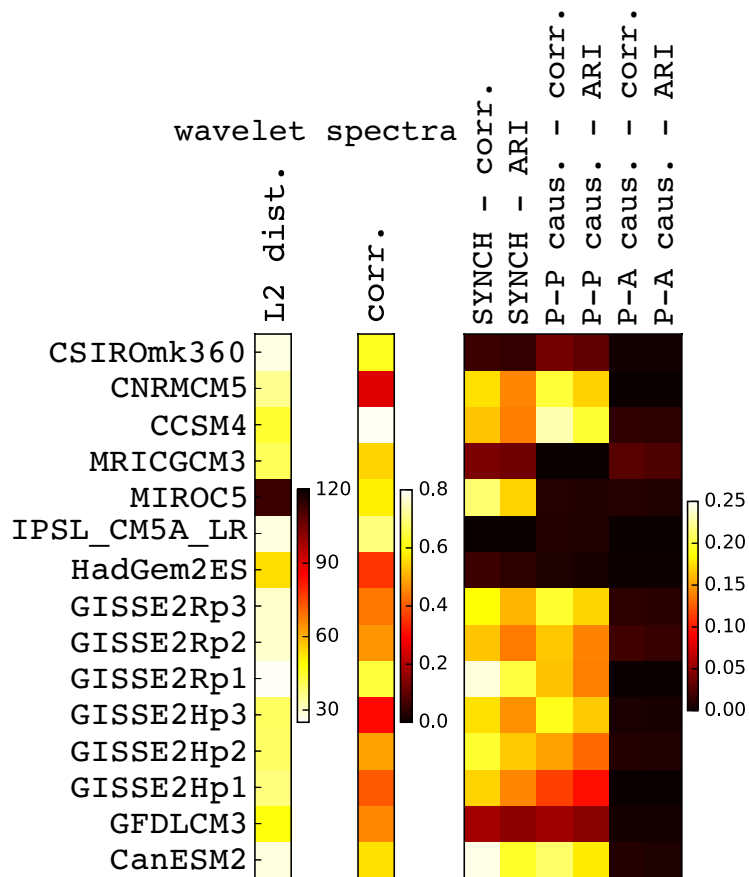
FIG. 5.15. | Measures of similarity between various characteristics of the observed and CMIP5 simulated Niño 3.4 time series. Shown are ensemble averages of these characteristics over multiple runs of individual models (see the model acronyms on the left). The first two columns compare the observed and simulated wavelet spectra, using the root-mean-square (rms) distance (labelled as L2 dist.) and Pearson's correlation (corr.), both computed in the frequency space. Next three pairs of columns display measures of similarity between the observed and simulated interaction maps analogous to the observed maps of Fig. 5.5, namely the phase synchronisation, phase-phase causality, and phase-amplitude causality maps. Each pair presents two distinct similarity measures: the Pearson's correlation (corr) in the phase space of the corresponding map, as well as the Adjusted Rand Index (ARI; see text).

map (Fig. 5.5, B) at the 0.41 level, and captures correctly the observed LF – QA, LF – QA and QA – QB connections. Note that the best matches to the observed maps in terms of phase synchronisation and phase-phase causality come from individual simulations of different models, meaning that neither model run was able to capture the entirety of the observed interactions. Finally, no model was able to capture the observed phase-amplitude causal connection between the LF and QB modes (Fig. 5.5, C). The highest ensemble-mean correlation between the observed and simulated maps is only 0.03 (*MRI-CGCM3*), with the highest correlation of 0.1 for one of the *CSIRO–mk360* simulations (the corresponding causality map is shown in Fig. 5.16, C). The phase synchronisation and

best CMIP5 individual runs
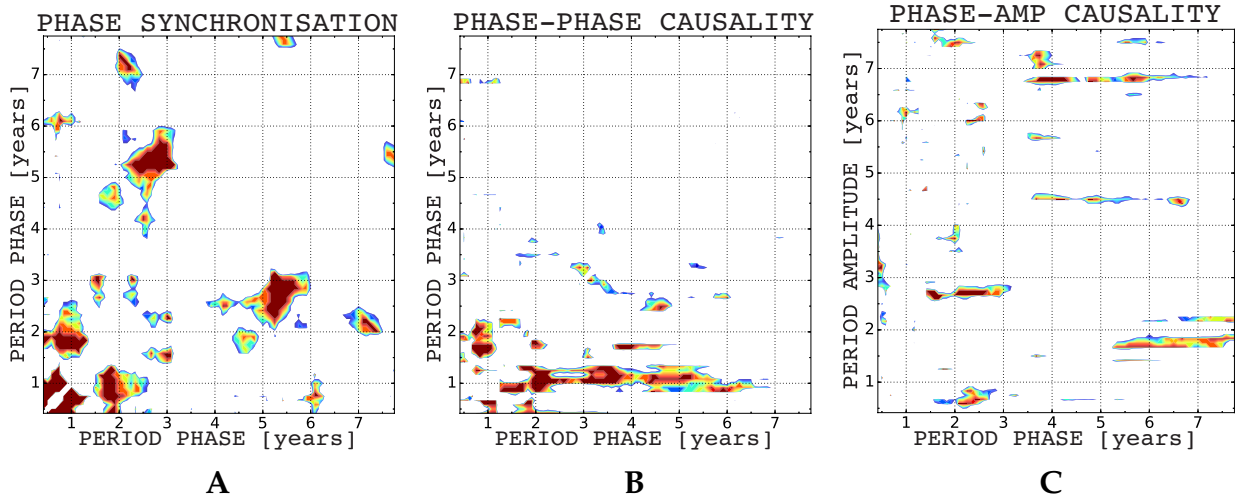
Fɪɢ. 5.16. | The same as in Fig. 5.5, but for the individual simulations of CMIP5 models that best match the observed structures: (**A**) phase synchronization in *CanESM2* model; (**B**) phase-phase causality in *CCSM4* model; and (**C**) phase-amplitude causality in *CSIRO–mk360* model.

phase-phase causality maps for the latter run are, however, inferior to those from other models in terms of their similarity to the observed maps (not shown).

To summarise, the CMIP5 models exhibit great sampling variations in the simulated ENSO characteristics. Some of the simulations do exhibit certain aspects of interactions between the processes of different time scales which match the observed interactions. However, no single simulation is able to reproduce the entire sequence of causal connections inferred from the observed data. Additional information concerning the CMIP5 modelled data are presented in the appendix (sec. A.3.1). In particular, Table A.2 states the models and number of respective realisations used in this study, and Table A.3 states the values of similarity measures for individual runs — the ensemble means are depicted in Fig. 5.15.

5.5 Robustness analysis

In order to assess the robustness of our results, we estimated the (conditional) mutual information using equiquantal binning method (using 4 bins) and compared the results to the *k*-nearest neighbours estimate (*k* = 64); see sec. 3.4.4, *Hlaváčková-Schindler et al. [2007]*, and references therein for a comprehensive review of (conditional) mutual information estimators and their caveats. Both estimates underwent the statistical significance testing using 500 Fourier transform surrogates and were computed using the Niño 3.4 index data for a full available period 1870 – 2016. The conditional mutual information, which reflects phase-phase causality, was averaged over forward time lags 1 – 30 months, $\tau = 1, \ldots, 30$ *[Paluš and Vejmelka, 2007]*.

As can be seen from the robustness analysis result in Fig. 5.17, both estimates provide

equiquantal estimate

A

B

k-nearest neighbours estimate

C

D
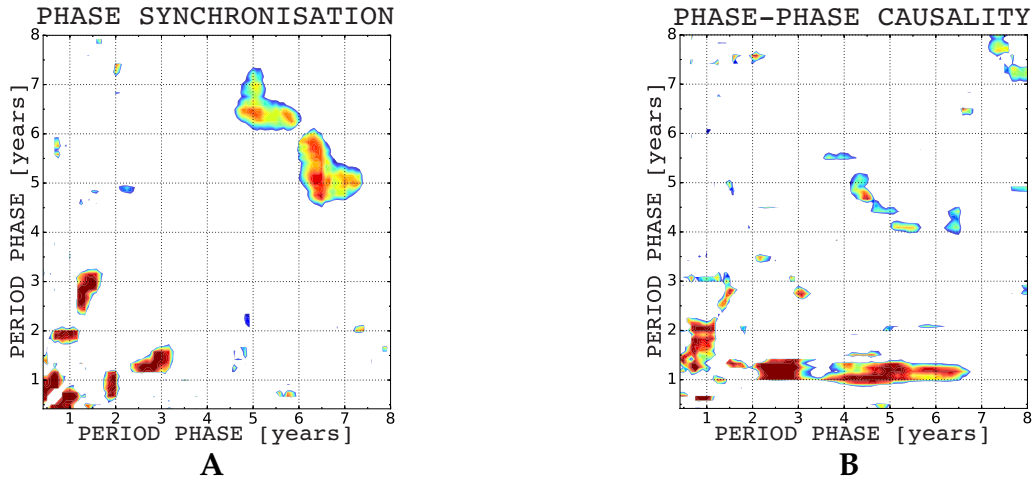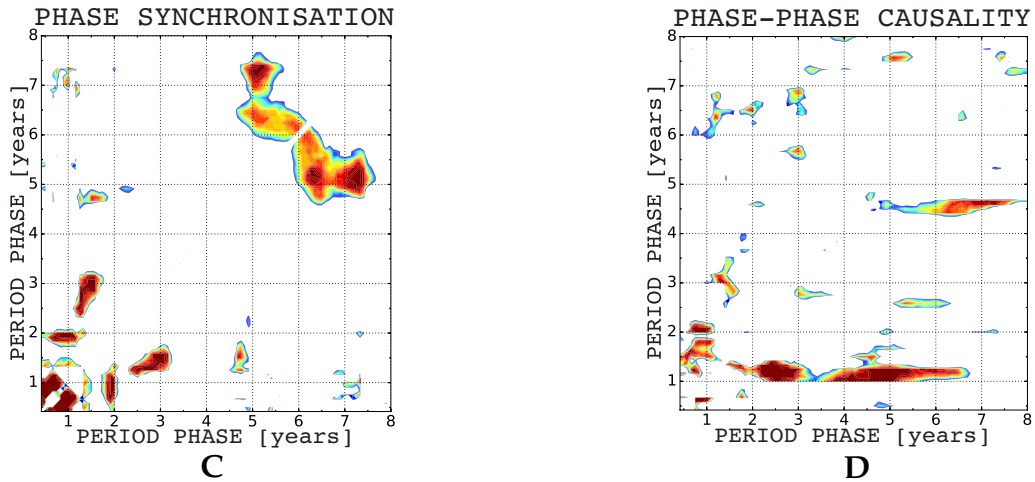
Fɪɢ. 5.17. | (**A** and **C**) Cross-scale phase synchronization and (**B** and **D**) phase-phase causality in the observed Niño 3.4 time series for a full period 1870 – 2016. Shown are (positive) significance-level deviations from the 95thpercentile of the (**A** and **B**) equiquantal binning estimates and (**C** and **D**) of the *k*-nearest neighbours estimates of (conditional) mutual information, tested using 500 Fourier transform surrogates.

the same picture with only small deviations, which we consider to be statistical fluctuations. Cross-scale interactions, which are of main interest here, are virtually the same — we can clearly identify the phase synchronisation between the annual cycle (AC) and quasi-biennial (QB; periods of 1.8 – 2.1 yr) mode and between the AC and combination tones (CT; periods approximately 9 and 14 months). As for the phase-phase causality, one could distinctly detect the low-frequency (LF; periods 4 – 6 yr) phase driving the AC phase and that the phase of QB is partially slaved to the phase of AC.

For the second phase of robustness analysis, we divided the full Niño 3.4 data period into two equally long periods, namely 1870 – 1943 and 1943 – 2016 periods, and estimated

1st half: 1870 – 1943

PHASE SYNCHRONISATION

PHASE–PHASE CAUSALITY

A

B

2nd half: 1943 – 2016

PHASE SYNCHRONISATION

PHASE–PHASE CAUSALITY

C

D
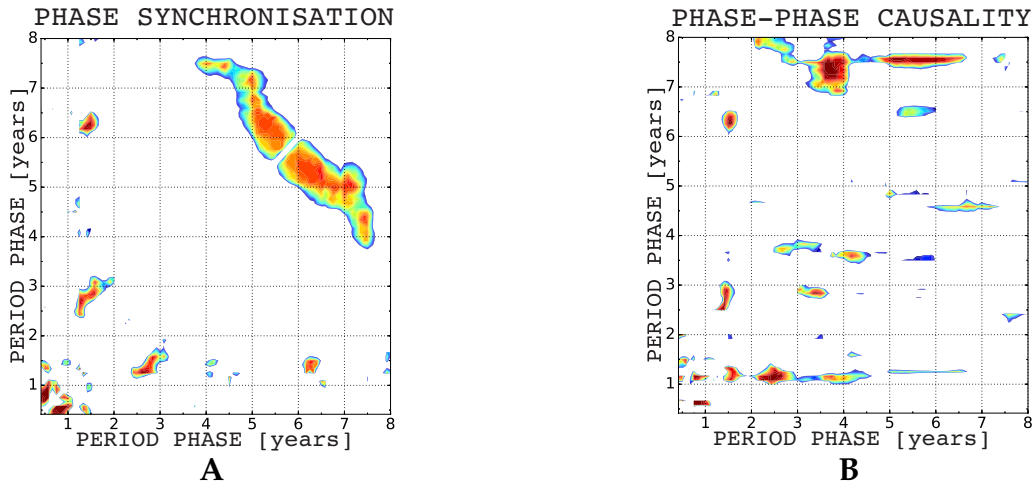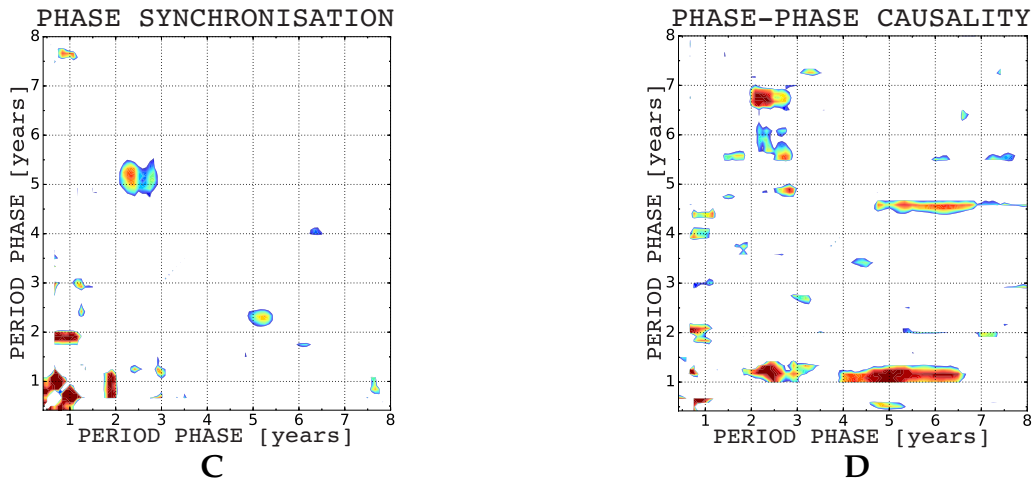
Fɪɢ. 5.18. | (**A** and **C**) Cross-scale phase synchronization and (**B** and **D**) phase-phase causality in the observed Niño 3.4 time series for (**A** and **B**) the first half of the full period 1870 – 1943 and (**C** and **D**) the second half of the full period 1943 – 2016. Shown are (positive) significance-level deviations from the 95th percentile of the k-nearest neighbours estimates of (conditional) mutual information, tested using 500 Fourier transform surrogates.

the phase synchronisation and phase-phase causality for each of these periods separately. The causality estimates from the two different periods exhibit substantial differences (Fig. 5.18), which can either be due to the true change in ENSO dynamics between the two periods or due to the less robust estimation of the mutual information for a shorter time series. The wavelet power spectra of the Niño 3.4 time series computed for the full (1870 – 2016) period, as well as for the 1870 – 1943 and 1943 – 2016 sub-periods (Fig. 5.19) suggest that the former possibility is more likely. Indeed, the ENSO variability in the second part of the record (1943 – 2016) exhibited more power at QB periods compared

with the first part of the record (1870 – 1943); thus the phase synchronisation between AC and QB modes was more pronounced during 1943 – 2016 compared to 1870 – 1943, consistent with Fig. 5.18.
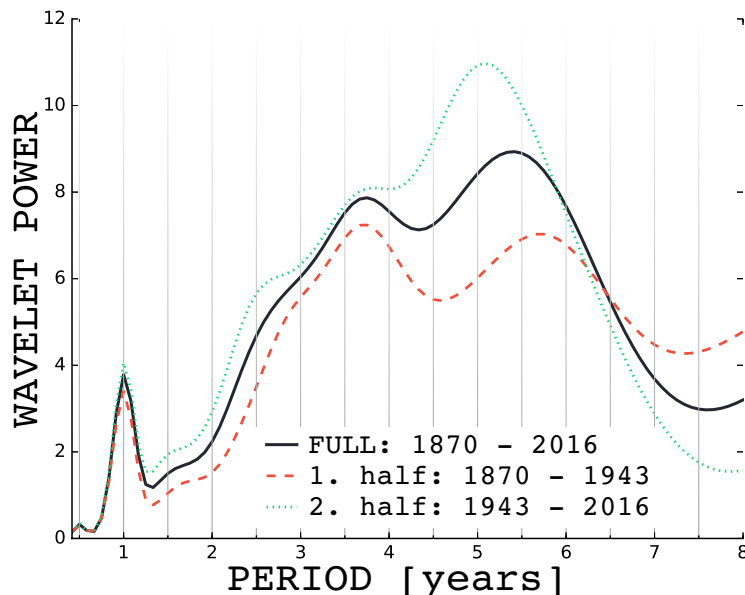
FIG. 5.19. | Power spectra of Niño 3.4 SSTs, as a function of period. These three spectra are computed by time-averaging the spectral power from the wavelet analysis using the Morlet mother wavelet *[Torrence and Compo, 1998]*. Spectrum for the full period of 1870 – 2016 in solid black, and dashed red and dotted green for the first (1870 – 1943) and second (1943 – 2016) halves of the data, respectively.

Note that neither of the three Niño 3.4 spectra shown here exhibits an enhanced power at QB frequencies. However, the QB component of ENSO variability can be detected via advanced spectral methods, such as the Singular Spectrum Analysis *[Jiang et al., 1995]*. The low relative power of QB modes is due to the fact that these modes are only intermittently active. Despite that, our analysis suggests that the QB modes are central to, and in a sense define ENSO variability, and ENSO events occur when a wide suite of these QB modes synchronise. The QA and LF modes serve as the pacemakers of ENSO events, through the direct and indirect causal connections established previously (Figs. 5.5 through 5.10). Similarly, the LF ENSO variability (periods of 4 – 6 yr) was also more pronounced in the second part of the record, leading to a more distinct detection of LF phase→AC phase causality during that period (Fig. 5.18). This apparent change in ENSO dynamics is in agreement with the studies which indicate that ENSO behaviour can exhibit multidecadal epochs characterised by pronounced differences in diverse ENSO characteristics, but what causes ENSO to change and whether these changes are stochastically or dynamically driven are still unresolved questions in the community *[Wittenberg, 2009; Vecchi and Wittenberg, 2010; Li et al., 2011; McGregor et al., 2013]*.

On the other hand, the observed phase-phase causality, where the AC partially drives the variability in the QB range as seen in the estimates of the conditional mutual information for the whole period (see Fig. 5.17) was not be found to be statistically significant

in neither of the half-period estimates, perhaps with a slight hint to this behaviour in the second part of the record. (Fig. 5.18). This is most likely to be attributed to the insufficient length of the analysed time series. It is well known that the sensitivity of detection of the causal relationships strongly depends on the length of the time series, as well as on the dimensionality of the joint probability distribution *[Paluš and Vejmelka, 2007; Vejmelka and Paluš, 2008]*. When we halved the time series of Niño 3.4 for robustness analysis, the number of monthly observations with each half dropped accordingly (from approximately 1700 to 850 data points), leading to a larger uncertainty of higher-dimensional probability distribution estimation and the ensuing loss of statistical significance.

5.6 Discussion & Outlook

The tools of information theory, used throughout this thesis, enabled us to uncover an intricate network of interactions underlying the observed ENSO variability. In particular, we showed that the (phase of) low-frequency (LF), interannual ENSO mode directly affects the amplitude of QB variability. It also indirectly affects the phase of QB variability, via the intermediate causal connection with the phase of the annual cycle (AC) and its combination tones (CT) associated with the LF mode *[Stuecker et al., 2015]*. The AC/CT modes combined constitute the quasi-annual (QA) variability (changes in the shape of the annual cycle). The above LF→QA→QB phase interactions and LF phase→QB amplitude interactions result in intermittent synchronizations among different QB modes that occur preferentially during certain phases of the LF mode, thus leading to extreme (biennial) ENSO events (Fig. 5.10). This allows multiple QB modes, which are normally desynchronised and are thus associated with small overall energy, to occasionally produce a signal with the amplitude exceeding those of QA and LF cycles. One of the key messages from our work is to suggest a much more important role of the quasi-biennial (QB) modes in ENSO dynamics than, perhaps, thought previously.

The three important time scales — QA, QB and LF — detected by our independent analysis of ENSO interactions have been identified in previous studies as well *[Barnett, 1991; Kim, 2002; Yeo and Kim, 2014]*. Our results on synchronisation of QB and QA modes are also consistent with previous work *[Rasmusson et al., 1990; Stein et al., 2014]*. However, the novelty of our work, aside from applying an original methodology to analyse climate data, is in obtaining a new compact description of the causal interactions instrumental in ENSO dynamics. The causal connection between the phase of the LF variability and that of the QA variability — that is, changes in the shape of the annual cycle depending on the state of the LF ENSO mode — is conceptually similar to the effect of low-frequency component of North Atlantic Oscillation variability on the annual cycle of surface temperature over Europe *[Paluš et al., 2005]*. A mechanistic explanation of the QA→QB phase causality remains elusive, with possible hints from empirical modelling (see below).

The observed ENSO interactions are poorly represented in the historical simulations of CMIP5 climate models, which exhibit large sampling variations in ENSO spectra and causality maps, both from model to model and among different runs of a single model. Some of the model simulations match time scales or select causality characteristics of

the observed ENSO variability, but no single simulation is able to reproduce the full picture of the observed interactions. The ENSO variability in long pre-industrial control runs of CMIP5-type models is known to exhibit multidecadal epochs characterised by different ENSO behaviour *[Wittenberg, 2009]*. Hence, there is still a possibility that the models possess correct ENSO dynamics, but the sample of 89 20th century simulations considered here was simply not large enough to generate the ENSO epoch that would match the observed epoch. Analyses of long pre-industrial runs are in order to address this issue. However, the experiments with an empirical stochastic ENSO model of *Kondrashov et al. [2005]* suggest that the chances of reproducing the observed ENSO behaviour in ensemble simulations of the 20th century climate are much higher than the CMIP5 ensemble results. This implies that CMIP5 models do indeed misrepresent ENSO dynamics. The same conclusion holds for the conceptual parametric recharge oscillator model of *Stein et al. [2014]*, which also fails to capture the observed cross-scale causal relationships in ENSO. By contrast, the success of the empirical ENSO model in reproducing the essential phase interactions among LF, QA and QB modes allows one to address, in a mechanistic fashion, the dynamics of these interactions, with initial indications pointing to the importance of both deterministic dynamics and state-dependent (multiplicative) noise in controlling the QB variability.

Thus, neither conceptual nor state–of–the–art dynamical climate models studied here were able to mimic the structure of the observed ENSO interactions, while the empirical models considered did quite a bit better. Understanding the discrepancies between the observed interactions and the interactions simulated by the dynamical models — especially with respect to their ability to model the QB modes — may be the key to an improved ENSO prediction. Finally, the observed interactions may pose as a starting point in developing a conceptual model capturing the cross-scale information transfer in ENSO dynamics.

A large portion of this chapter (from the Synchronisation and causality in El Niño/ Southern Oscillation section onwards) will tentatively appear as an article and is currently under review *[Jajcay et al., 2018]*.

Summary & Conclusion

*The scientist only imposes two things, namely truth and sincerity,
imposes them upon himself and upon other scientists.*
  Erwin Schrödinger

A better understanding of dynamics of complex systems, such as Earth's climate or the human brain, is one of the key challenges for contemporary science and society in general. Huge amounts of experimental data that are being produced every day require new mathematical tools for their description and also new computational tools to make sense of them. This thesis aims for bridging various scientific fields, namely climate science, information theory, and complex systems analysis. Moreover, I attempted to show that such an interdisciplinary approach could indeed deliver new paradigms, concepts, and results into the climate science field.

Not a long time ago (a couple of decades at most *[Ledford, 2015]*) scientists began to describe some of the observed phenomena by the moniker complex systems. Examples of these complex systems include Earth's climate, the human brain, an ecosystem, a cell, and few argue that ultimately the universe in its entirety is also a complex system. A common property of these systems is an intrinsic difficulty to model them, sometimes even to describe them properly, due to the dependencies, relationships, and interactions between their individual parts. Stemming from these properties are nonlinearity, emergence, spontaneous order, adaptation, and feedback loops to name a few *[Bar-Yam, 2002]*. The second chapter of the thesis (first being the Introduction) was devoted to building a theoretical background and, in a sense, imagination in order to successfully grasp the intricacies of the complex networks paradigm.

One of the adequate ways how to efficiently describe a complex system is a network (a discrete graph) *[Boccaletti et al., 2006]*. The nodes of the network would represent the parts of the system, while the links in the network their interactions. These might be directed or not directed (cf. Fig. 2.3). The notion of complex network turned out to be very useful in imagining the very nature of causal relations. Recalling Fig. 2.2, from a set of three nodes representing three distinct autonomous oscillators with different natural frequencies and a set of causal relations connecting the nodes, emerges the observable we are measuring, e.g. the temperature. The collective dynamics of the oscillators coupled in a way that is described by their causal relationships causes the signal, the time series we collect. Now, by applying causal discovery algorithms, we are trying to reverse-engineer the nature and from the observable, we extract candidates for the nodes in the network (hence the oscillatory phenomena, or pacemakers in the climate system), as well as the causal relations (the links between them).

Of course, this is a very high-level depiction of the complex climate system with autonomous oscillators and links between them. The physical reality is, as usual, much more complicated. As we saw later in this thesis, two main interpretations emerge: the nodes might represent distinct physical processes operating on particular time scales and the links would then be the couplings between the processes, or another possibility is that the nodes are themselves oscillatory representation (with a particular period) of coupled physical processes that interact together (e.g. feedback loop) and then the causal links would represent higher level connections or coupling between a set of processes. Unfortunately, figuring out which of these interpretations is more likely is beyond the scope of the thesis and I leave the potential contemplation to a reader.

Now, let us return back to the climate science. The physical laws of nature work with a notion of scales. Generally, a scale is a measure of the distance of our interest. As an example, consider a research dealing with atmospheric fronts — that also means

that we are dealing with spatial scales of thousands of kilometres and temporal scales of days to weeks. Chapter 3 is dedicated to the problem of temporal scaling in the atmospheric dynamics. Namely, I first showed that the physical laws governing the atmospheric dynamics are formally scale-invariant (sec. 3.1). Concretely, the governing equations are scale-invariant under isotropic "zooms" as long as other variables are rescaled as well *[Lovejoy and Schertzer, 2013]*. The outcome of this mathematical practice is an interesting fact that the dynamics repeats itself scale after scale (again, after needed renormalisations). However, this scaling (captured by the eqn. (3.6)) breaks down at the smallest observable scales (due to viscosity), and at the largest, planetary scales (due to the forcing term — energy injection from the Sun).

Making a transition from theory and equations to the observations in the climate science — we have energy injection at the planetary scale, then we have a scaling range of roughly 10 orders of magnitude where the scale-invariance holds and plethora of processes exist which exchange energy and in general interact with each other in a non-trivial way, and finally we have the viscous scale, where the energy is effectively dissipated due to molecular nature of considered fluid. Fig. 3.1 and Table 3.1 summarise the above written and state various atmospheric and oceanic processes and their typical scales. Injecting the energy at the largest scales and dissipating it in the smallest scales mean that the energy transfer must take place in-between and via this energy transfer, the scales are interacting with each other. Taken the side of the theory of information, one might argue that the distinct scales engage in information transfer,because they are coupled and affect each other — typically the neighbouring scales affect each other, but actually, there are no restrictions in this (at least theoretically).

Now I shall collect all the building blocks introduced earlier and provide the synthesis for studying the information transfer in atmospheric dynamics, or more concretely, across temporal scales in atmospheric dynamics. A few necessary tools in order to synthesise the topic are as follows: we would need a method which is able to extract an oscillatory mode of a given frequency from a time series, then we would need some kind of a measure of dependence which will tell us whether the two time series have something in common, and finally we would need to design a statistical test, able to recognise if the estimated dependence could arise simply by chance or it is truly statistically significant.

Since we are looking for recurrent patterns and oscillatory, or quasi-oscillatory behaviour, we exploited the phase dynamics approach, where an arbitrary signal can be written as a complex function of time, or more precisely as the product of the instantaneous amplitude and cosine of the instantaneous phase (cf. eqn. (3.9)). In order to obtain the imaginary part of the signal (needed for the analytic description) we utilised the continuous complex wavelet transform (CCWT) *[Torrence and Compo, 1998]* and the beauty of this approach is that in each scale (predefined period of the mother wavelet) the complex wavelet coefficients can be directly used to estimate the phase and amplitude time series (eqns. (3.10) and (3.11)). The illustration of the workings of CCWT is provided in Fig. 3.4, where aside from the raw time series (the surface air temperature) are shown the CCWT-extracted instantaneous phase and amplitude time series.

Having extracted the time series of our interest, now we would like to measure their mutual dependence. This can be done using any of the wealth of methods mathematics

offers us. We can use classical covariance or sample correlation in order to detect a linear relationship, lagged correlation to detect lagged relationships, but in any case, the result would be indicative of a mere visual similarity, an apparent relationship if you will. One step further would be to assess the possible causal relationship, in this framework, we speak about predictive, or Granger, causality *[Granger, 1980]*. The idea behind predictive causality is that in order to claim a causal relationship between two variables, they need to comply two rules: the cause precedes the effect, and the cause contains information about the effect that is unique and is in no other variable. The standard test for Granger causality is based on a linear regression model and consists of series of t-tests and F-tests on lagged values (cf. eqn. (3.21)). Note that Granger causality is defined to seek only linear causal dependence.

The linearity constraint of Granger causality can be tackled by estimating the nonlinear predictive causality and this can be conveniently done employing measures emerging from information theory. A quick introduction to information theory is provided in sec. 3.4.2. One of the key measures in information theory is the mutual information, which quantifies the amount of information that can be obtained about one random variable by observing another. It measures how much the probability distribution of one variables changes when we include another variable (cf. eqn. (3.33)). From this can be seen that it also measures the nonlinear dependence, as the mutual information is zero if and only if the two random variables are independent (hence their joint probability distribution is simply the product of two marginals). Now the conditional mutual information, as the name suggests, measures the amount of information two random variables share, but this time conditioned on the third variable. All possible combinations of information theoretical measures are visualised as Venn diagram in Fig. 3.6.

In order to estimate the (conditional) mutual information from observed data, one has to estimate the probability density function. This is known problem for a long time, without the one correct answer. As usual, a wealth of methods exist and few of them are described in sec. 3.4.3. The concrete example how to infer causality from information theoretical measures in two unidirectionally coupled Rössler systems, taken from *Paluš and Vejmelka [2007]*, is provided in Fig. 3.8 and in the surrounding text. Shortly, numerical experiments due to *Paluš and Vejmelka [2007]* suggest that if one estimates the conditional mutual information between variable X now, variable Y in the τ-future and condition on variable Y now and eventually on variable Y in the $(n - 1)\eta$-past (with n being the dimensionality of condition), she is is fact estimating the causality $X \rightarrow Y$.

The final building block is provided in sec. 3.5 as a short introduction to statistical hypothesis testing. This is a very needed part of the overall analysis since the value of (conditional) mutual information does not provide us with any definite answer. The theoretical distribution is not known in this case, hence we opt out to generate an empirical distribution of the test statistics using Monte Carlo methods. Briefly, after computing the value of (conditional) mutual information between the pair of variables, we shall generate a synthetic dataset that copies some of the properties of tested variables and omits others, for example 1000 Fourier Transform surrogates *[Theiler et al., 1992]* and then estimate the value of (conditional) mutual information in the synthetic data set. That creates our test statistics from which we subsequently assess the statistical significance

of our result.

We are finally approaching the interesting part of this work — the results. In order to understand the complex behaviour of the atmospheric dynamics from meteorological data researchers back in the 1980s opted for complicated nonlinear methods: from studying the climate attractor of low dimensions *[Nicolis and Nicolis, 1984; Tsonis and Elsner, 1988]*, to claiming such an attractor as spurious *[Grassberger, 1986; Lorenz, 1991]*. Some authors claim that the non-Gaussian statistics of the circulation are consistent with the paradigm for a linear system perturbed by multiplicative noise (e.g. *Sura et al. [2005]*), therefore nonlinearity is not needed. On the other hand, search for local patterns on specific temporal scales led to an identification of various oscillatory phenomena possibly possessing nonlinear origin and actively interacting with global modes of atmospheric variability (e.g. *Paluš and Novotná [2004]; Paluš and Novotná [2009]; Feliks et al. [2010]*). The task of detecting the oscillatory phenomena and inferring the relationship between them and other modes of climate (or even oceanic) variability gained momentum lately and is associated with reward by the means of possible successful forecasting of such phenomena with high societal impact.

Although typically, the causal relation is sought between pairs of different variables or different modes of atmospheric variability, we build here upon the results of *Paluš [2014a,b]*, where the complexity is examined by identifying causal relations between processes operating on different temporal scales within a single climatic time series. This makes sense when we recall Fig. 2.2 where a number of autonomous oscillatory subsystems with their dependencies gave rise to a process, which we can measure (an observable). Now, with the suggested approach of identifying causal relationship within one variable, we are effectively adapting the view as depicted in the figure, when the variable we are studying is observable, and the sought causal phenomena are the interactions between the subsystems in the left-hand side of the figure.

Studying interactions between dynamics on various time scales in long-term daily SAT records from European locations, *Paluš [2014b]* has observed an information transfer from larger to smaller time scales in the form of a causal influence of the phase of slow temperature oscillations on the amplitude of faster temperature variability. The influenced faster variability is characterised by the temporal scales from a few months to 4–5 years, while the periods of the influencing oscillatory phenomenon vary between 6 and 11 years; however, the most probable period is between 7 and 8 years (see either Figs. 4.10 and 4.11 here, or original *Paluš [2014b]*, Figure 3a).

However, the statistical evidence provided by *Paluš [2014b]* is enough for claiming qualitative cross-scale coupling, the quantitative study of the effect of this cross-scale coupling was provided by *Jajcay et al. [2016]* and is in detail also supplied here. For evaluating the effect of cross-scale interactions we opted for a simple method by the name of conditional means. This method works by dividing the full period of slow oscillations into bins (in our case the 8-year cycle was divided into 8 bins, hence one bin represents approximately one year of the cycle) and then for each bin one has to compute the conditional mean (or any other statistical moment for that matter) in order to obtain the discretised estimate of the quantity. If the 8-year cycle has no influence on the studied variable, the conditional means in all 8 bins should be the same, equal to the unconditional, global mean. Or rather, due to finite sample effect, the conditional

means would randomly fluctuate around the unconditional mean. On the other hand, if the conditional means vary as a function of the phase of the particular cycle, we would conclude that that cycle has an effect on a studied variable, and the overall size of the effect can be approximated by taking the difference between the maximum and minimum conditional mean. The method of conditional means is visualised in Fig. 4.12.

In this thesis, I studied two separate quantities on which the 8-year cycle should have an effect. That is the annual cycle (or, rather its amplitude, so the amplitude of annual cycle — AAC) and the short-term overall variability, represented by the anomalies of surface air temperatures — SATA. The conditional means of AAC in various periods of the full record are depicted in Fig. 4.14. The effect of the 8-year cycle on the AAC seems to vary in time but overall is non-negligible at values around 0.6°C – 0.8°C. The similar figures for the different stations than Prague – Klementinum are depicted in the appendix (Figs. A.5, A.6, and A.7).

Similarly, the effect of the 8-year cycle was studied with an association to the overall temperature variability represented by SATA in Fig. 4.16 in Prague – Klementinum station and in Figs. A.8, A.9, and A.10 for other European stations. The effect is also variable in time and it reaches up to 1.5°C in the case of Prague station and 1962 – 2009 period. A numerical experiment confirming that this difference in SATA cannot be explained solely by the very existence of the 8-year cycle linearly added to the background variability, but rather must be a manifestation of the cross-scale coupling is depicted in Fig. 4.18 and described in detail in the surrounding text.

From the conditional means in all used stations estimated for different periods, we saw that the effect seem to vary in time. The nonstationarity of the cross-scale effect was further studied by applying a sliding temporal window on the full available data record. For each window of effective length 16 384 daily values (approximately 44 years and 10 months) the conditional means were computed and the effect of the 8-year cycle estimated as a difference between the minimum (the coldest) and the maximum (the warmest) bin. In order to establish a statistical significance of this result, in each window 5000 surrogate data realisations of three different types were generated and the p-value was subsequently computed. Three different types of surrogate data signify three different null hypotheses, but all three show consistent results. That is, the effect of the 8-year cycle on AAC in Prague – Klementinum station varies significantly over time, having values between 0.2°C up to 1.3°C, and in the last decades is usually statistically significant. The Figs. 4.19, 4.20, and 4.21 show the temporal variations of the effect, tested using 5000 autoregressive surrogates of order 1, Fourier Transform surrogates, and multifractal surrogates, respectively. Similarly, the effect of the 8-year cycle on overall SATA variability strongly varies between the minimum value of 0.5°C to the maximum of more than 2°C. As in the case of AAC, the effect on SATA is usually significant during last decades, with values exceeding 1.4°C (Figs. 4.22 – 4.24 for the three types of null hypotheses).

As suggested by repeating the analyses on data from different European stations, the effect also seems to possess spatial variability, which was further assessed by repeating the analysis on both AAC and SATA in gridded analysis data provided by the ECA&D project *[Haylock et al., 2008]*. For each point on a 0.5°×0.5° grid, the phase of the 8-year cycle was extracted, as well as the amplitude of the annual cycle, and conditional means

were computed. The significance was tested using 1000 Fourier Transform surrogates and the results for AAC are rendered in Fig. 4.25 and for the SATA variability in Fig. 4.26. Our initial hypothesis of spatial variability was confirmed — the effect on AAC varies between 0.1°C in south-western Europe and 1.6°C in the Baltics and is usually statistically significant. On the other hand, the effect on SATA also varies considerably but is non-significant over a huge portion of the grid points with a small exception in western Russia.

The final piece of the puzzle was to estimate the seasonal dependency of the effect. This is easily done by selecting only some months in the data and repeat the analysis, including the statistical testing. In accordance with a huge body of climatological literature, we worked with seasons defined as follows: the winter season, including months December, January, and February (*DJF*); the spring season, including March, April, and May (*MAM*); the summer season, including June, July, and August (*JJA*), and finally, the autumn season with September, October, and November (*SON*). As it turned out, the strength of the cross-scale effect heavily depends on the season: it is the strongest in the winter (*DJF*). For the Prague – Klementinum data, the effect in winter time reach higher than 5°C and is almost always significant. On the other hand, other seasons exhibit lower effect (between 1°C and 2°C) and are mostly not statistically significant. For all other European stations the same holds (Figs. A.20 — A.24): the effect is strongest in the winter season in comparison with the other (the winter effect ranges from 2°C to over 6°C), the east-west gradient modulates the strength of the effect itself (eastern stations exhibiting stronger effect of the 8-year cycle) and also the seasonal dependence — western stations show lesser seasonal modulation of the effect, while the effect in the eastern stations heavily depends on the season. This was confirmed using the gridded dataset (Fig. 4.28) with the strength of the effect in winter season reaching up to 7°C in western Russia. Also, over much of the central and western Europe and parts of Scandinavia, the effect was deemed as significant under surrogate testing.

These results suggest that the weak 7–8-year cycle plays a very important role in the temperature variability on interannual and shorter time scales. Therefore, this phenomenon deserves further study and understanding of its mechanisms. *Paluš [2014b]* hypothesises that in the analysed SAT data, we have observed a regional manifestation of a general phenomenon of cross-scale interactions in the atmospheric dynamics in which global, low-frequency modes influence local, high-frequency variability. For instance, *Chekroun et al. [2011]* reported that the phase of the low-frequency modes of the El Niño/ Southern Oscillation influences high-frequency variability ("weather noise") of the sea surface temperature in the tropical Pacific. For the data analysed in this study, the most relevant global mode is probably the North Atlantic Oscillation (NAO). The influence of the NAO on the air temperature in Europe is known *[Marshall et al., 2001]*, and its mechanisms depending on the phase of the NAO are described, e.g. by *Hurrell and Dickson [2005]*. Typically, Pearson's correlations have been computed between (mostly winter) air temperature records and NAO indices (see e.g. *Beranová and Huth [2008]; Pokorná and Huth [2015]*) however, specific time scales have not been considered yet, although the 7–8-year cycle has also been detected in the NAO index *[Gámiz-Fortis et al., 2002; Paluš and Novotná, 2004]*. These results demonstrate the importance of understanding the climate variability in scale-specific regional modes and their cross-

scale interactions and causal relations with global circulation variability modes which are localised not only in space *[Vejmelka et al., 2015]* but also in a time scale or in a frequency range *[Groth and Ghil, 2011, 2015]*.

The latter result of identifying the cross-scale interactions motivated a similar study of a more global phenomenon with a huge socio-economical impact — the El Niño/ Southern Oscillation (ENSO). The next chapter of this thesis (chapter 5) is devoted to the basic description of physical mechanisms, typical time scales involved, modelling, and of course, assessing the cross-scale interactions in ENSO phenomenon. ENSO is one of the oldest observed, coupled ocean-atmosphere phenomenon, which manifests itself as a quasi-periodic fluctuation in a sea surface temperature (El Niño part) and air pressure of the overlying atmosphere (Southern Oscillation part) across the equatorial Pacific Ocean. The warming phase of the sea surface temperature is known as El Niño and is accompanied with high air surface pressure in the tropical western Pacific, while the cooling phase of the sea surface temperature is known as La Niña, and is, in turn, accompanied with low air surface pressure. The two periods last several months each, they are typically occurring every few years (with exceptions), and their effects vary in intensity.

Although the exact causes for initiating warm or cool ENSO events are not fully understood, the two components of ENSO — sea surface temperature and atmospheric pressure — are strongly related and the first possible mechanism in the form of a positive feedback loop in the ocean-atmosphere coupled system was due to *Bjerknes [1969]*. For us, data-driven researchers, the interesting part is how scientists usually observe ENSO. The equatorial Pacific ocean is divided into 3 main regions (Fig. 5.1) from which stem various ENSO indices — they are always the spatial average of sea surface temperature (SST) in given region. The most used one is undoubtedly the Niño 3.4 region which spans approximately central equatorial Pacific. All four indices (with an addition of derived Niño indices ONI and TNI) are plotted as time series in Fig. 5.2. Table 5.1 summarises their basic statistical properties, their mutual interdependence in the form of correlation, and their histogram.

The visual depiction of circulation patterns associated with neutral, warm, and cold events is provided in Fig. 5.4 and described in the surrounding text. Briefly, the normal state consists of Walker circulation (easterly surface trade winds, convection in the western Pacific, westerly upper-level wind and descending air in the eastern Pacific) and inclined thermocline, where it is deeper than the upwelling level in the western Pacific (thus upwelling brings warm water to the surface) and shallower in the eastern Pacific (thus brings cold water to the surface). The warm event usually starts with weakening or even reversing of the Walker circulation which causes the ocean surface to warm up. Westerly surface wind anomalies then further cause the thermocline to deepen in the eastern Pacific via Bjerknes feedback. Moreover, due to westerly wind anomalies, the belt of permanent precipitation shifts eastward and rich energy budget in the form of latent heat that is released due to condensation disturbs the storminess and heating in the tropics. All this ultimately supercharges the poleward flow (disturbs Hadley circulation), which in turn causes further changes in the circulation, including jet stream over the Pacific. Through these profound changes in the atmospheric flow, even if El Niño is specific to the tropical Pacific, it does have worldwide impacts. As expected, the

La Niña event displays the opposite behaviour of aforementioned fields. That is, the Walker circulation is strengthened, meaning the trade winds exhibit easterly anomalies, warm pool shifted even more westward and the slope of the thermocline is more inclined — shallower in the eastern Pacific and deeper in the western Pacific. The belt of permanent precipitation is shifted westward.

The theoretical explanations of ENSO can be loosely grouped into two frameworks: in the first El Niño is one phase of a self-sustained, unstable, and naturally oscillatory mode of the coupled ocean-atmosphere system; in the second El Niño is a stable (or damped) mode triggered by, or interacted with, stochastic forcing or noise such as westerly wind bursts and Madden–Julian oscillation events (e.g. *Gebbie et al. [2007]; Wang et al. [2016]*), and the tropical instability waves in the eastern Pacific (e.g. *An [2008]*). Both of the frameworks involves the *Bjerknes*'s *[1969]* feedback. Both frameworks are briefly explained in the second part of sec. 5.1.2.

One of the results of the extensive research refers to the temporal scales involved in ENSO dynamics. *Barnett [1991]* came to the conclusion that ENSO is principally a three time-scales process, consisting of an annual cycle, a quasi-biennial oscillation, and a lower frequency variation pattern. A few years later, *Latif et al. [1997]* also identified three modes of variability, namely an interannual mode, a decadal mode, and a trend or unresolved ultra-low frequency variability pattern. *Kim [2002]* decomposed tropical Pacific SST variability into two dominant modes — a biennial mode and a low-frequency mode, while *Yeo and Kim [2014]*, again, identified three leading modes: a global warming mode (ultra-low frequency), a low-frequency variability mode, and a biennial oscillation mode. The biennial (or rather quasi-biennial) mode was noted by several authors *[Rasmusson et al., 1990; Jiang et al., 1995]*. Another important fact is that the frequency of ENSO is dependent on the spatial structure of zonal wind stress anomalies, in particular, the longitudinal position of the westerly anomalies *[An and Wang, 2000; Wang and An, 2001]*. Since our analysis will focus on faster-than-decadal variability in the ENSO dynamics, the most prominent modes for us to note shall be the annual cycle, the (quasi-) biennial mode and the low-frequency mode.

Finally, after an extensive review of known facts about the ENSO and its dynamics, let us dive into the analysis of possible cross-scale interactions. Having adopted the phase dynamics principle as in the case of European temperatures, from the Niño 3.4 we extracted the quasi-oscillatory modes with periods ranging from 5 to 96 months by the means of CCWT. We were interested in three types of relationships: the phase synchronisation (eqn. (5.4)), the phase-phase causality (eqn. (5.5)), and the phase-amplitude causality (eqn. (5.6)), and these were computed between each pair of quasi-oscillatory modes. The statistical significance of our results was estimated using a randomisation procedure by generating Fourier Transform surrogate data from the Niño 3.4 time series.

The results of our analysis are depicted in Fig. 5.5, where we identified the three fundamental time scales in ENSO dynamics — the annual cycle (AC), the quasi-biennial mode (QB), and low-frequency mode (LF) — consistent with previous work *[Barnett, 1991; Kim, 2002; Yeo and Kim, 2014]*, but offers further details on the interaction between these modes. Some of the interactions we identified rigorously here have been previously theorised to exist, but, to the best of our knowledge, were never detected in a data-driven way. We observe a pronounced connection between the (phase of) the slower LF mode

and both the phase and amplitude of the faster QB mode. In particular, the slower LF mode affects the phase of the QA (which we defined as the combined AC and combination tones processes (CT), defined by *Stuecker et al. [2013]*) mode, and, therefore, — indirectly — the phase of the faster QB mode, which tends to be affected by and phase-synchronized with the QA mode; the slow LF mode also directly affects the amplitude of the faster QB mode. The connections between the phase of slow LF mode and the phase of QA mode important in the causal sequence above are both direct and indirect. In the latter indirect case, the connection works through the phase synchronisation between the slow LF mode and the slow QB mode and subsequent causal effect of the latter on the phase of the QA mode. The faster LF modes add to the picture by also affecting the phase of the QA mode, and, therefore, indirectly, the phase of the faster QB mode.

One of the main findings of our study is the apparent importance, in ENSO dynamics, of the LF phase→QA phase→QB phase causal linkages, as well as LF phase→QB amplitude causal linkages. To illustrate these causal connections further, we utilised an approach of conditional composites (based on conditional means technique introduced earlier). Fig. 5.6 visualises the response of the AC frequency to changes in the phase of the LF ENSO variability, thus illustrating the LF phase→QA phase causal linkage. The results suggest that the positive phase of the LF cycle speeds up the annual cycle (thus shortens its period and increases its frequency), while the negative period of LF cycle causes the AC period to become longer than a year. In fact, not only the effective frequency but also the entire shape of the annual cycle changes depending on the phase of the LF ENSO mode. Figs. 5.7 and 5.8 illustrate this fact by plotting the conditional composites of the annual cycle associated with distinct phases of the LF mode. Moreover, Fig. 5.9 identifies clear growth in the amplitude of the BC and QB variability as the low-frequency phase changes from La Niña (LF−) to El Niño (LF+) conditions, consistent with the LF phase→QB amplitude causal interaction.

Finally, we hypothesise that the interactions identified above are instrumental in setting up extreme ENSO events, which is depicted in Fig. 5.10. In particular, during all of the strong El Niño events of years 72/73, 82/83 and 97/98, the QA, QB and LF modes were characterised by synchronous pronounced maxima. What appears to be essential for an extreme ENSO to occur is the synchronisation of multiple QB modes with each other. We believe that this "internal" QB synchronisation is what has been picked up by our conditional mutual information analysis in the form of LF→QA→QB phase connections and also LF phase→QB amplitude connections (since synchronisation of phases of different QB modes should automatically result in a large-amplitude event). By contrast, during a moderate El Niño of 87/88, the LF, QB and QA modes exhibited phase shifts, with lower-frequency modes leading the higher-frequency modes (in particular a suite of QB modes) instead of being "stacked" on top of one another, thus limiting the magnitude of this event.

Apart from seeking cross-scale interactions in the observed Niño 3.4 time series, we also sought these interactions in synthetic time series obtained from a variety of models. In particular, we were interested in seeking the interaction in a conceptual, low-dimensional dynamical model due to *Stein et al. [2014]* — the parametric recharge oscillator, then in the empirical stochastic model of Pacific sea surface temperatures due to *Kondrashov et al. [2005]*, and finally in the ENSO representations (the Niño 3.4 spatial

average) within the Coupled Model Intercomparison Project Phase 5 (the famous CMIP5 framework) *[Taylor et al., 2012]*.

In a nutshell, the PRO dynamical model fails to reproduce any of the observed causal interactions: the neutral realisation is not a multi-scale process and therefore all the oscillatory modes extracted from the time series are coherent and provide a picture of mutually phase-synchronised modes over a wide range of periods (Fig. 5.11); and in the damped realisations (as driven by noise, we integrated 20 of them) the presence of noise destroys the synchronisation and causality phenomena observed in the deterministic neutral model and the interactions (depicted in Fig. 5.12) exhibit huge variance from one model realisation to another, and no significant interactions seem to be systematically present.

Unlike the low-order dynamical PRO model, the empirical stochastic model (significant cross-scale interactions depicted in Fig. 5.13) is clearly able to simulate synchronisation phenomena, in which QB mode is synchronised with the AC and that the AC is phase synchronised with the combination tones. The same synchronisation behaviour was observed in the observational data. The majority (though not all) of the empirical model realisations were also able to correctly simulate the observed phase-phase causal relationships, with a directional connection from LF mode to the AC modes, as well as from the AC modes to the modes in the QB range. However, only a few realisations of the empirical stochastic model could capture the observed phase-amplitude causality from the LF mode to the QB mode; hence, we conclude that the present empirical model is not able to accurately simulate this aspect of the observed phase-amplitude causal relationships in ENSO. As a final piece, Fig. 5.14 shows phase-phase causality results for the EMR model utilising three different stochastic forcing schemes (details in the text). Note that the LF→QA→QB causal links become progressively more pronounced from the scheme utilising additive noise, to the one with multiplicative noise, to, finally, the scheme using multiplicative noise snippets. This interesting behaviour suggests that the QB modes in the EMR model are inherently present in the algebraic structure of this model's deterministic propagator, but are strongly influenced by the feedbacks that involve state-dependent (multiplicative) noise.

For the purpose of validating the dynamical representation of ENSO and its cross-scale interactions, we analysed, in the same manner, the time series of the sea surface temperature obtained from the individual runs of COAGCMs within The Coupled Model Intercomparison Project Phase 5 (CMIP5) *[Taylor et al., 2012]* framework. Table A.2 summarises used realisations and modelling centres in this study. The overview of comparison between the observed Niño 3.4 and simulated time series from CMIP5 models is visualised in Fig. 5.15. To start with, we measured the similarity between the observed and simulated wavelet spectra (first two columns): the models exhibit great variations in their ability to match the observed Niño 3.4 spectra, with correlation coefficients ranging from 0.2 to 0.8 and rms distances from 30 to 120. This means that the ENSO tends to exhibit different epochs of sampling variability in models, in which its strength, spectrum and other properties may vary significantly *[Wittenberg, 2009]*. The next 6 columns in the Fig. 5.15 show Pearson's correlation and Adjusted Rand Index (ARI — details in text) for synchronisation, phase-phase causality, and phase-amplitude causality maps. To summarise, the CMIP5 models exhibit great sampling variations in

the simulated ENSO characteristics. Some of the simulations do exhibit certain aspects of interactions between the processes of different time scales which match the observed interactions. However, no single simulation is able to reproduce the entire sequence of causal connections inferred from the observed data. The best realisations (the most similar to the observed data) are depicted in Fig. 5.16.

In order to validate our results, we performed the robustness analysis, which summary can be found in sec. 5.5. The robustness analysis firstly compares two different computational algorithms for estimating the (conditional) mutual information: equiquantal estimate and k-nearest neighbours estimate (the algorithms themselves are described in sec. 3.4.3 and references therein). As can be seen from the analysis result in Fig. 5.17, both estimates provide the same picture with only small deviations, which we consider to be statistical fluctuations.

For the second phase of robustness analysis, we divided the full Niño 3.4 data period into two equally long periods, namely 1870 – 1943 and 1943 – 2016 periods, and estimated the phase synchronisation and phase-phase causality for each of these periods separately. The causality estimates from the two different periods exhibit substantial differences (Fig. 5.18), which can either be due to the true change in ENSO dynamics between the two periods or due to a less robust estimation of the mutual information for a shorter time series. The wavelet power spectra of the Niño 3.4 time series computed for the full (1870 – 2016) period, as well as for the 1870 – 1943 and 1943 – 2016 sub-periods (Fig. 5.19) suggest that the former possibility is more likely. Indeed, the ENSO variability in the second part of the record (1943 – 2016) exhibited more power at QB periods compared with the first part of the record (1870 – 1943); thus the phase synchronisation between AC and QB modes was more pronounced during 1943 – 2016 compared to 1870 – 1943, consistent with Fig. 5.18.

The tools of information theory, used throughout this thesis, enabled us to uncover an intricate network of interactions underlying the observed ENSO variability. In particular, we showed that the (phase of) low-frequency (LF), interannual ENSO mode directly affects the amplitude of QB variability. It also indirectly affects the phase of QB variability, via the intermediate causal connection with the phase of the annual cycle (AC) and its combination tones (CT) associated with the LF mode. The AC/CT modes combined constitute the quasi-annual (QA) variability (changes in the shape of the annual cycle). The above LF→QA→QB phase interactions and LF phase→QB amplitude interactions result in intermittent synchronizations among different QB modes that occur preferentially during certain phases of the LF mode, thus leading to extreme (biennial) ENSO events (Fig. 5.10). This allows multiple QB modes, which are normally desynchronised and are thus associated with small overall energy, to occasionally produce a signal with the amplitude exceeding those of QA and LF cycles. One of the key messages from our work is to suggest a much more important role of the quasi-biennial (QB) modes in ENSO dynamics than, perhaps, thought previously.

The novelty of our work, aside from applying an original methodology to analyse climate data, is in obtaining a new compact description of the causal interactions instrumental in ENSO dynamics. The causal connection between the phase of the LF variability and that of the QA variability — that is, changes in the shape of the annual cycle depending on the state of the LF ENSO mode — is conceptually similar to the effect

of low-frequency component of North Atlantic Oscillation variability on the annual cycle of surface temperature over Europe *[Paluš et al., 2005]*. A mechanistic explanation of the QA→QB phase causality remains elusive, with possible hints from empirical modelling.

The observed ENSO interactions are poorly represented in the historical simulations of CMIP5 climate models, which exhibit large sampling variations in ENSO spectra and causality maps, both from model to model and among different runs of a single model. Some of the model simulations match time scales or select causality characteristics of the observed ENSO variability, but no single simulation is able to reproduce the full picture of the observed interactions. The ENSO variability in long pre-industrial control runs of CMIP5-type models is known to exhibit multidecadal epochs characterized by different ENSO behaviour *[Wittenberg, 2009]*. Hence, there is still a possibility that the models possess correct ENSO dynamics, but the sample of 89 20[th]century simulations considered here was simply not large enough to generate the ENSO epoch that would match the observed epoch. Analyses of long pre-industrial runs are in order to address this issue. However, the experiments with an empirical stochastic ENSO model of *Kondrashov et al. [2005]* suggest that the chances of reproducing the observed ENSO behaviour in ensemble simulations of the 20[th]century climate are much higher than the CMIP5 ensemble results. This implies that CMIP5 models do indeed misrepresent ENSO dynamics. The same conclusion holds for the conceptual parametric recharge oscillator model of *Stein et al. [2014]*, which also fails to capture the observed cross-scale causal relationships in ENSO. By contrast, the success of the empirical ENSO model in reproducing the essential phase interactions among LF, QA and QB modes allows one to address, in a mechanistic fashion, the dynamics of these interactions, with initial indications pointing to the importance of both deterministic dynamics and state-dependent (multiplicative) noise in controlling the QB variability.

Thus, neither conceptual nor state–of–the–art dynamical climate models studied here were able to mimic the structure of the observed ENSO interactions, while the empirical models considered did quite a bit better. Understanding the discrepancies between the observed interactions and the interactions simulated by the dynamical models — especially with respect to their ability to model the QB modes — may be the key to an improved ENSO prediction. Finally, the observed interactions may pose as a starting point in developing a conceptual model capturing the cross-scale information transfer in ENSO dynamics.

One idea of such a model emerges from the realm of machine learning, concretely adapting a recurrent neural network architecture. A recurrent neural network (RNN) is a class of artificial neural network where connections between units form a directed graph along a sequence. This allows it to exhibit dynamic temporal behaviour in a time sequence. A type of RNN named an echo state network, contains a sparsely connected hidden layer with fixed weights. Thus this hidden layer acts as a so-called dynamical reservoir that produces dynamical states which the RNN (after sufficient training) is able to harvest and reproduce specific temporal patterns. The idea is to exploit causal connections found by our analysis and to build a dynamical reservoir using the parts of conceptual dynamical models of ENSO, couple them according to found causal linkages and then finally, train the weights between the input time series and this conceptual causal dynamical reservoir. The obvious option how to conceptually model

synchronisation and causality phenomena in the network of oscillators is to exploit the *Kuramoto [1975, 1984]* model of synchronising oscillators: one would define oscillators as per different oscillatory modes found in our analysis, and then couple them with symmetric matrix as for modelling synchronisation, and finally with non-symmetric matrix as for modelling the phase-phase causality:

$$\frac{\mathrm{d}\phi_i}{\mathrm{d}t} = \omega_i + \xi_i + \frac{K_{syn}}{N} \sum_{j=1}^{N} A_{ij}^{syn} \sin\left(\phi_j - \phi_i\right) + \frac{K_{caus}}{N} \sum_{j=1}^{N} A_{ij}^{caus} \sin\left(\phi_j(t - \eta) - \phi_i(t)\right), \quad (6.1)$$

where the system is composed of N oscillators with their natural frequencies ω_i and phases ϕ_i; K_{syn} denotes the synchronisation strength, A_{ij}^{syn} is symmetric binary matrix with 1 for interacting oscillators i and j, K_{caus} is coupling strength for causal connections, and A_{ij}^{caus} is non-symmetric binary matrix causally connecting oscillators $j \rightarrow i$ with backward delay η, and finally, ξ_i poses as Gaussian white noise. This would be an addition to slowly growing literature considering neural networks as a time series predictors in climate science (see e.g. *Lins et al. [2010]; Patil et al. [2016]; Zhang et al. [2017]*).

On a broader scale, the framework we used here is applicable to analysing phenomena across a wide range of disciplines — for example, in neuroscience, where cross-frequency phase-amplitude coupling has recently been observed in electrophysiological signals reflecting the brain dynamics. This cross-frequency coupling enriches the cooperative behaviour of neuronal networks and apparently plays an important functional role in neuronal computation, communication, and learning *[Canolty and Knight, 2010]*.

Bibliography

K. AchutaRao and K. Sperber. Simulation of the El Niño Southern Oscillation: Results from the coupled model intercomparison project. *Climate Dynamics*, 19(3-4):191–209, 2002.

H. Akaike. Statistical predictor identification. *Annals of the Institute of Statistical Mathematics*, 22 (1):203–217, 1970.

R. Albert and A.-L. Barabási. Statistical mechanics of complex networks. *Reviews of modern physics*, 74(1):47, 2002.

M. A. Alexander, I. Bladé, M. Newman, J. R. Lanzante, N.-C. Lau, and J. D. Scott. The atmospheric bridge: The influence of ENSO teleconnections on air-sea interaction over the global oceans. *Journal of Climate*, 15(16):2205–2231, 2002.

M. R. Allen. *Interactions between the atmosphere and oceans on time scales of weeks to years.* PhD thesis, University of Oxford, 1992.

M. R. Allen and L. A. Smith. Investigating the origins and significance of low-frequency modes of climate variability. *Geophysical Research Letters*, 21(10):883–886, 1994.

S.-I. An. Interannual variations of the tropical ocean instability wave and ENSO. *Journal of Climate*, 21(15):3680–3686, 2008.

S.-I. An and F.-F. Jin. Collective role of thermocline and zonal advective feedbacks in the ENSO mode. *Journal of Climate*, 14(16):3421–3432, 2001.

S.-I. An and B. Wang. Interdecadal change of the structure of the ENSO mode and its impact on the ENSO frequency. *Journal of Climate*, 13(12):2044–2055, 2000.

S.-I. An, F.-F. Jin, and I.-S. Kang. The role of zonal advection feedback in phase transition and growth of ENSO in the Cane-Zebiak model. *Journal of the Meteorological Society of Japan. Ser. II*, 77(6):1151–1160, 1999.

A. A. Andronov, A. A. Vitt, and S. E. Khaikin. *Theory of Oscillators (in Russian).* Gostekhizdat, Moscow, 1937. English translation: Pergamon Press, Oxford, New York, Toronto, 1966.

A. A. Andronov, A. A. Vitt, and S. E. Khaikin. *Theory of Oscillators: Adiwes International Series in Physics*, volume 4. Elsevier, 2013.

C. Angelini, D. Cava, G. Katul, and B. Vidakovic. Resampling hierarchical processes in the wavelet domain: A case study using atmospheric turbulence. *Physica D: Nonlinear Phenomena*, 207(1-2):24–40, 2005.

A. Arneodo, E. Bacry, and J.-F. Muzy. Random cascades on wavelet dyadic trees. *Journal of Mathematical Physics*, 39(8):4142–4164, 1998.

Y. Bar-Yam. General features of complex systems. *Encyclopedia of Life Support Systems (EOLSS), UNESCO, EOLSS Publishers, Oxford, UK*, 2002.

J. Barnes, P. Tryon, and H. Sargent III. Sunspot cycle simulation using random noise. In *The Ancient Sun: Fossil Record in the Earth, Moon and Meteorites*, pages 159–163, 1980.

T. Barnett. The interaction of multiple time scales in the tropical climate system. *Journal of Climate*, 4(3):269–285, 1991.

A. G. Barnston and R. E. Livezey. Classification, seasonality and persistence of low-frequency atmospheric circulation patterns. *Monthly Weather Review*, 115(6):1083–1126, 1987.

D. S. Battisti and A. C. Hirst. Interannual variability in a tropical atmosphere-ocean model: Influence of the basic state, ocean geometry and nonlinearity. *Journal of the Atmospheric Sciences*, 46(12):1687–1712, 1989.

J. J. Benedetto. *Harmonic analysis and applications*, volume 23. CRC Press, 1996.

Y. Benjamini and Y. Hochberg. Controlling the false discovery rate: a practical and powerful approach to multiple testing. *Journal of the Royal Statistical Society. Series B (Methodological)*, pages 289–300, 1995.

R. Beranová and R. Huth. Time variations of the effects of circulation variability modes on European temperature and precipitation in winter. *International Journal of Climatology*, 28(2): 139–158, 2008.

J. O. Berger et al. Could Fisher, Jeffreys and Neyman have agreed on testing? *Statistical Science*, 18(1):1–32, 2003.

A. Bérut, A. Arakelyan, A. Petrosyan, S. Ciliberto, R. Dillenschneider, and E. Lutz. Experimental verification of Landauer's principle linking information and thermodynamics. *Nature*, 483 (7388):187, 2012.

J. Bjerknes. Atmospheric teleconnections from the equatorial Pacific. *Monthly Weather Review*, 97 (3):163–172, 1969.

S. Boccaletti, V. Latora, Y. Moreno, M. Chavez, and D.-U. Hwang. Complex networks: Structure and dynamics. *Physics reports*, 424(4):175–308, 2006.

R. N. Bracewell and R. N. Bracewell. *The Fourier transform and its applications*, volume 31999. McGraw-Hill New York, 1986.

M. Breakspear, M. Brammer, and P. A. Robinson. Construction of multivariate surrogate sets from nonlinear data using the wavelet transform. *Physica D: Nonlinear Phenomena*, 182(1-2): 1–22, 2003.

S. A. Broughton and K. M. Bryan. *Discrete Fourier analysis and wavelets: applications to signal and image processing*. John Wiley & Sons, 2011.

R. S. Burington and D. C. May. *Handbook of probability and statistics with tables*. Handbook Publishers, Inc.; Ohio, 1953.

A. J. Butte and I. S. Kohane. Mutual information relevance networks: functional genomic clustering using pairwise entropy measurements. In *Biocomputing 2000*, pages 418–429. World Scientific, 1999.

R. T. Canolty and R. T. Knight. The functional role of cross-frequency coupling. *Trends in Cognitive Sciences*, 14(11):506–515, 2010.

K.-S. Chan. On the validity of the method of surrogate data. *Nonlinear Dynamics and Time Series*, 11:77–97, 1997.

M. D. Chekroun, D. Kondrashov, and M. Ghil. Predicting stochastic systems by noise sampling, and application to the El Niño-Southern Oscillation. *Proceedings of the National Academy of Sciences*, 108(29):11766–11771, 2011.

D. Chen and C. Hellström. The influence of the North Atlantic Oscillation on the regional temperature variability in Sweden: spatial and temporal variations. *Tellus A*, 51(4):505–516, 1999.

Y.-Y. Chen and F.-F. Jin. Dynamical diagnostics of the SST annual cycle in the eastern equatorial Pacific: part I a linear coupled framework. *Climate Dynamics*, pages 1–22, 2017.

J. W. Cooley and J. W. Tukey. An algorithm for the machine calculation of complex Fourier series. *Mathematics of computation*, 19(90):297–301, 1965.

D. Coufal, J. Jakubík, N. Jajcay, J. Hlinka, A. Krakovská, and M. Paluš. Detection of coupling delay: A problem not yet solved. *Chaos: An Interdisciplinary Journal of Nonlinear Science*, 27(8): 083109, 2017.

T. M. Cover and J. A. Thomas. *Elements of information theory*. John Wiley & Sons, 2012.

cpc.ncep.noaa.gov. North Atlantic Oscillation (NAO). `http://www.cpc.ncep.noaa.gov/data/teledoc/nao.shtml`. Retrieved: 2018-02-14.

R. B. Darlington and A. F. Hayes. *Regression analysis and linear models: Concepts, applications, and implementation*. Guilford Publications, 2016.

I. Daubechies. *Ten lectures on wavelets*, volume 61. Siam, 1992.

M. Davey, M. Huddleston, K. Sperber, P. Braconnot, F. Bryan, D. Chen, R. Colman, C. Cooper, U. Cubasch, P. Delecluse, et al. STOIC: a study of coupled model climatology and variability in tropical ocean regions. *Climate Dynamics*, 18(5):403–420, 2002.

M. deCastro, N. Lorenzo, J. J. Taboada, M. Sarmiento, I. Alvarez, and M. Gomez-Gesteira. Influence of teleconnection patterns on precipitation variability and on river flow regimes in the Miño River basin (NW Iberian Peninsula). *Climate Research*, 32(1):63–73, 2006.

D. P. Dee, S. Uppala, A. Simmons, P. Berrisford, P. Poli, S. Kobayashi, U. Andrae, M. Balmaseda, G. Balsamo, P. Bauer, et al. The ERA-Interim reanalysis: Configuration and performance of the data assimilation system. *Quarterly Journal of the Royal Meteorological Society*, 137(656):553–597, 2011.

P. Delecluse, M. K. Davey, Y. Kitamura, S. Philander, M. Suarez, and L. Bengtsson. Coupled general circulation modeling of the tropical Pacific. *Journal of Geophysical Research: Oceans*, 103 (C7):14357–14373, 1998.

T. L. Delworth. North Atlantic interannual variability in a coupled ocean-atmosphere model. *Journal of Climate*, 9(10):2356–2375, 1996.

M. D. Dettinger, M. Ghil, and C. L. Keppenne. Interannual and interdecadal variability in United States surface-air temperatures, 1910-87. *Climatic Change*, 31(1):35–66, 1995.

R. V. Donner, S. Barbosa, J. Kurths, and N. Marwan. Understanding the Earth as a Complex System-recent advances in data analysis and modelling in Earth sciences. *The European Physical Journal-Special Topics*, 174(1):1–9, 2009.

R. V. Donner, M. Wiedermann, and J. F. Donges. Complex network techniques for climatological data analysis. *Nonlinear and Stochastic Climate Dynamics, edited by: Franzke, CL E. and O'Kane, TJ, Cambridge University Press, Cambridge*, pages 159–183, 2017.

O. J. Dunn. Estimation of the means of dependent variables. *The Annals of Mathematical Statistics*, pages 1095–1111, 1958.

I. Ebert-Uphoff and Y. Deng. A new type of climate network based on probabilistic graphical models: Results of boreal winter versus summer. *Geophysical Research Letters*, 39(19), 2012.

ecad.eu. ECA&D Daily data. `https://www.ecad.eu//dailydata/index.php`. Retrieved: 2017-02-13.

B. Efron and R. J. Tibshirani. *An introduction to the bootstrap*. CRC press, 1994.

J. Egger and H. Schilling. Stochastic forcing of planetary scale flow. *Journal of the Atmospheric Sciences*, 41(5):779–788, 1984.

A. V. Fedorov and S. G. Philander. A stability analysis of tropical ocean-atmosphere interactions: Bridging measurements and theory for El Niño. *Journal of Climate*, 14(14):3086–3101, 2001.

Y. Feliks, M. Ghil, and A. W. Robertson. Oscillatory climate modes in the Eastern Mediterranean and their synchronization with the North Atlantic Oscillation. *Journal of Climate*, 23(15):4060–4079, 2010.

I. Fernández, C. N. Hernández, and J. M. Pacheco. Is the North Atlantic Oscillation just a pink noise? *Physica A: Statistical Mechanics and its Applications*, 323:705–714, 2003.

C. K. Folland, T. N. Palmer, and D. E. Parker. Sahel rainfall and worldwide sea temperatures, 1901–85. *Nature*, 320(6063):602, 1986.

C. K. Folland, T. R. Karl, and M. Jim Salinger. Observed climate variability and change. *Weather*, 57(8):269–278, 2002.

I. Fountalis, A. Bracco, and C. Dovrolis. ENSO in CMIP5 simulations: network connectivity from the recent past to the twenty-third century. *Climate Dynamics*, 45(1-2):511–538, 2015.

K. Fraedrich. Estimating weather and climate predictability on attractors. *Journal of the Atmospheric Sciences*, 44(4):722–728, 1987.

A. M. Fraser and H. L. Swinney. Independent coordinates for strange attractors from mutual information. *Physical Review A*, 33(2):1134, 1986.

S. Frenzel and B. Pompe. Partial mutual information for coupling analysis of multivariate time series. *Physical Review Letters*, 99(20):204101, 2007.

X. Fu, B. Wang, T. Li, and J. P. McCreary. Coupling between northward-propagating, intraseasonal oscillations and sea surface temperature in the Indian Ocean. *Journal of the Atmospheric Sciences*, 60(15):1733–1753, 2003.

S. Gámiz-Fortis, D. Pozo-Vázquez, M. Esteban-Parra, and Y. Castro-Díez. Spectral characteristics and predictability of the NAO assessed through singular spectral analysis. *Journal of Geophysical Research: Atmospheres*, 107(D23), 2002.

F. Gans, A. Y. Schumann, J. W. Kantelhardt, T. Penzel, and I. Fietze. Cross-modulated amplitudes and frequencies characterize interacting components in complex systems. *Physical Review Letters*, 102(9):098701, 2009.

G. Gebbie, I. Eisenman, A. Wittenberg, and E. Tziperman. Modulation of westerly wind bursts by sea surface temperature: A semistochastic feedback for ENSO. *Journal of the Atmospheric Sciences*, 64(9):3281–3295, 2007.

M. Ghil and R. Vautard. Interdecadal oscillations and the warming trend in global temperature time series. *Nature*, 350(6316):324, 1991.

R. Glaser and D. Riemann. A thousand-year record of temperature variations for Germany and Central Europe based on documentary data. *Journal of Quaternary Science*, 24(5):437–449, 2009.

L. Goddard, S. J. Mason, S. E. Zebiak, C. F. Ropelewski, R. Basher, and M. A. Cane. Current approaches to seasonal to interannual climate predictions. *International Journal of Climatology*, 21(9):1111–1152, 2001.

G. H. Golub and C. F. Van Loan. Matrix computations. 1996. *Johns Hopkins University, Press, Baltimore, MD, USA*, pages 374–426, 1996.

C. W. Granger. Investigating causal relations by econometric models and cross-spectral methods. *Econometrica: Journal of the Econometric Society*, pages 424–438, 1969.

C. W. Granger. Testing for causality: a personal viewpoint. *Journal of Economic Dynamics and control*, 2:329–352, 1980.

C. W. Granger. Time series analysis, cointegration, and applications. *American Economic Review*, 94(3):421–425, 2004.

P. Grassberger. Do climatic attractors exist? *Nature*, 323(6089):609, 1986.

C. M. Grinstead and J. L. Snell. *Introduction to probability*. American Mathematical Soc., 2012.

A. Groth and M. Ghil. Multivariate singular spectrum analysis and the road to phase synchronization. *Physical Review E*, 84(3):036206, 2011.

A. Groth and M. Ghil. Monte Carlo singular spectrum analysis (SSA) revisited: Detecting oscillator clusters in multivariate datasets. *Journal of Climate*, 28(19):7873–7893, 2015.

A. Hannachi, I. Jolliffe, and D. Stephenson. Empirical orthogonal functions and related techniques in atmospheric science: A review. *International journal of climatology*, 27(9):1119–1152, 2007.

K. Hasselmann. Stochastic climate models part I. Theory. *Tellus*, 28(6):473–485, 1976.

S. Hastenrath and P. Lamb. On the dynamics and climatology of surface flow over the equatorial oceans. *Tellus*, 30(5):436–448, 1978.

G. H. Haug, R. Tiedemann, R. Zahn, and A. C. Ravelo. Role of panama uplift on oceanic freshwater balance. *Geology*, 29(3):207–210, 2001.

S. Hayes, L. Mangum, J. Picaut, A. Sumi, and K. Takeuchi. TOGA-TAO: A moored array for real-time measurements in the tropical Pacific Ocean. *Bulletin of the American Meteorological Society*, 72(3):339–347, 1991.

M. Haylock, N. Hofstra, A. Klein Tank, E. Klok, P. Jones, and M. New. A european daily high-resolution gridded data set of surface temperature and precipitation for 1950–2006. *Journal of Geophysical Research: Atmospheres*, 113(D20), 2008.

A. C. Hirst. Unstable and damped equatorial modes in simple coupled ocean-atmosphere models. *Journal of the Atmospheric Sciences*, 43(6):606–632, 1986.

K. Hlaváčková-Schindler, M. Paluš, M. Vejmelka, and J. Bhattacharya. Causality detection based on information-theoretic approaches in time series analysis. *Physics Reports*, 441(1):1–46, 2007.

J. Hlinka, D. Hartman, N. Jajcay, M. Vejmelka, R. Donner, N. Marwan, J. Kurths, and M. Palus. Regional and inter-regional effects in evolving climate networks. *Nonlinear Processes in Geophysics*, 21(2):451–462, 2014a.

J. Hlinka, D. Hartman, M. Vejmelka, D. Novotná, and M. Paluš. Non-linear dependence and teleconnections in climate data: sources, relevance, nonstationarity. *Climate Dynamics*, 42(7-8): 1873–1886, 2014b.

J. Hlinka, D. Hartman, N. Jajcay, D. Tomeček, J. Tintěra, and M. Paluš. Small-world bias of correlation networks: From brain to climate. *Chaos: An Interdisciplinary Journal of Nonlinear Science*, 27(3):035812, 2017a.

J. Hlinka, N. Jajcay, D. Hartman, and M. Paluš. Smooth information flow in temperature climate network reflects mass transport. *Chaos: An Interdisciplinary Journal of Nonlinear Science*, 27(3): 035811, 2017b.

R. V. Hogg and A. T. Craig. *Introduction to mathematical statistics.(5"" edition)*. Upper Saddle River, New Jersey: Prentice Hall, 1995.

S. Holm. A simple sequentially rejective multiple test procedure. *Scandinavian Journal of Statistics*, pages 65–70, 1979.

A. C. Hope. A simplified Monte Carlo significance test procedure. *Journal of the Royal Statistical Society. Series B (Methodological)*, pages 582–598, 1968.

B. Huang, V. F. Banzon, E. Freeman, J. Lawrimore, W. Liu, T. C. Peterson, T. M. Smith, P. W. Thorne, S. D. Woodruff, and H.-M. Zhang. Extended reconstructed sea surface temperature version 4 (ERSST. v4). Part I: upgrades and intercomparisons. *Journal of Climate*, 28(3):911–930, 2015.

L. Hubert and P. Arabie. Comparing partitions. *Journal of Classification*, 2(1):193–218, 1985.

J. Hurrell, Y. Kushnir, G. Ottersen, and M. Visbeck. The North Atlantic Oscillation: climatic significance and environmental impact. AGU. *Geophysical Monograph Series*, 134, 2003.

J. W. Hurrell. Decadal trends in the North Atlantic Oscillation: regional temperatures and precipitation. *Science*, 269(5224):676–679, 1995.

J. W. Hurrell. Influence of variations in extratropical wintertime teleconnections on Northern Hemisphere temperature. *Geophysical Research Letters*, 23(6):665–668, 1996.

J. W. Hurrell and R. Dickson. Climate variability over the North Atlantic. In *Marine Ecosystems and Climate Variation: The North Atlantic—A Comparative Perspective*, pages 15–314. Oxford, 2005.

J. W. Hurrell and H. Van Loon. Decadal variations in climate associated with the North Atlantic Oscillation. In *Climatic change at high elevation sites*, pages 69–94. Springer, 1997.

R. Huth. Potential of continental-scale circulation for the determination of local daily surface variables. *Theoretical and Applied Climatology*, 56(3-4):165–186, 1997.

I. Iglesias, M. N. Lorenzo, and J. J. Taboada. Seasonal predictability of the East atlantic pattern from sea surface temperatures. *PloS one*, 9(1):e86439, 2014.

M. Ionita, C. Boroneanț, and S. Chelcea. Seasonal modes of dryness and wetness variability over Europe and their connections with large scale atmospheric circulation and global sea surface temperature. *Climate Dynamics*, 45(9-10):2803–2829, 2015.

N. Jajcay and M. Paluš. Information transfer across temporal scales in atmospheric dynamics. In A. Banerjee, W. Ding, J. Dy, V. Lyubchich, and A. Rhines, editors, *Proceedings of the 6th International Workshop on Climate Informatics: CI 2016*, pages 113–116. NCAR Technical Note NCAR/TN-529+PROC, 2016a.

N. Jajcay and M. Paluš. Statistical modelling in climate science. In B. Brejová, editor, *Proceedings of the 16th ITAT Conference Information Technologies - Applications and Theory*, pages 102–109, 2016b.

N. Jajcay and M. Paluš. Štatistické modelovanie javu El Niño-Južná oscilácia v klimatológii (in Slovak). *Pokroky matematiky, fyziky a astronomie*, (1):52–70, 2017.

N. Jajcay, J. Hlinka, S. Kravtsov, A. A. Tsonis, and M. Paluš. Time scales of the European surface air temperature variability: The role of the 7–8 year cycle. *Geophysical Research Letters*, 43(2): 902–909, 2016.

N. Jajcay, S. Kravtsov, G. Sugihara, A. A. Tsonis, and M. Paluš. Synchronization and causality across time-scales in El Niño/Southern Oscillation. In review in *npj Climate and Atmospheric Science*, 2018.

N. Jiang, J. D. Neelin, and M. Ghil. Quasi-quadrennial and quasi-biennial variability in the equatorial pacific. *Climate Dynamics*, 12(2):101–112, 1995.

E. K. Jin, J. L. Kinter, B. Wang, C.-K. Park, I.-S. Kang, B. Kirtman, J.-S. Kug, A. Kumar, J.-J. Luo, J. Schemm, et al. Current status of ENSO prediction skill in coupled ocean-atmosphere models. *Climate Dynamics*, 31(6):647–664, 2008.

F.-F. Jin. Tropical ocean-atmosphere interaction, the Pacific cold tongue, and the El Niño-Southern Oscillation. *Science*, 274(5284):76–78, 1996.

F.-F. Jin. An equatorial ocean recharge paradigm for ENSO. Part I: Conceptual model. *Journal of the Atmospheric Sciences*, 54(7):811–829, 1997a.

F.-F. Jin. An equatorial ocean recharge paradigm for ENSO. Part II: a stripped-down coupled model. *Journal of the Atmospheric Sciences*, 54(7):830–847, 1997b.

F.-F. Jin, J. D. Neelin, and M. Ghil. El Niño on the devil's staircase: annual subharmonic steps to chaos. *Science*, 264(5155):70–72, 1994.

F.-F. Jin, S. T. Kim, and L. Bejarano. A coupled-stability index for ENSO. *Geophysical Research Letters*, 33(23), 2006.

V. Jirsa and V. Müller. Cross-frequency coupling in real and virtual brain networks. *Frontiers in Computational Neuroscience*, 7:78, 2013.

S. D. Johnson, D. S. Battisti, and E. Sarachik. Empirically derived Markov models and prediction of tropical Pacific sea surface temperature anomalies. *Journal of Climate*, 13(1):3–17, 2000a.

S. D. Johnson, D. S. Battisti, and E. Sarachik. Seasonality in an empirically derived Markov model of tropical Pacific sea surface temperature anomalies. *Journal of Climate*, 13(18):3327–3335, 2000b.

P. Jones, T. Jonsson, and D. Wheeler. Extension to the North Atlantic Oscillation using early instrumental pressure observations from Gibraltar and south-west Iceland. *International Journal of climatology*, 17(13):1433–1450, 1997.

P. Jones, K. Trenberth, P. Ambenje, R. Bojariu, D. Easterling, T. Klein, D. Parker, J. Renwick, M. Rusticucci, B. Soden, et al. Observations: surface and atmospheric climate change. *Climate Change*, pages 235–336, 2007.

P. Jones, C. Harpham, and B. Vinther. Winter-responding proxy temperature reconstructions and the North Atlantic Oscillation. *Journal of Geophysical Research: Atmospheres*, 119(11):6497–6505, 2014.

P. D. Jones, T. J. Osborn, and K. R. Briffa. Pressure-Based Measures of the North Atlantic Oscillation (NAO): A Comparison and an Assessment of Changes in the Strength of the NAO and in its Influence on Surface Climate Parameters. *The North Atlantic Oscillation: climatic significance and environmental impact*, pages 51–62, 2003.

S. A. Josey, S. Somot, and M. Tsimplis. Impacts of atmospheric modes of variability on Mediterranean Sea surface heat exchange. *Journal of Geophysical Research: Oceans*, 116(C2), 2011.

H. F. Kaiser. The varimax criterion for analytic rotation in factor analysis. *Psychometrika*, 23(3): 187–200, 1958.

E. Kalnay, M. Kanamitsu, R. Kistler, W. Collins, D. Deaven, L. Gandin, M. Iredell, S. Saha, G. White, J. Woollen, et al. The NCEP/NCAR 40-year reanalysis project. *Bulletin of the American meteorological Society*, 77(3):437–471, 1996.

Y. Kang, D. Belušić, and K. Smith-Miles. Detecting and classifying events in noisy time series. *Journal of the Atmospheric Sciences*, 71(3):1090–1104, 2014.

R. A. Kerr. Did the tropical Pacific drive the world's warming? *Science*, 266(5185):544–546, 1994.

K.-Y. Kim. Investigation of ENSO variability using cyclostationary EOFs of observational data. *Meteorology and Atmospheric Physics*, 81(3-4):149–168, 2002.

A. Klein Tank, J. Wijngaard, G. Können, R. Böhm, G. Demarée, A. Gocheva, M. Mileta, S. Pashiardis, L. Hejkrlik, C. Kern-Hansen, et al. Daily dataset of 20th-century surface air temperature and precipitation series for the European Climate Assessment. *International journal of climatology*, 22(12):1441–1453, 2002.

A. N. Kolmogorov. The local structure of turbulence in incompressible viscous fluid for very large Reynolds numbers. In *Dokl. Akad. Nauk SSSR*, volume 30, pages 299–303, 1941.

D. Kondrashov, S. Kravtsov, A. W. Robertson, and M. Ghil. A hierarchy of data-based ENSO models. *Journal of Climate*, 18(21):4425–4444, 2005.

D. Kondrashov, M. D. Chekroun, and M. Ghil. Data-driven non-Markovian closure models. *Physica D: Nonlinear Phenomena*, 297:33–55, 2015.

A. Krakovská, J. Jakubík, M. Chvosteková, D. Coufal, N. Jajcay, and M. Paluš. Comparison of six methods for the detection of causality in a bivariate time series. *Physical Review E*, 97(4): 042207, 2018.

A. Kraskov, H. Stögbauer, and P. Grassberger. Estimating mutual information. *Physical Review E*, 69(6):066138, 2004.

S. Kravtsov, D. Kondrashov, and M. Ghil. Multilevel regression modeling of nonlinear processes: Derivation and applications to climatic variability. *Journal of Climate*, 18(21):4404–4424, 2005.

S. Kullback and R. A. Leibler. On information and sufficiency. *The Annals of Mathematical Statistics*, 22(1):79–86, 1951.

A. Kumar, A. Leetmaa, and M. Ji. Simulations of atmospheric variability induced by sea surface temperatures and implications for global warming. *Science*, 266(5185):632–634, 1994.

Y. Kuramoto. Self-entrainment of a population of coupled non-linear oscillators. In *International symposium on mathematical problems in theoretical physics*, pages 420–422. Springer, 1975.

Y. Kuramoto. *Chemical oscillations, waves, and turbulence*. Springer-Verlag, New York, NY, USA, 1984.

N. K. Larkin and D. Harrison. Enso warm (el niño) and cold (la niña) event life cycles: Ocean surface anomaly patterns, their symmetries, asymmetries, and implications. *Journal of Climate*, 15(10):1118–1140, 2002.

M. Latif and T. P. Barnett. Causes of decadal climate variability over the North Pacific and North America. *Science*, 266(5185):634–637, 1994.

M. Latif and T. P. Barnett. Interactions of the tropical oceans. *Journal of Climate*, 8(4):952–964, 1995.

M. Latif, R. Kleeman, and C. Eckert. Greenhouse warming, decadal variability, or El Niño? An attempt to understand the anomalous 1990s. *Journal of Climate*, 10(9):2221–2239, 1997.

K.-M. Lau. Elements of a stochastic-dynamical theory of the long-term variability of the El Niño/Southern Oscillation. *Journal of the Atmospheric Sciences*, 42(14):1552–1558, 1985.

N.-C. Lau and M. J. Nath. Impact of ENSO on SST variability in the North Pacific and North Atlantic: Seasonal dependence and role of extratropical sea-air coupling. *Journal of Climate*, 14 (13):2846–2866, 2001.

W. K.-M. Lau and D. E. Waliser. *Intraseasonal variability in the atmosphere-ocean climate system*. Springer Science & Business Media, 2011.

H. Ledford. How to solve the world's biggest problems. *Nature*, 525:308–311, 2015.

J. Lee Rodgers and W. A. Nicewander. Thirteen ways to look at the correlation coefficient. *The American Statistician*, 42(1):59–66, 1988.

K. Lehnertz, S. Bialonski, M.-T. Horstmann, D. Krug, A. Rothkegel, M. Staniek, and T. Wagner. Synchronization phenomena in human epileptic brain networks. *Journal of Neuroscience Methods*, 183(1):42–48, 2009.

J. Li, S.-P. Xie, E. R. Cook, G. Huang, R. D'arrigo, F. Liu, J. Ma, and X.-T. Zheng. Interdecadal modulation of El Niño amplitude during the past millennium. *Nature Climate Change*, 1(2):114, 2011.

I. Lins, M. Moura, M. Silva, E. Droguett, D. Veleda, M. Araujo, and C. Jacinto. Sea surface temperature prediction via support vector machines combined with particle swarm optimization. In *Proceedings of the 10th International Probabilistic Safety Assessment and Management Conference-PSAM*, volume 10, 2010.

E. N. Lorenz. Dimension of weather and climate attractors. *Nature*, 353(6341):241, 1991.

S. Lovejoy and D. Schertzer. *The weather and climate: emergent laws and multifractal cascades*. Cambridge University Press, 2013.

H. Lütkepohl. *New introduction to multiple time series analysis*. Springer Science & Business Media, 2005.

M. E. Mann and J. Park. Spatial correlations of interdecadal variation in global surface temperatures. *Geophysical Research Letters*, 20(11):1055–1058, 1993.

M. E. Mann and J. Park. Global-scale modes of surface temperature variability on interannual to century timescales. *Journal of Geophysical Research: Atmospheres*, 99(D12):25819–25833, 1994.

M. E. Mann and J. Park. Greenhouse warming and changes in the seasonal cycle of temperature: Model versus observations. *Geophysical Research Letters*, 23(10):1111–1114, 1996a.

M. E. Mann and J. Park. Joint spatiotemporal modes of surface temperature and sea level pressure variability in the Northern Hemisphere during the last century. *Journal of Climate*, 9(9):2137–2162, 1996b.

N. J. Mantua and D. S. Battisti. Evidence for the delayed oscillator mechanism for ENSO: The "observed" oceanic Kelvin mode in the far western Pacific. *Journal of Physical Oceanography*, 24 (3):691–699, 1994.

J. Marshall, Y. Kushnir, D. Battisti, P. Chang, A. Czaja, R. Dickson, J. Hurrell, M. McCARTNEY, R. Saravanan, and M. Visbeck. North Atlantic climate variability: phenomena, impacts and mechanisms. *International Journal of Climatology*, 21(15):1863–1898, 2001.

P. McCullagh and J. A. Nelder. *Generalized Linear Models*. Chapman and Hall, 1989.

S. McGregor, A. Timmermann, M. England, O. Elison Timm, and A. Wittenberg. Inferred changes in El Niño-Southern Oscillation variance over the past six centuries. *Climate of the Past*, 9(5): 2269–2284, 2013.

M. J. McPhaden. The tropical atmosphere ocean array is completed. *Bulletin of the American Meteorological Society*, 76(5):739–741, 1995.

M. J. McPhaden, A. J. Busalacchi, R. Cheney, J.-R. Donguy, K. S. Gage, D. Halpern, M. Ji, P. Julian, G. Meyers, G. T. Mitchum, et al. The Tropical Ocean-Global Atmosphere observing system: A decade of progress. *Journal of Geophysical Research: Oceans*, 103(C7):14169–14240, 1998.

G. A. Meehl. The annual cycle and interannual variability in the tropical Pacific and Indian Ocean regions. *Monthly Weather Review*, 115(1):27–50, 1987.

metoffice.gov.uk. Hadley Centre Central England Temperature (HadCET) dataset. `https://www.metoffice.gov.uk/hadobs/hadcet/`. Retrieved: 2018-02-26.

W. Metz. Transient eddy forcing of low-frequency atmospheric variability. *Journal of the Atmospheric Sciences*, 44(17):2407–2417, 1987.

T. P. Mitchell and J. M. Wallace. The annual cycle in equatorial convection and sea surface temperature. *Journal of Climate*, 5(10):1140–1156, 1992.

A. H. Monahan, J. C. Fyfe, M. H. Ambaum, D. B. Stephenson, and G. R. North. Empirical orthogonal functions: The medium is the message. *Journal of Climate*, 22(24):6501–6514, 2009.

V. Moron, R. Vautard, and M. Ghil. Trends, interdecadal and interannual oscillations in global sea-surface temperatures. *Climate Dynamics*, 14(7-8):545–569, 1998.

ncdc.noaa.gov. North Atlantic Oscillation (NAO). `https://www.ncdc.noaa.gov/teleconnections/nao/`. Retrieved: 2018-02-14.

ncep.noaa.gov. East Atlantic (EA). `http://www.cpc.ncep.noaa.gov/data/teledoc/ea.shtml`. Retrieved: 2018-02-15.

J. D. Neelin, D. S. Battisti, A. C. Hirst, F.-F. Jin, Y. Wakata, T. Yamagata, and S. E. Zebiak. ENSO theory. *Journal of Geophysical Research: Oceans*, 103(C7):14261–14290, 1998.

M. E. Newman. The structure and function of complex networks. *SIAM review*, 45(2):167–256, 2003.

J. Neyman and E. S. Pearson. IX. On the problem of the most efficient tests of statistical hypotheses. *Phil. Trans. R. Soc. Lond. A*, 231(694-706):289–337, 1933.

C. Nicolis and G. Nicolis. Is there a climatic attractor? *Nature*, 311(5986):529, 1984.

E. W. Noreen. *Computer-intensive methods for testing hypotheses*. Wiley New York, 1989.

T. J. Osborn, K. R. Briffa, S. F. Tett, P. D. Jones, and R. M. Trigo. Evaluation of the North Atlantic Oscillation as simulated by a coupled climate model. *Climate Dynamics*, 15(9):685–702, 1999.

M. Paluš. Testing for nonlinearity using redundancies: Quantitative and qualitative aspects. *Physica D: Nonlinear Phenomena*, 80(1-2):186–205, 1995.

M. Paluš. Detecting nonlinearity in multivariate time series. *Physics Letters A*, 213(3-4):138–147, 1996.

M. Paluš. From nonlinearity to causality: statistical testing and inference of physical mechanisms underlying complex dynamics. *Contemporary Physics*, 48(6):307–348, 2007.

M. Paluš. Bootstrapping multifractals: Surrogate data from random cascades on wavelet dyadic trees. *Physical Review Letters*, 101(13):134101, 2008.

M. Paluš. Cross-scale interactions and information transfer. *Entropy*, 16(10):5263–5289, 2014a.

M. Paluš. Multiscale atmospheric dynamics: cross-frequency phase-amplitude coupling in the air temperature. *Physical Review Letters*, 112(7):078702, 2014b.

M. Palus and D. Hoyer. Detecting nonlinearity and phase synchronization with surrogate data. *IEEE Engineering in Medicine and Biology Magazine*, 17(6):40–45, 1998.

M. Paluš and D. Novotná. Testing for nonlinearity in weather records. *Physics Letters A*, 193(1):67–74, 1994.

M. Paluš and D. Novotná. Phase-coherent oscillatory modes in solar and geomagnetic activity and climate variability. *Journal of Atmospheric and Solar-Terrestrial Physics*, 71(8-9):923–930, 2009.

M. Paluš and M. Vejmelka. Directionality of coupling from bivariate time series: How to avoid false causalities and missed connections. *Physical Review E*, 75(5):056211, 2007.

M. Paluš, V. Albrecht, and I. Dvořák. Information theoretic test for nonlinearity in time series. *Physics Letters A*, 175(3-4):203–209, 1993.

M. Paluš, V. Komárek, Z. Hrnčíř, and K. Štěrbová. Synchronization as adjustment of information rates: detection from bivariate time series. *Physical Review E*, 63(4):046211, 2001.

M. Paluš, D. Novotná, and P. Tichavský. Shifts of seasons at the European mid-latitudes: Natural fluctuations correlated with the North Atlantic Oscillation. *Geophysical Research Letters*, 32(12), 2005.

M. Paluš. Detecting phase synchronization in noisy systems. *Physics Letters A*, 235(4):341–351, 1997.

M. Paluš and D. Novotná. Enhanced Monte Carlo Singular System Analysis and detection of period 7.8 years oscillatory modes in the monthly NAO index and temperature records. *Nonlinear Processes in Geophysics*, 11(5/6):721–729, 2004.

M. Paluš and D. Novotná. Northern Hemisphere patterns of phase coherence between so-lar/geomagnetic activity and NCEP/NCAR and ERA40 near-surface air temperature in period 7-8 years oscillatory modes. *Nonlinear Processes in Geophysics*, 18(2):251, 2011.

Y. H. Pan and A. H. Oort. Correlation analyses between sea surface temperature anomalies in the eastern equatorial Pacific and the world ocean. *Climate Dynamics*, 4(3):191–205, 1990.

H. Panofsky and I. Van der Hoven. Spectra and cross-spectra of velocity components in the mesometeorological range. *Quarterly Journal of the Royal Meteorological Society*, 81(350):603–606, 1955.

D. Parker, P. Jones, C. Folland, and A. Bevan. Interdecadal changes of surface temperature since the late nineteenth century. *Journal of Geophysical Research: Atmospheres*, 99(D7):14373–14399, 1994.

D. Parker, E. Horton, D. Cullum, and C. Folland. Global and regional climate in 1995. *Weather*, 51(6):202–210, 1996.

K. Patil, M. Deo, and M. Ravichandran. Prediction of sea surface temperature by combining numerical and neural techniques. *Journal of Atmospheric and Oceanic Technology*, 33(8):1715–1726, 2016.

K. Pearson. X. On the criterion that a given system of deviations from the probable in the case of a correlated system of variables is such that it can be reasonably supposed to have arisen from random sampling. *The London, Edinburgh, and Dublin Philosophical Magazine and Journal of Science*, 50(302):157–175, 1900.

C. Penland. Random forcing and forecasting using principal oscillation pattern analysis. *Monthly Weather Review*, 117(10):2165–2185, 1989.

C. Penland. A stochastic model of Indo-Pacific sea surface temperature anomalies. *Physica D: Nonlinear Phenomena*, 98(2-4):534–558, 1996.

C. Penland and L. Matrosova. Prediction of tropical Atlantic sea surface temperatures using linear inverse modeling. *Journal of Climate*, 11(3):483–496, 1998.

C. Penland and P. D. Sardeshmukh. The optimal growth of tropical sea surface temperature anomalies. *Journal of Climate*, 8(8):1999–2024, 1995.

J. Perlwitz and H.-F. Graf. The statistical connection between tropospheric and stratospheric circulation of the Northern Hemisphere in winter. *Journal of Climate*, 8(10):2281–2295, 1995.

S. Philander, T. Yamagata, and R. Pacanowski. Unstable air-sea interactions in the tropics. *Journal of the Atmospheric Sciences*, 41(4):604–613, 1984.

S. G. Philander and A. Fedorov. Is El Niño sporadic or cyclic? *Annual Review of Earth and Planetary Sciences*, 31(1):579–594, 2003.

S. G. H. Philander. El niño southern oscillation phenomena. *Nature*, 302(5906):295, 1983.

J. Picaut, F. Masia, and Y. Du Penhoat. An advective-reflective conceptual model for the oscillatory nature of the ENSO. *Science*, 277(5326):663–666, 1997.

A. Pikovsky, M. Rosenblum, and J. Kurths. *Synchronization: a universal concept in nonlinear sciences*, volume 12. Cambridge university press, 2003.

G. Plaut and R. Vautard. Spells of low-frequency oscillations and weather regimes in the Northern Hemisphere. *Journal of the Atmospheric Sciences*, 51(2):210–236, 1994.

G. Plaut, M. Ghil, and R. Vautard. Interannual and interdecadal variability in 335 years of central England temperatures. *Science*, 268(5211):710–713, 1995.

L. Pokorná and R. Huth. Climate impacts of the NAO are sensitive to how the NAO is defined. *Theoretical and Applied Climatology*, 119(3-4):639–652, 2015.

L. L. Portes and L. A. Aguirre. Matrix formulation and singular-value decomposition algorithm for structured varimax rotation in multivariate singular spectrum analysis. *Physical Review E*, 93(5):052216, 2016.

D. Pozo-Vázquez, M. Esteban-Parra, F. Rodrigo, and Y. Castro-Diez. An analysis of the variability of the north atlantic oscillation in the time and the frequency domains. *International Journal of Climatology*, 20:1675–1692, 2000.

D. Pozo-Vázquez, M. Esteban-Parra, F. Rodrigo, and Y. Castro-Diez. A study of NAO variability and its possible non-linear influences on European surface temperature. *Climate Dynamics*, 17 (9):701–715, 2001.

M. B. Priestley. Spectral analysis and time series. 1981.

E. M. Rasmusson and T. H. Carpenter. Variations in tropical sea surface temperature and surface wind fields associated with the Southern Oscillation/El Niño. *Monthly Weather Review*, 110(5): 354–384, 1982.

E. M. Rasmusson, X. Wang, and C. F. Ropelewski. The biennial component of ENSO variability. *Journal of Marine Systems*, 1(1-2):71–96, 1990.

N. Rayner, D. E. Parker, E. Horton, C. Folland, L. Alexander, D. Rowell, E. Kent, and A. Kaplan. Global analyses of sea surface temperature, sea ice, and night marine air temperature since the late nineteenth century. *Journal of Geophysical Research: Atmospheres*, 108(D14), 2003.

F. Rodrigo, D. Pozo-Vázquez, M. Esteban-Parra, and Y. Castro-Díez. A reconstruction of the winter North Atlantic Oscillation index back to AD 1501 using documentary data in southern Spain. *Journal of Geophysical Research: Atmospheres*, 106(D14):14805–14818, 2001.

E. Rodriguez, N. George, J.-P. Lachaux, J. Martinerie, B. Renault, and F. J. Varela. Perception's shadow: long-distance synchronization of human brain activity. *Nature*, 397(6718):430, 1999.

C. Rodríguez-Puebla, A. H. Encinas, L. A. García-Casado, and S. Nieto. Trends in warm days and cold nights over the Iberian Peninsula: relationships to large-scale variables. *Climatic Change*, 100(3-4):667–684, 2010.

J. C. Rogers. The association between the North Atlantic Oscillation and the Southern Oscillation in the northern hemisphere. *Monthly Weather Review*, 112(10):1999–2015, 1984.

J. C. Rogers. Patterns of low-frequency monthly sea level pressure variability (1899–1986) and associated wave cyclone frequencies. *Journal of Climate*, 3(12):1364–1379, 1990.

H. Rose and P. Sulem. Fully developed turbulence and statistical mechanics. *Journal de Physique*, 39(5):441–484, 1978.

J. Runge, V. Petoukhov, J. F. Donges, J. Hlinka, N. Jajcay, M. Vejmelka, D. Hartman, N. Marwan, M. Paluš, and J. Kurths. Identifying causal gateways and mediators in complex spatio-temporal systems. *Nature Communications*, 6, 2015.

D. Rybski, S. Havlin, and A. Bunde. Phase synchronization in temperature and precipitation records. *Physica A: Statistical Mechanics and its Applications*, 320:601–610, 2003.

J. Sáenz, C. Rodríguez-Puebla, J. Fernández, and J. Zubillaga. Interpretation of interannual winter temperature variations over southwestern Europe. *Journal of Geophysical Research: Atmospheres*, 106(D18):20641–20651, 2001.

N. Salmaso. Influence of atmospheric modes of variability on a deep lake south of the Alps. *Climate Research*, 51(2):125–133, 2012.

B. Saltzman. *Dynamical paleoclimatology: generalized theory of global climate change*, volume 80. Academic Press, 2002.

C. Schäfer, M. G. Rosenblum, J. Kurths, and H.-H. Abel. Heartbeat synchronized with ventilation. *Nature*, 392(6673):239, 1998.

E. R. Scheinerman. *Invitation to dynamical systems*. Courier Corporation, 2012.

D. Schertzer, M. Larchevêque, and S. Lovejoy. Beyond multifractal phenomenology of intermittency: Nonlinear dynamics and multifractal renormalization. *Chaos, Fractals and models*, 96: 53–64, 1998.

E. K. Schneider, B. P. Kirtman, D. G. DeWitt, A. Rosati, L. Ji, and J. J. Tribbia. Retrospective ENSO forecasts: sensitivity to atmospheric model and ocean resolution. *Monthly Weather Review*, 131 (12):3038–3060, 2003.

T. Schreiber. Interdisciplinary application of nonlinear time series methods. *Physics Reports*, 308 (1):1–64, 1999.

T. Schreiber. Measuring information transfer. *Physical Review Letters*, 85(2):461, 2000.

T. Schreiber and A. Schmitz. Improved surrogate data for nonlinearity tests. *Physical Review Letters*, 77(4):635, 1996.

T. Schreiber and A. Schmitz. Surrogate time series. *Physica D: Nonlinear Phenomena*, 142(3-4): 346–382, 2000.

G. Schwarz et al. Estimating the dimension of a model. *The Annals of Statistics*, 6(2):461–464, 1978.

C. E. Shannon. A mathematical theory of communication. *ACM SIGMOBILE Mobile Computing and Communications Review*, 5(1):3–55, 2001.

shorstmayer.com. Scales of Atmospheric Motion. `http://www.shorstmeyer.com/msj/geo165/scales.html`. Retrieved: 2018-01-26.

J. Shukla. Predictability in the midst of chaos: A scientific basis for climate forecasting. *Science*, 282(5389):728–731, 1998.

K. Stein, N. Schneider, A. Timmermann, and F.-F. Jin. Seasonal synchronization of ENSO events in a linear stochastic model. *Journal of Climate*, 23(21):5629–5643, 2010.

K. Stein, A. Timmermann, N. Schneider, F.-F. Jin, and M. F. Stuecker. ENSO seasonal synchronization theory. *Journal of Climate*, 27(14):5285–5310, 2014.

D. B. Stephenson, V. Pavan, and R. Bojariu. Is the North Atlantic Oscillation a random walk? *International Journal of Climatology*, 20(1):1–18, 2000.

W. Stern and K. Miyakoda. Feasibility of seasonal forecasts inferred from multiple GCM simulations. *Journal of Climate*, 8(5):1071–1085, 1995.

R. Steuer, J. Kurths, C. O. Daub, J. Weise, and J. Selbig. The mutual information: detecting and evaluating dependencies between variables. *Bioinformatics*, 18(suppl_2):S231–S240, 2002.

A. R. Stine, P. Huybers, and I. Y. Fung. Changes in the phase of the annual cycle of surface temperature. *Nature*, 457(7228):435, 2009.

A. Stuart, K. Ord, and S. Arnold. Kendall's Advanced Theory of Statistics, Classical Inference and the Linear Model, volume Volume 2A (2007 reprint), 1999.

M. F. Stuecker, A. Timmermann, F.-F. Jin, S. McGregor, and H.-L. Ren. A combination mode of the annual cycle and the El Niño/Southern Oscillation. *Nature Geoscience*, 6(7):540, 2013.

M. F. Stuecker, F.-F. Jin, and A. Timmermann. El Niño-Southern Oscillation frequency cascade. *Proceedings of the National Academy of Sciences*, 112(44):13490–13495, 2015.

M. J. Suarez and P. S. Schopf. A delayed action oscillator for ENSO. *Journal of the Atmospheric Sciences*, 45(21):3283–3287, 1988.

P. Suppes. *A probabilistic theory of causality*. North-Holland Publishing Company Amsterdam, 1970.

P. Sura, M. Newman, C. Penland, and P. Sardeshmukh. Multiplicative noise and non-Gaussianity: A paradigm for atmospheric regimes? *Journal of the atmospheric sciences*, 62(5):1391–1409, 2005.

F. Takens. Detecting strange attractors in turbulence. In *Dynamical systems and turbulence, Warwick 1980*, pages 366–381. Springer, 1981.

A. H. Taylor and J. A. Stephens. The north atlantic oscillation and the latitude of the gulf stream. *Tellus A: Dynamic Meteorology and Oceanography*, 50(1):134–142, 1998.

K. E. Taylor, R. J. Stouffer, and G. A. Meehl. An overview of CMIP5 and the experiment design. *Bulletin of the American Meteorological Society*, 93(4):485–498, 2012.

J. Theiler, S. Eubank, A. Longtin, B. Galdrikian, and J. D. Farmer. Testing for nonlinearity in time series: the method of surrogate data. *Physica D: Nonlinear Phenomena*, 58(1-4):77–94, 1992.

M. Thiel, M. C. Romano, J. Kurths, M. Rolfs, and R. Kliegl. Twin surrogates to test for complex synchronisation. *EPL (Europhysics Letters)*, 75(4):535, 2006.

C. Thompson and D. Battisti. A linear stochastic dynamical model of ENSO. Part I: Model development. *Journal of Climate*, 13(15):2818–2832, 2000.

C. Thompson and D. Battisti. A linear stochastic dynamical model of ENSO. Part II: Analysis. *Journal of Climate*, 14(4):445–466, 2001.

A. Timmermann, M. Latif, R. Voss, and A. Grötzner. Northern Hemispheric interdecadal variability: A coupled air-sea mode. *Journal of Climate*, 11(8):1906–1931, 1998.

C. Torrence and G. P. Compo. A practical guide to wavelet analysis. *Bulletin of the American Meteorological society*, 79(1):61–78, 1998.

C. Torrence and P. J. Webster. The annual cycle of persistence in the El Nño/Southern Oscillation. *Quarterly Journal of the Royal Meteorological Society*, 124(550):1985–2004, 1998.

K. E. Trenberth. Recent observed interdecadal climate changes in the Northern Hemisphere. *Bulletin of the American Meteorological Society*, 71(7):988–993, 1990.

K. E. Trenberth. The definition of El Niño. *Bulletin of the American Meteorological Society*, 78(12): 2771–2777, 1997.

K. E. Trenberth and D. P. Stepaniak. Indices of El Niño evolution. *Journal of Climate*, 14(8): 1697–1701, 2001.

R. M. Trigo, D. Pozo-Vázquez, T. J. Osborn, Y. Castro-Díez, S. Gámiz-Fortis, and M. J. Esteban-Parra. North Atlantic Oscillation influence on precipitation, river flow and water resources in the Iberian Peninsula. *International Journal of Climatology*, 24(8):925–944, 2004.

A. Tsonis and J. Elsner. The weather attractor over very short timescales. *Nature*, 333(6173):545, 1988.

A. A. Tsonis and P. J. Roebber. The architecture of the climate network. *Physica A: Statistical Mechanics and its Applications*, 333:497–504, 2004.

A. A. Tsonis, K. L. Swanson, and P. J. Roebber. What do networks have to do with climate? *Bulletin of the American Meteorological Society*, 87(5):585–595, 2006.

E. Tziperman, L. Stone, M. A. Cane, and H. Jarosh. El Nino chaos: Overlapping of resonances between the seasonal cycle and the Pacific ocean-atmosphere oscillator. *Science*, 264(5155): 72–74, 1994.

H. Van den Dool. *Empirical methods in short-term climate prediction*. Oxford University Press, 2007.

D. A. Vasseur and P. Yodzis. The color of environmental noise. *Ecology*, 85(4):1146–1152, 2004.

R. Vautard and M. Ghil. Singular spectrum analysis in nonlinear dynamics, with applications to paleoclimatic time series. *Physica D: Nonlinear Phenomena*, 35(3):395–424, 1989.

G. A. Vecchi and A. T. Wittenberg. El Niño and our future climate: where do we stand? *Wiley Interdisciplinary Reviews: Climate Change*, 1(2):260–270, 2010.

M. Vejmelka and M. Paluš. Inferring the directionality of coupling with conditional mutual information. *Physical Review E*, 77(2):026214, 2008.

M. Vejmelka, L. Pokorná, J. Hlinka, D. Hartman, N. Jajcay, and M. Paluš. Non-random correlation structures and dimensionality reduction in multivariate climate data. *Climate Dynamics*, 44 (9-10):2663–2682, 2015.

V. Venema, S. Bachner, H. W. Rust, and C. Simmer. Statistical characteristics of surrogate data based on geophysical measurements. *Nonlinear Processes in Geophysics*, 13(4):449, 2006.

S. M. Vicente-Serrano and J. I. López-Moreno. The influence of atmospheric circulation at different spatial scales on winter drought variability through a semi-arid climatic gradient in northeast Spain. *International Journal of Climatology*, 26(11):1427–1453, 2006.

O. Viron, J. Dickey, and M. Ghil. Global modes of climate variability. *Geophysical Research Letters*, 40(9):1832–1837, 2013.

H. von Storch and F. W. Zwiers. Statistical analysis in climate research, 2002.

G. Walker. On periodicity in series of related terms. *Proceedings of the Royal Society of London*, 131 (818):518–532, 1931.

G. Walker. World Weather V Memories R. *Meteor. Soc.*, 4:53–84, 1932.

C. J. Wallace and T. J. Osborn. Recent and future modulation of the annual cycle. *Climate Research*, 22(1):1–11, 2002.

J. M. Wallace and D. S. Gutzler. Teleconnections in the geopotential height field during the Northern Hemisphere winter. *Monthly Weather Review*, 109(4):784–812, 1981.

B. Wang. On the annual cycle in the tropical eastern central Pacific. *Journal of Climate*, 7(12): 1926–1942, 1994.

B. Wang and S.-I. An. Why the properties of El Niño changed during the late 1970s. *Geophysical Research Letters*, 28(19):3709–3712, 2001.

B. Wang, Q. Ding, X. Fu, I.-S. Kang, K. Jin, J. Shukla, and F. Doblas-Reyes. Fundamental challenge in simulation and prediction of summer monsoon rainfall. *Geophysical Research Letters*, 32(15), 2005.

C. Wang. A unified oscillator model for the El Niño-Southern Oscillation. *Journal of Climate*, 14 (1):98–115, 2001.

C. Wang, R. H. Weisberg, and J. I. Virmani. Western Pacific interannual variability associated with the El Niño-Southern Oscillation. *Journal of Geophysical Research: Oceans*, 104(C3):5131–5149, 1999.

C. Wang, C. Deser, J.-Y. Yu, P. DiNezio, and A. Clement. El Niño and southern oscillation (ENSO): a review. *Coral Reefs of the Eastern Pacific*, pages 85–106, 2016.

L. Wang, J.-Y. Yu, and H. Paek. Enhanced biennial variability in the Pacific due to Atlantic capacitor effect. *Nature Communications*, 8:14887, 2017.

P. Webster. The annual cycle and the predictability of the tropical coupled ocean-atmosphere system. *Meteorology and Atmospheric Physics*, 56(1-2):33–55, 1995.

R. H. Weisberg and C. Wang. A western Pacific oscillator paradigm for the El Niño-Southern Oscillation. *Geophysical Research Letters*, 24(7):779–782, 1997.

G. B. Wetherill. *Regression analysis with application*. Chapman & Hall, Ltd., 1987.

M. Wiedermann, A. Radebach, J. F. Donges, J. Kurths, and R. V. Donner. A climate network-based index to discriminate different types of El Niño and La Niña. *Geophysical Research Letters*, 43 (13):7176–7185, 2016.

N. Wiener. The theory of prediction. In *Modern Mathematics for Engineers;*. McGraw-Hill: New York, 1956.

wikipedia.org. El Niño–Southern Oscillation. `https://en.wikipedia.org/wiki/El_Ni%c3%b1o-Southern_Oscillation`, a. Retrieved: 2018-03-15.

wikipedia.org. Causality. `https://en.wikipedia.org/wiki/Causality`, b. Retrieved: 2018-01-22.

wikipedia.org. Correlation and dependence. `https://en.wikipedia.org/wiki/Correlation_and_dependence`, c. Retrieved: 2018-01-30.

wikipedia.org. Length scale. `https://en.wikipedia.org/wiki/Length_scale`, d. Retrieved: 2018-01-26.

windows2universe.org. The North Atlantic Oscillation — illustration. `https://www.windows2universe.org/?page=/earth/climate/images/nao_lg_gif_image.html`. Retrieved: 2018-02-14.

C. R. Winkler, M. Newman, and P. D. Sardeshmukh. A linear model of wintertime low-frequency variability. Part I: Formulation and forecast skill. *Journal of Climate*, 14(24):4474–4494, 2001.

A. T. Wittenberg. Are historical records sufficient to constrain ENSO simulations? *Geophysical Research Letters*, 36(12), 2009.

K. Wyrtki. The annual and semiannual variation of sea surface temperature in the North Pacific Ocean. *Limnology and Oceanography*, 10(3):307–313, 1965.

K. Wyrtki. El Niño—the dynamic response of the equatorial Pacific Oceanto atmospheric forcing. *Journal of Physical Oceanography*, 5(4):572–584, 1975.

K. Wyrtki. Water displacements in the Pacific and the genesis of El Niño cycles. *Journal of Geophysical Research: Oceans*, 90(C4):7129–7132, 1985.

S.-R. Yeo and K.-Y. Kim. Global warming, low-frequency variability, and biennial oscillation: an attempt to understand the physical mechanisms driving major ENSO events. *Climate Dynamics*, 43(3-4):771–786, 2014.

S. E. Zebiak and M. A. Cane. A model el niño-southern oscillation. *Monthly Weather Review*, 115 (10):2262–2278, 1987.

Q. Zhang, H. Wang, J. Dong, G. Zhong, and X. Sun. Prediction of sea surface temperature using long short-term memory. *IEEE Geoscience and Remote Sensing Letters*, 14(10):1745–1749, 2017.

Y. Zheng, D. Waliser, W. Stern, and C. Jones. The role of coupled sea surface temperatures in the simulation of the tropical intraseasonal oscillation. *Journal of Climate*, 17(21):4109–4134, 2004.

I. Zveryaev. Climatology and long-term variability of the annual cycle of air temperature over Europe. *Russian Meteorology and Hydrology*, 32(7):426–430, 2007.

List of publications

- A. Krakovská, J. Jakubík, M. Chvosteková, D. Coufal, N. Jajcay, and M. Paluš. Comparison of six methods for the detection of causality in a bivariate time series. *Physical Review E*, 97 (4):042207, 2018.

- D. Coufal, J. Jakubík, N. Jajcay, J. Hlinka, A. Krakovská, and M. Paluš. Detection of coupling delay: A problem not yet solved. *Chaos: An Interdisciplinary Journal of Nonlinear Science*, 27 (8):083109, 2017.

- J. Hlinka, D. Hartman, N. Jajcay, D. Tomeček, J. Tintěra, and M. Paluš. Small-world bias of correlation networks: From brain to climate. *Chaos: An Interdisciplinary Journal of Nonlinear Science*, 27(3):035812, 2017a.

- J. Hlinka, N. Jajcay, D. Hartman, and M. Paluš. Smooth information flow in temperature climate network reflects mass transport. *Chaos: An Interdisciplinary Journal of Nonlinear Science*, 27(3):035811, 2017b.

- N. Jajcay and M. Paluš. Štatistické modelovanie javu El Niño-Južná oscilácia v klimatológii (in Slovak). *Pokroky matematiky, fyziky a astronomie*, (1):52–70, 2017.

- N. Jajcay and M. Paluš. Statistical modelling in climate science. In B. Brejová, editor, *Proceedings of the 16th ITAT Conference Information Technologies - Applications and Theory*, pages 102–109, 2016b.

- N. Jajcay and M. Paluš. Information transfer across temporal scales in atmospheric dynamics. In A. Banerjee, W. Ding, J. Dy, V. Lyubchich, and A. Rhines, editors, *Proceedings of the 6th International Workshop on Climate Informatics: CI 2016*, pages 113–116. NCAR Technical Note NCAR/TN-529+PROC, 2016a.

- N. Jajcay, J. Hlinka, S. Kravtsov, A. A. Tsonis, and M. Paluš. Time scales of the European surface air temperature variability: The role of the 7–8 year cycle. *Geophysical Research Letters*, 43(2):902–909, 2016.

- J. Runge, V. Petoukhov, J. F. Donges, J. Hlinka, N. Jajcay, M. Vejmelka, D. Hartman, N. Marwan, M. Paluš, and J. Kurths. Identifying causal gateways and mediators in complex spatio-temporal systems. *Nature Communications*, 6, 2015.

- M. Vejmelka, L. Pokorná, J. Hlinka, D. Hartman, N. Jajcay, and M. Paluš. Non-random correlation structures and dimensionality reduction in multivariate climate data. *Climate Dynamics*, 44(9-10):2663–2682, 2015.

- J. Hlinka, D. Hartman, N. Jajcay, M. Vejmelka, R. Donner, N. Marwan, J. Kurths, and M. Palus. Regional and inter-regional effects in evolving climate networks. *Nonlinear Processes in Geophysics*, 21(2):451–462, 2014a.

Appendix

A.1 `pyCliTS` — Python Climate Time Series package

This appendix gives an overview (not a full documentation) of the Python Climate Time Series package — `pyCliTS`. This package was written by me in the course of analysing data for this thesis. However, I thought that some other people analysing climate data within Python environment might find the package useful. The package is currently in the 0.2 version, licensed under the MIT licence.

A.1.1 Introduction and installation

As usual with Python libraries, there are no executables in `pyclits`, but it is intended to be used in small Python scripts. Its object-oriented architecture allows for a clean and flexible source code representing the logical dependencies between various concepts and methods. Its design also supports fully flexible use of the package, from interactive local session in IPython to massive parallel computations on clusters. It can be deployed on Linux, Mac OS X, as well as Windows systems with appropriate dependencies. Among the required dependencies one might find `numpy` and `scipy`, which are among the most widely spread libraries for scientific computing in Python. Other, recommended dependencies, include `sklearn` (machine learning package), `cython` (Python to C compiler), `matplotlib` (powerful plotting in Python), `netCDF4` (Python interface to netCDF C library), `basemap` toolkit (library for plotting 2D data on maps in Python), `pywavelets` (wavelet transforms in Python), and `pathos multiprocessing` (parallel graph management in heterogeneous computing). Although these packages are not required, I strongly advise to install them all in order to ensure smooth running and performance of `pyclits` library.

The homepage of this package resides at `https://github.com/jajcayn/pyclits`, and the package (with its dependencies) can be installed either from github, or using `pip` with

```bash
1  pip install pyclits
```

Alternatively, the latest version can be installed from `github.com` directly with

```bash
1  pip install git+https://github.com/jajcayn/pyclits.git
```

The installation automatically takes care about the dependencies, and with the exception of `basemap` toolkit, it installs all required and recommended packages.

The package is, as of now, compatible with Python version 2.7. Compatibility with Python version 3+ is planned in near future.

A.1.2 Software structure

The pyclits package consists of one main class that holds the geophysical data (`DataField`), two classes for computations: `SSA` class (holds the data and performs SSA) and `VARmodel` (holds the data and is able to fit an AR model). The base `DataField` class is subsequently inherited in `SurrogateField` class (able to construct surrogate data) and in `EmpiricalModel` class (able to construct spatio-temporal model of geodata based on the idea of linear inverse models). Apart from these classes, the package offers a wealth of convenience functions. The basic architecture is depicted in Fig. A.1, which also renders the dependencies between various classes and functions in the package.
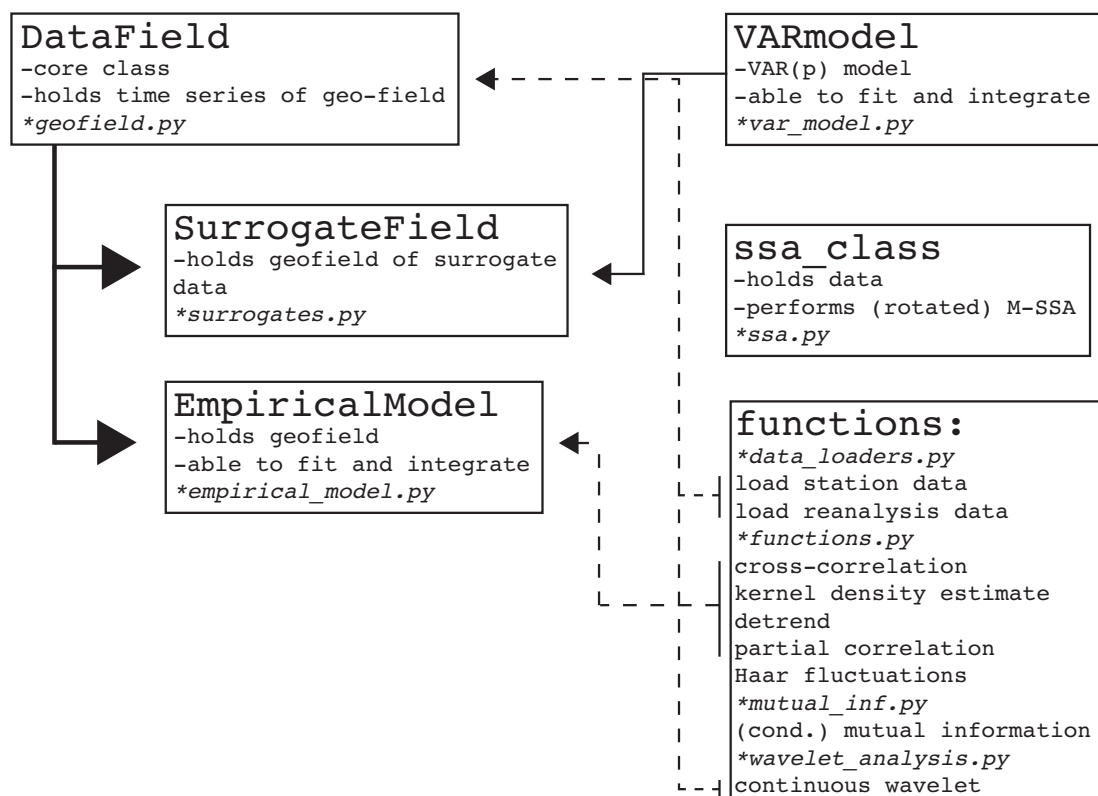
Fig. A.1. | Illustration of the `pyclits` architecture. Thick black lines signify inheritance of classes, dashed lines mean that the function is (or may be) used in the class. The file names containing the respective class or function are typeset in italics.

In the following text, I will briefly describe the core functionality of various classes and functions. Furthermore, the package is accompanied with 8 examples — Python scripts that illustrate various capabilities of the package. The examples can be found

on the homepage of the package in the examples folder: `https://github.com/jajcayn/pyclits/tree/master/examples`.

DataField class (in *geofield.py*)

This class holds the time series of a geophysical field. The fields for gridded data (re-analyses, CMIP5 model outputs, etc.) are generally 3-dimensional (*time* x *latitudes* x *longitudes*), for stations data the fields are typically 1-dimensional, containing just temporal dimension. The class has four basic properties and those are: `DataField.data`, `DataField.time`, `DataField.lats`, and `DataField.lons`. All of them are, by default, `numpy` arrays. The time field is stored as ordinal values with 1 January of year 1 being 1. The class can be initialised empty and then filled with

```python
1  ...
2  from pyclits.geofield import DataField
3  gf = DataField()
4  gf.data = some_array_created_earlier
```

or, alternatively, filled with data using `load` function as

```python
1  from pyclits.geofield import DataField
2  gf = DataField()
3  gf.load(filename='slp.mon.mean.nc', variable_name='slp', dataset='NCEP')
```

This construction fills all four basic properties of the class. The class also offers a convenience function `create_time_array`, which, when filling data manually, automatically fills the temporal field given the starting date of the data and their temporal sampling.

```python
1  ...
2  from pyclits.geofield import DataField
3  from datetime import date
4  gf = DataField()
5  gf.data = some_array_created_earlier
6  gf.create_time_array(date_from=date(1950,1,1), sampling='m')
```

Finally, the class also supports loading of the station data, although it only works with the file format as ECA&D project *[Klein Tank et al., 2002]* uses:

```python
1  from pyclits.geofield import DataField
2  gf = DataField()
3  gf.load_station_data(filename='Prague_ECA_TG.txt', dataset='ECA-station')
```

After the data is loaded and saved in the `DataField` structure, a wealth of methods is available for manipulating the data:

`copy` returns a copy of a DataField instance, it is also possible to copy just a temporal slice passing the boolean array of temporal indices (compatible with indices returned by `select_date` function)

`select_date` selects the date range in the data

`get_sliding_window_indexes` returns list of indices for sliding window analysis

`get_date_from_ndx` returns date given the index

`find_date_ndx` returns an index which corresponds to a given date

`get_spatial_dims` return spatial dimensions of the data

`get_closest_lat_lon` return closest grid point in gridded data to a given latitude and longitude pair

`select_months` selects only certain months from the data

`select_lat_lon` selects region given by pair of latitudes and pair of longitudes

`cut_lat_lon` cuts selected regions from the data (e.g. the equatorial belt)

`latitude_cos_weights` returns a grid with scaling weights based on cosine of latitude

`flatten_field` reshape the field to 2 dimensions, useful for PCA etc.

`reshape_flat_field` reshape flattened field to its original shape

`get_data_of_precise_length` selects the data either from starting or ending date, such that they have the exact length given as integer

`get_annual_data` converts daily or monthly data into annual means or sums

`get_monthly_data` converts daily data into monthly means or sums

`average_to_daily` averages sub-daily values into daily means

`interpolate_into_finer_temporal_resolution` interpolates data to finer resolution

`subsample_spatial` subsamples the data onto given grid

`smoothing_running_avg` smooths the time series using running average

`plots_FFT_spectrum` estimates and plots the power spectrum using Welch method

`temporal_filter` filters the data using low-, high-, or bandpass, or bandstop filters

`spatial_filter` filters the data in spatial sense with weights

`interpolate_spatial_nans` interpolates data with spatial NaNs

`pca_components` estimates the PCA (EOF) *[Hannachi et al., 2007]* components of geodata, able to estimate VARIMAX rotation, and also works with spatial NaNs (e.g. sea surface temperatures which are masked)

`invert_pca` inverts the PCA and returns the original data, also suitable for modelling as the Principal Components time series could be different (e.g. modelled) than obtained from the original data

`anomalise` removes the seasonal/annual cycle from the data, the climatology period can be passed as parameter

`get_seasonality` removes the seasonality both in mean and standard deviation (as `anomalise`)

`save_field` saves the entire `DataField` using cPickle `bin` format

`get_parametric_phase` computes the phase of analytic signal using parametric method

`wavelet` performs continuous complex wavelet transform with selected central period

`quick_render` plots the filled contours of the data onto map using the latitude and longitude fields in the data.

All of the aforementioned methods of the DataField class has a number of parameters and it is beyond the scope of this appendix to list them all. Potential user of the package will easily find them in the source code or in the examples that accompany the package.

SurrogateField class   (in *surrogates.py*)
This class holds the spatio-temporal field and can construct surrogates. Since it inherits all the properties and methods from the `DataField` class, statistical testing using surrogate data is convenient. Typical usage of SurrogateField would be as follows

```python
1  import pyclits as clt
2  from pyclits.surrogates import SurrogateField
3  from datetime import date
4  # load Prague SAT station data
5  prg = clt.data_loaders.load_station_data('Prague_ECA_TG.txt',
6          date(1770,1,1), date(2016,1,1),
7          anom=False, to_monthly=False)
8  # init empty SurrogateField
9  surr = SurrogateField()
10 # deseasonalise the data
11 mean, var, trend = prg.get_seasonality(detrend=True,
12         base_period=[date(1981,1,1), date(2010,12,31)])
13 # copy deseasonalised data to SurrogateField
14 surr.copy_field(prg)
15 # return seasonality to original data
16 prg.return_seasonality(mean, var, trend)
17 # construct e.g. AAFT surrogates
18 surr.construct_fourier_surrogates(algorithm='AAFT')
19 # add seasonality to surrogate data
20 surr.add_seasonality(mean, var, trend)
```

Deseasonalising the data as done on lines 11 and 12 in the code above is necessary, since algorithms for generating surrogate data have problems with replicating such strong cycles as seen in temperature data (recall sec. 3.5.1 and references therein). After copying the field into `SurrogateField` class instance (line 14 in the code example above), the original data is stored as `SurrogateField.original_data`. Then, generated surrogate data are stored in `SurrogateField.data`, hence all the methods as described in the previous section works on generated surrogate data and not on the original data. If the `SurrogateField` holds spatio-temporal 3-dimensional field, the methods for constructing surrogate data will construct surrogates for all the grid points. The `SurrogateField` class offers following methods (in addition to the methods provided by `DataField`):

`construct_fourier_surrogates` constructs Fourier Transform surrogates *[Theiler et al., 1992]*, and is able to construct also amplitude adjusted FT and iterative amplitude adjusted FT

`construct_multifractal_surroagtes` constructs multifractal surrogates *[Paluš, 2008]*

`prepare_AR_surrogates` prepare for generating AR surrogates by selecting an optimal order of AR model per grid point, fitting the model and estimating residuals

`construct_surrogates_with_residuals` constructs surrogate data from AR model by random shuffling the residuals

`amplitude_adjust_surrogates` performs amplitude adjustment to already created surrogate data.

All the methods for constructing surrogate data has optional parameter `pool`, and in the case that multiprocessing Pool (e.g. from `pathos.multiprocessing` package) is provided, the generation of surrogates is done in parallel.

EmpiricalModel class   (in *empirical_model.py*)
This class also inherits from `DataField` class and, besides storing and operating on a spatio-temporal field, is able to fit and then integrate a statistical model based on the idea of linear inverse models. The model is coded according to *Kondrashov et al. [2005]* and tested on the same dataset as used in the paper. The typical example of using this model with comments on each step is given in example that accompanies the package at `https://github.com/jajcayn/pyclits/blob/master/examples/8-empirical_model.py`. However, I will describe the general approach of to build such model.

The model operates on empirical orthogonal functions (EOFs) of the spatio-temporal data field, where their respective Principal Components (PCs) are modelled via extending the ideas of linear inverse models (LIMs) *[Penland and Sardeshmukh, 1995]*. The model carries multiple levels (three by default), where in the first level the PCs themselves are modelled using (non)linear inverse model, then, in the second level, the residual from the first one is modelled linearly, and so on until the final level. The residuals in the last level should be white in time, and only allowed to exhibit spatial correlation between grid points. Additional levels may, and should, be added until the last level's residual is white in time. After fitting the respective linear coefficients in the inverse models, the model is integrated by starting in the last level with white noise and feeding it to the trained inverse model, and subsequently using its result as a residual in the upper level. Finally, the first level result of the integration is the modelled PCs, which are then combined with EOFs to yield the modelled spatio-temporal field we started with.

The class offers various settings and upgrades to the general approach mentioned above. Before fitting the model, it is recommended to remove the low-frequency variability from the data in order to suppress drifting of the EOFs in time. This is done by running boxcar mean over 50 years and subtracting first 5 EOFs from the data, leaving the not-so-low frequency variability untouched. Afterwards, the data are anomalised, decomposed into some number of EOFs and their respective PCs are fitted to the suite of inverse models. By default, the first level is nonlinear, with quadratic nonlinearity.

For the actual fitting, user may choose among four regression algorithms (partial least squares, linear least squares, linear least squares with L2 regularization, or Bayesian ridge model). The integration of the fitted model can be run parallel or single thread, and with three types of noise (described in the example and source code). The user has an option to plot the diagnostics of the model, that is the first four moments (mean, variance, skewness, and kurtosis), integral correlation time scale, autocorrelation, and kernel density estimate. All the plots show these variables in data, and 97.5thand 2.5thpercentile of the distribution from the modelled data. The reconstructed modelled spatio-temporal fields, as well as the model itself, can be saved on the disk for further use.

`ssa_class` class   (in *ssa.py*)
This class is somewhat by its own, and has no connection via inheritance to other classes in the package. This class is able to hold the 2-dimensional data, and can perform singular spectrum analysis (SSA) *[Vautard and Ghil, 1989]*. By default, function `run_ssa` performs a multi-channel version of SSA (M-SSA) and is written according to *Groth and Ghil [2011]*. The result of such analysis is the eigenvalues of the problem, the oscillatory modes (also called components) — in fact, they are the eigenvectors of the lagged covariance matrix, the principal components (i.e. the time series), and so-called reconstructed components, which are the sum of M components got from the SSA decomposition, where M is the embedding window.

The class is also able to perform a varimax rotation on M-SSA eigenvectors with two options: first is to apply the basic orthomax rotation *[Kaiser, 1958]*, while the second is to apply so-called structured varimax rotation *[Portes and Aguirre, 2016]*. One of the problems with SSA analysis is usually the discrimination of the actual data components from the noise components. *Groth and Ghil [2015]* uses for this problem the Monte Carlo SSA, which computes n realisations of stochastic AR(1) process fitted to the data and then compares the eigenvalues from this "surrogates" to the eigenvalues from the actual data in order to separate noise from the signal. Finally, the class is prepared to run also the enhanced Monte Carlo SSA, according to *Paluš and Novotná [2004]*, where the dynamics of individual modes are also taken into an account.

Other functions
Apart from the basic classes, the package comes with a number of convenience function useful for various analysis of (not only) climate data. All the functions are listed below:

`load_station_data` (in *data_loaders.py*) loader for station data

`load_NCEP_data_monthly` (in *data_loaders.py*) loader for NCEP/NCAR reanalysis monthly data *[Kalnay et al., 1996]*

`load_NCEP_data_daily` (in *data_loaders.py*) loader for NCEP/NCAR reanalysis daily data *[Kalnay et al., 1996]*

`load_ERA_data_daily` (in *data_loaders.py*) loader for ERA-40/ERA-Interim daily data *[Dee et al., 2011]*

`load_ECA_D_data_daily` (in *data_loaders.py*) loader for ECA&D European analysis data *[Haylock et al., 2008]*

`load_enso_index` (in *data_loaders.py*) loader for various ENSO indices

`cross_correlation` (in *functions.py*) computes cross-correlation with lag

`kdensity_estimate` (in *functions.py*) estimates the kernel density, using `sklearn` package

`detrend_with_return` (in *functions.py*) removes the linear trend in the data, ignores NaNs and returns the trend

`partial_corr` (in *functions.py*) computes partial correlation

`get_haar_flucts` (in *functions.py*) computes the Haar fluctuations, inspired by *Lovejoy and Schertzer [2013]*

`get_time_series_condition` (in *mutual_inf.py*) returns time series shifted in a desired way with forward lag τ, backward lag η and dimension of conditioning, ideal for computing (conditional) mutual information

`mutual_information` (in *mutual_inf.py*) estimates the mutual information using equidistant or equiquantal binning *[Hlaváčková-Schindler et al., 2007]*

`knn_mutual_information` (in *mutual_inf.py*) estimates the mutual information using the *k*-nearest neighbours algorithm *[Kraskov et al., 2004]*

`cond_mutual_information` (in *mutual_inf.py*) estimates the conditional mutual information using equidistant binning, equiquantal binning, or Gaussian estimate using eigenvalues of the correlation matrix

`knn_cond_mutual_information` (in *mutual_inf.py*) estimates the conditional mutual information using the *k*-nearest neighbours algorithm *[Frenzel and Pompe, 2007]*

`get_p_vals` (in *surrogates.py*) returns one- or two-tailed p-values with respect to surrogate testing

`bonferroni_test` (in *surrogates.py*) runs a Bonferroni multiple testing procedure *[Dunn, 1958]*, written by Martin Vejmelka

`fdr_test` (in *surrogates.py*) runs a False Discovery rate multiple testing procedure *[Benjamini and Hochberg, 1995]*, written by Martin Vejmelka

`holm_test` (in *surrogates.py*) runs a Holm–Bonferroni multiple testing procedure *[Holm, 1979]*, written by Martin Vejmelka

`get_single_`*`x`*`_surrogate` (in *surrogates.py*) returns a single surrogate from given time series, instead of a *x* one of the following can be used: *FT* for Fourier Transform surrogates, *AAFT* for amplitude adjusted FT surrogates, *IAAFT* for iterative amplitude adjusted FT, *MF* for multifractal surrogates, and *AR* for autoregressive surrogate of desired order.

`morlet` (in *wavelet_analysis.py*) returns a Morlet mother wavelet as a function of Fourier frequency

`paul` (in *wavelet_analysis.py*) return a Paul mother wavelet as a function of Fourier frequency

`DOG` (in *wavelet_analysis.py*) return a Derivative of Gaussian mother wavelet as a function of Fourier frequency

`continuous_wavelet` (in *wavelet_analysis.py*) computes a wavelet transform of the vector.

A.2 *Supplement to* Time scales of the European surface air temperature variability

In this appendix, the reader might find additional figures relating to chapter 4 — Time scales of the European surface air temperature variability, not needed to fully comprehend the main text, however, they pose as a supplementary block to the overall puzzle.

A.2.1 Evaluating the effect of cross-scale interactions (sec. 4.3)

In this section, additional figures studying the annual cycle and its relationships with 8-year cycle are shown. In the main text, the figure from Prague – Klementinum station is given (Fig. 4.13), here additional stations with the sufficiently long uninterrupted record are shown. The list of used stations, with their temporal span, is given in Table A.1. Spatial locations of all used stations are rendered in Fig. A.2.

station	country	temporal span
Stockholm	SWE	1/1/1756 – 1/1/2016
Prague – Klementinum	CZ	1/1/1775 – 1/1/2016
Zagreb – Gric	HR	1/1/1861 – 1/1/2016
Quickborn (Kruzer Kamp)	DE	1/1/1891 – 1/1/2016
Hamburg	DE	1/1/1891 – 1/1/2016
Orenburg	RU	1/1/1886 – 1/1/2016
St. Petersburg	RU	1/1/1881 – 1/1/2016
CET Central England	UK	1/1/1881 – 1/1/2016
Bamberg	DE	1/1/1879 – 1/1/2016
Potsdam	DE	1/1/1893 – 1/1/2016

TABLE A.1. | Summary of stations from which the daily average surface air temperature was used in the analysis. All station metadata and surface air temperature data compiled by *Klein Tank et al. [2002]*, downloaded from *ecad.eu*.

Please note, that in Fig. A.2 the location of CET is only approximate as Central England Temperature is representative of a roughly triangular area of the UK enclosed by Lancashire, London, and Bristol *[metoffice.gov.uk]*.
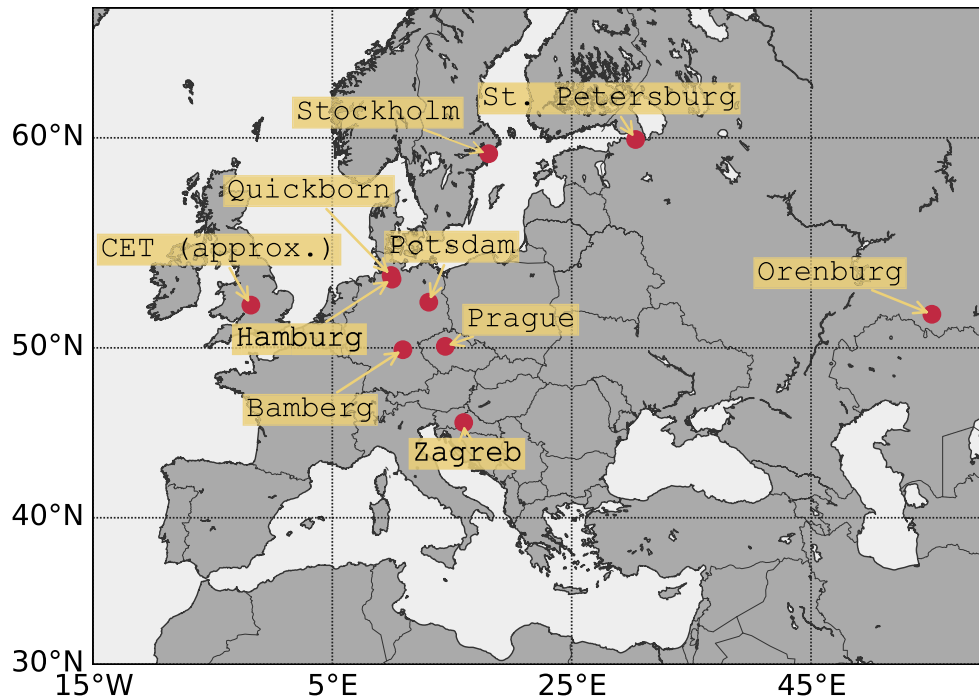
Fɪɢ. A.2. | Spatial locations of stations used in the analysis. The stations are listed in Table A.1. Location of CET is only approximate as Central England Temperature *"is representative of a roughly triangular area of the UK enclosed by Lancashire, London, and Bristol" [metoffice.gov.uk].* Here is shown an arithmetic average of coordinates of the three cities.

A.2.2 Conditional means of the annual amplitude (sec. 4.3.1)

Here, the effect of 8-year cycle on the amplitude of annual cycle (AAC) is investigated in a similar fashion as was for the Prague – Klementinum station (recall sec. 4.3.1 and figures therein) for other stations compiled by the ECA&D. Stations used in this analysis were the same as in Table A.1 (recall that their spatial locations are depicted in Fig. A.2). The conditional means of the AAC are shown in Figs. A.5, A.6, and A.7. As seen from the figures, the overall change within the full period of available data is between 0.29°C for CET time series and 0.87°C for Potsdam station. From the variability of these results, we suspect that the effect, having the temporal variability also possesses spatial variability. From the premature observations, the spatial variability appears to have an approximately east-west gradient with the higher overall change due to the 8-year cycle (hence the effect of the cycle itself is stronger) in the eastern part of Europe. Later, we will try to confirm this hypothesis by estimating the effect on gridded data from Europe. As with the case of Prague – Klementinum station (Fig. 4.14), here we also observe that the effect is variable in the temporal sense and, again, seem to fluctuate around the overall value, sometimes being lower, sometimes higher.
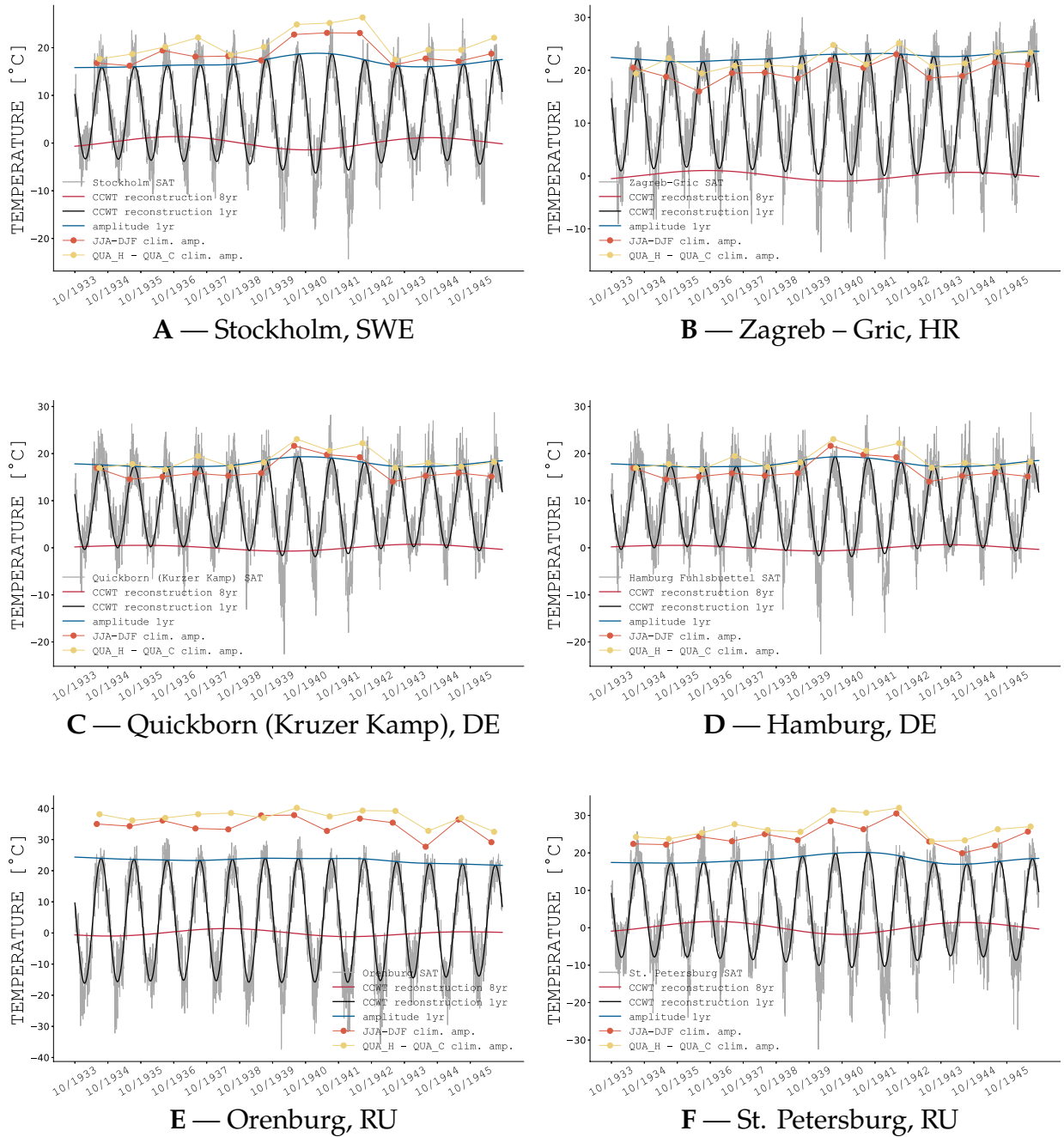
FIG. A.3. | Cycles of our interest in SAT data from (**A**) Stockholm, SWE; (**B**) Zagreb – Gric, HR; (**C**) Quickborn (Kruzer Kamp), DE; (**D**) Hamburg, DE; (**E**) Orenburg, RU; and (**F**) St. Petersburg, RU station *[Klein Tank et al., 2002]* in the period 10 October 1933 to 30 September 1946. Shown are the SAT daily average in grey, the CCWT reconstruction $A_{8yr}(t) \cos \phi_{8yr}(t)$ of the 8-year cycle in red, the CCWT reconstruction $A_{1yr}(t) \cos \phi_{1yr}(t)$ of the annual cycle in black, the CCWT amplitude $A_{1yr}(t)$ in blue, and two various estimates of climatological amplitude (see text for details) as orange and yellow circular marks.

A — CET, UK

B — Bamberg, DE
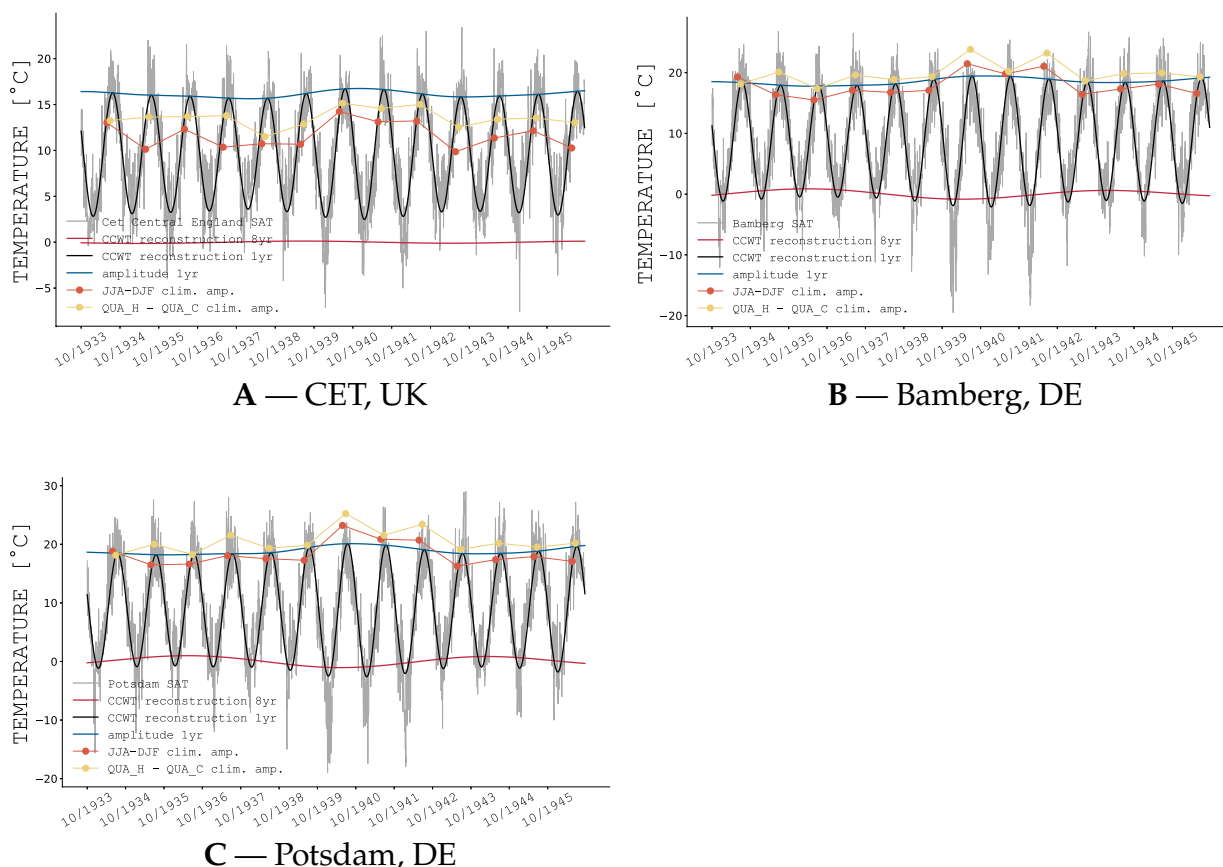
C — Potsdam, DE

FIG. A.4. | Same as Fig. A.3 but for stations (**A**) CET — Central England Temperature, UK; (**B**) Bamberg, DE; and (**C**) Potsdam, DE.

A.2.3 Overall temperature variability in the 8-year cycle (sec. 4.3.2)

The effect of 8-year cycle on the overall temperature variability, represented by the surface air temperature anomalies data (SATA), is further studied here. In addition to studying this effect in Prague – Klementinum station (Fig. 4.16), here 9 additional stations from the ECA&D data set are studied (stations listed in Table. A.1 and their spatial locations depicted in Fig. A.2). The conditional means of SATA, dependent on the phase of 8-year cycle, $\phi_{8yr}(t)$ are shown in Figs. A.8, A.9, and A.10. In the case of overall variability, the highest effect can be seen in St. Petersburg with the difference between the maximum and minimum bin at 1.43°C, while the lowest effect in, again, seen in CET — Central England Temperature record at 0.58°C level. Similarly, as in the case of conditional means of AAC from all stations, the effect has profound variability both in a temporal and spatial sense. The temporal variability can be seen from panels B and C in the respective figures, where two distinct periods are taken in order to estimate the effect of the 8-year cycle. Again, this effect seems to fluctuate around the overall value, and this will be studied later using the temporal windows analysis. As for the spatial variability of the effect, note again approximately east-west gradient with a stronger effect in the eastern part of Europe. Although this effect seems to be variable both in space and time, the basic properties of the influence holds — that is the cold bins tend to be located in
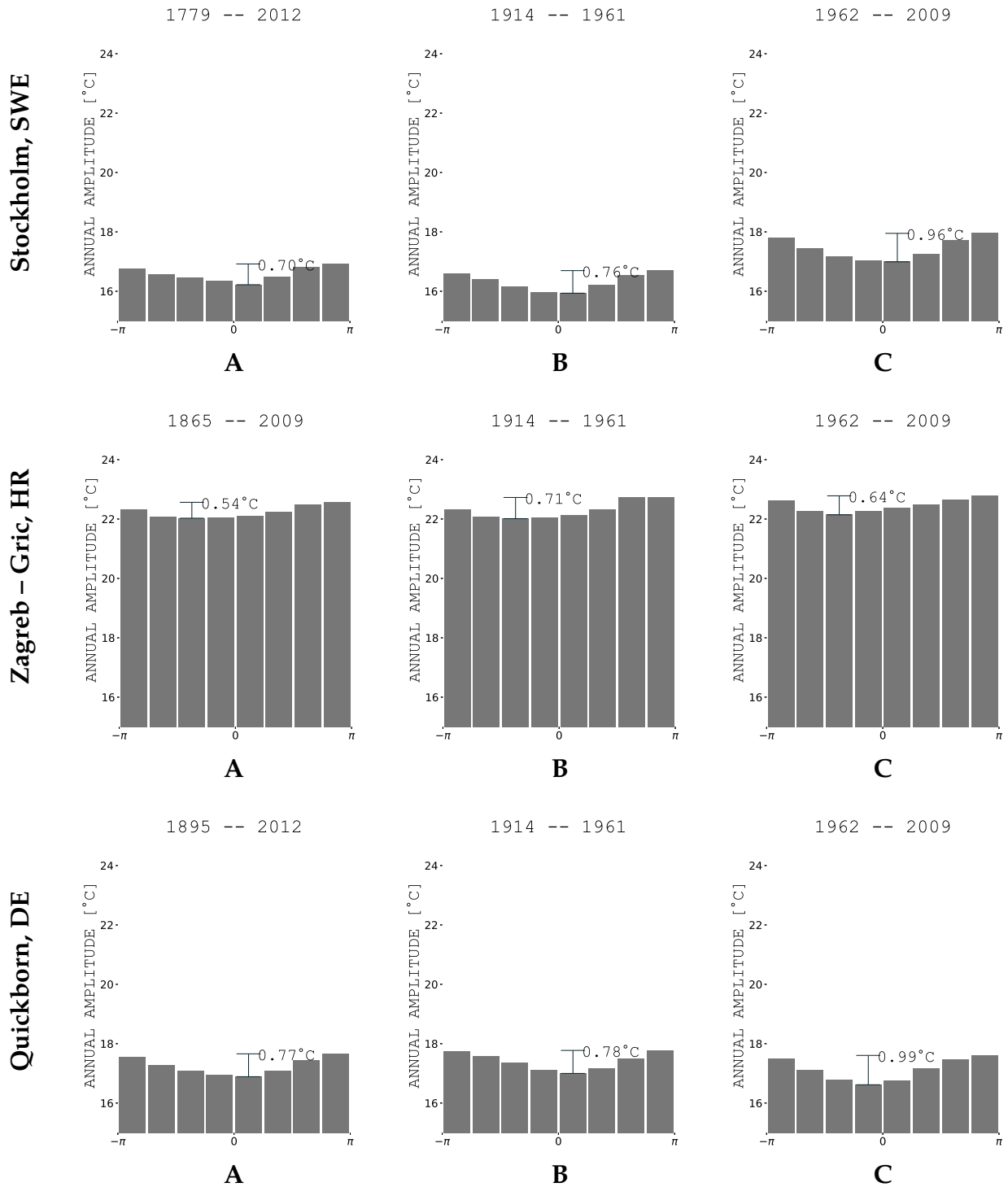
FIG. A.5. | Conditional means for the amplitude of annual cycle (AAC), $A_{1yr}(t)$, for the (top) Stockholm, SWE; (middle) Zagreb – Gric, HR; and (bottom) Quickborn (Kruzer Kamp), DE SAT data within the period (**A**) full (depends on station); (**B**) 1 January 1914 to 31 December 1961; and (**C**) 1 January 1962 to 31 December 2009, conditioned on the phase of the 8-year cycle, $\phi_{8yr}(t)$, divided into 8 equidistant bins. Note, that each bin represents approximately 1 year of the 8-year cycle.
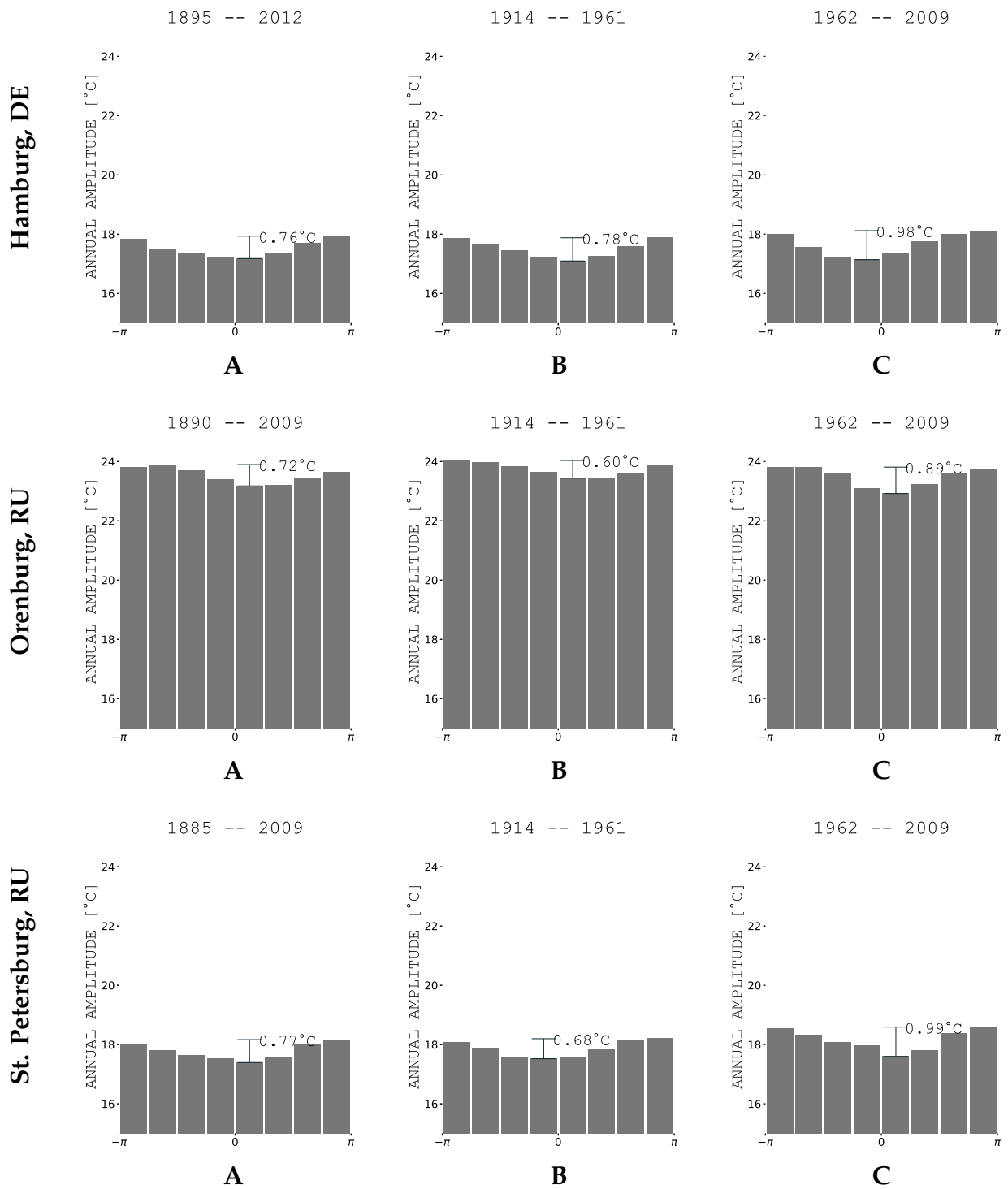
FIG. A.6. | Same as Fig. A.5, but for the (top) Hamburg, DE; (middle) Orenburg, RU; and (bottom) St. Petersburg, RU stations.
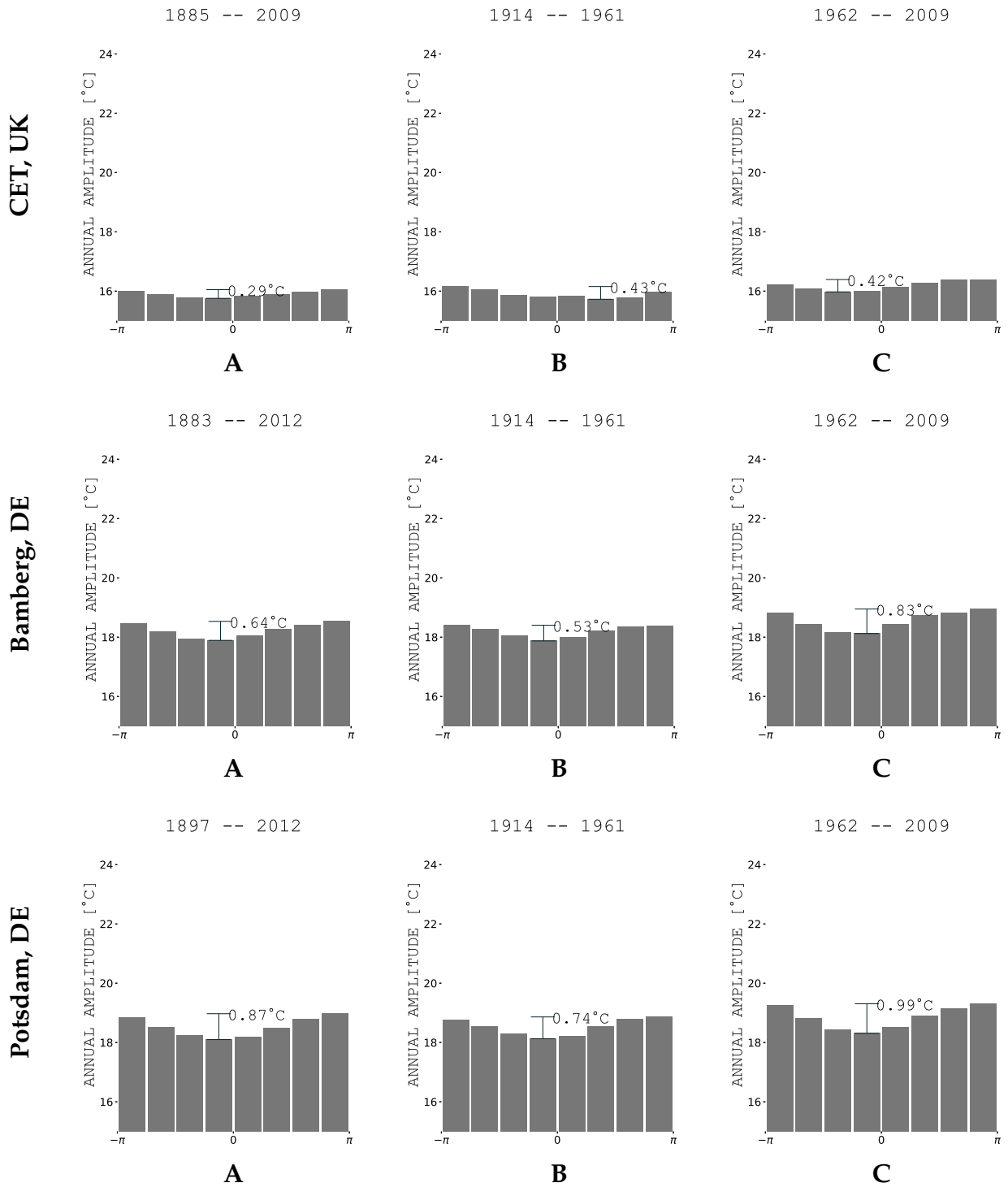
Fig. A.7. | Same as Fig. A.5, but for the (top) CET — Central England Temperature, UK; (middle) Bamberg, DE; and (bottom) Potsdam, DE stations.

the beginning and the end of the 8-year cycle, while the warm bins tend to occupy the middle of the cycle, however, some fluctuations from this rule exist.

A.2.4 Temporal variations in the effect of the 8-year cycle (sec. 4.3.3)

The temporal variations of the effect of the 8-year cycle on both, the amplitude of annual cycle and the overall temperature variability represented by the surface air temperature anomalies (SATA) was studied in the Prague – Klementinum station data (Figs. 4.19 – 4.24). Here, 9 additional stations from the ECA&D data set are studied (stations listed in Table. A.1 and their spatial locations depicted in Fig. A.2) and subsequently plotted in Figs. A.11 – A.19.

In all of the 9 studied stations, the effect of 8-year cycle is somewhat different for AAC and SATA. As an example, consider Stockholm station (Fig. A.11): the effect on AAC peaked in the first half of the 19[th]century and then with the same intensity in the middle of 20[th]century. On the other hand, the effect on SATA fluctuated a lot around a mean of approximately 1.4°C with rather high variance. Moreover, the significance patterns differ, for AAC the effect is usually statistically significant during its peaks and during the whole 20[th]century, while for SATA the significance is spread during the whole period almost uniformly. Nevertheless, we might conclude that for the Stockholm station the effect of the 8-year cycle onto faster temporal variability is quite large, up to 1.4°C for AAC and 2°C for overall variability represented by SATA.

The picture of the effect of 8-year cycle for other stations is similar to the Stockholm one — the maxima for the effect differ in AAC and in SATA, as well as the significance patterns. However, we can conclude that the effect on both the AAC and SATA seem rather stronger in the last century (with an exception of CET station, Fig. A.17) and usually statistically significant, at least for the last couple of temporal windows. The weakest effect of the 8-year cycle on AAC is attributed to the CET — Central England Temperature time series, as well as the weakest effect on SATA. Since CET is the westernmost station in our compiled data set, we hypothesise that the effect indeed exhibits an east-west gradient. This hypothesis is further supported by observing the German stations (Figs. A.13, A.14, A.18, and A.19), where the effect on both the AAC and SATA peaks at approximately 1.2°C and 1.8°C, respectively. Finally, studying the easternmost stations — St. Petersburg and Orenburg (Figs. A.15 and A.16) yield the highest effect both in AAC (peak at 1.5°C) and in SATA (up to 2.6°C). The hypothesis of an east-west gradient is further studied in gridded temperature analysis data.

A.2.5 Seasonal effects of the 8-year cycle (sec. 4.3.5)

In addition to studying the seasonal effect of the 8-year cycle in Prague – Klementinum station (recall Fig. 4.27) in the main text, the 9 complementary stations from ECA&D data set are studied as well (stations are listed in Table A.1 and their spatial locations rendered in Fig. A.2), with the respective results plotted in Figs. A.20 – A.24.

All of the additional studied stations follow the same seasonal pattern as Prague –

Fig. A.8. | Conditional means for the surface air temperature anomalies (SATA) for the (top) Stockholm, SWE; (middle) Zagreb – Gric, HR; and (bottom) Quickborn (Kruzer Kamp), DE SAT data within the period (**A**) full (depends on station); (**B**) 1 January 1914 to 31 December 1961; and (**C**) 1 January 1962 to 31 December 2009, conditioned on the phase of the 8-year cycle, $\phi_{8yr}(t)$, divided into 8 equidistant bins. Note, that each bin represents approximately 1 year of the 8-year cycle.

Fig. A.9. | Same as Fig. A.8, but for the (top) Hamburg, DE; (middle) Orenburg, RU; and (bottom) St. Petersburg, RU stations.
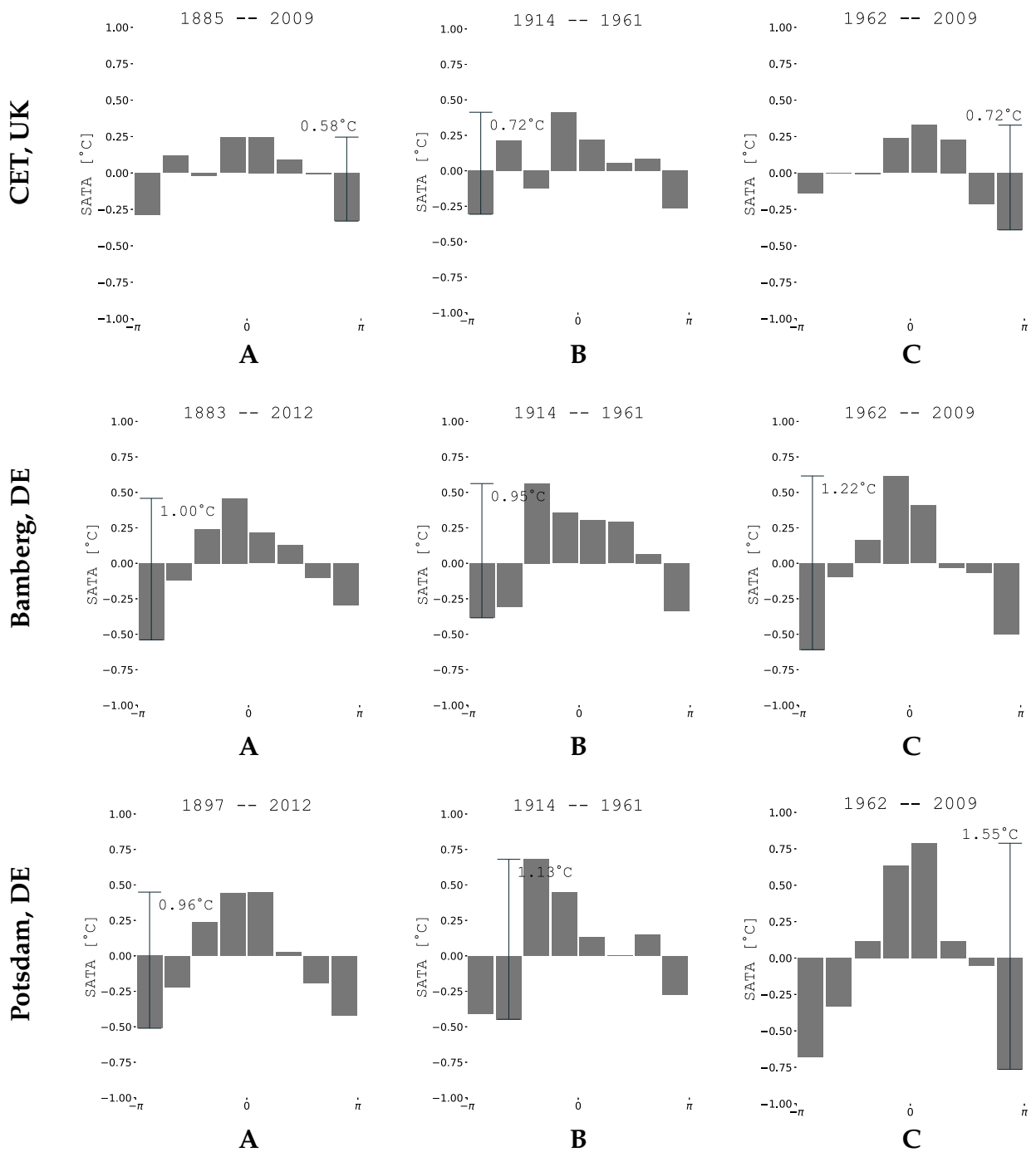
Fig. A.10. | Same as Fig. A.8, but for the (top) CET — Central England Temperature, UK; (middle) Bamberg, DE; and (bottom) Potsdam, DE stations.
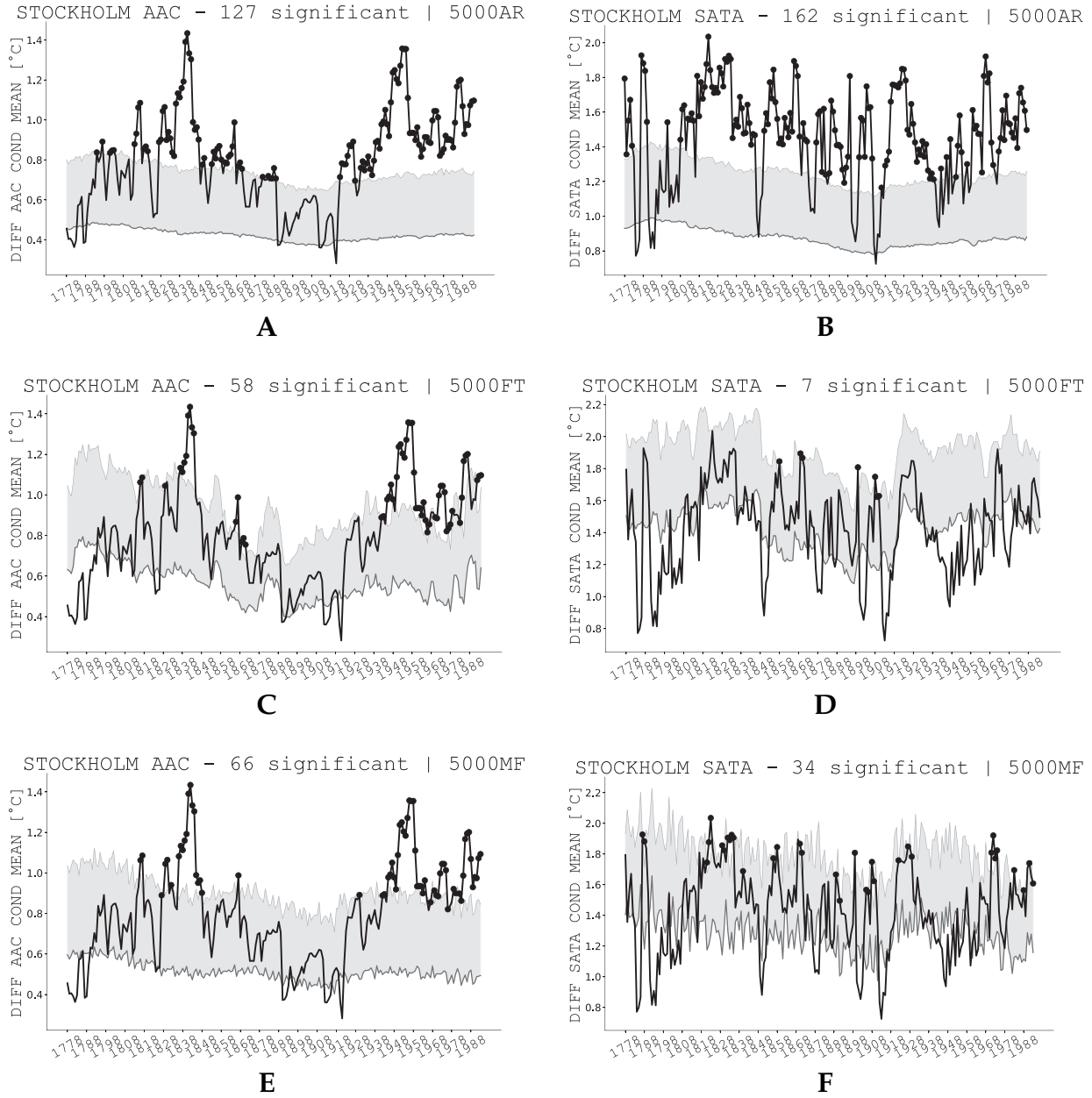
Fig. A.11. | Temporal evolution of the effect of 8-year cycle on (left column, panels **A**, **C**, **E**) the amplitude of annual cycle, $A_{1yr}(t)$, and on (right column, panels **B**, **D**, **F**) the overall temperature variability — SATA in the Stockholm, SWE daily SAT. The differences between minimum and maximum AAC or SATA conditional means (thick black curve), tested against 5000 (top row, panels **A** and **B**) AR1 surrogates, (middle row, panels **C** and **D**) FT surrogates, and (bottom row, panels **E** and **F**) MF surrogates (the means over the surrogate distribution as thinner grey curve; the 95[th]percentile of the distribution is plotted using light grey curve, connected with the mean by grey filling). Windows with statistically significant differences are marked with black dots, plotted in the middle of the window of the effective length 36.86 years.
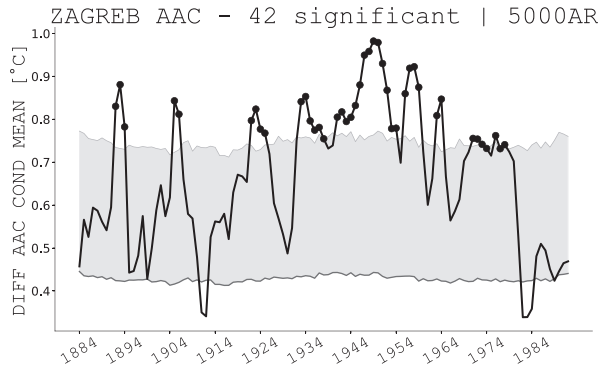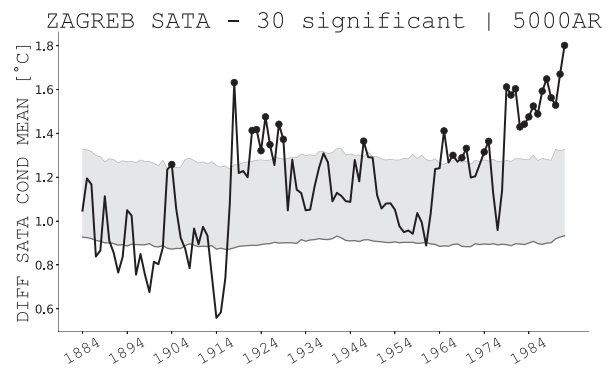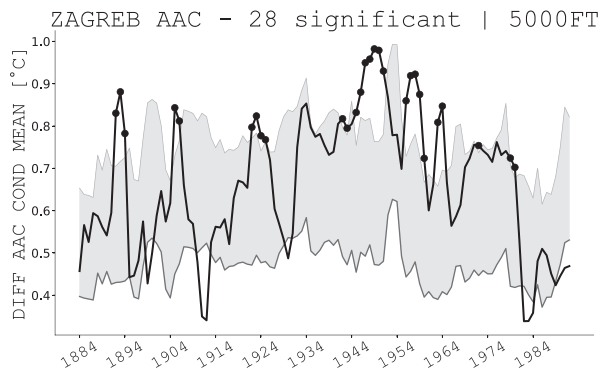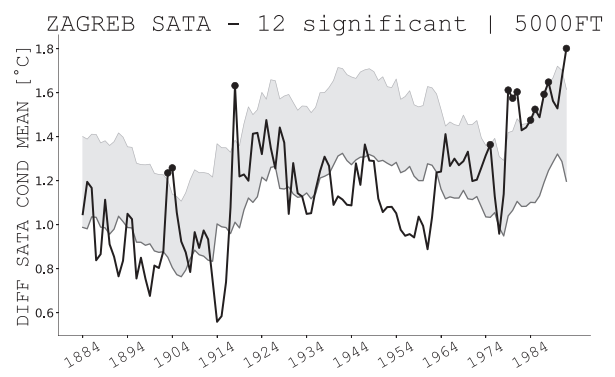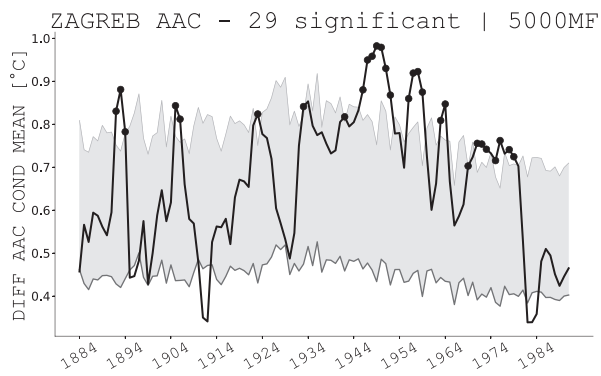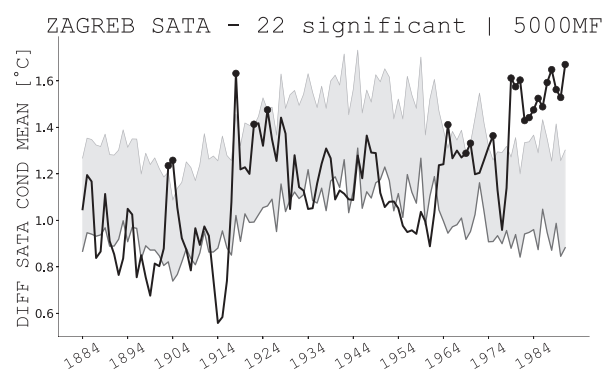
Fig. A.12. | Same as Fig. A.11, but for Zagreb – Gric, HR station.
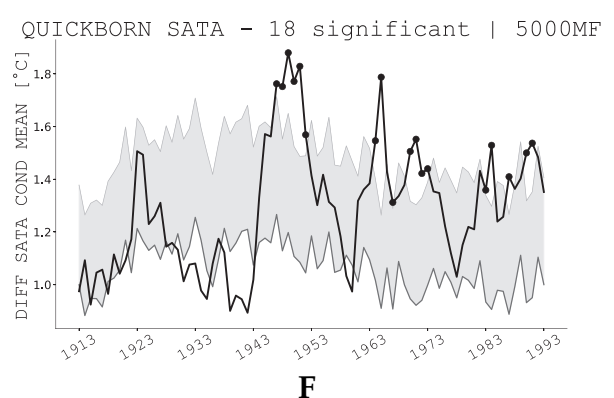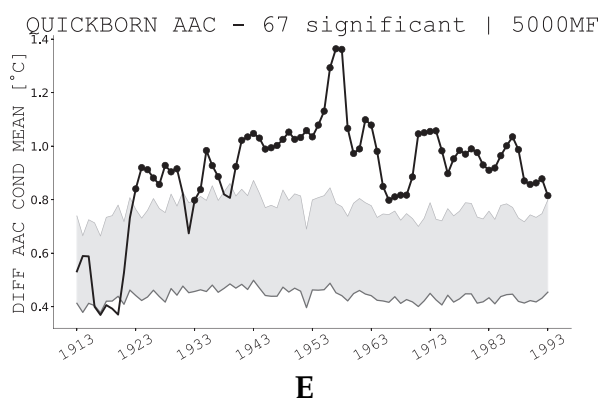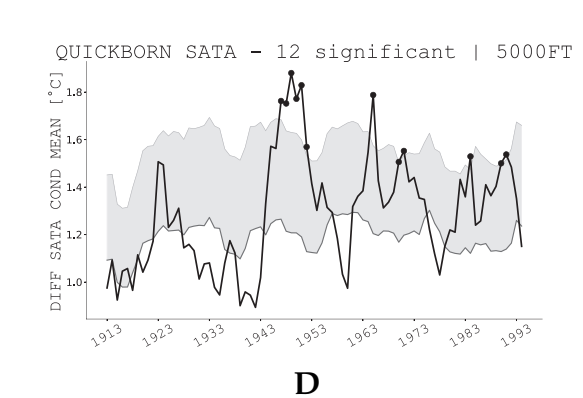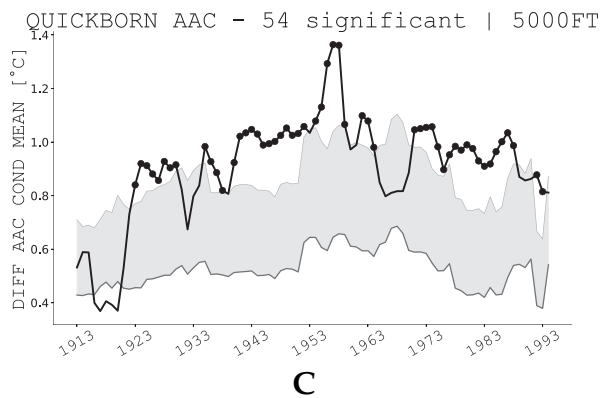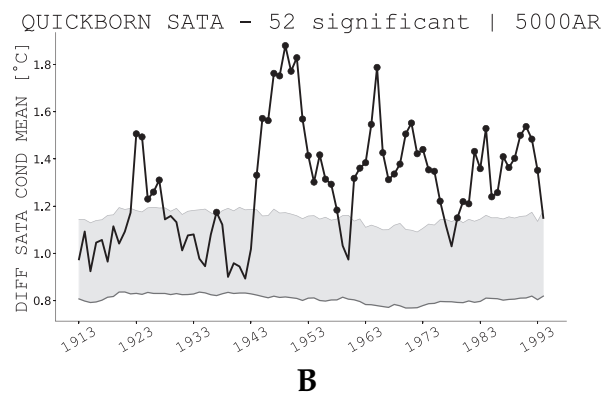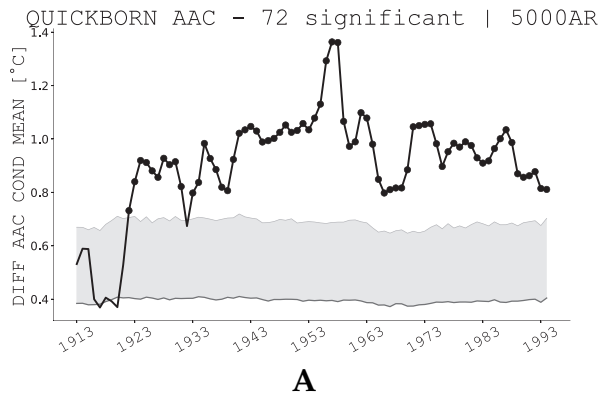
Fɪɢ. A.13. | Same as Fig. A.11, but for Quickborn (Kruzer Kamp), DE station.
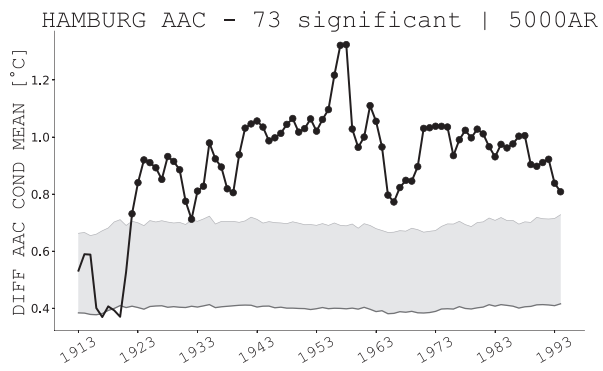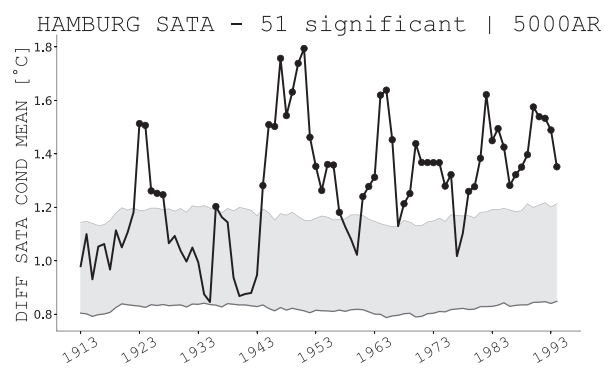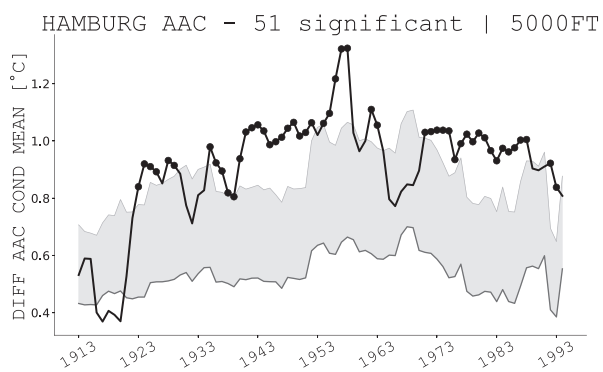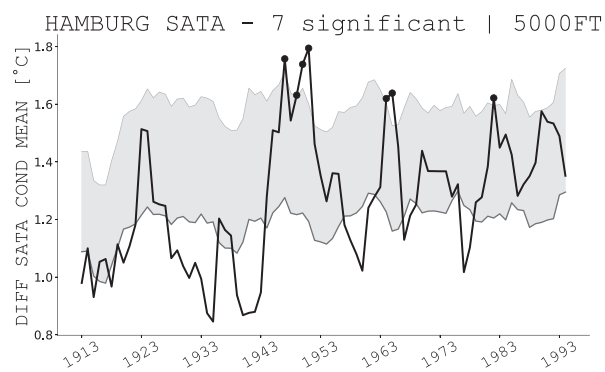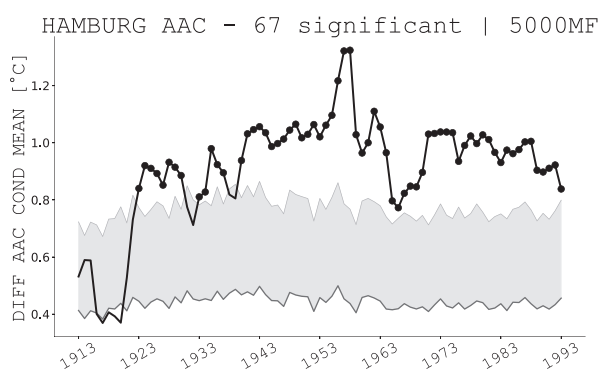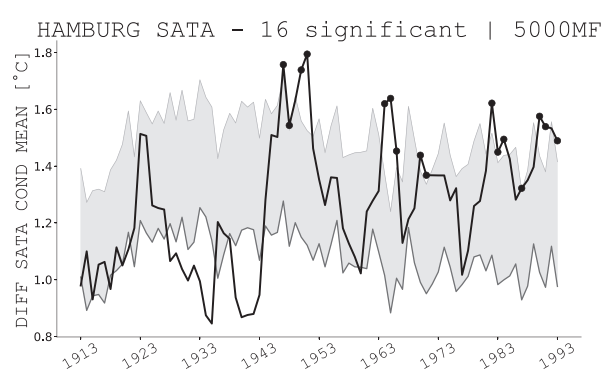
FIG. A.14. | Same as Fig. A.11, but for Hamburg, DE station.
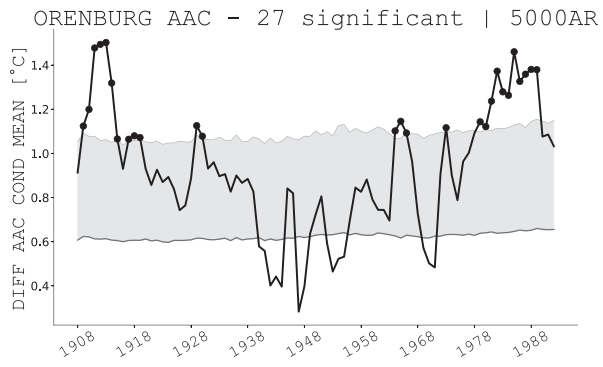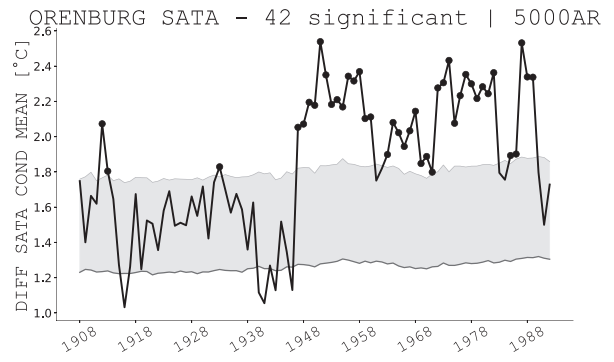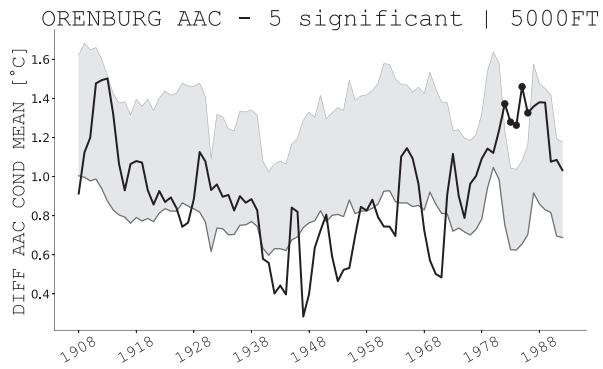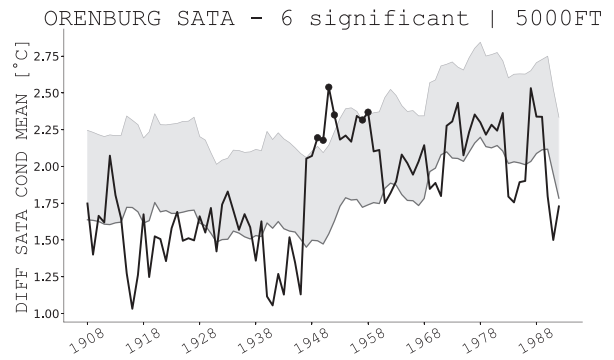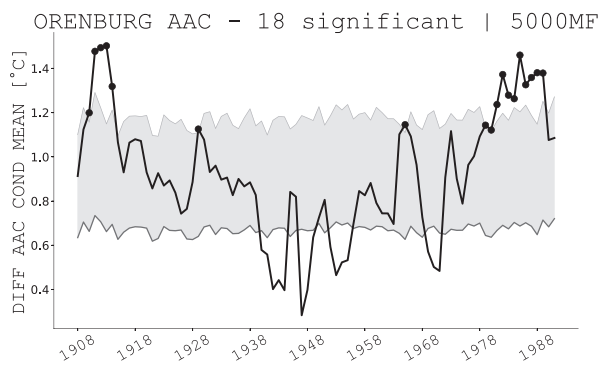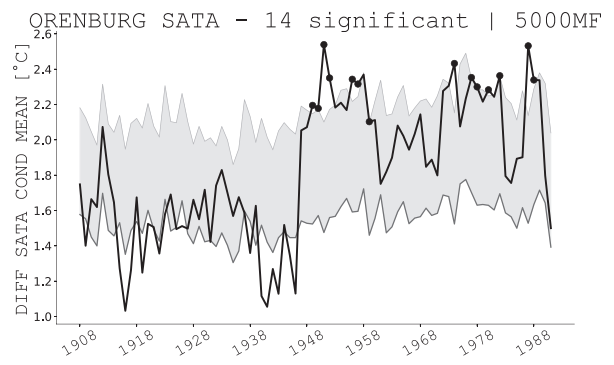
FIG. A.15. | Same as Fig. A.11, but for Orenburg, RU station.
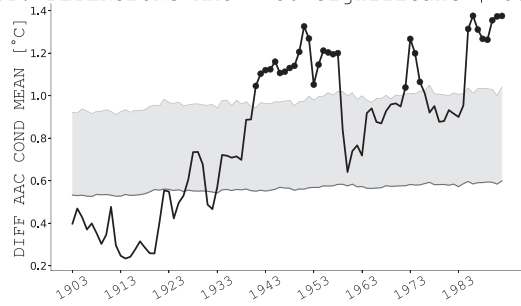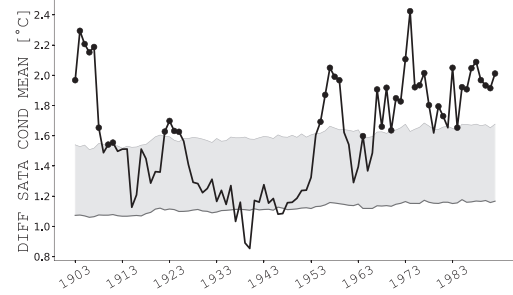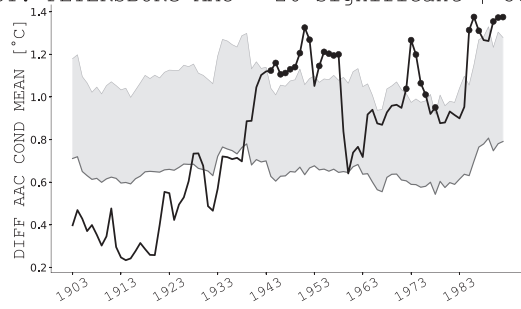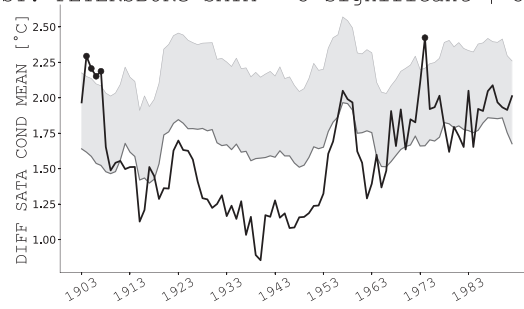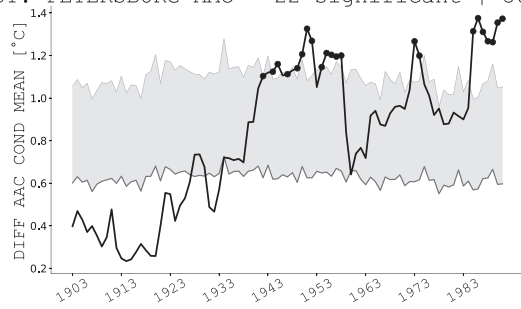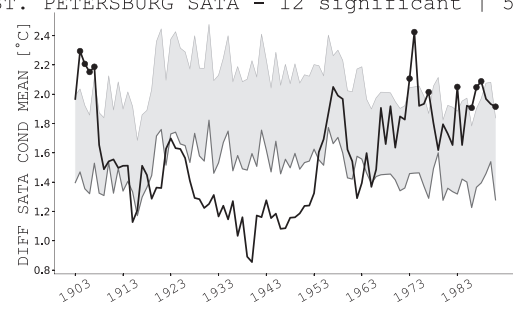
Fɪɢ. A.16. | Same as Fig. A.11, but for St. Petersburg, RU station.
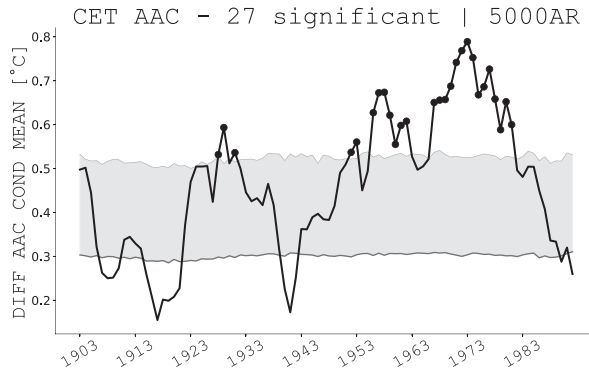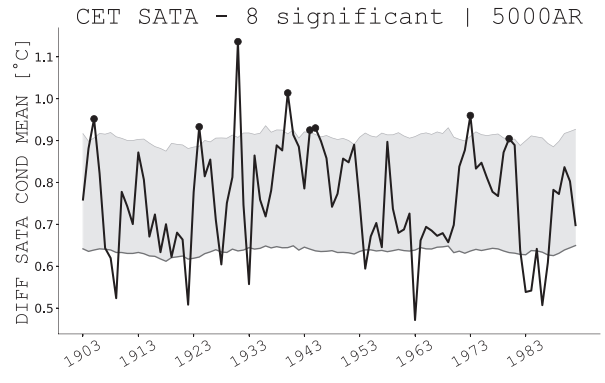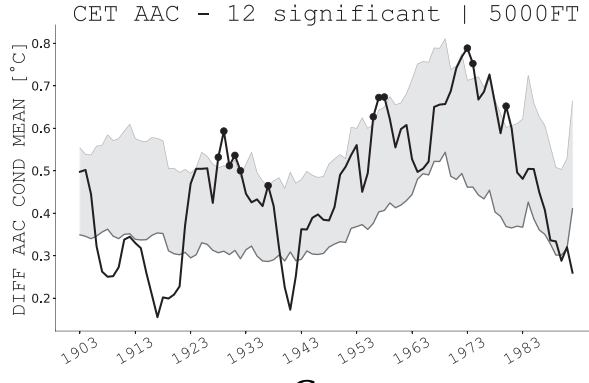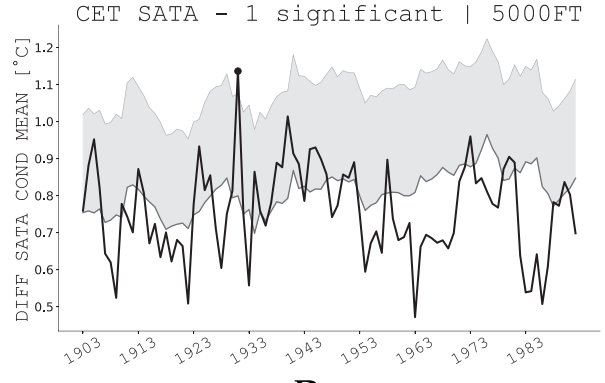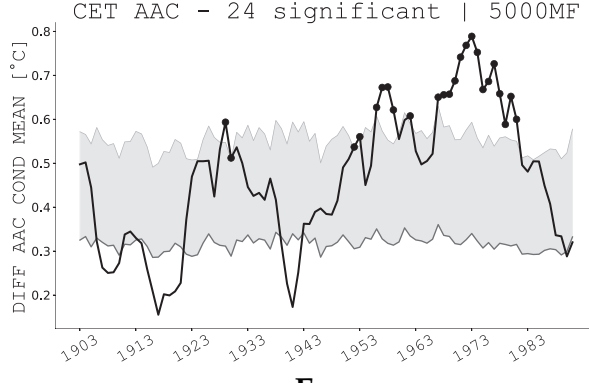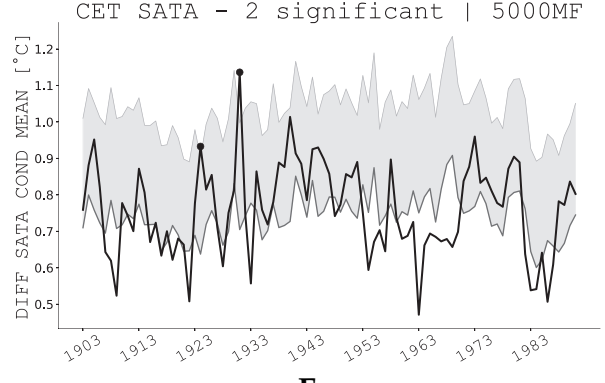
Fig. A.17. | Same as Fig. A.11, but for CET — Central England Temperature, UK station.
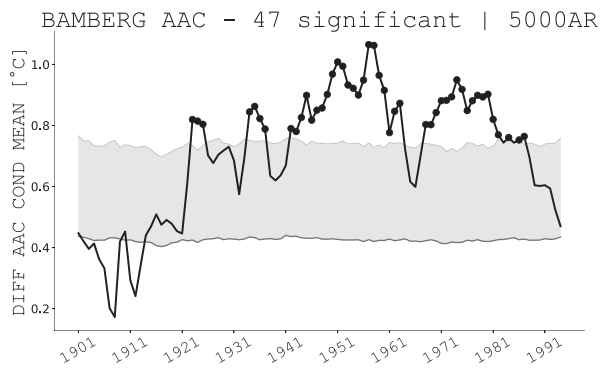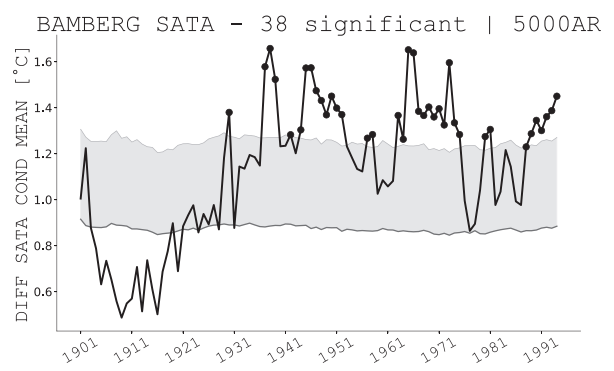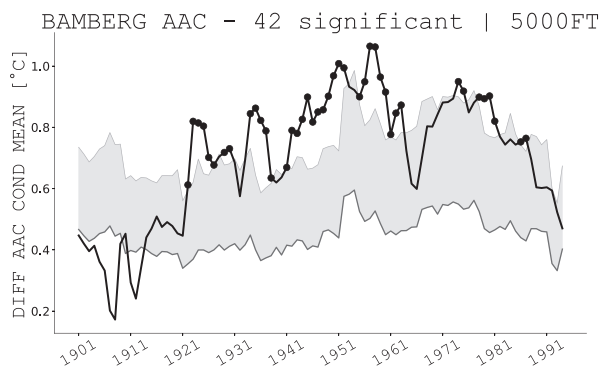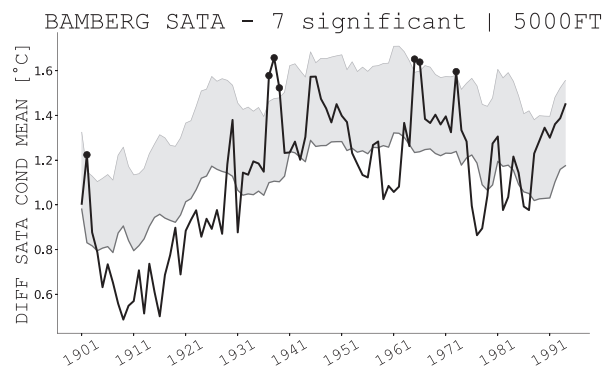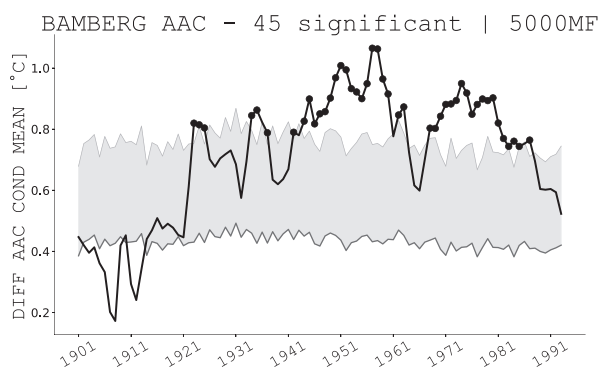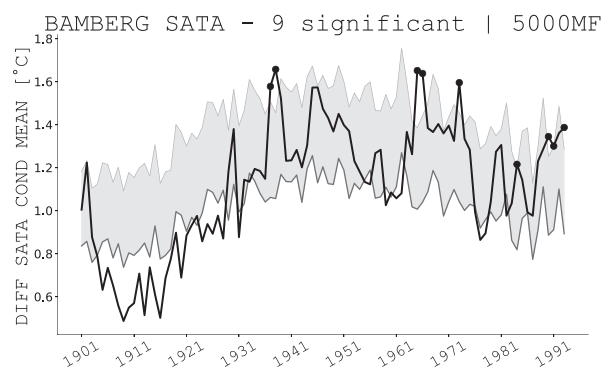
FIG. A.18. | Same as Fig. A.11, but for Bamberg, DE station.
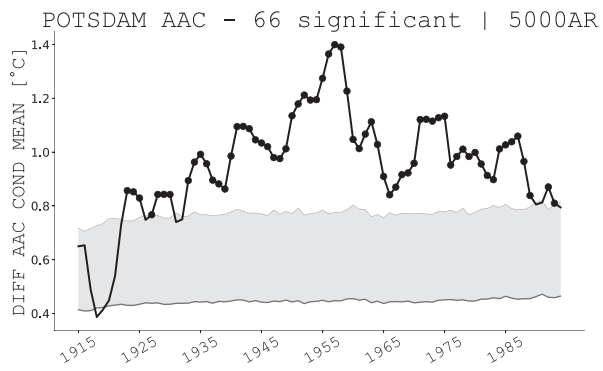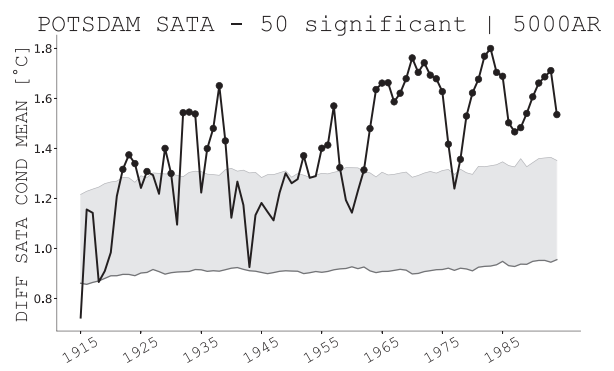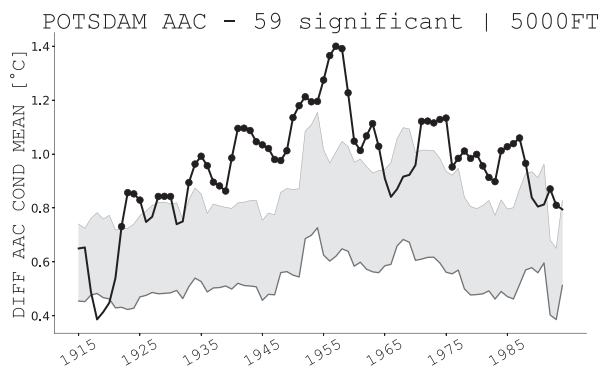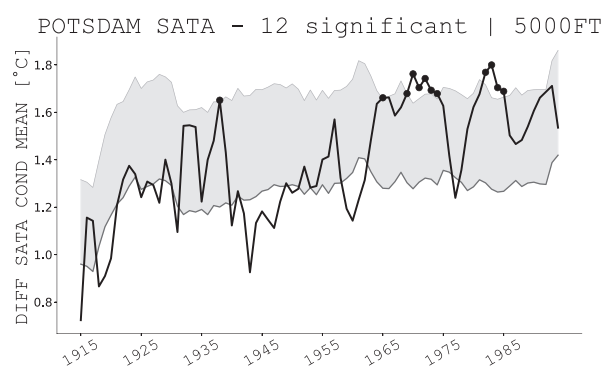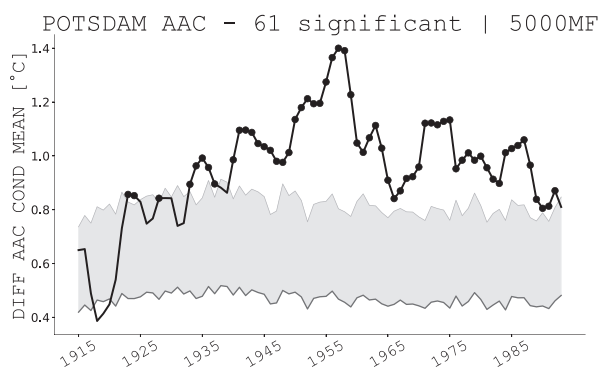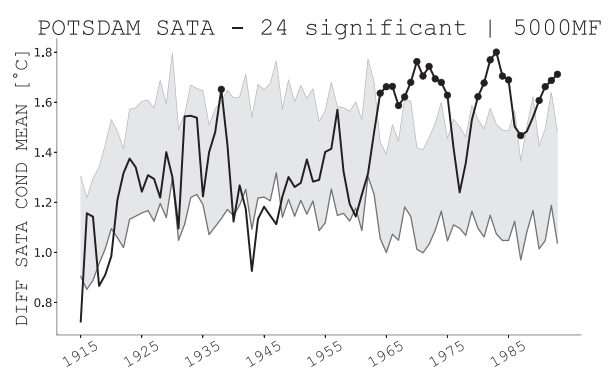
Fɪɢ. A.19. | Same as Fig. A.11, but for Potsdam, DE station.

Klementinum station, that is considerably elevated effect of the 8-year cycle onto overall temperature variability in the winter seasons (December through February, panels A in Figs. A.20 – A.24), ranging from approximately 2°C in the case of CET — Central England Temperature in the UK to the maximum slightly exceeding 6°C in the case of Russian stations St. Petersburg and Orenburg.

Contrarily, in the other seasons than winter, the effect of the 8-year cycle is relatively weaker, any many cases the decrease is about 50%. Also, as expected the statistical significance patterns are different — in the winter season roughly a half of the total record per station exhibit statistically significant effect of the 8-year cycle, while in other seasons the effect is well reproduced by the surrogate data, and therefore is probably the result of another type of interactions than cross-scale coupling.

Our final observations relate to the east-west gradient of the strength of the effect. In the previous sections, we noted that eastern stations exhibit larger effect of the 8-year cycle both on AAC and SATA than western stations. Now it also appears that the difference between seasons (e.g. compare DJF and JJA plots) is larger in the eastern stations than in the western ones. Consider e.g. CET — Central England Temperature seasonal effect (Fig. A.23, panels E – H) as the westernmost station, where the difference between DJF plot and other seasons is roughly 0.5°C. On the other hand, the easternmost station such as St. Petersburg and Orenburg, both RU, exhibit far stronger seasonal effect — the DJF differences between warm and cold bins reach up to 6°, while in the other seasons the difference peaks slightly over 3°C and usually is even lower. This makes the seasonal dependence much stronger than in the western stations. In conclusion, the east-west gradient appears first of all in the strength of the effect itself, being stronger in eastern Europe, and secondly, in the seasonal dependence where in the west the dependence is low, and the effect in various seasons is more-or-less constant, and in the east where the effect of the 8-year cycle heavily depends on the season. The hypothesis of an east-west gradient in the effect of the 8-year cycle is further supported when estimating the effect on the gridded data set, see Figs. 4.25 and 4.26.

A.3 *Supplement to* Complex dynamics and extremes in El Niño / Southern Oscillation

A.3.1 CMIP5 additional information

For the study of cross-scale interactions in the El Niño/Southern Oscillation phenomenon, also the modelled time series from coupled ocean-atmosphere global circulation models within the Coupled Model Intercomparison Project Phase 5 (CMIP5) were considered (see sec. 5.4.2). We used in total 89 20th century historical realisations (runs) from 15 different models, the number of runs from a particular model is summarised in Table A.2.

For each run from the CMIP5 modelling suite, the phase synchronisation, phase-phase causality, and phase-amplitude causality were estimated using the framework described in sec. 5.3. Firstly, for each run, we measured the similarity between the
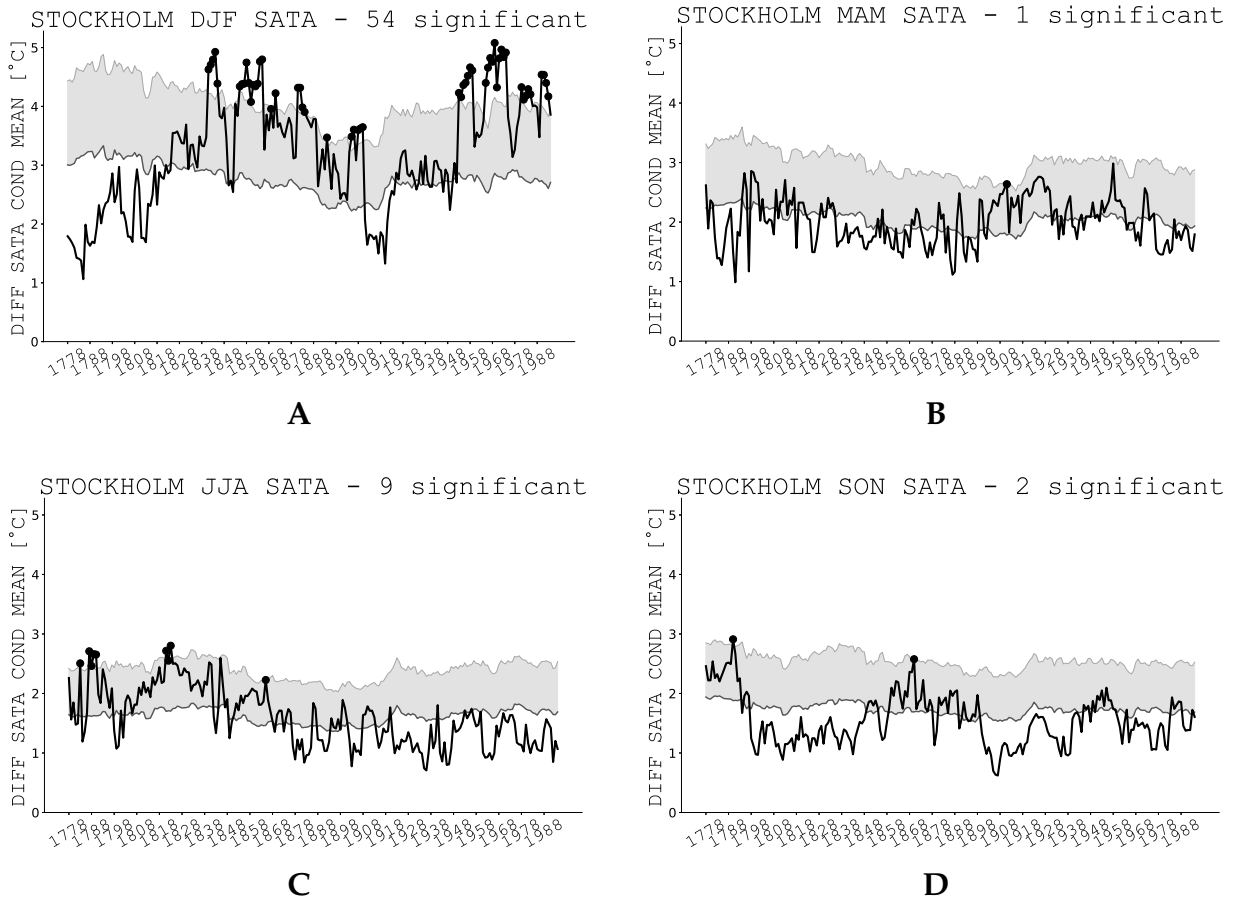
FIG. A.20. | Temporal evolution of the effect of 8-year cycle on the surface air temperature anomalies (SATA) in the Stockholm, SWE daily SAT for (**A**) winter, DJF, season; (**B**) spring, MAM, season; (**C**) summer, JJA, season; and (**D**) winter, DJF, season. The differences between minimum and maximum SATA conditional means (thick black curve), tested against 5000 FT surrogates (the means over the surrogate distribution as thinner grey curve; the 95th percentile of the distribution is plotted using light grey curve, connected with the mean by grey filling). Windows with statistically significant differences are marked with black dots, plotted in the middle of the window of the effective length 36.86 years.
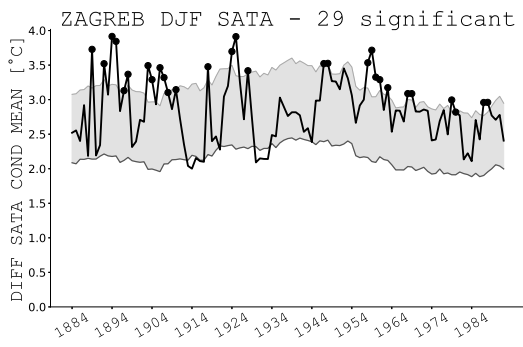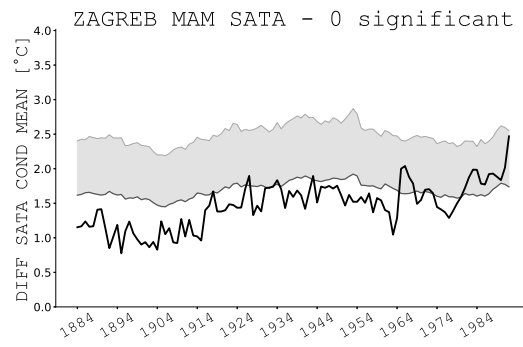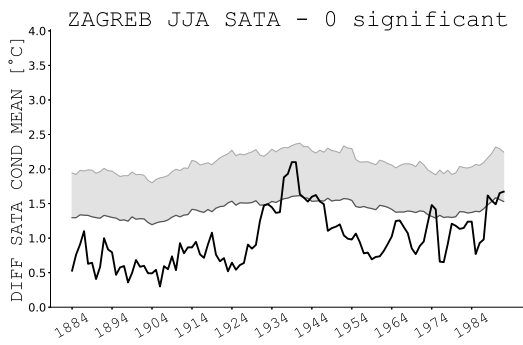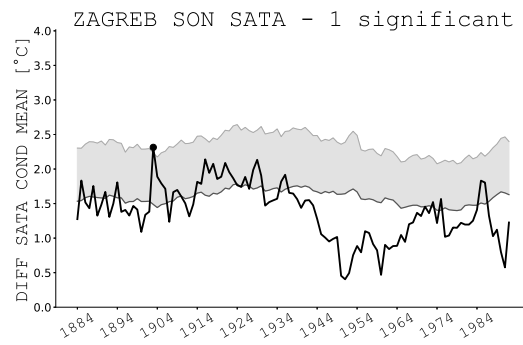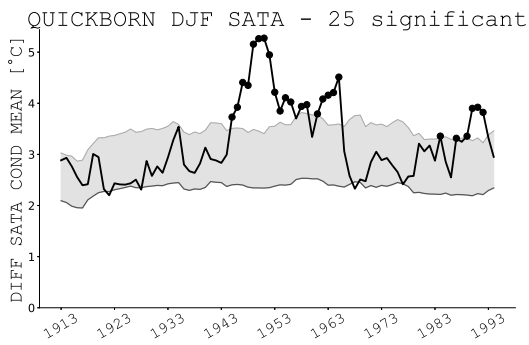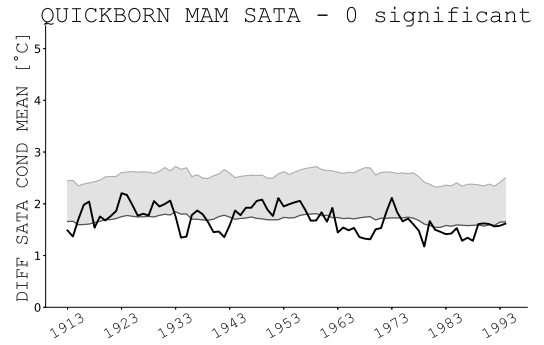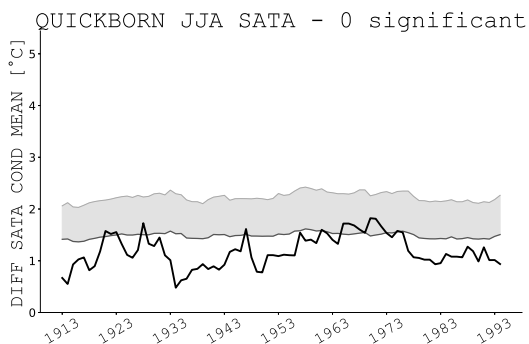
FIG. A.21. | Same as Fig. A.20, but for Zagreb – Gric, HR station (A – D) and for Quickborn (Kurzer Kamp), DE station (E – H).
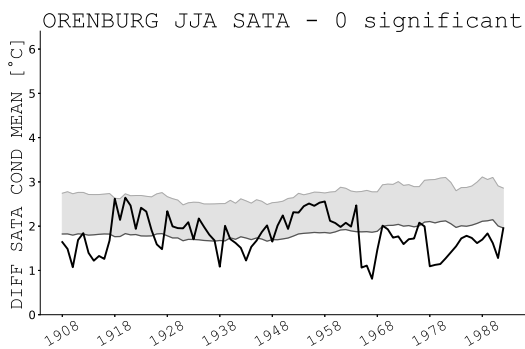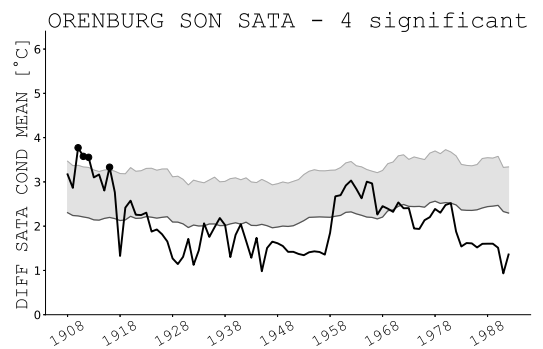
Fig. A.22. | Same as Fig. A.20, but for Hamburg, DE station (**A – D**) and for Orenburg, RU station (**E – H**).

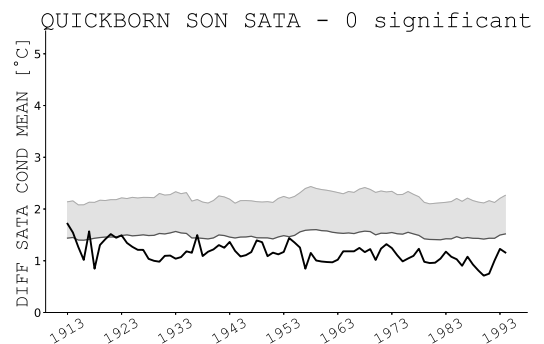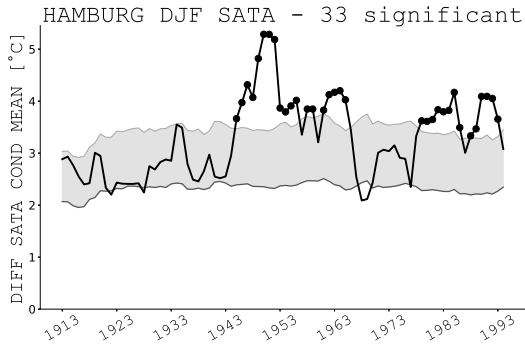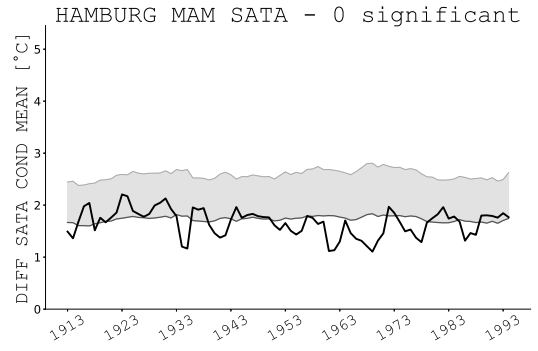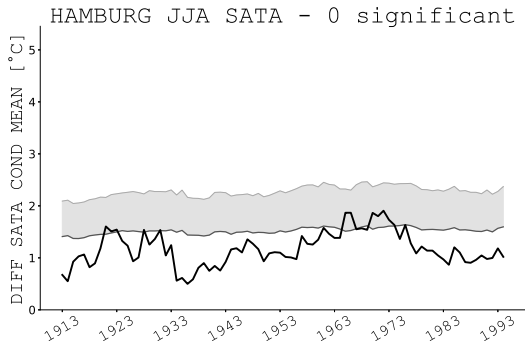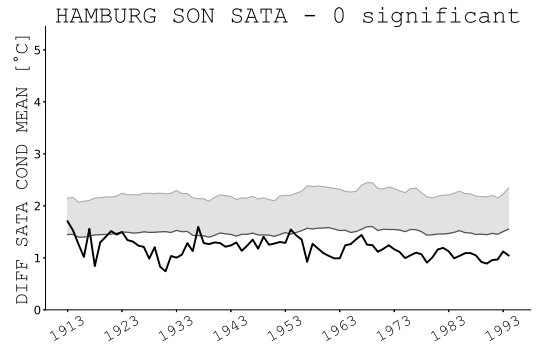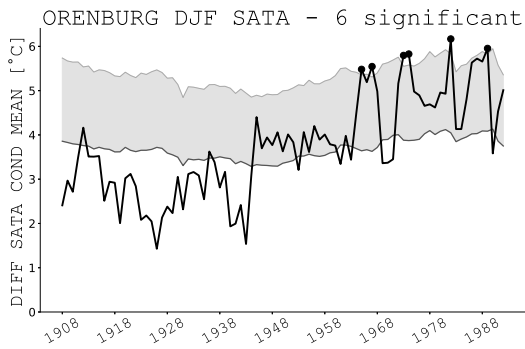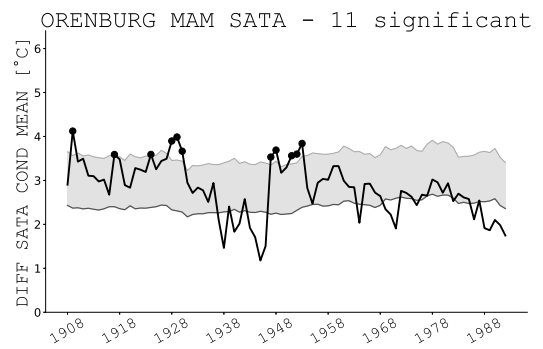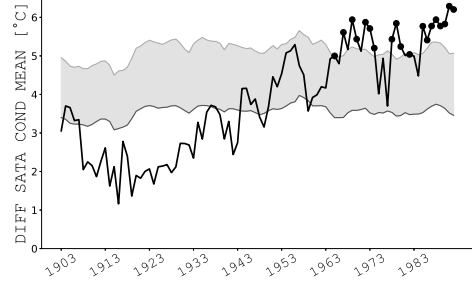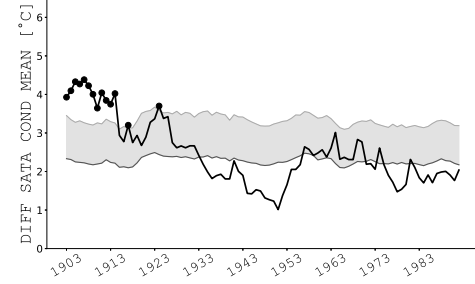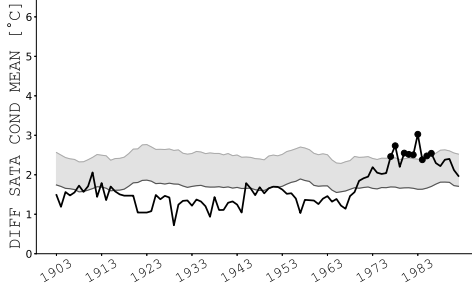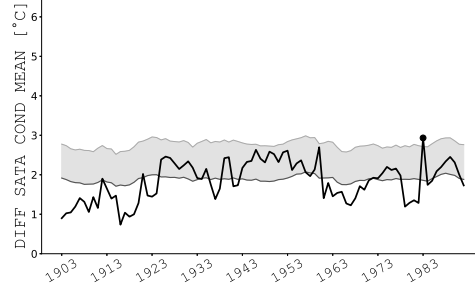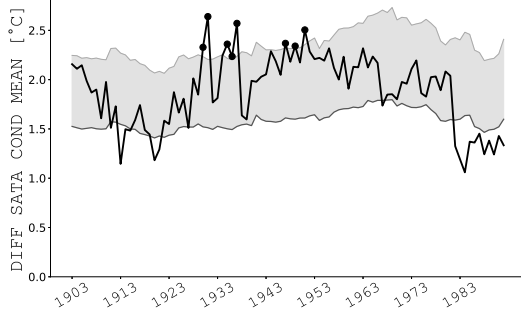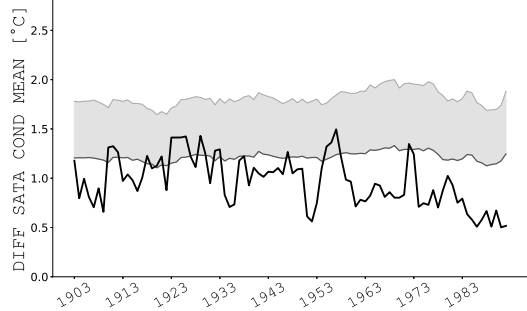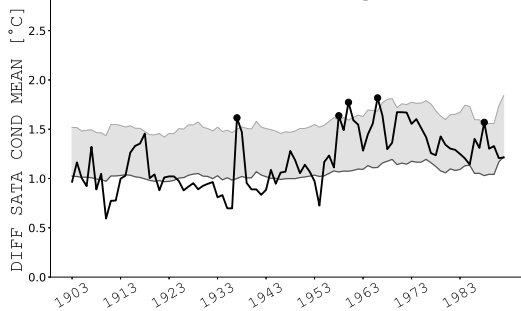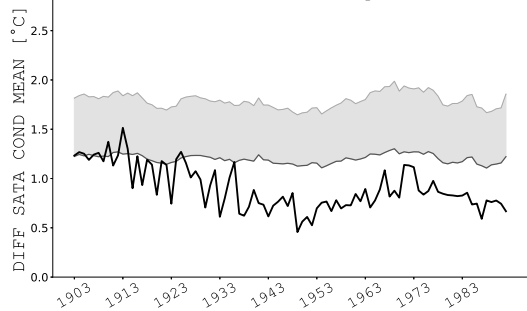**Fig. A.23.** | Same as Fig. A.20, but for St. Petersburg, RU station (**A** – **D**) and for CET — Central England Temperature, UK station (**E** – **H**).
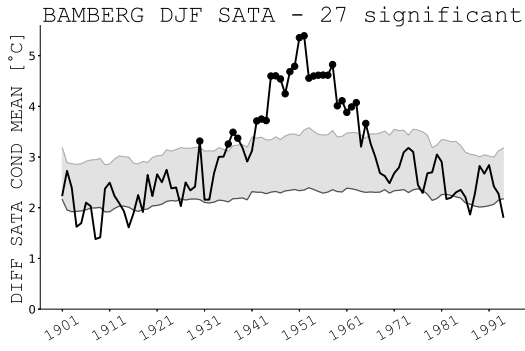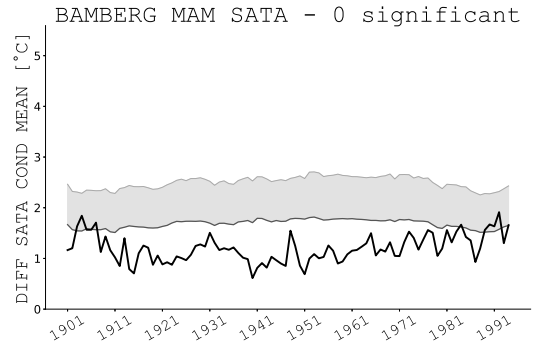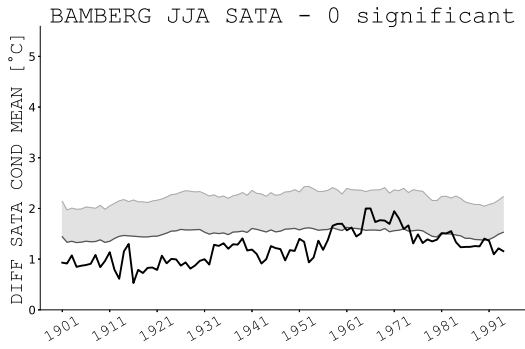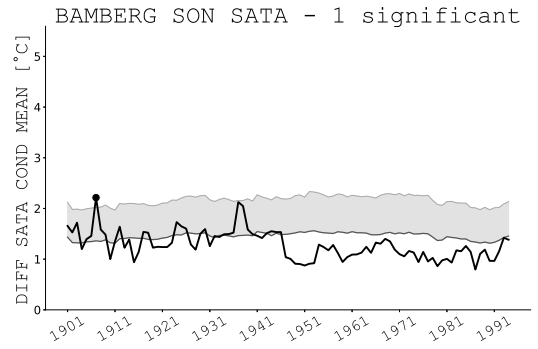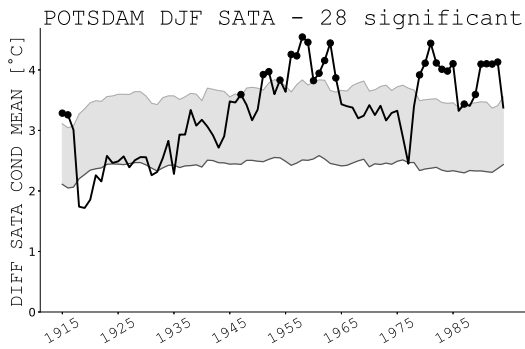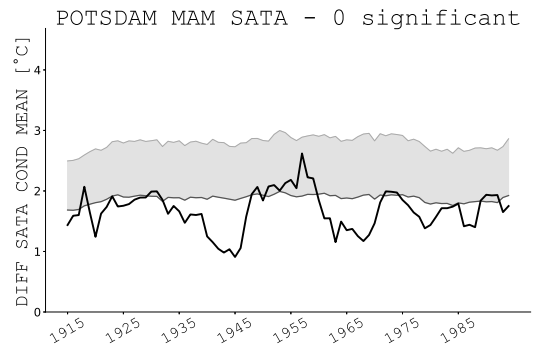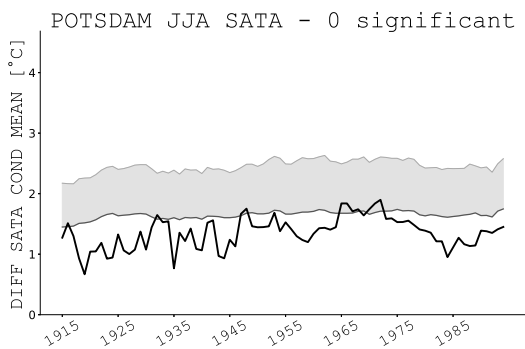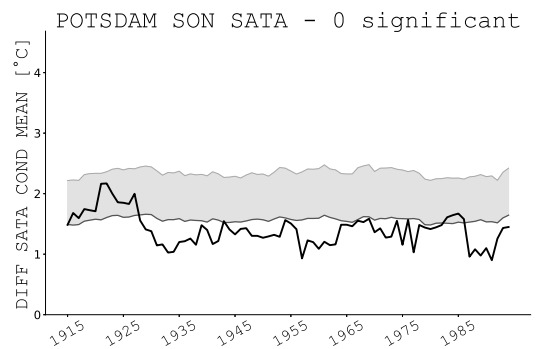
Fig. A.24. | Same as Fig. A.20, but for Bamberg, DE station (**A** – **D**) and for Potsdam, DE station (**E** – **H**).

#	model acronym	no. runs
1.	CCSM4	6
2.	CNRM-CM5	10
3.	CSIRO-Mk3-6-0	10
4.	CanESM2	5
5.	GFDL-CM3	5
6.	GISS-E2-Hp1	6
7.	GISS-E2-Hp2	5
8.	GISS-E2-Hp3	6
9.	GISS-E2-Rp1	6
10.	GISS-E2-Rp2	6
11.	GISS-E2-Rp3	6
12.	HadGEM2-ES	5
13.	IPSL-CM5A-LR	6
14.	MIROC5	4
15.	MRI-CGCM3	3

TABLE A.2. | Coupled Model Intercomparison Project Phase 5 (CMIP5) 20thcentury simulations considered in this thesis.

observed and simulated wavelet spectra using root-mean-square distance and Pearson's correlation, with zero distance and unit correlation indicating the perfect match. The observed and simulated causal maps were compared using, once again, the standard Pearson's correlation coefficient, as well as the so-called Adjusted Rand Index (ARI). Both measures were computed for the pairs of interaction maps (observation vs. individual simulation) filled with ones or zeros depending on whether the significant interaction between the processes of different time scales was identified or not. The ensemble means of these measures are depicted in Fig. 5.15, while the values for all 89 individual runs are presented in Table A.3.

model	run	spectrum			synch.		P-P caus.		P-A caus.	
		L1	rms	corr.	corr.	ARI	corr.	ARI	corr.	ARI
CanESM2	0	255.83	33.50	0.46	0.34	0.29	0.25	0.21	-0.01	-0.01
	1	206.09	26.44	0.68	0.24	0.21	0.13	0.11	0.02	0.02
	2	239.06	31.44	0.40	0.19	0.16	0.26	0.23	-0.00	-0.00
	3	213.64	27.15	0.50	0.19	0.13	0.21	0.18	-0.01	-0.01
	4	163.10	22.97	0.77	0.25	0.20	0.21	0.17	0.04	0.04
	mean	215.55	28.30	0.56	0.24	0.20	0.21	0.18	0.01	0.01
	std	35.42	4.18	0.15	0.06	0.06	0.05	0.05	0.02	0.02
GFDLCM3	0	226.32	30.89	0.73	0.25	0.22	0.09	0.08	0.07	0.06
	1	369.12	55.57	0.40	0.04	0.03	0.06	0.05	-0.03	-0.03
	2	370.19	57.13	0.42	0.02	0.01	0.03	0.03	-0.04	-0.03
	3	359.84	47.20	0.35	0.01	0.01	0.05	0.04	0.00	0.00
	4	338.64	50.35	0.37	-0.03	-0.03	0.06	0.05	0.02	0.01
	mean	332.82	48.23	0.45	0.06	0.05	0.06	0.05	0.00	0.00
	std	60.87	10.48	0.16	0.11	0.10	0.02	0.02	0.04	0.04
GISSE2Hp1	0	298.44	37.25	0.53	0.26	0.21	0.14	0.12	0.01	0.01
	1	319.19	44.98	0.22	0.11	0.09	0.13	0.12	-0.04	-0.04
	2	294.96	37.56	0.49	0.20	0.17	0.05	0.04	-0.02	-0.02
	3	329.87	44.67	0.19	0.22	0.18	0.13	0.11	-0.03	-0.03
	4	231.76	30.94	0.40	0.13	0.11	0.14	0.12	0.01	0.01
	5	219.36	30.13	0.57	0.10	0.09	0.09	0.07	0.04	0.04

model	run	spectrum			synch.		P-P caus.		P-A caus.	
		L1	rms	corr.	corr.	ARI	corr.	ARI	corr.	ARI
	mean	282.26	37.59	0.40	0.17	0.14	0.11	0.10	-0.01	-0.00
	std	45.96	6.40	0.16	0.06	0.05	0.04	0.03	0.03	0.03
GISSE2Hp2	0	336.96	45.19	0.53	0.26	0.22	0.21	0.18	0.00	0.00
	1	146.18	18.81	0.81	0.20	0.16	0.20	0.17	0.01	0.01
	2	332.06	43.50	0.27	0.16	0.13	0.05	0.05	-0.00	-0.00
	3	360.31	49.07	0.42	0.19	0.16	0.16	0.14	0.01	0.01
	4	275.13	40.98	0.40	0.18	0.15	0.14	0.12	0.03	0.02
	mean	290.13	39.51	0.49	0.20	0.17	0.15	0.13	0.01	0.01
	std	86.35	11.94	0.20	0.04	0.03	0.06	0.05	0.01	0.01
GISSE2Hp3	0	305.46	46.99	0.36	0.24	0.20	0.25	0.21	0.04	0.03
	1	267.36	36.56	0.46	0.28	0.22	0.26	0.23	0.01	0.01
	2	266.40	34.66	0.29	0.22	0.19	0.21	0.19	0.00	0.00
	3	307.34	42.73	0.21	0.15	0.13	0.14	0.12	-0.04	-0.03
	4	287.15	38.97	0.25	0.04	0.03	0.15	0.13	-0.01	-0.01
	5	299.09	40.12	0.23	0.12	0.10	0.14	0.12	0.04	0.03
	mean	288.80	40.00	0.30	0.17	0.15	0.19	0.17	0.01	0.01
	std	18.39	4.42	0.09	0.09	0.07	0.05	0.05	0.03	0.02
GISSE2Rp1	0	150.93	19.67	0.77	0.24	0.20	0.21	0.18	-0.01	-0.01
	1	150.93	19.67	0.77	0.23	0.20	0.19	0.16	-0.01	-0.01
	2	233.87	31.48	0.60	0.28	0.24	0.14	0.12	-0.01	-0.01

model	run	spectrum			synch.		P-P caus.		P-A caus.	
		L1	rms	corr.	corr.	ARI	corr.	ARI	corr.	ARI
	3	165.82	24.14	0.65	0.20	0.16	0.13	0.11	-0.03	-0.02
	4	223.57	30.95	0.53	0.20	0.16	0.10	0.09	-0.03	-0.03
	5	211.45	28.78	0.53	0.30	0.26	0.21	0.18	-0.00	-0.00
	mean	189.43	25.78	0.64	0.24	0.20	0.16	0.14	-0.02	-0.01
	std	37.81	5.39	0.11	0.04	0.04	0.05	0.04	0.01	0.01
	0	263.73	36.43	0.24	0.20	0.17	0.15	0.12	0.04	0.03
	1	195.15	26.74	0.56	0.17	0.15	0.19	0.17	-0.00	-0.00
	2	296.74	38.06	0.20	0.18	0.15	0.20	0.18	0.06	0.05
GISSE2Rp2	3	182.57	26.23	0.65	0.15	0.12	0.19	0.17	0.01	0.01
	4	202.83	27.79	0.53	0.15	0.13	0.14	0.12	0.04	0.04
	5	179.12	25.07	0.65	0.13	0.11	0.12	0.10	-0.03	-0.02
	mean	220.02	30.05	0.47	0.16	0.14	0.17	0.14	0.02	0.02
	std	48.55	5.66	0.20	0.02	0.02	0.04	0.03	0.03	0.03
	0	202.88	25.05	0.59	0.14	0.11	0.18	0.16	0.00	0.00
	1	345.19	42.50	-0.04	0.22	0.19	0.22	0.19	0.03	0.03
	2	167.37	23.75	0.70	0.20	0.17	0.23	0.20	0.02	0.02
GISSE2Rp3	3	241.36	31.25	0.32	0.26	0.22	0.15	0.13	0.01	0.01
	4	224.62	32.69	0.39	0.12	0.10	0.23	0.20	0.04	0.03
	5	193.89	24.10	0.66	0.18	0.15	0.18	0.15	-0.02	-0.02
	mean	229.22	29.89	0.44	0.19	0.16	0.20	0.17	0.01	0.01

model	run	spectrum			synch.		P-P caus.		P-A caus.	
		L1	rms	corr.	corr.	ARI	corr.	ARI	corr.	ARI
	std	62.27	7.26	0.28	0.05	0.05	0.03	0.03	0.02	0.02
HadGem2ES	0	323.43	53.66	0.13	-0.01	-0.01	-0.00	-0.00	-0.02	-0.01
	1	218.69	33.73	0.66	0.19	0.14	0.09	0.07	0.02	0.02
	2	546.59	99.96	-0.15	-0.06	-0.05	-0.01	-0.01	0.03	0.02
	3	201.72	28.16	0.77	-0.05	-0.04	-0.05	-0.04	-0.03	-0.02
	mean	322.61	53.88	0.35	0.02	0.01	0.01	0.01	0.00	0.00
	std	158.72	32.61	0.44	0.12	0.09	0.06	0.05	0.03	0.02
IPSL_CM5A_LR	0	245.36	36.88	0.67	0.00	0.00	-0.03	-0.02	0.00	0.00
	1	228.21	39.03	0.45	-0.03	-0.02	-0.01	-0.00	-0.03	-0.03
	2	117.71	14.95	0.91	-0.06	-0.05	-0.02	-0.02	-0.02	-0.01
	3	220.38	29.35	0.50	0.06	0.04	-0.01	-0.01	0.01	0.01
	4	164.27	21.44	0.78	0.01	0.00	0.03	0.03	0.01	0.01
	5	199.99	26.35	0.88	-0.03	-0.02	0.08	0.07	-0.01	-0.01
	mean	195.99	28.00	0.70	-0.01	-0.01	0.01	0.01	-0.01	-0.00
	std	47.37	9.15	0.19	0.04	0.03	0.04	0.04	0.02	0.01
MIROC5	0	743.84	99.74	0.82	0.20	0.16	0.10	0.08	0.05	0.04
	1	983.79	150.34	0.15	0.25	0.21	-0.01	-0.01	-0.01	-0.01
	2	705.02	92.86	0.85	0.27	0.22	-0.01	-0.01	-0.02	-0.02
	3	1013.64	148.17	0.53	0.17	0.13	-0.03	-0.02	0.03	0.03
	4	538.51	74.42	0.55	0.18	0.13	-0.00	-0.00	-0.00	-0.00

model	run	spectrum			synch.		P-P caus.		P-A caus.	
		L1	rms	corr.	corr.	ARI	corr.	ARI	corr.	ARI
	mean	796.96	113.11	0.58	0.21	0.17	0.01	0.01	0.01	0.01
	std	199.95	34.28	0.28	0.04	0.04	0.05	0.04	0.03	0.02
MRICGCM3	0	494.99	68.81	0.06	-0.04	-0.03	-0.03	-0.02	0.00	0.00
	1	222.48	30.43	0.79	0.00	0.00	0.04	0.03	0.09	0.08
	2	150.15	23.49	0.79	0.17	0.14	-0.02	-0.01	-0.00	-0.00
	mean	289.21	40.91	0.55	0.04	0.04	-0.00	-0.00	0.03	0.03
	std	181.84	24.41	0.42	0.11	0.09	0.04	0.03	0.05	0.04
CCSM4	0	306.30	41.79	0.83	0.15	0.13	0.19	0.16	0.00	0.00
	1	320.18	46.14	0.74	0.16	0.13	0.26	0.21	0.07	0.06
	2	333.52	47.07	0.57	0.11	0.09	0.12	0.10	0.00	0.00
	3	215.04	26.69	0.97	0.30	0.25	0.24	0.21	0.02	0.02
	4	297.87	49.97	0.78	0.17	0.15	0.18	0.15	0.00	0.00
	5	397.94	55.47	0.84	0.09	0.07	0.41	0.36	-0.01	-0.01
	mean	311.81	44.52	0.79	0.16	0.14	0.23	0.20	0.01	0.01
	std	59.24	9.84	0.13	0.07	0.06	0.10	0.09	0.03	0.02
CNRMCM5	0	337.05	43.68	0.04	0.21	0.18	0.25	0.22	-0.01	-0.01
	1	319.58	42.20	0.14	0.27	0.23	0.19	0.16	0.02	0.01
	2	296.14	37.78	0.09	0.17	0.14	0.21	0.17	-0.00	-0.00
	3	285.90	37.43	0.15	0.15	0.12	0.13	0.10	-0.02	-0.02
	4	285.07	39.34	0.31	0.17	0.13	0.24	0.19	0.06	0.05

model	run	spectrum			synch.		P-P caus.		P-A caus.	
		L1	rms	corr.	corr.	ARI	corr.	ARI	corr.	ARI
	5	156.01	20.67	0.75	0.14	0.12	0.25	0.21	-0.00	-0.00
	6	282.05	39.05	0.10	0.19	0.16	0.25	0.22	-0.02	-0.02
	7	235.25	28.30	0.46	0.12	0.08	0.17	0.14	0.02	0.02
	8	326.29	42.56	-0.02	0.21	0.18	0.17	0.14	-0.02	-0.02
	9	253.06	33.93	0.33	0.14	0.10	0.19	0.17	-0.03	-0.03
	mean	271.04	35.70	0.26	0.18	0.14	0.20	0.17	-0.00	-0.00
	std	51.74	7.11	0.24	0.05	0.04	0.04	0.04	0.03	0.02
CSIROmk360	0	188.47	26.30	0.66	-0.01	-0.01	0.07	0.06	0.10	0.09
	1	266.38	33.23	0.37	0.12	0.10	-0.01	-0.00	-0.01	-0.01
	2	155.07	20.38	0.77	-0.02	-0.01	0.01	0.01	-0.02	-0.01
	3	158.04	23.95	0.68	0.01	0.01	0.03	0.02	-0.02	-0.02
	4	153.50	20.97	0.76	0.01	0.01	0.03	0.03	0.04	0.03
	5	146.96	20.43	0.79	0.04	0.04	0.08	0.07	-0.01	-0.01
	6	294.90	40.98	0.70	-0.05	-0.04	0.02	0.01	0.02	0.01
	7	231.63	33.85	0.36	0.00	0.00	0.13	0.11	0.02	0.02
	8	189.17	23.66	0.71	0.03	0.02	0.04	0.03	0.02	0.02
	9	252.70	31.98	0.45	0.02	0.02	0.04	0.03	-0.01	-0.01
	mean	205.37	27.72	0.62	0.02	0.01	0.04	0.03	0.00	0.00
	std	56.79	7.46	0.18	0.05	0.04	0.04	0.03	0.02	0.02

model	run	spectrum			synch.		P-P caus.		P-A caus.	
		L1	rms	corr.	corr.	ARI	corr.	ARI	corr.	ARI

TABLE A.3. | Measures of similarity between observed Niño 3.4 time series and modelled within the CMIP5 framework. The first three columns reflect similarity of the spectra using *L1* distance, L2 distance (root-mean-square, *rms*), and Pearson's correlation (*corr.*), then two columns measuring the similarity of phase synchronisation (**synch.**) maps (*corr.* and adjusted rand index — *ARI*) and the same measures for phase-phase causality (**P-P caus.**), and phase-amplitude causality (**P-A caus.**) maps. The ensemble means for the models also shown in Fig. 5.15.